



Preparation and studies of properties of nanostructured magnetic films for applications in magnetoacoustic and spintronic devices

Anastasia Pavlova

► **To cite this version:**

Anastasia Pavlova. Preparation and studies of properties of nanostructured magnetic films for applications in magnetoacoustic and spintronic devices. Micro and nanotechnologies/Microelectronics. Ecole Centrale de Lille, 2014. English. <NNT : 2014ECLI0010>. <tel-01308812>

HAL Id: tel-01308812

<https://tel.archives-ouvertes.fr/tel-01308812>

Submitted on 28 Apr 2016

HAL is a multi-disciplinary open access archive for the deposit and dissemination of scientific research documents, whether they are published or not. The documents may come from teaching and research institutions in France or abroad, or from public or private research centers.

L'archive ouverte pluridisciplinaire **HAL**, est destinée au dépôt et à la diffusion de documents scientifiques de niveau recherche, publiés ou non, émanant des établissements d'enseignement et de recherche français ou étrangers, des laboratoires publics ou privés.

N° d'ordre: 248

ECOLE CENTRALE DE LILLE

THÈSE

Présentée en vue d'obtenir le grade de

DOCTEUR

En

Spécialité: Micro et Nano technologies, Acoustique et Télécommunications

Par

Anastasia PAVLOVA

DOCTORAT DÉLIVRÉ SIMULTANÉMENT PAR L'ÉCOLE CENTRALE DE LILLE ET L'UNIVERSITÉ TECHNIQUE
D'ÉTAT DE SARATOV DANS LE CADRE D'UNE COTUTELLE INTERNATIONALE DE THESE

Titre de la thèse:

**Préparation et études des propriétés des films magnétiques nanostructures pour
des applications en dispositifs magneto-acoustiques et spintroniques**

Soutenue le 8 septembre 2014 devant le jury d'examen:

Président	Mr Didier ROUXEL	Professeur à l'Institut Jean-Lamour et Université de Lorraine
Rapporteur	Mr Yuri FETISOV	Professeur à l'Institut de Radiotechnique, d'Electronique et d'Automatique de Moscou MIREA
Rapporteur	Mr Jean-Marie LEBRETON	Professeur à l'Université de Rouen
Examineur	Mr Michail LOGUNOV	Professeur à l'Université d'État de Mordovia-Ogarev
Encadrant	Mr Alexander SIGOV	Professeur à l'Institut de Radiotechnique, d'Electronique et d'Automatique de Moscou MIREA
Directeur de thèse	Mr Philippe PERNOD	Professeur à l'École Centrale de Lille
Directeur de thèse	Mr Vladimir PREOBRAZHENSKY	Professeur à l'École Centrale de Lille
Directeur de thèse	Mr Yuri FILIMONOV	Directeur SB IRE RAS
Invité	Mr Nicolas TIERCELIN	Chargé de recherche CNRS IEMN
Invité	Mr Abdelkrim TALBI	Maître de Conférences à l'Ecole Centrale de Lille

Thèse préparée dans le Laboratoire International Associé LICs/LEMAs
Institut d'Électronique, Micro-Électronique et Nanotechnologies (IEMN, UMR CNRS 8520, France)
et dans le Laboratoire de Magnétoelectronique
Saratov Branche V.A. Kotelnikov Institut de Radiotechnique et d'Electronique de l'Académie des sciences de Russie
(SB IRE RAS, Russie)
Ecole Doctorale SPI 072 (Lille I, Lille III, Artois, ULCO, UVHC, EC Lille)
PRES Université Lille Nord de France

Table of contents

Remerciements	6
List of abbreviations.....	8
List of figures	9
List of tables.....	17
Introduction	18
1. Lithography methods and its application for fabrication of micro- and nanostructures	20
1.1 Scanning probe lithography methods	22
1.1.1 Force-assisted scanning probe lithography.....	25
1.1.2 Bias-assisted scanning probe lithography.....	27
1.1.3 Atomic force microscope principle	29
1.1.4 Local anodic oxidation by atomic force microscope: principle and application.....	34
1.2 Electron-beam lithography	43
1.2.1 Electron-beam resists.....	44
1.2.2 Exposure parameters.....	45
1.2.3 Electron-beam lithography challenges	46
1.2.4 Electron-beam lithography application	50
1.3 Conclusions	51
2. Local anodic oxidation of ferromagnetic metal films	52

2.1	Introduction	52
2.2	Ferromagnetic thin film deposition	53
2.3	Experimental description.....	54
2.4	Local anodic oxidation reproducibility and sample drift	57
2.5	Dependence of local anodic oxidation results on parameters of the process	59
2.5.1	Dependence on bias voltage between tip and surface	59
2.5.2	Dependence on oxidation time	61
2.5.3	Dependence on relative humidity	64
2.5.4	Dependence on oscillating amplitude set point of the tip.....	64
2.5.5	Dependence on other factors	66
2.6	Local anodic oxidation and tip state	70
2.7	Conclusions	73
3.	Local anodic oxidation of textured ferromagnetic metal films.....	74
3.1	Introduction	74
3.2	Film texture and oxidation of textured metal films	75
3.3	Local anodic oxidation of textured polycrystalline Ni(111) and Ni(200) films.....	77
3.3.1	Fabrication and properties of textured Ni films.....	77
3.3.2	Local anodic oxidation results for textured Ni films	79
3.4	Local anodic oxidation of textured polycrystalline Fe(110) and Fe(200) films.....	82
3.5	Conclusions	84
4.	Studying of the properties of nanostructures made by scanning probe lithography	85
4.1	Introduction	85
4.2	Current-voltage characteristics of nanostructures made by local anodic oxidation	86
4.3	Auger spectroscopy of nanostructures made by local anodic oxidation	93
4.4	Current-voltage characteristics and magnetoresistance of nanostructures made by mechanical scratching	96
4.5	Conclusions	101
5.	Hypersonic magnetically tunable surface phononic crystals	102

5.1	Introduction	102
5.2	Feasibility to fabrication of surface phononic crystalsby local anodic oxidation	105
5.3	Fabrication of surface phononic crystals by electron-beam lithography	111
5.3.1	1D surface phononic crystals devices design	111
5.3.2	Definition of 1D surface phononic crystals fabrication process.....	113
5.3.3	Investigation of 1D surface phononic crystals fabricated by electron-beam lithography	133
5.3.4	Feasibility to fabrication of 2D surface phononic crystals	136
5.4	Conclusions	143
Conclusions and future prospects.....		144
Résumé étendu en Français.....		146
References		149
Appendix A		166

Remerciements

Ce travail a été réalisé au sein du Laboratoire International associé en Magnéto-Acoustique non-linéaire de la matière condensée (LICS/LEMAC), à l'Institut d'Electronique de Microélectronique et de Nanotechnologie (IEMN, CNRS UMR 8520, France) en cotutelle avec l'Université Technique d'État de Saratov (SSTU, Russie).

Je tiens à remercier tout d'abord, mes directeurs de thèse du côté français les Professeurs Philippe PERNOD et Vladimir PREOBRAZHENSKY de l'Ecole Centrale de Lille pour m'avoir accueilli dans leur équipe (LICS/LEMAC-IEMN), pour leur encadrement et pour la confiance qu'ils m'ont témoigné tout au long de ces années de travail.

Je remercie au même titre mon directeur de thèse du côté Russe, le Professeur de l'Université Technique d'État de Saratov Yuri FILIMONOV. Je tiens à lui exprimer toute ma reconnaissance pour l'intensité de son partage et de son soutien. Je remercie également mon encadrant dans l'IRE RAS Y. KHIVINTSEV pour son attention et son soutien. Je tiens à souligner que son expérience a permis de guider de ce travail et de m'orienter dans cet environnement scientifique.

Un grand merci à mes amis et collègues du LICS/LEMAC. Je remercie vivement Yulia KUTLUBAEVA pour le temps passé ensemble en France et en Russie. Vivre en France aurait été très différent sans sa compagnie. J'espère que notre amitié continuera encore long temp. Grâce aux discussions avec Abdelkrim TALBI et ses bonnes idées, cette thèse est devenue plus homogène et sans l'aide de Jean-Claude GERBEDOEN, je n'aurais pas pu mettre en oeuvre ces idées. Je le remercie donc pour le temps qu'il a passé avec moi en Salle Blanche. Je tiens aussi à remercier Nicolas TIERCELIN pour son aide technologique. Merci à mes collègues, professeurs Leonid KRUTYANSKI, Alexey KLIMOV et Yuri PYLNOV pour les discussions et leurs conseils précieux. J'exprime ma gratitude à mon ami et collègue Vladislav ALESHIN et mes confrères de programme co-tutelle Sergey YANKIN, Sergey KOSHELYUK, Nikolay SMAGIN et Pavel SHIRKOVSKY qui m'ont toujours encouragée durant ces années. Je souhaite également aux deux Sergey, qu'ils soutiennent leur thèse aisément.

Merci à mes amis français Adrien B., Alain A., Marina D., Cyrille G. pour leur compagnie durant les activités extérieures.

Mes remerciements vont également à tous le personnel de la centrale de technologie, de la plateforme de microscopie champ proche et de la centrale de caractérisation de l'IEMN qui ont permis ces recherches, en particulier F. VAURETTE, M. FRANÇOIS, D. DERESMES, C. BRILLARD, A. LEROY, A. FATTORINI, V. AVRAMOVIC-SBRUGNERA et S. LEPILLIET. Je souhaite par ailleurs remercier mes collègues de l'IRE RAS Y. NIKULIN, V. SAHAROV, E. PAVLOV, A. DZHUMALIEV, A. TEMIRYAZEV.

J'associe également à ces remerciements le Professeur Jean-Marie LEBRETON de Groupe de Physique des Matériaux de l'Université de Rouen et le Professeur Yuri FETISOV de l'Institut de Radiotechnique, d'Electronique et d'Automatique de Moscou MIREA d'avoir accepté de rapporter ce travail, ainsi que les membres du jury, le Professeur Michail LOGUNOV de l'Université d'État de Mordovia-Ogarev, Professeur Alexander SIGOV de l'Institut de Radiotechnique, d'Electronique et d'Automatique de Moscou MIREA et Professeur Didier ROUXEL de l'Institut Jean-Lamour.

Je remercie aussi l'Ambassade de France à Moscou et le Ministère des Affaires Etrangères français pour la bourse de thèse qu'ils m'ont attribuée, ce qui m'a permis de venir en France durant la moitié de ce travail.

Enfin, je remercie toute ma famille, en particulier mon mari Oleg pour son attention et son soutien affectif au cours de ces trois années, mon père Yuri, ma mère Lidia et ma sœur Ekaterina pour leur soutien.

Je n'en serais pas là aujourd'hui sans le soutien de toutes ces personnes. Je leur en suis reconnaissante.

List of abbreviations

AES	Auger electron spectroscopy
AFM	Atomic force microscope
AMR	Anisotropic magnetoresistance
DIW	Deionized water
EBL	Electron beam lithography
ESB	Energy selective backscattered detector
FEM	Finite element analysis
HMDS	Hexamethyldisilazane
IDT	Interdigital transducer
IPA	Isopropanol alcohol
LAO	Local anodic oxidation
MFM	Magnetic force microscopy
MIBK	Methyl isobutyl ketone
PMMA	Polymethyl methacrylate
PnC	Phononic crystal
SAW	Surface acoustic wave
SEM	Scanning electron microscope
SPL	Scanning probe lithography
SPM	Scanning probe microscope
STM	Scanning tunneling microscope
UV	Ultraviolet radiation
XRD	X-Ray diffraction

List of figures

1.1	Main kinds of SPM probes: a) STM and b) AFM probes	22
1.2	Force-assisted (a) and bias-assisted (b) SPL methods	22
1.3	Schematic image of nanoindentation by AFM tip (a) and the depth of holes obtained by it (b)	25
1.4	30 nm Ga As particles structure fabricated by nanoscale manipulation to form the letters “nm”	26
1.5	Schematic image of dip-pen nanolithography.....	26
1.6	Schematic image of thermomechanical writing (a) and schematic and photo images of 32x32 probe array system “Millipede” (b)	27
1.7	SEM image of gold nanowires fabricated by tip field evaporation	28
1.8	AFM image of the rhodium dots	28
1.9	Scanning electron images of microprobes with various shapes: a) rectangular, b) triangular. 1 – tip, 2 –flexible cantilever, 3 – chip	30
1.10	AFM probes in box (a) and in tip holder (b)	30
1.11	Dependence of the force F_{ts} (typical values) on distance z between center of front atom of the tip and the sample	31
1.12	Amplitude of the oscillating tip	32
1.13	Tapping mode height (a) and phase angle (b) images of magnetic metal particle tape	32

1.14	Topography (a) and MFM (b) images of magnetic tape.....	32
1.15	AFM system	33
1.16	Views of AFMs Solver P47 (a) and MultiMode (b)	34
1.17	General scheme of local anodic oxidation process for Ni film as an example	35
1.18	Line made by vector LAO on FeCo film.....	36
1.19	University symbol made by raster LAO on Ni film: a) original raster bitmap, b) AFM image, c) cross-sections of oxide structure along the lines 1 and 2	36
1.20	Oxide dot sizes (height and width) dependences on tip-sample voltage and oxidation time for InP.....	39
1.21	AFM images of oxide dots on Si (a) and sizes (height (b) and width (c)) dependences on oxidation time for contact and tapping modes	40
1.22	Current-voltage characteristics of two oxide lines with different widths at temperature 1.8 K.....	41
1.23	Schematic (a) and AFM (b) images of a Nb/NbO _x tunnel junction	42
1.24	Examples of magnetic structures made by LAO: anisotropic magnetoresistance in the constriction structure on GaMnAs (a) and MFM image and calculated image of magnetization configuration of Co rectangular nanostructure (b)	42
1.25	Schematic image of EBL system (a) and photo of LEICA EBPG 5000Plus EBL system used in our experiments	44
1.26	Undercut resist profile for clean lift-off	45
1.27	EBL resist patterns made with acceleration voltages of 100kV, 50kV and 30kV respectively	46
1.28	Phenomenas caused by electron beam-sample interaction	47
1.29	Proximity effect in positive resist pattern	47
1.30	Monte Carlo simulation of forward and backscattering at beam energies of 30 and 100 keV per electron	48

1.31	Arrows on exposed patterns in the absence of discharging layer	49
1.32	SEM image of mushroom-like pillars	50
1.33	SEM image of Fe magnetic dots	50
2.1	Schematic (a) and photo (b) images of magnetron sputtering system	53
2.2	AFM images of oxide dots on Fe film at different oxidation parameters	54
2.3	Images of films after LAO in vector mode: 2D AFM (a) and mirror phase (b) images of oxide lines on Fe film, 3D AFM image (c) and cross-section image (d) of oxide lines on FeCo film (h-height, d-width of oxide lines)	56
2.4	AFM image (a) and cross-section (b) of 3 oxide lines along the blue line made at the same oxidation parameters	57
2.5	AFM images of circles made by LAO showing a) big sample drift and b) absence of drift influence on oxidation results	58
2.6	Dependences of the oxide sizes (height – solid circles, width – open circles) on bias voltage of the tip for a) Ni, b) FeCo, c) Fe films	61
2.7	AFM images and cross-sections of oxide lines made at the same $T_{ox}=0.5$ s: T=0.05 s, N=10 (a) and T=0.1 s, N=5 (b)	62
2.8	AFM images and cross-sections of oxide lines made at different oxidation time on Fe film	63
2.9	Dependences of the oxide sizes (height – solid circles, width – open circles) on oxidation time for a) Ni, b) Fe, c) Co	63
2.10	Dependences of the oxide sizes (height – solid circles, width – open circles) on relative humidity for Fe film	64
2.11	AFM images and cross-sections of oxide lines made at different SP values	65
2.12	3D AFM images (a, c) and cross-sections of oxide lines (b, d) on FeCo (a, b) and Ni (c, d) film made by 1 (left) and 2 (right) passes of the tip	67
2.13	Oxide line on FeCo film made by 2 passes of the tip on $1*1 \mu\text{m}^2$ scan area: a) 3D AFM image and b) cross-section along the white line	69

2.14	3D AFM image (a) and cross-section (b) of 3 oxide lines along the white line made at the same oxidation parameters by an old tip	70
2.15	SEM image of used diamond coated tip	71
2.16	SEM images of Si tip before LAO (a), after LAO (b) and after mechanical cleaning (c)	71
3.1	Miller indices determination example (a)and Miller indices of important planes in a cubic crystal(the plane (200) is parallel to (100))	75
3.2	XRD patterns (a,b), SEM cross-sections (c,d), top views (e,f)and AMR curves (g,h)of Ni(200) (a,c,e, g) and Ni(111) (b,d,f, h) films	78
3.3	Dependences of the oxide lines height h (a) and width d (b) on oxidation time T for Ni(200) (1) and Ni(111) (2) films; AFM images (c, d) and cross-sections of oxide lines along the Ox (e, f) on Ni (200) and Ni(111) films at T=1, 2.5 and 5 s	80
3.4	Dependences of the oxide lines height h (a) and width d (b) on tip-sample voltage V for Ni(200) (1) and Ni(111) (2) films.....	80
3.5	XRD patterns of Fe(200) (a) and Fe(110) (b) films	82
3.6	Dependences of the oxide lines height h (a) and width d (b) on oxidation time T for Fe(200) (1) and Fe(110) (2) films.....	83
4.1	Microstripes geometry image (a) and AFM camera snapshot (b) and photo of fabricated sample (c).....	86
4.2	Scheme (a) and realization (b) of four-point probe current-voltage characteristics measuring method and whole measuring system (c).....	87
4.3	AFM images of oxide lines with different heights	88
4.4	AFM images of oxide lines on Ni (a) and FeCo (b) microstripes	89
4.5	Current-voltage characteristics of Ni microstripe before (a) and after (b) LAO at 300K and 77K	89
4.6	Current-voltage characteristics of FeCo microstripe before (a) and after (b) LAO at 300K and 77K	90

4.7	Barrier height determination of oxide lines on Ni (a) and FeCo (b) microstrips	91
4.8	MFM image of oxide lines on Ni microstripe.....	92
4.9	Sample for Auger-electron spectroscopy: a) schematic image, b) optical microscope image. 1 – Si(100)/SiO ₂ substrate, 2 – contact pads, 3 – Ni microstripe, 4 – oxide line, AB – line of Auger-electron passage	93
4.10	AFM image of oxide structure for AES.....	94
4.11	Current-voltage characteristics of sample before and after LAO.....	94
4.12	Plot of Ni and O distribution on sample surface obtained by AES.....	95
4.13	AFM (a) and SEM (b) images and made along the white line AFM cross-section image (c) of scanning probe fabricated scratches on Ni microstripe.....	96
4.14	Schematic geometry of modified Ni microstrips: a) 1 complete scratch crossing the whole microstripe, b) 2 incomplete scratches (CP – contact pad)	97
4.15	AFM (a) and cross-section images (b) of complete scratch crossing the whole Ni microstripe.....	97
4.16	Current-voltage characteristics of Ni microstripe before (a) and after (b) scanning probe scratching at 300K	98
4.17	Current-voltage characteristics of Ni microstripe after scanning probe scratching at different temperatures.....	98
4.18	AFM (a) and cross-section images (b) of 2 comb scratches on Ni microstripe.....	99
4.19	Current-voltage characteristics of Ni microstripe before and after fabrication of 2 comb scratches at 300K	100
4.20	AMR characteristics of Ni microstripe before and after fabrication of 2 comb scratches at 300K	100
5.1	Investigated SAW delay line	103
5.2	Periodic lines pattern in AFM software	105
5.3	AFM images of 1D periodic oxide lines array on Ni film: a) topography, b) phase	106

5.4	AFM images of topography and phase of 1D (a) and 2D (b) periodic oxide lines arrays on Ni film	106
5.5	Frequency dependences of transmission function S_{21} (a) for the structure with $N = 150$ oxide lines with period $a = 500$ nm and height $h = 1.5$ nm (solid line), $h = 3.5$ nm (dashed line), $h = 5$ nm (dotted line); (b) for the structure with period $a = 500$ nm, height $h = 3.5$ nm and with $N = 100$ oxide lines (solid line), $N = 150$ oxide lines (dashed line), $N = 200$ oxide lines (dotted line); (c) for the structure with period $a = 200$ nm, height $h = 3.5$ nm and with $N = 100$ oxide lines (solid line), $N = 150$ oxide lines (dashed line), $N = 200$ oxide lines (dotted line); (d) for the structure with period $a = 50$ nm, height $h = 3.5$ nm and with $N = 100$ oxide lines (solid line), $N = 150$ oxide lines (dashed line), $N = 200$ oxide lines (dotted line).....	108
5.6	Frequency dependences of transmission function S_{21} for the structure with $N = 150$ oxide lines, height $h = 3.5$ nm in the constant magnetic field (solid line) and without it (dashed line): period $a = 500$ nm (a) and for $a = 200$ nm (b).....	109
5.7	Scheme of PnC fabrication technology using local anodic oxidation by AFM multiprobe system.....	110
5.8	Schematic geometry of IDT (a) and lines array (b).....	111
5.9	Layout of patterns for surface PnC device on 4 GHz: whole device (a) and detailed views of IDTs (b) and lines (c) patterns	112
5.10	Layout of pattern for device connected to Au pad for AFM imaging	113
5.11	Lithography processes: etch-back and lift-off	114
5.12	SEM images of AZnLOF resist patterns of lines (a) and comb fingers 500 nm (b) and lines 250 nm (c) at dose $24 \mu\text{C}/\text{cm}^2$ for EB process	115
5.13	Used bi-layer lift-off technology	117
5.14	SEM and ESB SEM images of resist comb fingers patterns at doses $200 \mu\text{C}/\text{cm}^2$ (a), $220 \mu\text{C}/\text{cm}^2$ (b) and $260 \mu\text{C}/\text{cm}^2$ (c) for LO1 process	117
5.15	ESB SEM images of resist lines (a) and comb fingers (b) patterns for LO2 process	119

5.16	ESB SEM images of resist comb fingers patterns obtained without agitation during the development in MIBK:IPA (1:2) for LO3 process (a) and in MIBK:IPA (1:3) for LO4 process (b)	120
5.17	SEM images of resist comb fingers patterns obtained at 165 $\mu\text{C}/\text{cm}^2$ (a) and 200 $\mu\text{C}/\text{cm}^2$ (b) exposure doses for LO5 process	121
5.18	Another one used bi-layer lift-off technology	122
5.19	ESB SEM images of resist comb fingers (a) and lines (b) patterns for LO6 process	122
5.20	Used single resist layer lift-off process	123
5.21	SEM images of structures obtained at dose 560 $\mu\text{C}/\text{cm}^2$ using LO7 process: comb fingers 500 nm (a) and lines 500 nm (b), comb fingers 250 nm (c) and lines 250 nm (d).....	124
5.22	SEM images of residual metal on comb fingers 250 nm at doses 550 $\mu\text{C}/\text{cm}^2$ (a), 540 $\mu\text{C}/\text{cm}^2$ (b) and 530 $\mu\text{C}/\text{cm}^2$ (c) and on fingers 500 nm at dose 530 $\mu\text{C}/\text{cm}^2$ (d).....	125
5.23	Reflection frequency responses of IDTs 500 nm (a) and 250 nm (b) obtained at dose 560 $\mu\text{C}/\text{cm}^2$	125
5.24	Scheme of chosen device fabrication technology using e-beam lithography	128
5.25	Distortion of the patterns because of charge effect	129
5.26	Scheme of fabrication of golden contact pad	131
5.27	Photo of fabricated sample (a) and optical microscope image of device for AFM imaging (b).....	131
5.28	Optical microscope images of obtained devices 500 nm: IDT (a) and Ni lines (b).....	132
5.29	SEM image of IDT500 nm	132
5.30	SEM images of IDTs 500 nm (a) and 250 nm (b).....	133
5.31	SEM images of Ni lines 500 nm (a) and 250 nm (b).....	133
5.32	AFM image and cross-section images of Ni lines 500 nm	134
5.33	Used network analyzer and probe station	134

5.34	Measured transmission frequency responses of IDTs with (solid line) and without (dashed line) PnC for 2 GHz (a) and 4 GHz (b).....	135
5.35	Calculated (solid line) and measured (dashed line) transmission frequency responses of IDTs with PnC for 2 GHz (a) and 4 GHz (b).....	135
5.36	MFM image of Ni lines 500 nm	136
5.37	Calculated transmission frequency responses of PnC for 2 GHz (solid line) and same crystal in applied constant magnetic field $H=300$ Oe (dashed line).	136
5.38	Schematic geometry of pillars	137
5.39	Layout of pillars 160 and 320 nm	138
5.40	SEM images of resist patterns of pillars for EB (a) and LO6 (b) processes	138
5.41	SEM images of pillars obtained by LO7 process using different electron-beam doses: 560 (a), 550 (b), 540 (c), 530 (d) and 510 (e) $\mu\text{C}/\text{cm}^2$	139
5.42	SEM images of fabricated pillars 160 nm (a), 320 nm (b), 520 nm (c)	141
5.43	AFM (a) and cross-section (b) images of pillars 520 nm array	141
5.44	Detailed 3D AFM (a), 2D AFM (b) and cross-section (c) images of pillars 520 nm array	142

List of tables

1.1	Comparison of different kinds of nanolithographic techniques	21
1.2	SPL methods.....	23
1.3	Materials patterned by LAO	38
1.4	Examples of LAO application	40
1.5	Popular electron-beam resists	45
2.1	Tips used for experiments	55
2.2	Comparison of anodic and cathodic oxidation	59
2.3	Oxide lines sizes on Fe film at different SP values	65
2.4	Oxide lines sizes obtained on Ni film by different tips	66
2.5	Oxide lines sizes on Ni and FeCo films for 1 and 2 passes of the tip	67
2.6	Oxide lines sizes on FeCo and Fe films at different scan sizes	68
2.7	LAO parameters for fabrication 500 nm sized oxide lines	73
4.1	Nonlinear coefficient α of microstripes current-voltage characteristics before and after LAO at temperatures 300 and 77K.....	90
4.2	Content of Ni and O in several points of oxidized and not oxidized region	95
5.1	Design parameters of SAW devices	112
5.2	Summary of the fabrication processes for PnC structures.....	127
5.3	Exposition parameters	129
5.4	Design parameters of pillars.....	137
5.5	Exposition parameters for pillars fabrication	140

Introduction

Nowadays ferromagnetic materials and structures based on them are used very actively in different applications: magnetoresistive random-access memory, high precision magnetic sensors or even new electronic components – spintronic devices based on transfer of electron spins [1]. Also the main trend of modern electronics is a reduction of elements dimensions to submicron scale. Thereby investigation of the magnetic nanostructures is of great interest and their fabrication methods and properties are intensively studied.

One of the actively discussed applications of submicrometer structure arrays is high frequency range phononic crystals (PnCs) for surface acoustic waves (SAW). Simultaneously there is a number of papers [2-6] on variation of acoustic parameters of magnetoelastic PnCs using an external magnetic field (so-called ΔE -effect). The band gap of the phononic crystal can be shifted by applied magnetic field. This can be used for wireless and contactless bandwidth switching in microwave frequency SAW filters and sensors.

In this work an investigation of magnetic submicron structures fabrication using scanning probe lithography (SPL) and electron-beam lithography (EBL) was carried out. As SPL and especially probe oxidation of ferromagnetic materials still stays not well enough studied a great part of the work is focused on formation of structures by this technique and studying of properties of the fabricated structures. Challenging of nanoscaled structures obtained by SPL and EBL in magnetically adjusted PnCs for microwave frequency range SAW was shown. Similarly structures fabricated by the SPL are of great interest for fabrication of planar magnetic tunnel junctions as new basic elements for magnetoresistive and spintronic devices.

The thesis consists of five chapters. Chapter 1 describes the utilized lithographic processes. In Chapter 2 detailed study of scanning probe local anodic oxidation (LAO) of different ferromagnetic metal films is given. Key point of this study is investigation of influence of various parameters on sizes of structures fabricated on commonly used Ni films and on FeCo as well.

Influence of oxidation process on the probe was studied for the first time. Chapter 3 is focused on the probe oxidation of ferromagnetic metal films with different textures. Influence of film texture on the SPL oxidation was not studied previously and results of this study can be used in optimization of fabrication of nanostructures. Chapter 4 describes investigation of the electrical and chemical properties of submicrometer scaled structures fabricated using scanning probe lithography methods: LAO and mechanical scratching by the probe. The results showed that the properties of obtained structures differ from properties of initial material and it was concluded that these techniques could be implemented for fabrication of advanced nanostructures for application in different devices. Single structures can be utilized as tunnel and magnetoresistive structures for future realization of spintronic devices. Arrays of structures made by SPL can be used as hypersonic PnCs. In Chapter 5 a detailed description of technological processes for fabrication of magnetically controlled phononic structures by SPL and EBL is presented as well as results on theoretical and experimental investigation of these structures. Recommendations on further development of structures are also given.

From thesis content some main points presented to defense can be extracted:

1. Experimental results of investigation of LAO on Ni, Fe, FeCo and Co films. These results can be used for determination of LAO parameters and instruments required to obtain nanostructures with certain sizes by this lithographic method.
2. Experimental results of investigation of LAO on Ni(200), Ni(111), Fe(200) and Fe(110) films. These results can be used to control LAO process.
3. Technology of fabrication of hypersonic 1D magnetically tunable PnCs on Ni using LAO method. This technology can be used for further realization of phononic structures for application in magnetic sensors and wireless SAW filters.
4. Fabrication process suitable for realization of both 1D and 2D magnetically tunable PnCs on Ni for 2-6 GHz using EBL method. This fabrication process allows to obtain easily good phononic structures with different configurations.

1. Lithography methods and its application for fabrication of micro- and nanostructures

Basic process for fabrication of submicrometer scale structures is lithography. There is a lot of nanolithographic techniques. Main kinds of these techniques are given in Table 1.1.

For high frequency phononic crystal fabrication it is better to use a lithographic process with high resolution and easy processing. Electron-beam lithography is widely used for this purpose. For us scanning probe lithography also seems to be suitable method for phononic crystal fabrication.

Table 1.1. Comparison of different kinds of nanolithographic techniques.

Kind of lithography	Patterning principle	Environment	Resolution	Advantages	Challenges
Scanning probe lithography	Tip-substrate interaction	Ambient or vacuum	<10 nm	<ul style="list-style-type: none"> – High resolution – Variety of patterning materials – Low cost – Easy operation 	<ul style="list-style-type: none"> – Serial patterning difficulties – Poor accessibility and controllability of large scale patterning
Photolithography	Light exposure of polymer resist	Vacuum	>100 nm	<ul style="list-style-type: none"> – Parallel patterning – Good controllability 	<ul style="list-style-type: none"> – Multiple process steps – Poor resolution
Electron beam lithography	Electron exposure of polymer resist	Vacuum	<50 nm	<ul style="list-style-type: none"> – High resolution – Good controllability 	<ul style="list-style-type: none"> – High cost – Multiple-steps and long process
Focused ion beam lithography	Substrate cutting by ion beam	Vacuum	50 nm	<ul style="list-style-type: none"> – High resolution – Good controllability 	<ul style="list-style-type: none"> – High cost – Multiple-steps and long process
Nanoimprint lithography	Mechanical deformation of imprint resist	Vacuum or ambient	~100 nm	<ul style="list-style-type: none"> – Parallel patterning – Low cost 	<ul style="list-style-type: none"> – Multiple-steps for large scale patterning

1.1 Scanning probe lithography methods

One of the perspective and extensively studied methods to create nanostructures is scanning probe lithography (SPL) based on interaction between a tip of a scanning probe microscope (SPM) and a substrate on purpose to modify the substrate [7, 8]. The main advantages of this kind of nanopatterning are high resolution, variety of patterning materials, low cost and easy operation while most of other lithographic process are expensive and have multiple-steps [8]. The main drawback of SPL is poor controllability of large-scale patterning so it is mainly used for single nanostructures fabrication.

For substrate modification by SPL the same probes as for scanning probe microscopy are used: 1) scanning tunneling microscopy (STM) probe and 2) atomic force microscopy (AFM) probe (Figure 1.1) [9].

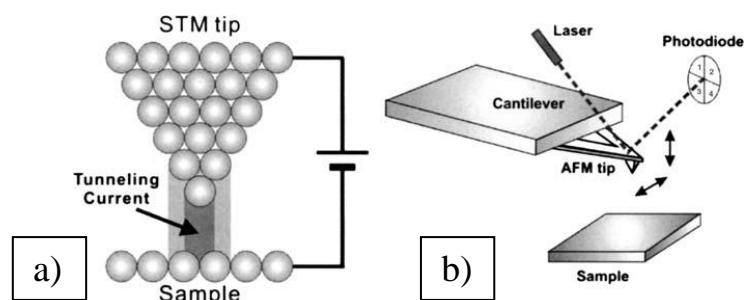


Figure 1.1. Main kinds of SPM probes: a) STM and b) AFM probes [9].

SPL can be carried out by mechanical or electrical interaction between the probe and the substrate. Therefore, there are two kinds of SPL: physical force SPL (or force-assisted SPL) and electrical SPL (or bias-assisted SPL) (Figure 1.2). All SPL methods are summarized in Table 1.2.

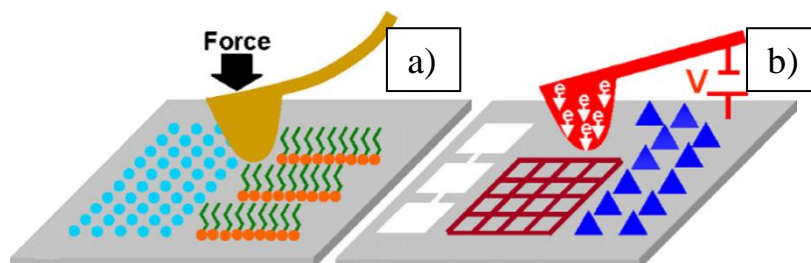


Figure 1.2. Force-assisted (a) and bias-assisted (b) SPL methods [8].

Table 1.2. SPL methods.

SPL method		Kind of probe	Mechanism	Environment	Resolution	Materials	Applications	Additional information	Examples
<u>Physical force SPL</u>	<u>Mechanical deformation</u>	AFM	Mechanical force	Ambient, in solution or in ultra-high vacuum	~10 nm	Soft materials: metals (Cu, Al, Au, Ni, Ag), semiconductors (Si, GaAs), polymers (photoresists)	Modification of photoresist, nanochannels, nanodevices based on it (single electron transistor)	Better to use diamond tips in tapping mode	[10-22]
	Nanoscale manipulation	STM, AFM	Van der Waals or electrostatic forces	Ambient (AFM) or ultra-high vacuum and low temperature (STM)	~0.1 nm (STM) or ~10 nm (AFM)	Atomes, nanoparticles (Ag, Au, Pd, Cu, GaAs, latex), biomolecules, carbon nanotubes	Molecular electronics, logic circuits, single electron transistors	Both contact and tapping modes are used	[23-27]
	Dip-pen nanolithography	AFM	Diffusion of one material into another	Ambient	~10 nm	Metals, inorganic compounds, organic molecules	Biodevices (biochip), nano devices,	Material of the ink can be the same to the tip	[28-34]
	Thermomechanical lithography	AFM	Mechanical force and heat	Ambient	~10 nm	Low melting point materials, polymers (PMMA)	Memory devices (Millepede)	Better to use multi-tip systems	[35-39]
<u>Bias-assisted SPL</u>	Field evaporation	AFM, STM	Field induced evaporation of tip coating	Ambient or ultra-high vacuum	~5 nm	Metals (Au, Al, Cu, Pt)	Nanodots, nanowires, memory devices	Limited length and amount of patterns	[40-46]

	Field vapor deposition	STM	Chemical vapor deposition	High vacuum with precursor gas	~5 nm	Metals (Cd, W, Fe, Rh)	Nanodots, magnetic arrays	M(CO) _n is the most common precursor	[47-50]
	Electron exposure	STM	Field initiated electron exposure of the resist	High vacuum	~20 nm	Resists (CaF ₂ , PMMA, PODA, SAL-601-ER7)	Lines, resistors	Resist should be thin as possible	[51-54]
	<u>Local oxidation</u>	AFM, STM	Electrochemical oxidation reaction in water meniscus	Humid air	~10 nm	Metals (Ti, Nb, Ni), semiconductors (Si, GaAs)	Dot arrays, nanowires, transistors	Conductive tips and samples	[55-61, 70-120]

1.1.1 Force-assisted scanning probe lithography

Force-assisted SPL is based on mechanical interaction between the tip and the surface. To pattern the substrate by such kind of lithography a large force should be applied to the tip. There are several methods of physical force SPL: mechanical deformation, nanomanipulation, thermomechanical writing and dip-pen nanolithography.

There are two types of mechanical deformation by the SPM tip: indentation and plowing [10]. Indentation is realized when the tip is placed in some place on the substrate and is loaded by a large force (Figure 1.3). Plowing is realized when the tip is scanning the substrate under a large force and scratch patterns are obtained. It can be done both in contact (static plowing) and tapping (dynamic plowing) modes. Utilization of tapping mode allows to reduce pattern irregularities caused by cantilever torsion. Applied force and lithography speed determines sizes of the obtained patterns. It should be noted that the tip can be contaminated, dull or broken during this lithographic process and reproducibility of the patterns will be reduced. Therefore, it is better to use rigid diamond or diamond coated tips. Mechanical deformation can be done on the wide range of soft materials: polymers [11-12], metals [13-15], semiconductors [16-17]. This method is quite studied in application for ferromagnetic metal films such as Ni [18], NiFe [19]. Fabrication of different devices such as field-effect transistors [20-21] and photonic crystals [22] is possible on the base of nanostructures made by probe scratching.

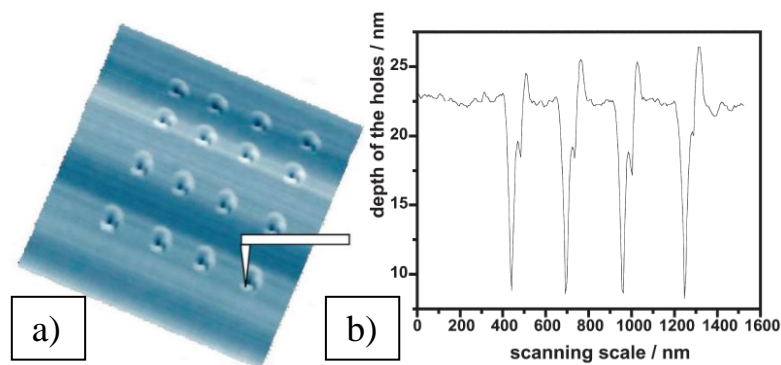


Figure 1.3. Schematic image of nanoindentation by AFM tip (a) and the depth of holes obtained by it (b) [10].

In nanoscale manipulation the AFM tip is used to cut and transport material for formation of desired patterns on the substrate. Atoms, nanoparticles, nanotubes and biological molecules (as DNA) can be used as transported materials [23-27]. On Figure 1.4 there is an example of artificial structure made of 30 nm GaAs particles by the AFM tip manipulation [27]. This kind of

SPL can be done in contact, tapping or non-contact modes of AFM. In contact mode particles are transported under the load higher than it used for imaging. In non-contact mode the tip can be brought into contact with the nanoparticle in purpose to transport it by switching off the feedback or by reducing the set point while the tip is scanning above the desired particle.

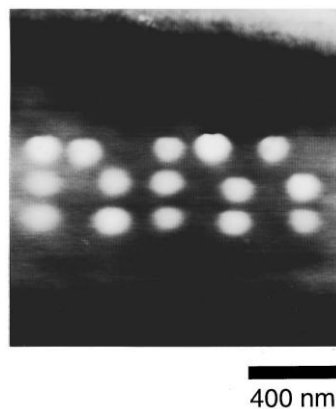


Figure 1.4. 30 nm Ga As particles structure fabricated by nanoscale manipulation to form the letters ‘nm’ [27].

Dip-pen nanolithography was invented in 1999 by Mirkin et al. [28]. In this technique the AFM tip is used as a pen to deliver required material as inks to a small nanosized place on the substrate during scanning or staying of the tip in this place for a certain time. The transport of ink coating from the tip to the substrate is provided through the water meniscus that is formed by capillary forces (Figure 1.5) [8]. Usually this SPL method is realized using a soft AFM tip in contact mode but tapping mode can also be used. By dip-pen nanolithography one can obtain structures of various materials: metals, organic and biological molecules [29-31]. Such structures made of magnetic materials (for example Fe_2O_3 , Fe_3O_4 and BaFe nanoparticles) are a big interest for high-density memory and sensors [32-34].

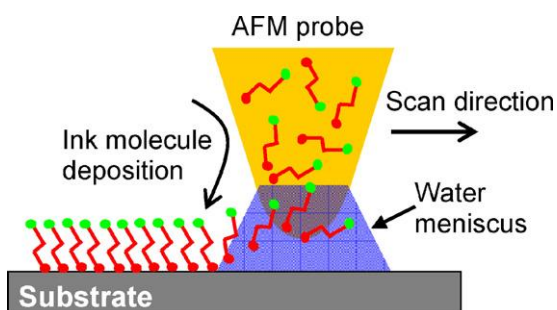


Figure 1.5. Schematic image of dip-pen nanolithography [8].

In thermomechanical writing the AFM tip loaded by a large mechanical force and heated by an electrical current passed through it, writes patterns on a polymer material (for example PMMA) during scanning (Figure 1.6). The temperature of the tip is higher than softening point of the polymer so it is easily indented in the shape of the tip. This method was developed by Mamin and Rugar at IBM for data storage [35-38]. They achieved patterns with 100 nm sizes and densities of 30 Gb/in². To increase lithography speed the multi-tip system for parallel data writing was developed. It was based on 32x32 probe arrays and was named “Millipede” [39].

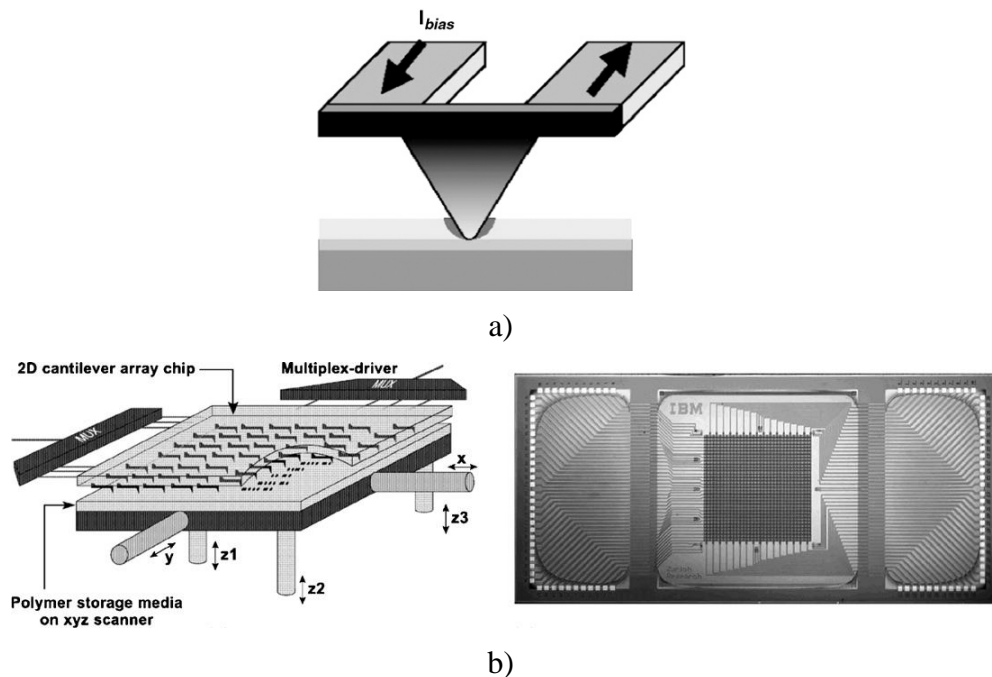


Figure 1.6. Schematic image of thermomechanical writing (a) [38] and schematic and photo images of 32x32 probe array system “Millipede” (b) [39].

1.1.2 Bias-assisted scanning probe lithography

Biased-assisted SPL is carried out by applying a bias to the SPM probe to create a localized electric field in a tip-sample gap. Because such gap is few nanometers in size, a bias of several volts can generate high field of hundreds and thousands V/m. This field can be used to pattern substrate physically or chemically: by field evaporation, field vapor deposition, electron exposure or local oxidation [8].

Field evaporation of tip coating is a process when bias is applied to a coated tip and the coating is evaporated from the tip and deposited onto the substrate. First this technique was applied for fabrication of Au nanostructures by STM in ultra-high vacuum [40]. Since that

various metallic tip coatings were used: Au [41-44], Al [41], Cu [45], Pt [46]. AFM tips in both air and ultra-high vacuum conditions were also used. This kind of lithography can be applied for fabrication of nanowires (Figure 1.7) and nanodots for electronic quantum devices and high-density memories. Length of nanopatterns that can be made by field evaporation is limited because of limited amount of material on the tip.

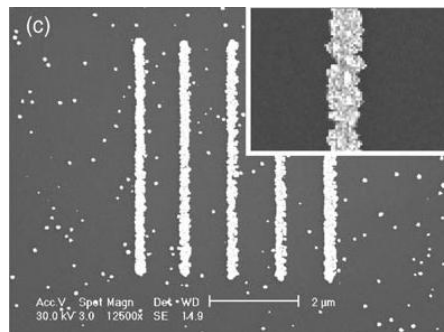


Figure 1.7. SEM image of gold nanowires fabricated by tip field evaporation [44].

Vapor deposition by SPM is carried out by applying bias to the tip–sample gap in precursor gas environment. Commonly metal carbonyl $M(\text{CO})_n$ is used [9]. Field-emitted electrons in the gap can provide dissociation of gas molecules resulting in metal deposition on the surface. Like field evaporation this technique can be used for fabrication of nanodots (Figure 1.8), arrays of magnetic dots and nanolines of different metals: Cd [47], W [48], Fe [49], Rh [50].

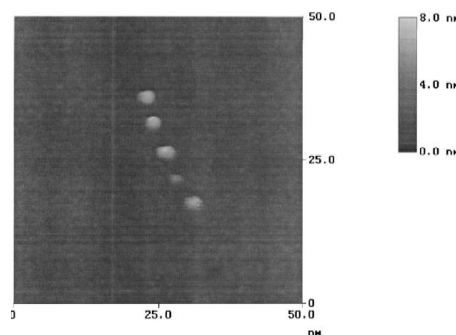


Figure 1.8. AFM image of the rhodium dots [50].

In electron exposure electric field is used to enable the emission of electrons from the STM tip and produced low voltage electron beam is used to expose the resist. For this kind of lithography it is better to use the thinnest possible resist layers to achieve exposure through the whole resist depth. Thicker films require higher accelerating voltage to be exposed and using of

high voltage reduces the resolution because of secondary electrons. This method was applied to different polymer resists: CaF_2 [51], PMMA [52-53], PODA [53], SAL-601-ER7 [54].

Probe oxidation is one of the most studied bias-assisted SPL techniques. In this method humid air environment is needed to form the water meniscus in the tip-sample gap. By applying the voltage to the tip-sample gap an electrochemical oxidation reaction on the sample surface is stimulated. This kind of lithography was first demonstrated on Si sample by positive biased STM probe in 1990 by Dagata [55]. In 1993 it was demonstrated using AFM probe [56]. Since that the process was applied using both STM and AFM positive or negative biased probes to a big variety of materials: semiconductors, metals, polymers. Oxidation process is most studied for Si [55, 57-59] and Ti [59-60]. AFM has become the most common tool for probe oxidation because its feedback system doesn't depend on tip-sample current that changes during oxidation process. Experiments on influence of polarity of probe bias on oxidation results showed that anodic process (negative biased probe) is more effective and helps to obtain higher oxide structures [55, 61]. By AFM local anodic oxidation different nanoscale devices such as metal-oxide-semiconductor transistors can be fabricated.

1.1.3 Atomic force microscopy principle

The atomic force microscope is a type of scanning probe microscopes that was invented in the 1986 by Binnig [62]. Study of the topography by SPM is based on interaction between microprobe (cantilever) and the sample surface. Probes are shown on Figure 1.9. Probe consists of a tip (1) and a flexible cantilever (2). Tip is attached to the cantilever underside. Tips can have different shapes (conical, pyramidal and tetrahedral) and various coatings (Au, Co, TiN, W_2C). The typical tip curvature radius is dozens nm and its length is 3-15 μm . The smaller tip curvature radius the higher resolution could be achieved. Reflective coating which is the part of detection system covers the cantilever underside. Cantilever is fixed on a hard chip (3), which installs into AFM tip holder (Figure 1.10) [63]. The most common are rectangular cantilevers, but triangular cantilevers are also used in order to minimize torsional deflections [64]. The most used materials for fabrication of cantilevers are silicon and silicon nitride, but diamond, silicon oxide and carbon nanotube cantilevers are also commercially available.

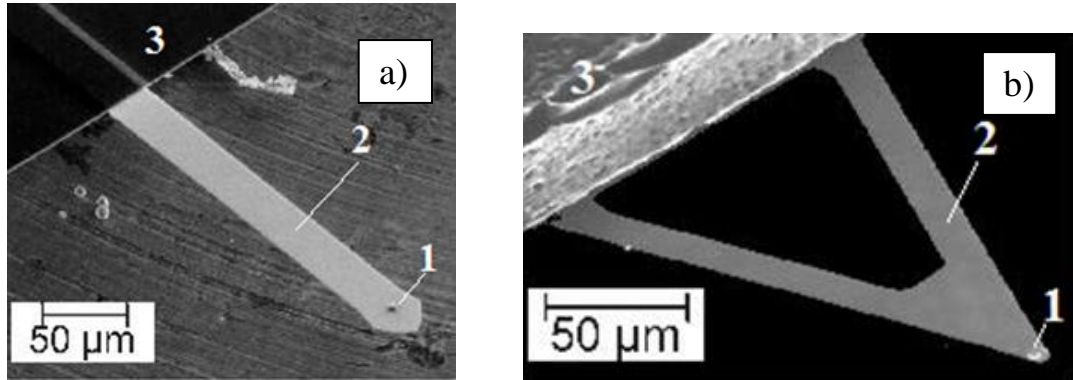


Figure 1.9. Scanning electron images of microprobes with various shapes: a) rectangular, b) triangular. 1 – tip, 2 – flexible cantilever, 3 – chip [64].

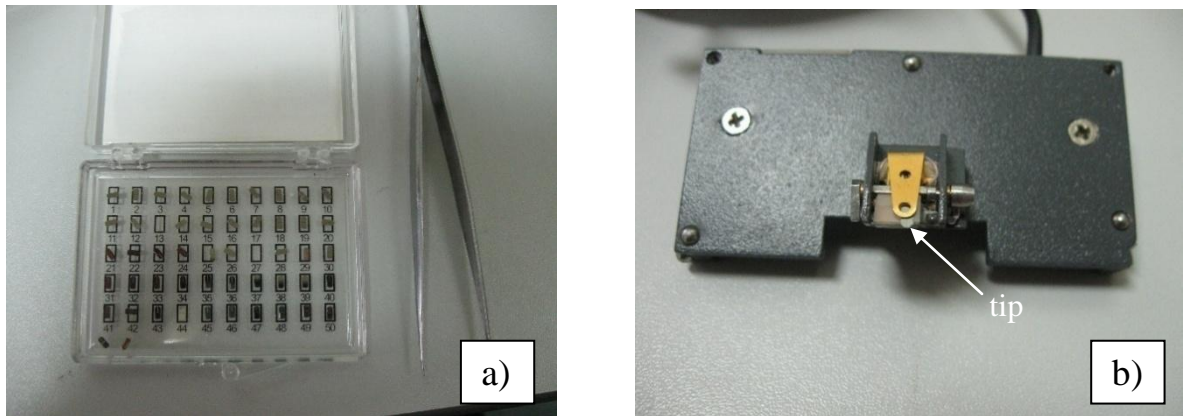


Figure 1.10. AFM probes in box (a) and in tip holder (b).

Work of AFM is based on measuring of Van der Waals attractive or repulsive forces resulting from interaction between the sample and the tip. Value of Van der Waals forces F_{ts} depends on distance between the sample and the tip, on Figure 1.11 there is given the curve of this dependence. The right part of the curve matches to a large distance between the tip and the sample. When this distance decreases the attractive force appears and increases until atomic orbitals starts to repulse. With further decrease of the distance, repulsive force will reduce attractive force exponentially. These forces will compensate each other when the distance between the tip and the sample will be about two angstroms. When total force F_{ts} becomes positive (repulsive) it means that the atoms came into contact [65].

The AFM can work in three modes with the respect to the contact between the tip and the surface: contact mode, non-contact mode and semi-contact or tapping mode. These modes are matched to sectors of a force curve on Figure 1.11.

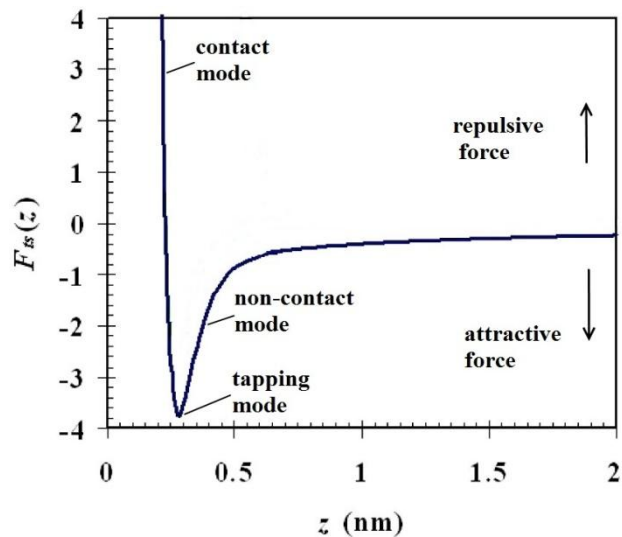


Figure 1.11. Dependence of the force F_{ts} (typical values) on distance z between center of front atom of the tip and the sample [65].

In contact mode the AFM tip physically contacts the surface. The interatomic force between the cantilever and the sample in this mode is repulsive. In this mode the tip can be dulled and the surface can be deformed so contact mode is not suitable for scanning of soft and springy surfaces. Simultaneously, the tip should be soft enough to be deflected by very small forces and should have high enough resonant frequency to be non-sensitive to vibrational instabilities.

The AFM in non-contact mode monitors attractive Van der Waals forces between the tip and the surface. A gap between the tip and the surface is 5-10 nm. This mode allows to scan soft and springy surfaces and not to contaminate it by the tip. Measured attractive forces are weak, so the layers of adsorbed water and gases can influence on surface image. For this mode the tips with high enough spring constant are used not to be stuck to the surface at small amplitudes.

Tapping mode was developed by Martin et al. in 1987 [66]. In this mode the tip is oscillating on its resonance frequency with some amplitude and touches the surface at the lowest point of its oscillation. In tapping mode the damage of the surface is less possible than in contact mode. This technique helps to overcome influence of adhesion or electrostatic forces on the tip and to obtain high-resolution images. Amplitude of the oscillating tip is set by Set Point (Figure 1.12). As Set Point decreases, amplitude decreases also, but tip-sample forces increase. To provide scanning Set Point should be smaller than for free oscillations in air, and to provide lithography Set Point should be even smaller than for scanning.

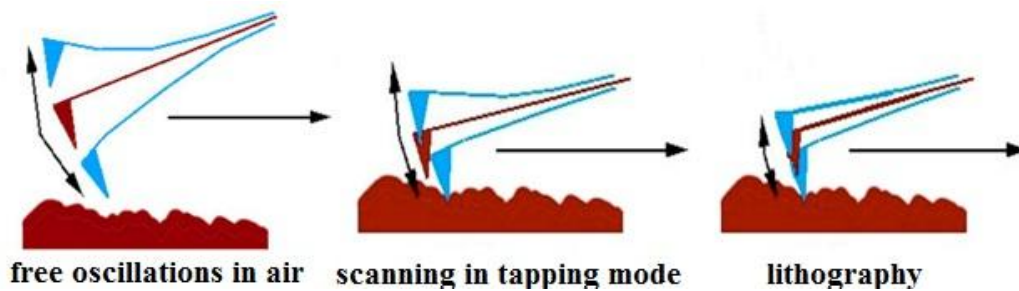


Figure 1.12. Amplitude of the oscillating tip.

When tip is working in the tapping mode atomic forces cause changes of the tip oscillation phase. These changes are presented in the phase image and help to see difference in mechanical, adhesive, viscoelasticity and composition properties (see Figure 1.13). On phase images low phase angle corresponds to materials with low viscoelastic properties [67]. Using of phase imaging together with magnetic coated tips and LiftMode procedure one can realize magnetic force microscopy (MFM) imaging. MFM helps to see the magnetic structure of the sample (Figure 1.14).

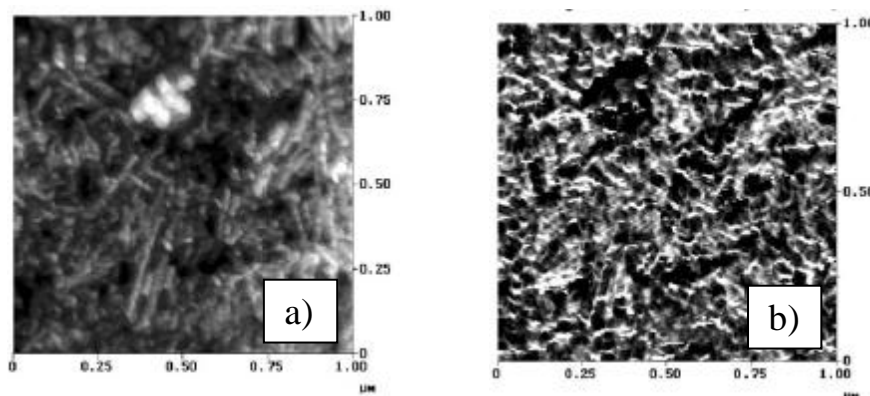


Figure 1.13. Tapping mode height (a) and phase angle (b) images of magnetic metal particle tape [67].

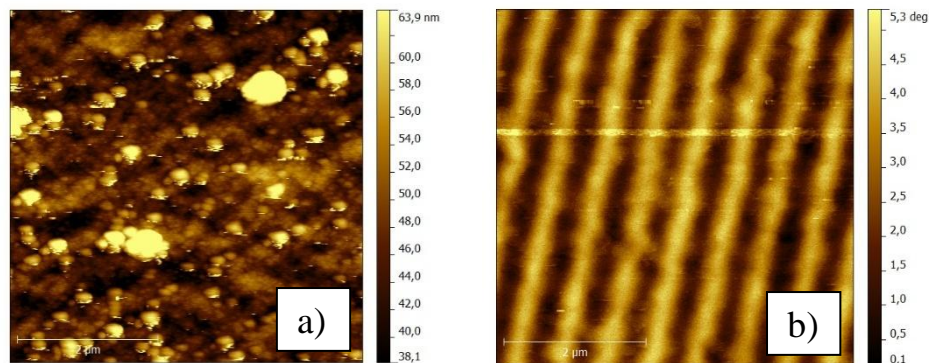


Figure 1.14. Topography (a) and MFM (b) images of magnetic tape.

The AFM system consists of two main parts: a scanner and an AFM detection system (Figure 1.15). The scanner is based on a piezoelectric transducer which moves the sample in the X, Y and Z directions. The detection system monitors the tip deflections under the effect of atomic forces. It consists of a laser, a reflective cantilever underside and a photodetector (four elements of the quad photodiode). Laser spot reflects from the cantilever onto the photodetector. When cantilever deflection changes the laser spot changes its position relatively to elements of the photodetector and SUM signal of photodetector changes also. SUM signal shift shows the amplitude of the cantilever deflection and the amplitude depends on atomic forces and distance to the sample surface.

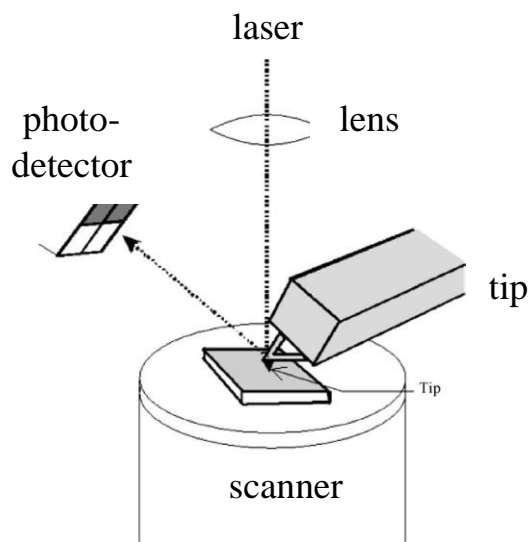


Figure 1.15.AFM system [68].

For scanning probe lithography in our experiments AFMs Solver P47 (NT-MDT) and MultiMode (VEECO) were used (Figure 1.16). AFMs consist of vibroprotection system (1), various scanners (2), SPM head (3) and controller (4), connected to the computer [63, 69].

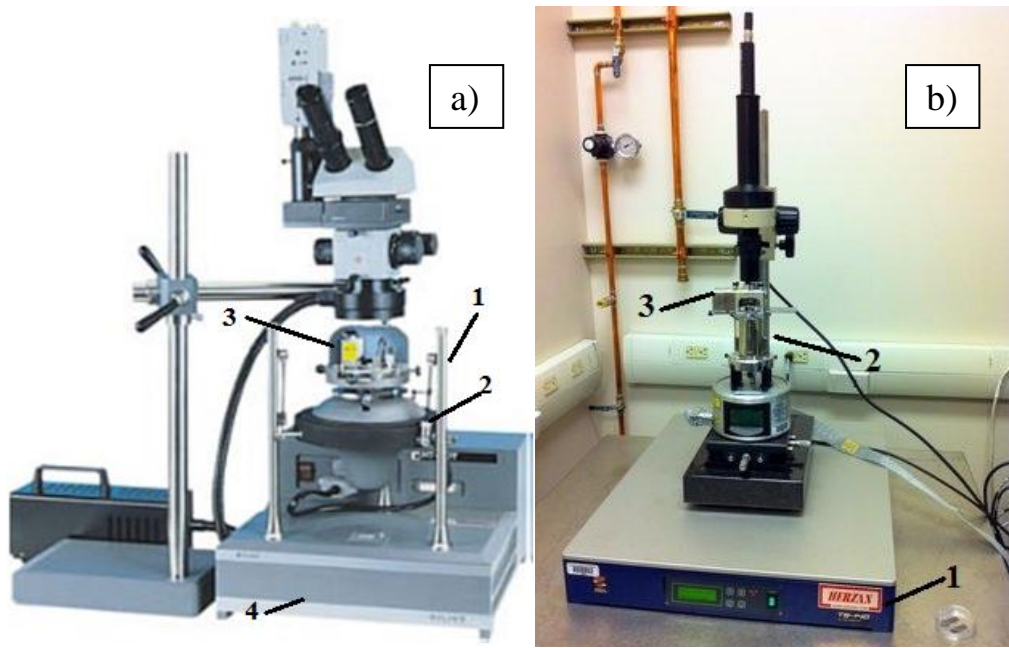


Figure 1.16. Views of AFMs Solver P47 (a) [63] and MultiMode (b)[69].

1.1.4 Local anodic oxidation by atomic force microscope: principle and application

Local anodic oxidation (LAO) is based on the electrochemical reaction of oxidation in the water meniscus under the sharp tip of the atomic force microscope. The reaction is stimulated by voltage applied between the tip and the sample [70]. The tip is a cathode and the meniscus is an electrolyte which provides the oxyanions (OH^- , O^-) for oxide formation. Incorporation of oxide ions into crystal lattice of conductive film during oxidation reaction [71] leads to material volume growth and formation of raised nanopatterns on the film.

The water meniscus is formed under capillary forces and electrostatic interactions. Dependence of the shape and the size of meniscus on tip-surface distance, field strength and humidity makes the oxidation process even more complicated and difficult to control.

Equations (1.1-1.2) show electrochemical reactions for tip-oxide and oxide-substrate interfaces [72-73]. Sample (anode) reaction:



Tip (cathode) reaction involving ionic dissociation of water and the diffusion of space charges under the field:



Conditions required for LAO process implementation are: 1) both the tip and the sample should be conductive, 2) the layer of the absorbed water should exist on the sample surface, 3) voltage should be applied between the tip and the sample (Figure 1.17). By this method of lithography one can obtain oxide structures nanometers in height and dozens or hundreds nanometers in width.

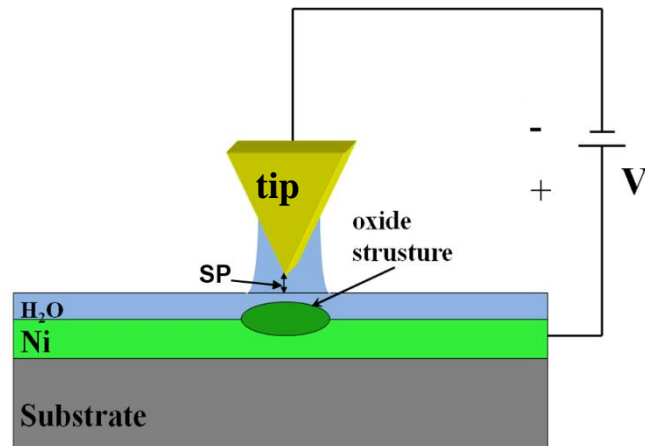


Figure 1.17. General scheme of local anodic oxidation process for Ni film as an example.

LAO can be provided in vector and raster modes. At vector oxidation lithography tip passes only points of the pattern to be oxidized and at each point the same tip-sample voltage is applied. Pattern in this mode is set by user as lines and geometric shapes. Raster mode is carried out during scanning of the sample and voltage is applied on the top in every point. Pattern at this mode is set by bitmap and voltage value in every point corresponds to the brightness of the point on the bitmap. On Figure 1.18 there is given AFM image of oxide line made by vector lithography on FeCo film. On Figure 1.19 there is given AFM image of university symbol made by raster lithography on Ni film.

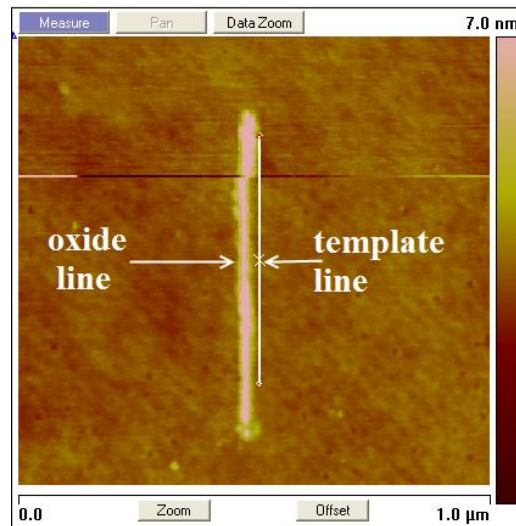
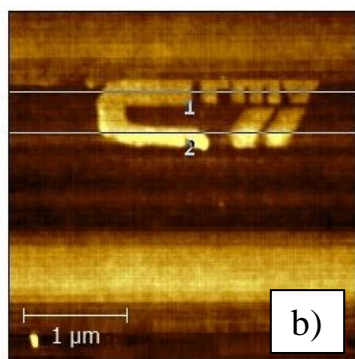


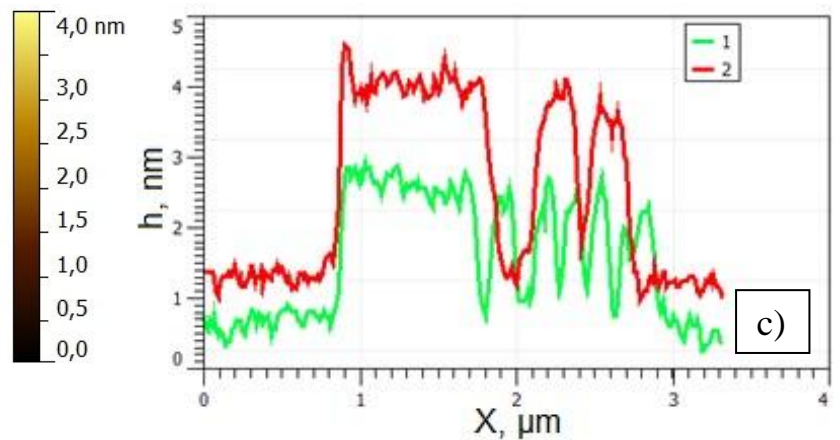
Figure 1.18. Line made by vector LAO on FeCo film.



a)



b)



c)

Figure 1.19. University symbol made by raster LAO on Ni film: a) original raster bitmap, b) AFM image, c) cross-sections of oxide structure along the lines 1 and 2.

The mechanism of LAO is not still clear. It was studied by several researchers and there are proposed various models of this process: Cabrera–Mott model [74-76], power-law model [77], log kinetic model [78-80] and space charge model [80-82]. It is suggested that the oxidation mechanism and its kinetics are related to electrical field, water meniscus formation, OH-diffusion, surface stress [75-84].

The most common theory to explain anodic oxidation process is Cabrera-Mott theory of the oxidation of metals which include oxidation of thin films [74]. Due to this theory electric field decreases the activation barrier for electrons and ions exchange across the oxide. Oxide height is growing with time (1.3):

$$h = h_c \ln \frac{t}{t_c}, \quad (1.3)$$

where h – oxide height, h_c – some length characterized by an electron exchange energy, t – oxidation time and t_c – threshold oxidation time [76].

An empirical power law was the best to fit experimental data in [77]. According to this model AFM oxidation only takes place at voltages higher than threshold and oxidation kinetics follow a power law (1.4):

$$h = \beta(V - V_{th})t^\gamma, \quad (1.4)$$

where β, γ – some constants, V – oxidation voltage and V_{th} – threshold oxidation voltage [77].

In log oxidation model the dependence of the oxide height on the applied voltage and tip velocity is proportional to $\log(I/v)$, where v – oxidation rate. The oxide growth rate decreases with oxide thickness increase due to field strength decrease and the buildup of stress [78].

Dagata et al. proposed space charge model. On this model oxidation process depends on space-charge which is the function of substrate doping type and level. It was concluded that LAO of Si is best described by Albery–Miller equations [82].

All these models depend on results of particular researcher and parameters and results of his experiments. Furthermore there is a large number of factors that influence on oxidation results. So it's hard to generalize all proposed models to a single oxidation kinetics model. Therefore most works are related with study of influence of different parameters on LAO results and determination of optimal parameters of oxidation for particular substrate materials (see Table 1.3).

Table 1.3. Materials patterned by LAO.

Material type	Material	References
Semiconductors	Si	[55, 57-59, 84-91]
	GaAs	[58, 92-93]
	GaAlAs, GaMnAs	[94-97]
	Si ₃ N ₄	[98]
	InP	[99]
	SrTiO ₃	[100]
	Metals	Ti
Mo		[101-102]
Nb		[103]
Ge		[104]
Zn		[105]
Ni		[106-109]
NiFe, FeCo		[109]
Cr		[61, 109]

LAO results (mainly the dimensions of oxide patterns) were investigated on following parameters: tip-sample voltage, oxidation time or tip velocity, relative air humidity, oscillating amplitude of the tip and AFM working mode.

Investigation of tip-sample voltage effect on LAO results was done for all patterned materials. Most experiments showed that with voltage increase oxide height and width increase linearly both for dots and lines [58-59], [99] (Figure 1.20 a). It was found that oxide pattern start to form at voltage higher than some threshold voltage. Every patterned material have its own threshold oxidation tip-sample voltage. Similar results were obtained on effect of the oxidation time on dimensions of oxide structures: an increase of the oxidation time leads to an increase of dimensions of oxide structures (Figure 1.20 b). But some researchers obtained liner dependencies [57], [84], [86] and some obtained logarithmic curves [89], [99].

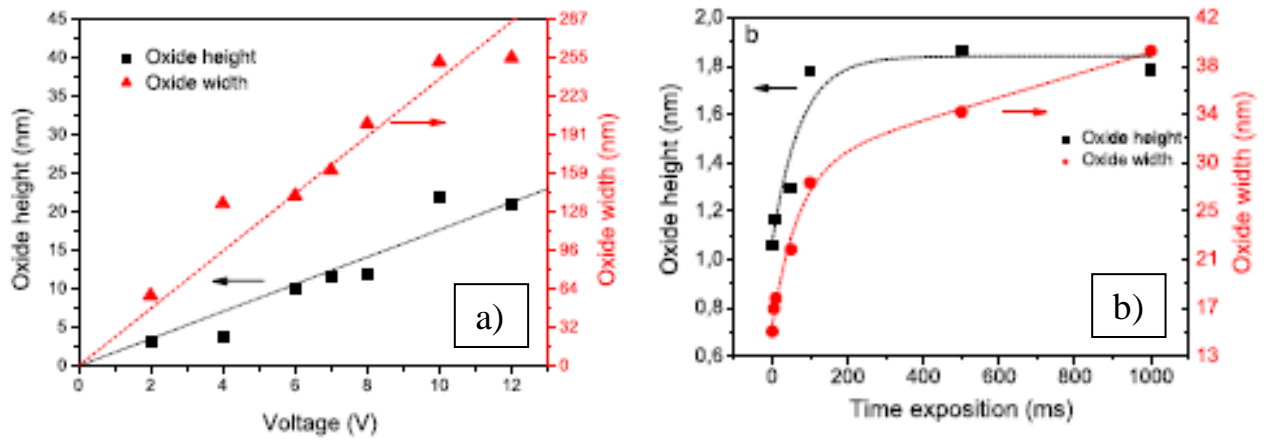


Figure 1.20. Oxide dot sizes (height and width) dependences on tip-sample voltage and oxidation time for InP [99].

The width and height of the oxide structures were found to increase slightly with the increase of relative air humidity [57]. Furthermore oxidation is impossible at humidity below 25% and it's impossible to obtain lines with homogeneous width at humidity lower 30% [60]. Authors suppose that at low humidity, the sample is not completely covered with a water film. A peak of the size distribution was observed at relative humidity 85% [85]. At humidity above 85% only width of oxide dots was increased while height was decreased.

The role of humidity in probe oxidation process is explained by the dependence of formation of water meniscus on humidity. That is why several studies are related with the numerical modelling of water bridge formation and comparison of these results with experiments. For example in [92] modelling of size and shape of meniscus at different humidity was done. But not only humidity influence on meniscus. In [110] it is suggested that once a water bridge was formed, its sizes can be modified by changing the tip-sample distance and electrical field between the tip and the surface.

AFM working mode (contact or tapping) and tip-sample contact force also influence on water bridge and therefore on oxide structure sizes. Comparison of LAO in contact and tapping mode showed that oxide structures patterned in tapping AFM mode are narrower and higher than those made using contact mode [89], [91] (Figure 1.21). Tip-sample contact force in tapping mode is determined by amplitude of tip oscillations. Dependence of oxide structures sizes on oscillation amplitude was investigated in [87-88].

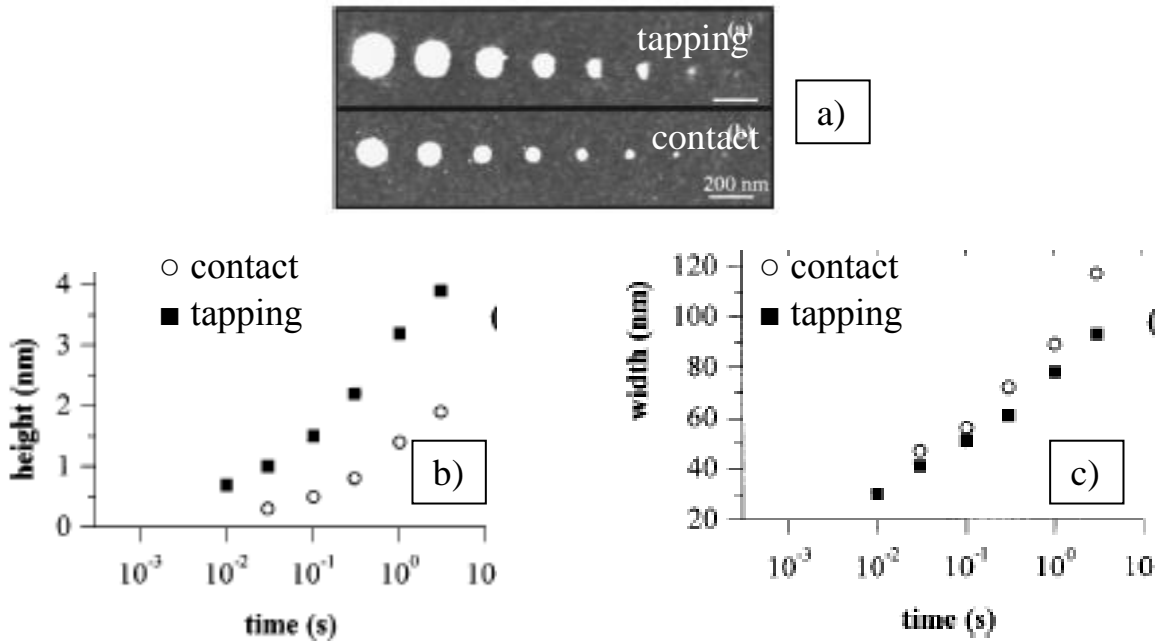


Figure 1.21. AFM images of oxide dots on Si (a) and sizes (height (b) and width (c)) dependences on oxidation time for contact and tapping modes [91].

AFM nanooxidation has been applied to produce oxide structures for different applications (Table 1.4). Examples of LAO application include nanodots and wires, diodes and transistors, special lithography processes.

Table 1.4. Examples of LAO application.

Nanostructures and nanodevices	Materials	References
Nanodots arrays	Si, Ti, GaAs	[111-114]
Nanowires	Si, GaAlAs	[94, 115]
Special lithographic processes	Ge, Mo	[101-102, 104]
Selective growth of carbon nanotubes	Ni	[107]
Tunnel barriers and transistors based on it	Si, Ti, Nb, Zn, Ni, NiFe	[60, 103, 105, 108, 116-119]
Magnetic nanostructures	Co, GaMnAs	[95-96, 120]

One of the first LAO applications were nanodots arrays and nanowires. Arrays of nanodots can be used for controllable data storage with very high densities of 1-1.5 Tbit/in². For example

in [113] 4864 dots on Si with a periodicity of 40 nm were fabricated. The dots density is approximately 1 Tbit/in². In [112] nanobits were at a 20 nm pitch, which is equivalent to a bit density of 1.6 Tbits/in². Dot array made on GaAs [114] showed the negative Hall effect and resistance oscillations from quantized periodic orbits. Nanowires with width down to 10 nm on Si [115], GaAlAs [94] or other materials can be fabricated by LAO and patterned by wet etching.

Application of LAO as a nanometer-scale lithographic tool is demonstrated in [101-102], [104]. A lithography schemes based on the probe oxidation are obtained with use of Ge [104], Mo [101-102] films and PMMA resist. As the Ge and Mo oxide can be easily removed by water, it is possible to use the patterned Ge or Mo film as a mask to transfer patterns (for example nanowires) to the underlying substrate surface. In [107] nickel oxide obtained by probe oxidation was used as a catalytic template for selective growth of carbon nanotubes. Vertically aligned carbon nanotubes with diameters of 30–80 nm were grown on the nickel oxide structures by chemical vapor deposition.

Oxide barriers are the most common structures fabricated by LAO. The low-temperature isolation performance of such oxide lines is excellent (Figure 1.22) [61]. Such barriers can be utilized as tunnel junctions and elements of field effect transistors. One of the first field effect transistors fabricated using AFM probe oxidation was presented in 1995 on Si substrate [116]. Field effect transistor had the gate width of 100 nm. Successful fabrication of transistors was done on Ti [61], Nb [103], [117], Zn [105]. For example on Figure 1.23 schematic and AFM images of a field effect transistor on Nb film are presented.

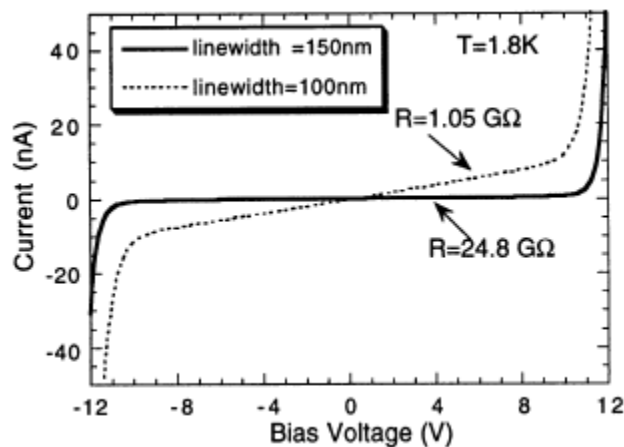


Figure 1.22. Current-voltage characteristics of two oxide lines with different widths at temperature 1.8 K [61].

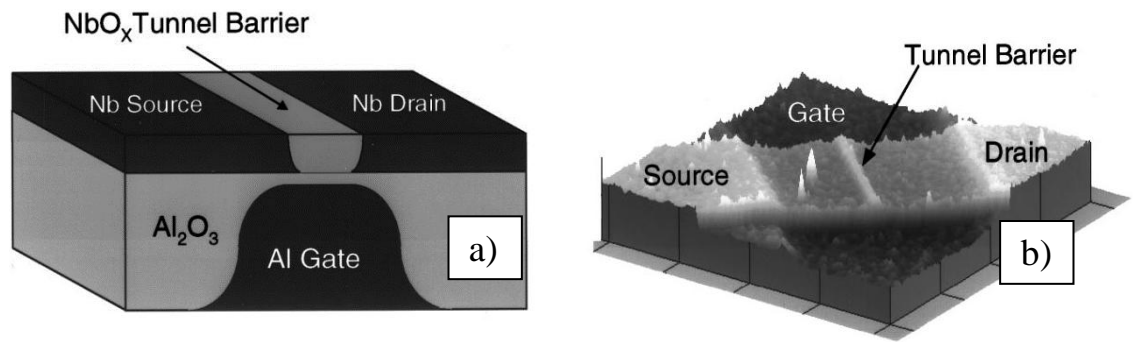


Figure 1.23. Schematic (a) and AFM (b) images of a Nb/NbO_x tunnel junction [117].

Oxide barriers were also obtained on ferromagnetic metal films: Ni [108] and NiFe [119]. Oxide structures on ferromagnetic films can be used not only for field effect transistors fabrication but also for fabrication of magnetic structures. For example in works [95-96] constrictions on ferromagnetic GaMnAs layer using LAO were prepared. These structures showed magnetoresistance effect for the different orientation of magnetic field at low temperatures (Figure 1.24 a). In [120] direct modifications of magnetic domain structures in Co nanostructures were done by AFM tip (Figure 1.24 b).

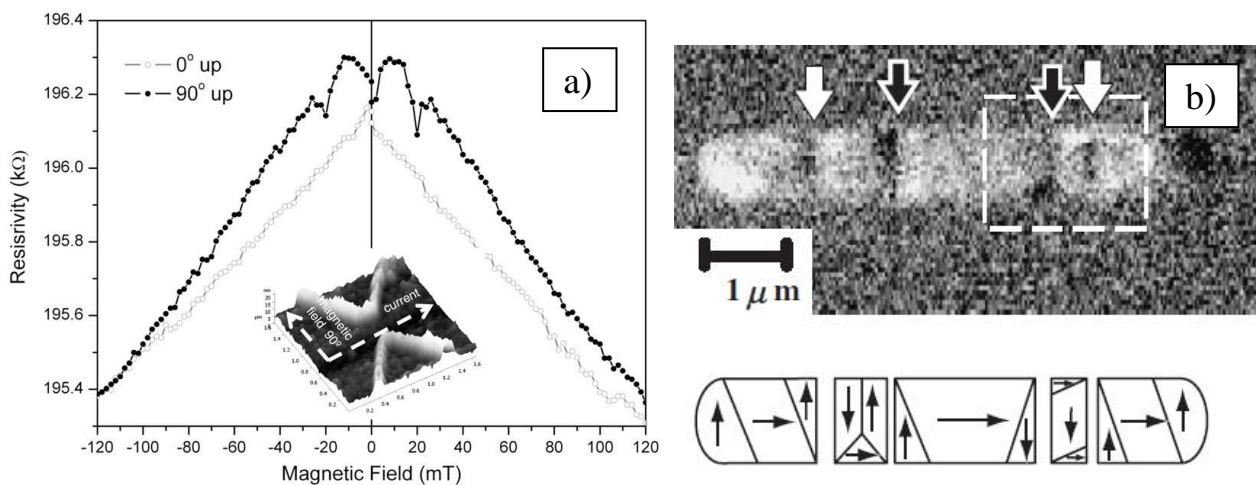


Figure 1.24. Examples of magnetic structures made by LAO: anisotropic magnetoresistance in the constriction structure on GaMnAs (a) [95] and MFM image and calculated image of magnetization configuration of Co rectangular nanostructure (b) [120].

1.2 Electron beam lithography

Electron beam lithography (e-beam lithography or EBL) is a kind of a lithographic process which uses a focused beam of electrons. Essentially the process of EBL is the same with conventional photolithography:

- to coat substrate by resist;
- to change resist dissolubility under the exposure;
- to dissolve exposed (or non-exposed) areas in a specific solvent so the patterns needed for material deposition (or etching) on the substrate will be obtained.

But in the contrast with photolithography which uses light for exposure EBL uses electron beam. Because of shorter wavelength of electrons (0.2-0.5 Å) and small diameter of beam this kind of lithography helps to produce patterns with much higher resolution. The size of smallest features fabricated by EBL was less than 5 nm [121-123]. One more benefit of EBL is that electron beam scans the surface so there is no need to use the mask unlike for optical lithography. User simply designs the pattern in the software and EBL system draws it on the resist by beam. But this advantage gives rise to the drawback: EBL is slower than the photolithography. But projection EBL [124] and the use of massively parallel beams [125] can help to overcome this drawback. But the main drawback is that e-beam system is complicated and expensive.

EBL system consists of electron gun, electron column, specimen chamber, mechanical stage, vacuum system and computer system (Figure 1.25) [126]. Electron column contains magnetic lenses needed to focus electron beam, accelerate it to the working voltage, to turn it on and off and to deflect it for pattern writing [127]. Typically EBL system uses electron beam with 10-100 keV energy per electron. Mechanical stage is used to position the sample relative to the electron beam. Vacuum system keeps the column and the chamber at high vacuum. Computer system serves to control the equipment.

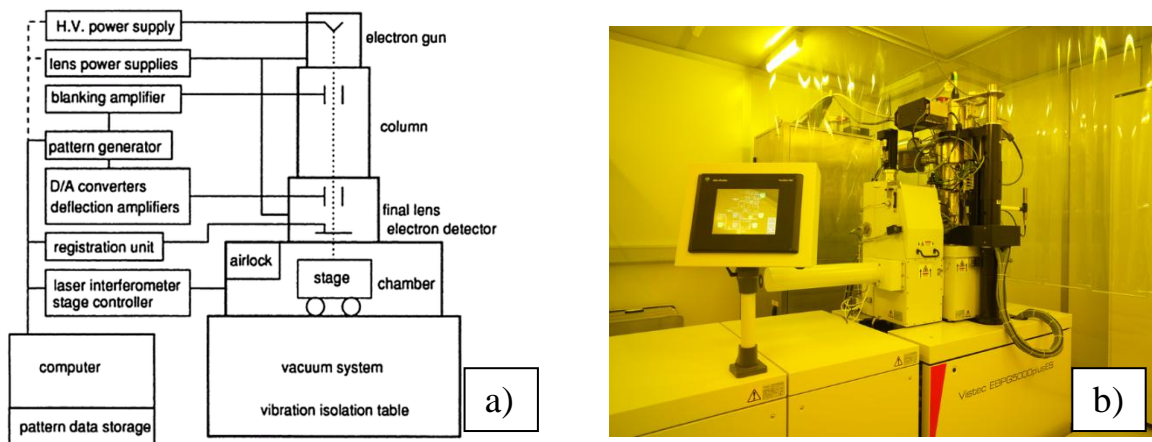


Figure 1.25. Schematic image of EBL system (a) [124] and photo of LEICA EBPG 5000Plus EBL system used in our experiments.

1.2.1 Electron-beam resists

For EBL process it is needed to use resist which will be chemically changed under the exposure. Resists sensitive to the exposure by electron beam are called electron beam resists (or e-beam resists). There is quite a large amount of resists of different types (positive and negative like for optical lithography) with different properties, which could be developed and striped by different chemicals. Positive e-beam resist produces the same pattern as electron beam drew (positive image) and negative resist produces the reverse pattern (negative image). Positive resist undergoes chain scission, decreases the molecular weight and becomes more soluble under the electron bombardment. Negative resist under exposure forms cross-links between polymer chains, increases the molecular weight and becomes less soluble.

The main problem to start EBL is to choose the resist to use. The choice depends on several characteristics of the resist:

- ease of processing - difficulties to apply, develop and strip the resist,
- etch resistance - ability of the resist to protect the substrate from etching,
- sensitivity - minimal dose of electrons required to modify resist through the whole thickness (it's also depends on accelerating voltage and development),
- resolution - the smallest achievable size of structure.

The first resist developed for EBL is polymethyl methacrylate (PMMA) [128]. Now it remains to be the most popular e-beam resist and one of the highest resolutions [128]. It is a positive resist but exposed by more than 10 times the optimal dose, PMMA will crosslink, forming a negative resist. The typical developer for PMMA is solution of methyl isobutyl ketone (MIBK)

and isopropanol alcohol (IPA) – MIBK/IPA (1:3) for high contrast and (1:1) for high sensitivity [129].

There is an opportunity to form a bi-layer of the resist: a high molecular weight PMMA on top of a low molecular weight PMMA. The low weight layer of PMMA is more sensitive to the exposure so it develops faster than top layer. Finally undercut profile is formed (Figure 1.26). Such technology uses to enable easy and clean lift-off. For thick layers of metal larger undercut is needed. It can be achieved by using PMMA on top of a P(MMA-MAA) copolymer.



Figure 1.26. Undercut resist profile for clean lift-off [130].

In Table 1.5 the most well known positive and negative e-beam resists are shown [131].

Table 1.5. Popular electron-beam resists [131].

	Tone	Resolution (nm)	Sensitivity ($\mu\text{C}/\text{cm}^2$)	Developer
PMMA	Positive	10	100	MIBK:IPA
EBR-9	Positive	200	10	MIBK:IPA
PBS	Positive	250	1	MIAC: 2-pentanone
ZEP	Positive	10	30	Xylene: p-dioxane
AZ5206	Positive	250	6	KLK-PPD-401
Ma-N 2400	Negative	50	120	MF-CD-26
COP	Negative	1000	0.3	MEK:ethanol
SAL-606	Negative	100	8.4	MF312:Water

1.2.2 Exposure parameters

Main exposure parameters for EBL are: beam energy (or acceleration voltage) and current, spot size (or resolution), exposure dose.

After electron beam was emitted from the electron gun, it enters into the acceleration system, where it will be accelerated to a specified energy [132]. The e-beam energy affects exposure resolution. The highest acceleration voltages help to obtain more uniform and fine patterns. The lithography examples with different acceleration voltages are shown on Figure 1.27.

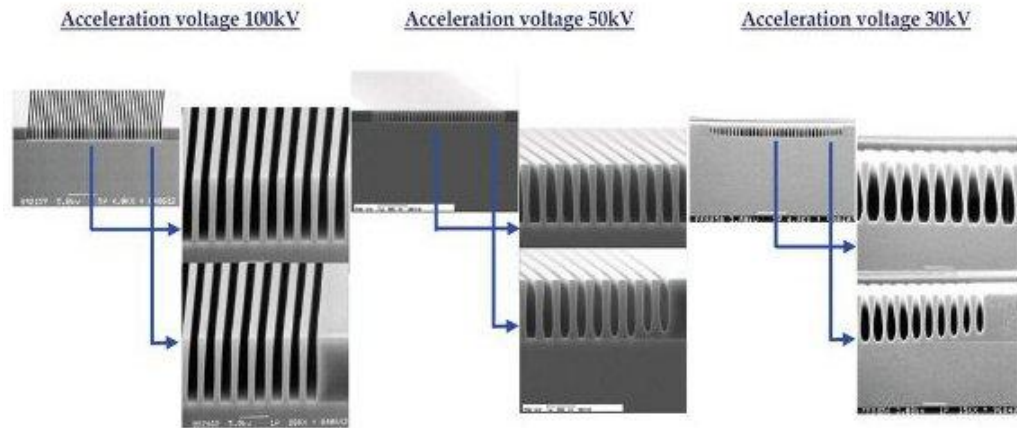


Figure 1.27. EBL resist patterns made with acceleration voltages of 100kV, 50kV and 30kV respectively [132].

Exposure dose is the product of the beam current and exposure time:

$$D = \frac{I \cdot t}{S^2}, \quad (1.5)$$

where D – dose, I – beam current, t – time to expose the object and S – area exposed. Electron beam current means those electrons that directly contribute to sample exposure and not the full emission from the tip. Beam current affects on resolution and uniformity of patterns. For the highest resolution the lowest beam current should be chosen. For the smallest beam current the smallest spot size is needed. The spot size is the diameter of electron beam at the sample. Smaller spot size gives higher resolution.

1.2.3 Electron-beam lithography challenges

The main objectives of EBL are to obtain patterns with high resolution, high density, high sensitivity and high reliability. There is a large number of EBL process parameters affecting these characteristics in interacting fashion: the choice of resist [128, 133-134], substrate [135], development conditions [136-138] and exposure parameters [123, 139]. There are some factors that complicate process objectives.

Proximity effect

The electron-electron interaction in resist produces forward scattering which can deflect the electrons in beam on small angles and to make the beam wider in the resist [140]. This effect increases with thickness and at low beam energies. When electrons reach the sample the interaction of electron beam with sample can cause different phenomenas (Figure 1.28) [140]:

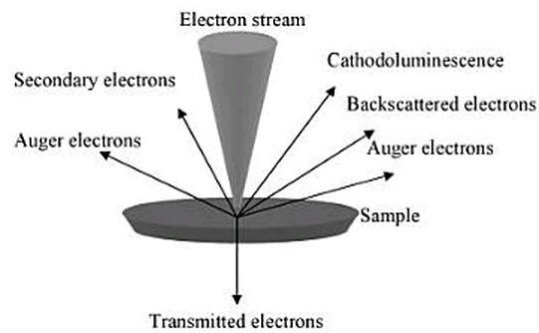


Figure 1.28. Phenomenas caused by electron beam-sample interaction [140].

The amount of backscattered electrons depends on the beam energy, the substrate material and the resist thickness. Backscattering have wide angle. Thus backscattered electrons can contribute to exposure of the resist far from the position of the electron beam resulting in wider images than what can be ideally produced by the e-beam diameter. In fact, closely placed areas can contribute to exposure of each others. This effect is called proximity effect and it influences on EBL resolution critically [126]. For example if there is a small feature between two large exposed areas this feature can receive too large dose and be completely developed or it can lose too much of its dose and be not developed enough (Figure 1.29) [126].

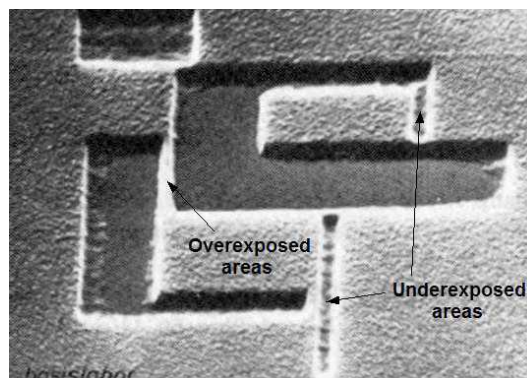


Figure 1.29. Proximity effect in positive resist pattern [126].

Electron scattering in the resist can be simulated using a Monte Carlo method [132, 141-142] (Figure 1.30). It is helpful to find the way to reduce the proximity effect.

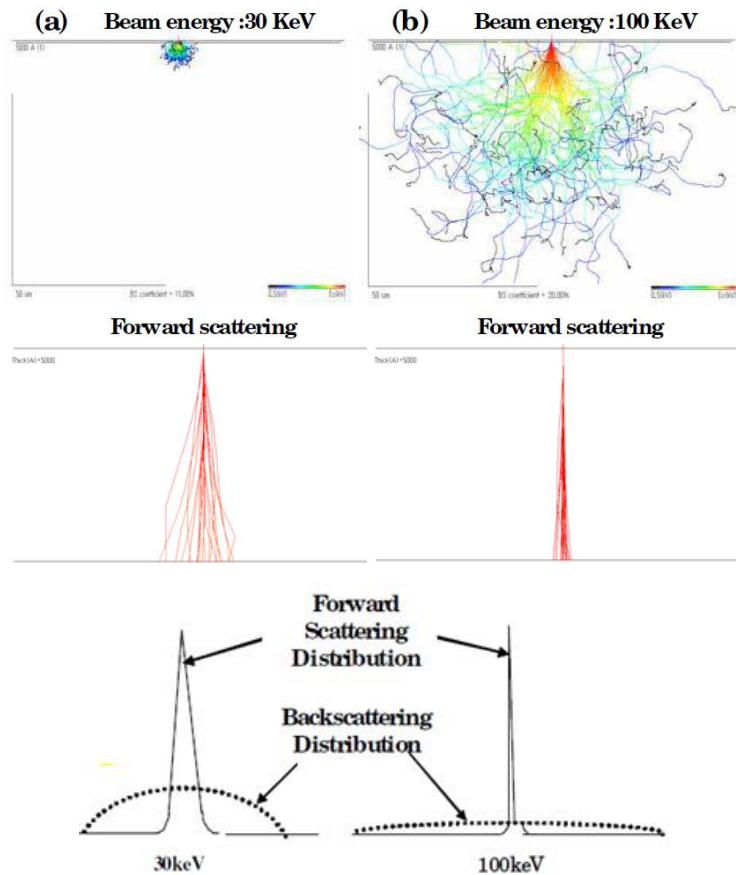


Figure 1.30. Monte Carlo simulation of forward and backscattering at beam energies of 30 and 100 keV per electron [132].

So the proximity effect can be overcome or reduced by following arrangements:

1. Use of high-energy electron beams. The forward scattering will be small and the backscattered electrons will be distributed over a larger area (Figure 1.30).
2. Use very low energy beams (<10 keV) and thin layers of resist. Backscattering becomes negligible at such low beam energy. But low energy will increase forward scattering. It can be decreased by using thin resist layer with a low electron density.
3. Use of bi-layer technology. Top layer of resist is thin and is used for patterning and bottom layer is about 10 times thicker and is used for reduction of backscattering. But this technology works only for quite large patterns ($\sim 1\mu\text{m}$) [130] and increases difficulty of the lithography process.

4. Use of proximity effect correction software [143]. This software can use shape modification or dose modification [144-146] to overcome proximity effect. Dose modification can be done by 2 ways:

- a) Small patterns are exposed less than large ones. The goal is to determine the required dose for each pattern size and to use different doses depending on the pattern.
- b) Calculating exposure dose that is received by every pixel directly from the beam and from other pixels, and compensating the excess dose by adapting the beam current (from pixel to pixel).

In shape modification method single dose is used for the entire structure. But the shapes of the patterns are modified in such a way that the developed structure will be close to the needed one.

5. Use of membranes as substrates for EBL to reduce backscattering [135].

6. Use of a layer of dense material (gold or tungsten) beneath the resist to absorb electrons and to reduce the number of backscattered electrons. But it makes fabrication process more complicated [147].

Electric discharge

A substrate for EBL should be relatively conductive. In opposite case there is no pathway for the absorbed electrons to dissipate and substrate will build up an electric charge which can make electron beam focusing more difficult, can deflect beam and distort exposed patterns or even destroy the sample (Figure 1.31) [148]. If it is needed to use insulating substrate a charge dissipation layer should be deposited above or below the resist. It can be a thin 5-20 nm conductive polymer [149] or metal layer (Cu, Al, Cr, Au, Ge) [150-153]. Main requirements to a charge dissipation layer are high conductivity (the higher conductivity the less charging effect) and good transparency (to view alignment marks).

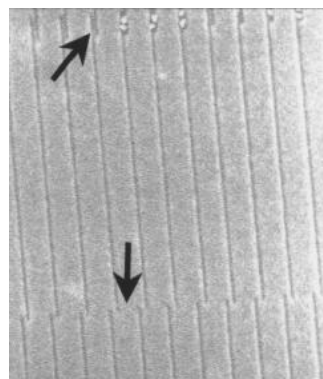


Figure 1.31. Arrows on exposed patterns in the absence of discharging layer [150].

1.2.4 Electron-beam lithography application

EBL is widely used in fabrication of different nanometer scaled devices: thin metallic wires [123], high-frequency transistors [154-155], photonic crystals [156], phononic crystals [152, 157]. This technique allows to obtain of high-quality arrays that's why it is suitable and the most used lithography process for photonic and phononic crystals fabrication (Figure 1.32) [158]. The main drawback of such crystals fabrication by EBL is high cost.

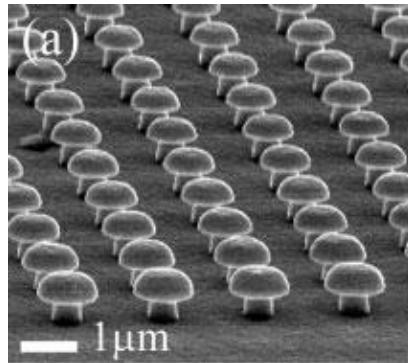


Figure 1.32. SEM image of mushroom-like pillars [158].

Similarly EBL is a good tool for patterning of ferromagnetic materials. Using this lithography method magnetic structures with dimensions comparable to or smaller than some fundamental length scales in magnetics, for example domain wall size and exchange interaction length, thus making the behavior different from that of a thin film [159]. There are a lot of works connected with magnetic structures fabrication using EBL. For example in [160] magnetoresistance and magnetization properties of Fe wires arrays with different sizes and orientations were studied. Properties of Fe magnetic dots (Figure 1.33) were investigated in [161], such structures are interesting for magnetic recording media fabrication and in the field of superconductivity.



Figure 1.33. SEM image of Fe magnetic dots [161].

1.3 Conclusions

In this chapter two lithographic techniques for high frequency phononic crystals fabrication are considered: EBL and SPL. Both these methods have high resolution and produce high quality nanostructures. But both techniques have their own advantages and drawbacks. As for EBL it is well studied and widely applied for nanostructures formation with good controllability. But it is rather high cost and requires a lot of steps (resist spincoating, resist baking, resist exposure, resist revelation, resist or material etching) and a lot of tools (spin-coaters, hot-plates, resists, etchants, developers, rinsers, removers). These drawbacks can be overcome using SPL especially mechanical scratching and local oxidation. These methods don't require any tools except SPM and cantilevers. Probe oxidation seems to be the most appropriate technique because it can produce another material from initial substrate and to make arrays of different materials without any additional procedures like etching. The main drawback of this method is that it is not studied well especially for ferromagnetic materials. Therefore this method is still not applied in serial patterning and producing of structures on large area.

2. Local anodic oxidation of ferromagnetic metal films

2.1 Introduction

Despite a lot of work on LAO of different materials, oxidation of ferromagnetic metal films is still not studied enough. There are only few works on LAO of Ni [106-109], FeCo [109] and NiFe [109]. Works [106] and [109] studied fabrication of nanodots on ferromagnetic films and only [108] studied fabrication of oxide lines. While such lines can be used as nanosized elements for fabrication of planar tunnel junctions [108] or periodic planar structures that can serve as surface phononic crystal (PnC) for hypersonic frequency range that could be controlled by magnetic field [5].

There are a lot of parameters for example oxidation time and tip applied voltage on which oxidation process depends. One should know optimal parameters of LAO to obtain well defined oxide lines with good reproducibility. In this chapter we investigated main features of LAO process and optimal LAO parameters for oxide lines fabrication on ferromagnetic metal films Ni, Fe, Co and FeCo.

2.2 Ferromagnetic thin film deposition

A thin film is a layer of a material with a small thickness from few nanometers to several microns. Thin films can be deposited by different methods. All deposition technologies are divided on chemical and physical methods: physical vapor deposition and chemical vapor deposition methods [162].

The best physical method to deposit uniform films is magnetron sputtering. In this method target plate made of deposited material is bombarded by accelerated ions generated in a discharge plasma. Such bombardment sputters target atoms, which are condense on a substrate as a thin film [163]. Plasma is generated by gas introduced into the chamber (usually argon (Ar)) and high voltage applied between the target (cathode) and the substrate (anode) (Figure 2.1). Basic parameters of the deposition process are chamber vacuum (base pressure), Ar pressure (work pressure), target voltage and sputtering power [163]. Additionally the distance between the target and the substrate can be changed. By magnetron sputtering films of different materials including ferromagnetic thin films can be deposited.

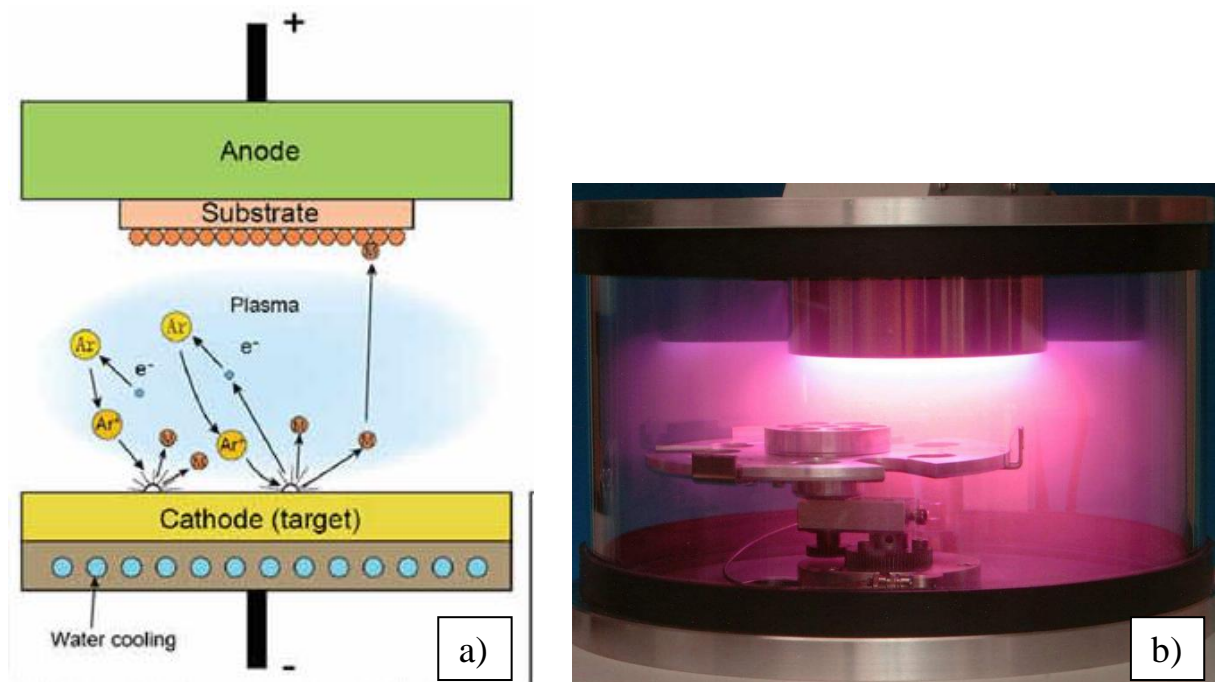


Figure 2.1. Schematic (a) and photo (b) images of magnetron sputtering system [164-165].

2.3 Experimental description

The experiments on LAO were performed on Ni, Fe, Co and FeCo with thickness $d=10$ nm. These films were fabricated by DC magnetron sputtering using systems VUP-5 and Leybold Z550 on monocrystalline Si(100) substrates with thermally oxidized $0.3 \mu\text{m}$ SiO_2 layer on top. Before sputtering substrates were cleaned in ultrasound bath by acetone, IPA and deionized water (DIW) and dried by nitrogen. Average roughness of deposited films was about $\sigma=0.15-0.2$ nm. AFMs MultiMode and Solver P47H in tapping mode were used to provide oxidation process on metal films. This mode was chosen because it doesn't damage surface and the tip can be used longer than in contact mode. Furthermore in earlier works it was shown that tapping mode helps to improve resolution and homogeneity of the oxide structures [89].

First we tried to obtain oxide dots by LAO on Fe film using different parameters of process to be sure in feasibility and controllability of this method (Figure 2.2). Then lithography was made in vector mode in the shape of lines along which the tip was moved on SPM scans areas of $1 \times 1 \mu\text{m}^2 - 10 \times 10 \mu\text{m}^2$. Different tips with different curvature radii (R_c) and coatings were used for experiments (Table 2.1). AFM images were analyzed using WSxM 5.0 and Gwyddion software [166-167].

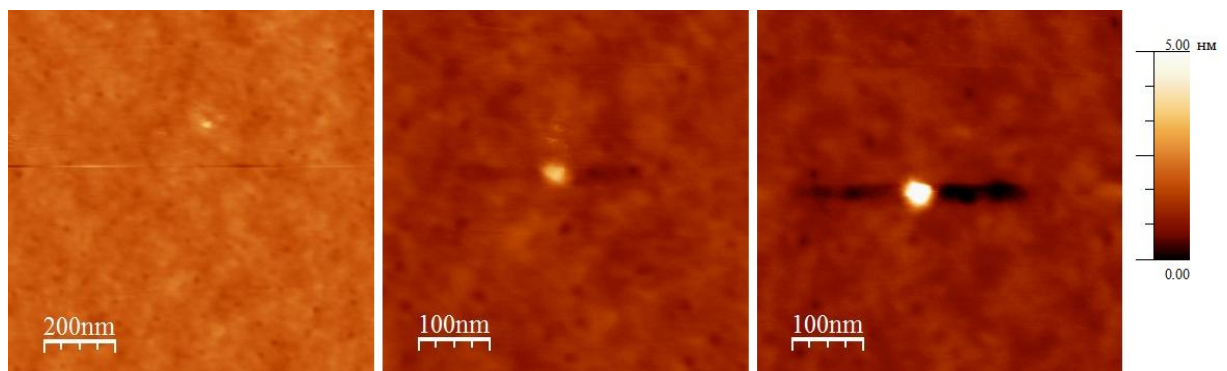


Figure 2.2. AFM images of oxide dots on Fe film at different oxidation parameters.

Table 2.1. Tips used for experiments.

Tip name	Tip R_c , nm	Shape tip/cantilever	Material tip/cantilever	Coating tip/cantilever	Resonant frequency, kHz
NSG10	<35	tetrahedral/ rectangular	Si/Si	W ₂ C/Au	240
CSC21	<50	tetrahedral/ rectangular	Si/Si	Cr-Au/Cr-Au	110
DCP20	100	tetrahedral/ triangular	Si/Si	Di doped with N/Au	420
ANSCM-PA	30	pyramidal/ rectangular	Si/Si	Pt-Ir/Pt-Ir	300
NSG30	35	tetrahedral/ rectangular	Si/SiN	TiN/Au	320
HYDRA 2R-50N	<10	tetrahedral/ rectangular	Si/Si	-/-	77

In order to understand the main features of ferromagnetic films LAO the influence of different parameters on oxidation results was studied. On Figures 2.3 a)-c) typical AFM images after LAO by lines are shown. Obtained oxide nanostructures have the form of protrusions on the modified sample. These protrusions appear because of incorporation of oxygen into the pattern during the oxidation and they can be easily observed by AFM: 2D (Figure 2.3 a) and 3D (Figure 2.3 c) AFM images show the change of film topography after LAO, phase image (Figure 2.3 b) is a function of the viscoelastic properties of the sample materials and shows change of these properties in the place where LAO was done (here phase is given as mirror image of topography). Height (h) and width (d, was determined as full width at half maximum to avoid

influence of tip convolution) of the protrusions were chosen as indicators of oxidation results. They were defined as average from five or seven cross-sections of oxide lines (Figure 2.3 d).

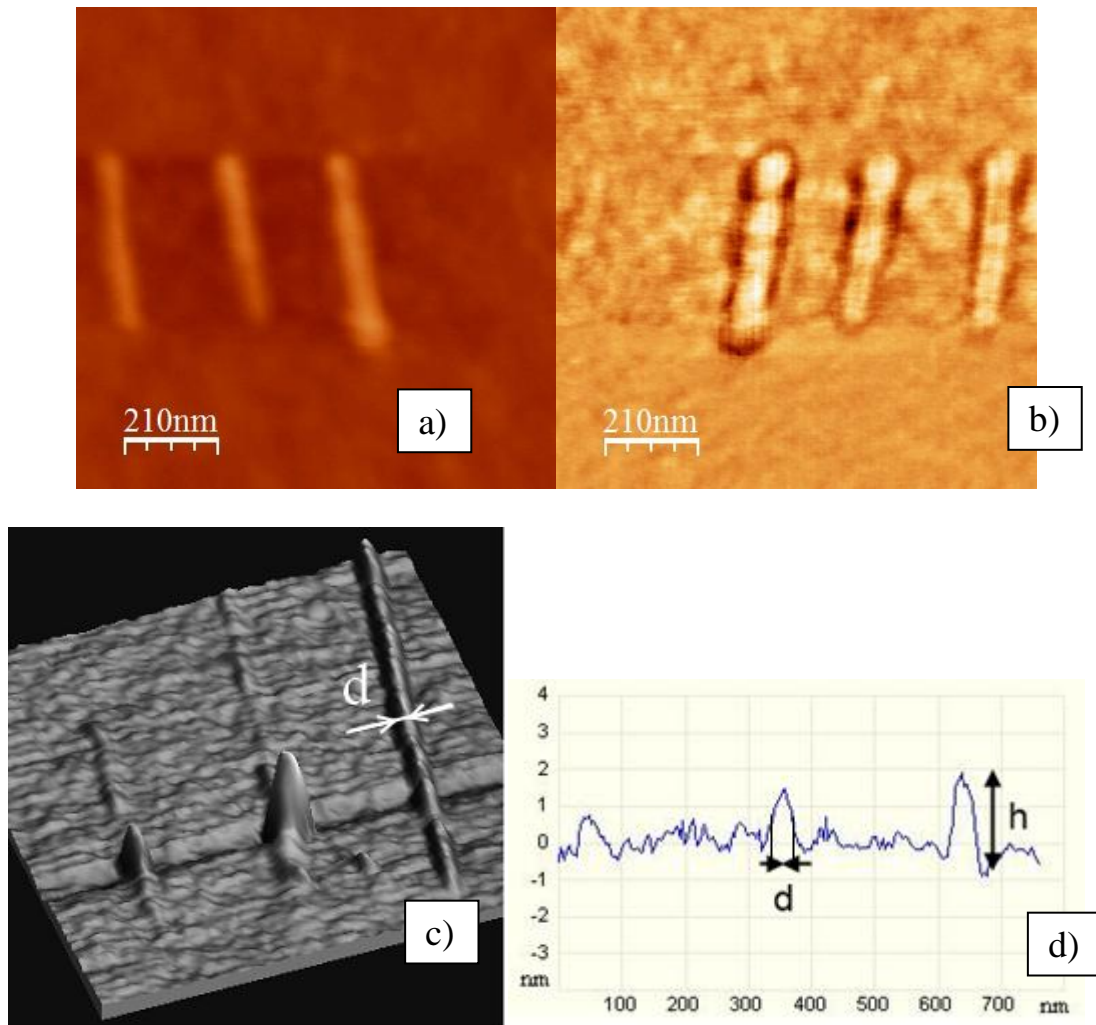


Figure 2.3. Images of films after LAO in vector mode: 2D AFM (a) and mirror phase (b) images of oxide lines on Fe film, 3D AFM image (c) and cross-section image (d) of oxide lines on FeCo film (h-height, d-width of oxide lines).

Oxidation time (T_{ox}), bias voltage between tip and sample (V), relative humidity (RH), oscillating amplitude set point of the tip (SP) and tip curvature radius (R_c) were chosen as main parameters of LAO process. Voltage and SP were changed by AFM tuning. Time of oxidation was set as tip velocity during oxidation (XY_v , AFM MultiMode) or by the duration of the voltage supply in each point of line pattern (AFM Solver P47H). To increase humidity the head of AFM was placed into a closed box with inlet for H_2O saturated nitrogen.

2.4 Local anodic oxidation reproducibility and sample drift

First we've decided to verify reproducibility of local anodic oxidation and to check the influence of thermal drift of the sample on local anodic oxidation results.

To test reproducibility of oxide lines sizes we fabricated 3 oxide lines on Fe film at the same oxidation parameters. Figure 2.4 shows that one can obtain lines the same width and height using same parameters. It means that LAO has a good reproducibility and we can define dependences of oxide lines sizes on oxidation parameters.

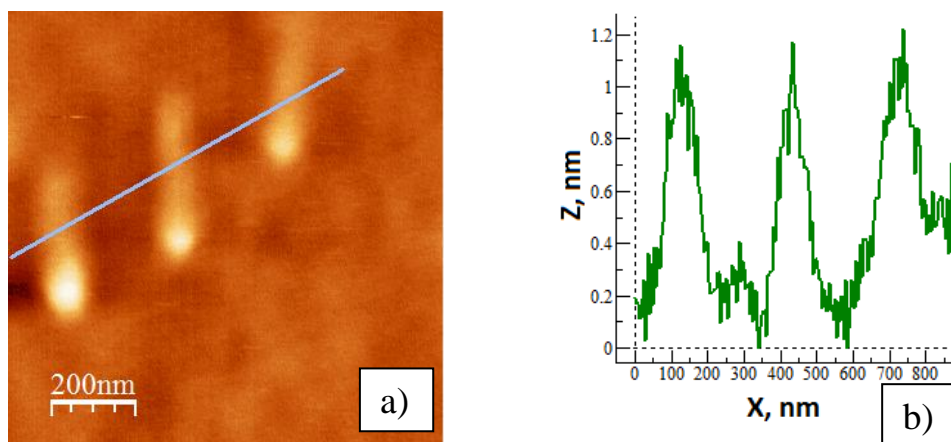


Figure 2.4. AFM image (a) and cross-section (b) of 3 oxide lines along the blue line made at the same oxidation parameters.

To check the influence of sample thermal drift on oxidation results we made oxidation in the shape of circle using big oxidation time. Figure 2.5 a) shows deviation of the oxide pattern topology from template due to the drift: start and end points of the circle do not converge forming a spiral. This effect should be taken into account in complex patterns oxidation and can be decreased by decreasing of oxidation time (Figure 2.5 b).

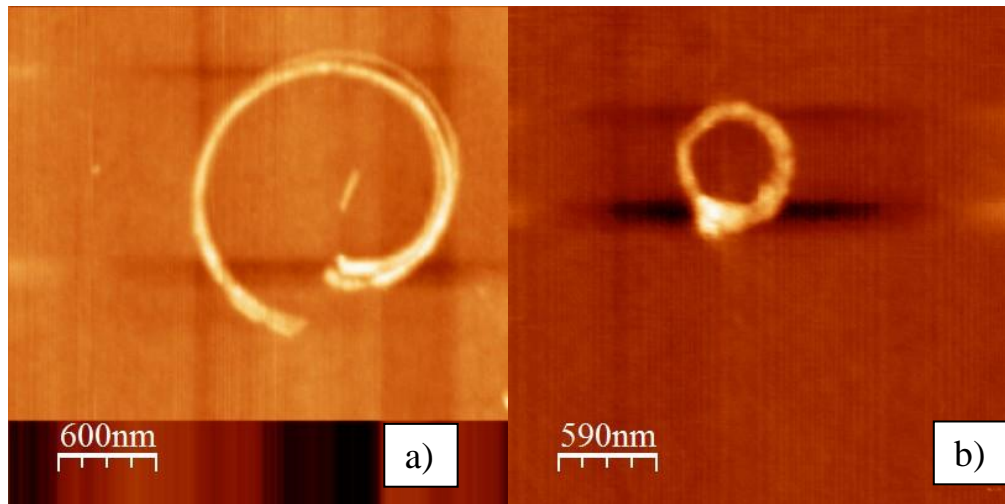


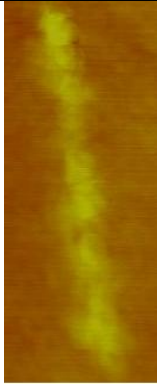

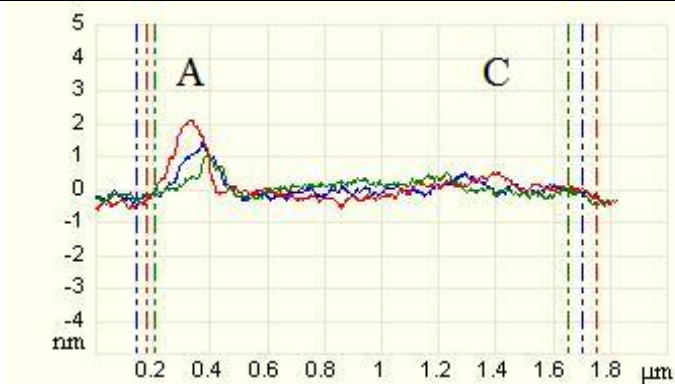
Figure 2.5. AFM images of circles made by LAO showing a) big sample drift and b) absence of drift influence on oxidation results.

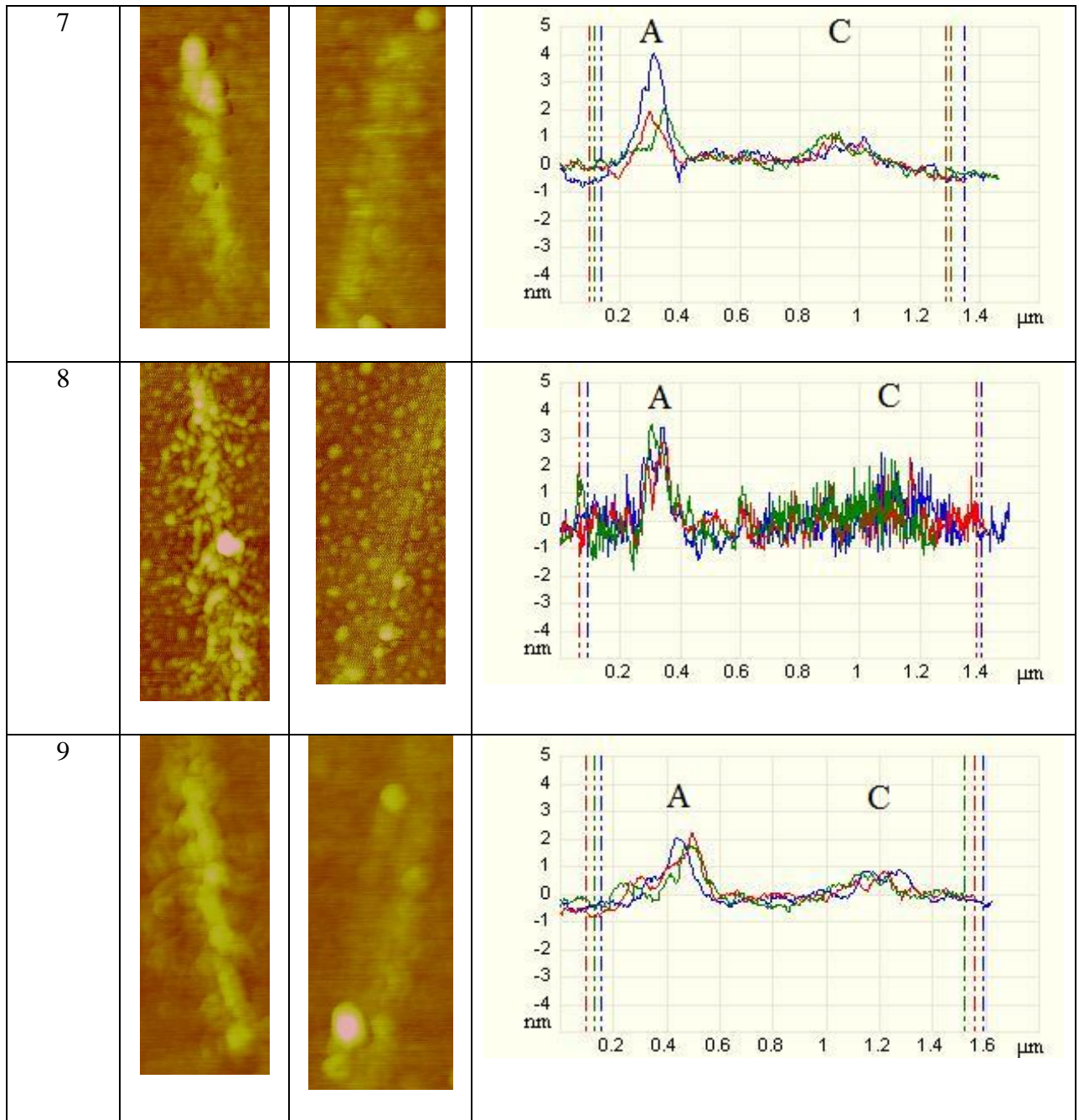
2.5 Dependence of local anodic oxidation results on parameters of the process

2.5.1 Dependence on bias voltage between tip and surface

To start determination of voltage influence on scanning probe oxidation the comparison of influence of positive and negative tip polarization was done. Experiments on study of anodic and cathodic oxidation were performed on FeCo film at the same oxidation time $XY_v=0.01 \mu\text{m/s}$ and scan size $2 \times 2 \mu\text{m}^2$ by ANSCM-PA tip. Voltage values varied from 6 to 9 V. In Table 2.2 there are AFM images and cross-sections of anodic and cathodic oxidation results. One can easily see that by applying negative bias to the tip better defined and higher oxide lines could be obtained while height of structures made by applying positive bias was too small and did not exceed 1 nm. It was decided that cathodic oxidation is not effective for fabrication of nanostructures on ferromagnetic metal films. It corresponds to previously obtained for Si [55] and Cr [61]. All following experiments were done by anodic oxidation.

Table 2.2. Comparison of anodic and cathodic oxidation.

Tip voltage, V	Anodic oxidation	Cathodic oxidation	Cross-sections
6			



Then the influence of negative tip voltage was investigated. Experiments were provided on Ni, Fe, Co and FeCo films. During experiments threshold oxidation voltages were found for oxide lines fabrication on investigated metals. The threshold voltage V_{tr} at which LAO starts are: $V_{tr}^{Ni} = V_{tr}^{FeCo} = -4V$ and $V_{tr}^{Fe} = V_{tr}^{Co} = -6V$. For all ferromagnetic metals except Co dependences of the oxide sizes on bias voltage of the tip were obtained. Oxidation of Co was not stable and reproducible at voltages below -10V so we couldn't find the clear dependence of oxide lines sizes on bias voltage. Height and width of oxide lines for Ni, Fe and FeCo increase with the increase of bias voltage (Figure 2.6). The most well defined lines were obtained at $V = -7 - -10V$.

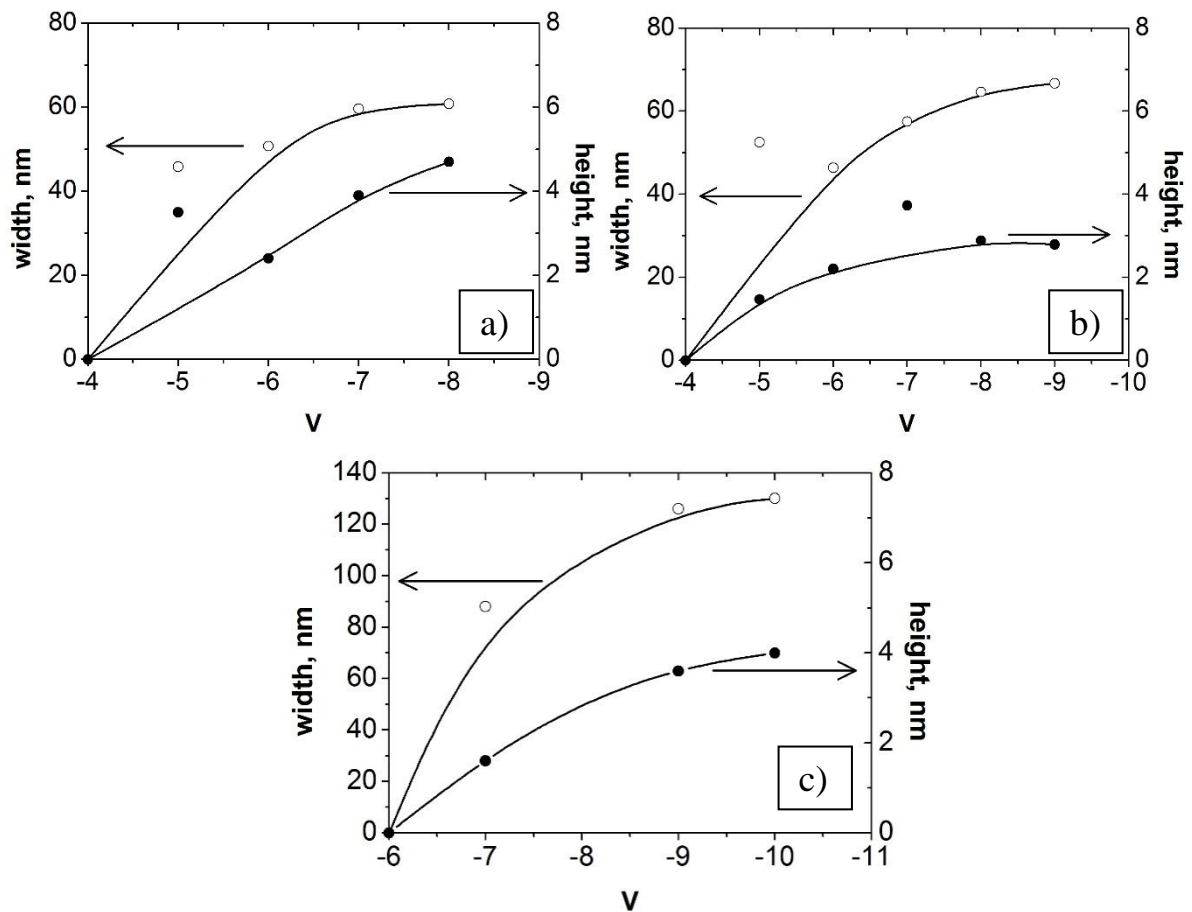


Figure 2.6. Dependences of the oxide sizes (height – solid circles, width – open circles) on bias voltage of the tip for a) Ni, b) FeCo, c) Fe films.

2.5.2 Dependence on oxidation time

Time of oxidation in these experiments was determined by the duration of the voltage supply T_{ox} in each point of line pattern. T_{ox} was set in the AFM software by the duration of the voltage pulse T and the number of pulses N . So first of all we made sure that $T_{ox}=T*N$. We've made 2 test oxide lines at the same $T_{ox}=0.5$ s but different T and N : $T=0.05$ s, $N=10$ and $T=0.1$ s, $N=5$. On Figure 2.7 there are given results of oxidation and one can see that oxide lines have the same height and width. So we made a conclusion that $T_{ox}=T*N$.

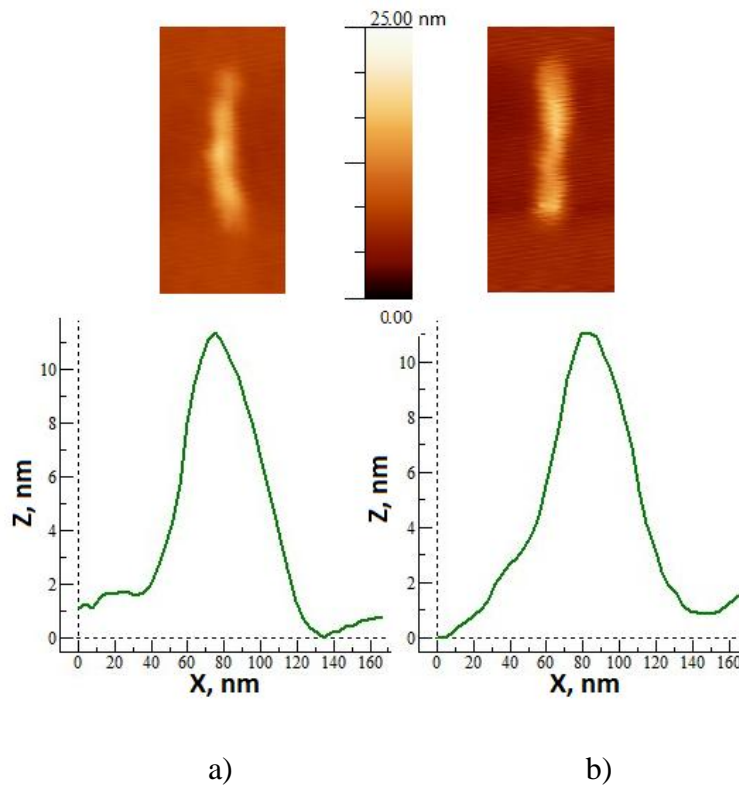


Figure 2.7. AFM images and cross-sections of oxide lines made at the same $T_{\text{ox}}=0.5$ s: $T=0.05$ s, $N=10$ (a) and $T=0.1$ s, $N=5$ (b).

Results on effect of the oxidation time on dimensions of oxide structures are in a good qualitative agreement with previous results obtained for Si and Ti [57]: an increase in the oxidation time leads to an increase in dimensions of oxide structures (Figures 2.8, 2.9). Best values of oxidation time to produce good lines with good reproducibility are: $T_{\text{ox}}=3-10$ s for Ni and FeCo and $T_{\text{ox}}=0.5-2$ s for Fe. Oxidation of Co was not very effective and reached the saturation of oxide lines sizes at $T_{\text{ox}}=1$ s.

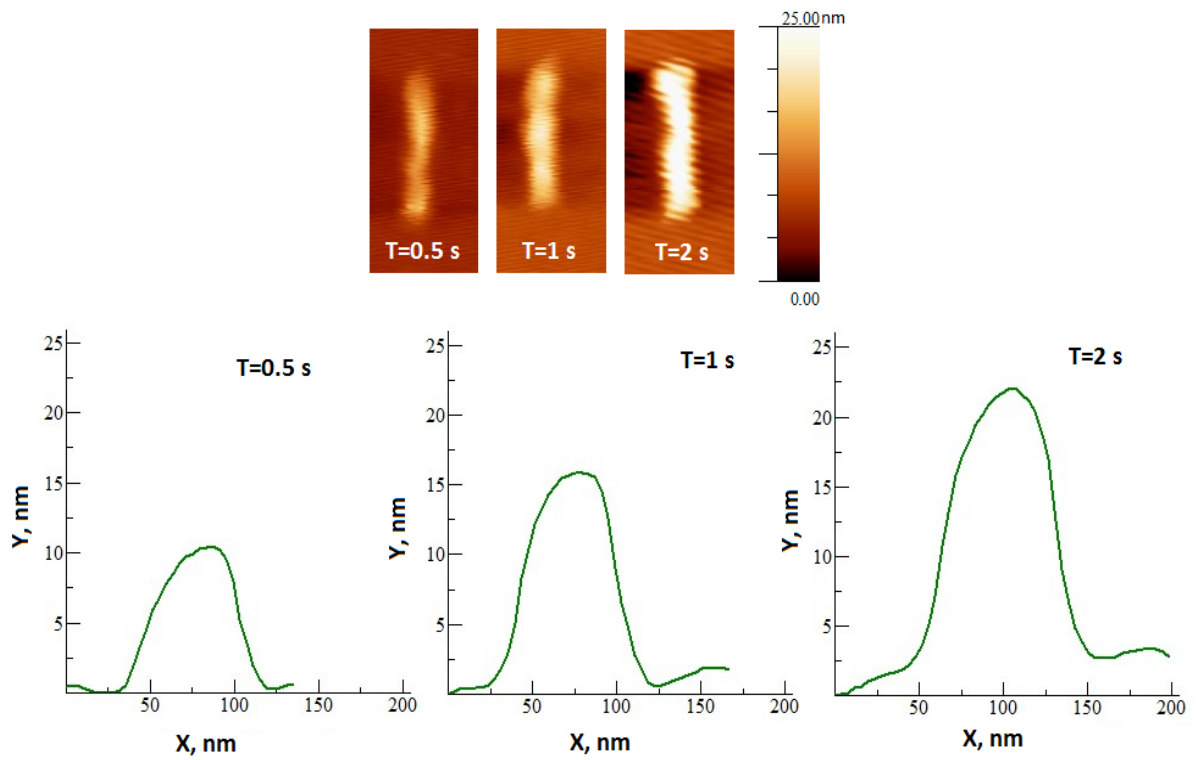


Figure 2.8. AFM images and cross-sections of oxide lines made at different oxidation time on Fe film.

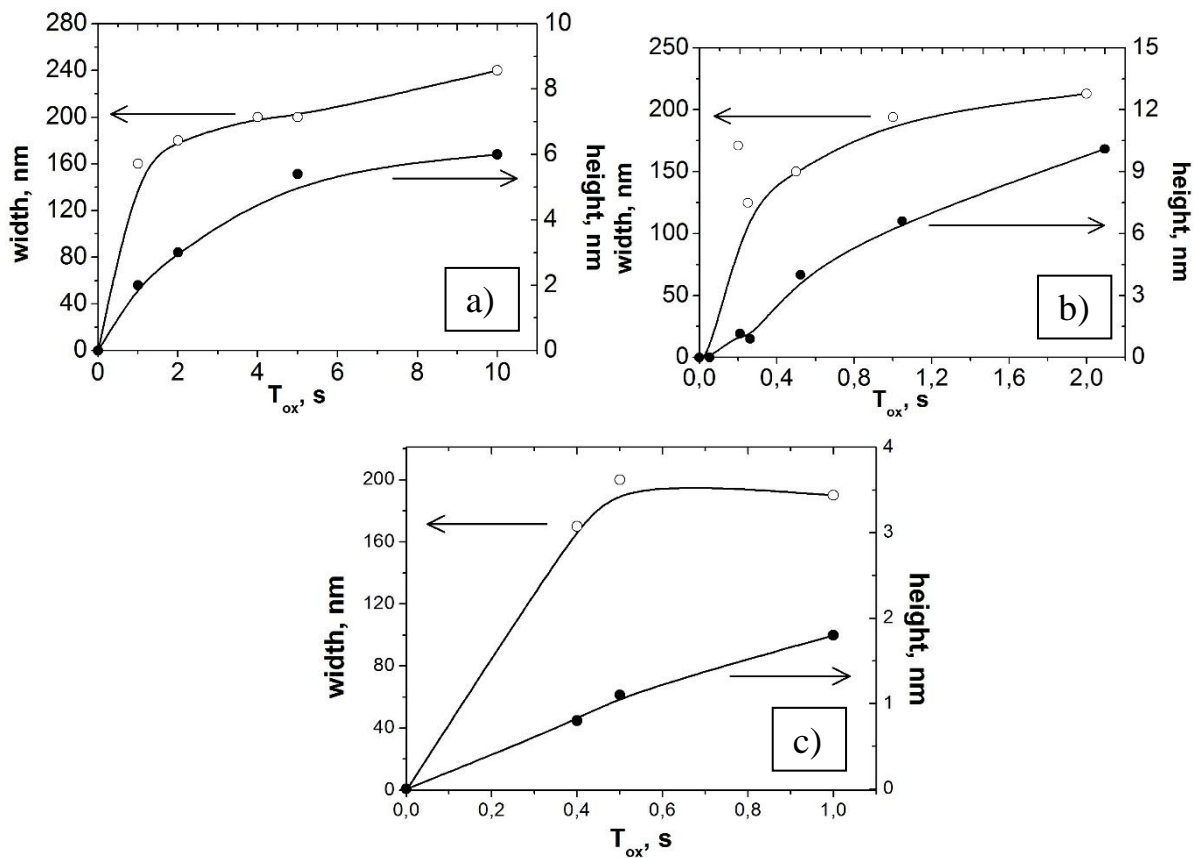


Figure 2.9. Dependences of the oxide sizes (height – solid circles, width – open circles) on oxidation time for a) Ni, b) Fe, c) Co.

2.5.3 Dependence on relative humidity

LAO at different relative humidity RH was studied on Fe film. Experiments were performed at the same oxidation time $T_{ox}=1$ s, tip-sample voltage $V=-10$ V and scan size 10×10 μm by NSG30 tip. Humidity varied from 28% to 75%. It was found that oxidation starts only at the humidity higher than 30%. Increase in humidity results in increase in dimensions of oxide structures (Figure 2.10). Obtained results are similar to those obtained for Ti earlier by other researchers [60]. The effect of the humidity on LAO can be used to adjust resolution of the lithography.

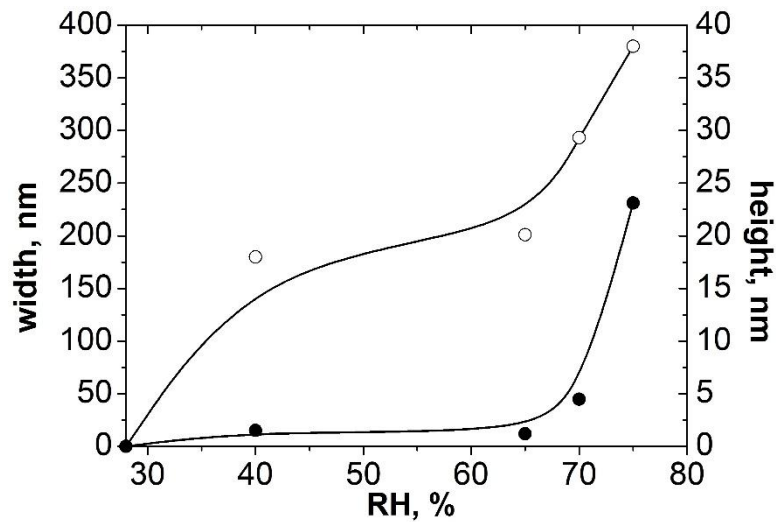


Figure 2.10. Dependences of the oxide sizes (height – solid circles, width – open circles) on relative humidity for Fe film.

2.5.4 Dependence on oscillating amplitude set point of the tip

Investigation of influence of oscillating amplitude set point of the tip on oxide lines sizes were provided on Fe film at voltage $V=-10$ V, oxidation time $T_{ox}=0.01$ s, humidity $\text{RH}=40\%$, scan size 1×1 μm^2 by DCP20 tip. SP varied from 0.2 to 6 (Figure 2.11).

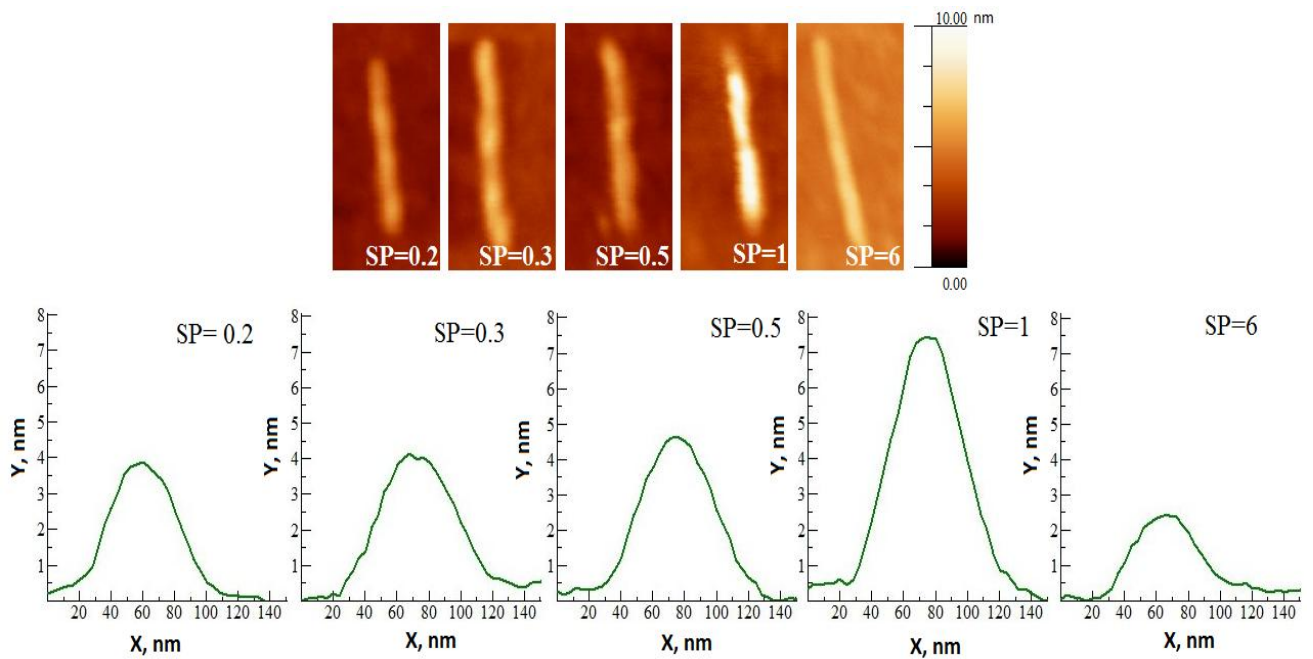


Figure 2.11. AFM images and cross-sections of oxide lines made at different SP values.

One can see that the increase of oscillating amplitude from 0.2 to 1 increases height of oxide lines by 60% (Table 2.3). At the same time there is a tendency of decreasing of oxide lines width. The same behavior of oxide sizes was shown in [87] on Si sample. Such behavior can be related with meniscus shape and size changes. Meniscus is considered to increase its height and decrease its diameter with increase of SP. This can be used to achieve higher resolution of lithography and to get more relief oxide images. But increase of tip oscillating amplitude to 6 which is commonly used for scanning leads to significant reduction of the oxide height. So the best SP values to provide oxidation lithography are 0.2 - 1.

Table 2.3. Oxide lines sizes on Fe film at different SP values.

SP	Fe	
	h, nm	d, nm
0.2	4	135
0.3	4.3	120
0.5	4.5	108
1	6.4	130
6	2.5	115

2.5.5 Dependence on other factors

Tip

It is clear that the tip curvature radius R_c significantly effects on the width of the oxide structure. In order to study this effect we performed experiments with tips of different radii. Experiments were provided on Ni film at voltage $V=-10$ V, oxidation time $T_{ox}=1$ s, $SP=0.2$ by NSG10, CSC21 and DCP20 tips. One can see that the bigger is tip for oxidation the wider is obtained oxide (Table 2.4). This fact can be used for changing lithography resolution by changing the tip. At the same time we can suppose the dependence of oxide height on tip coating work function. Using tip with coating that has smaller work function oxide with bigger height can be obtained.

Table 2.4. Oxide lines sizes obtained on Ni film by different tips.

Tip name/ coating	Tipradius R_c , nm	Tip coating work function, eV	Ni	
			h, nm	d, nm
NSG10/ W_2C	35	4.6	4.8	140
CSC21/ Cr- Au	<50	4.8	2.1	160
DCP20/ Di	100	5	3	250

Number of passes

We also tried to make LAO by 1 and 2 passes on the same line (Figure 2.12). In the case of 2 passes on the same line the width of the produced oxide line didn't change significantly compared to 1 pass while the oxide height increased on $\Delta=45-65\%$ (Table 2.5). We can suppose that second pass helps to increase the oxide depth without reducing the lithography resolution. LAO by more than 2 passes is not possible because of sample drift. LAO by 2 passes can be used for fabrication of single oxide element with high dimension but it is not suitable for fabrication of oxide lines arrays also because of sample drift.

Table 2.5. Oxide lines sizes on Ni and FeCo films for 1 and 2 passes of the tip.

	Ni		FeCo	
	h, nm	d, nm	h, nm	d, nm
1 pass	2.7	215	3.5	197
2 passes	4.5	248	5	213
Δ , %	67	15	43	8

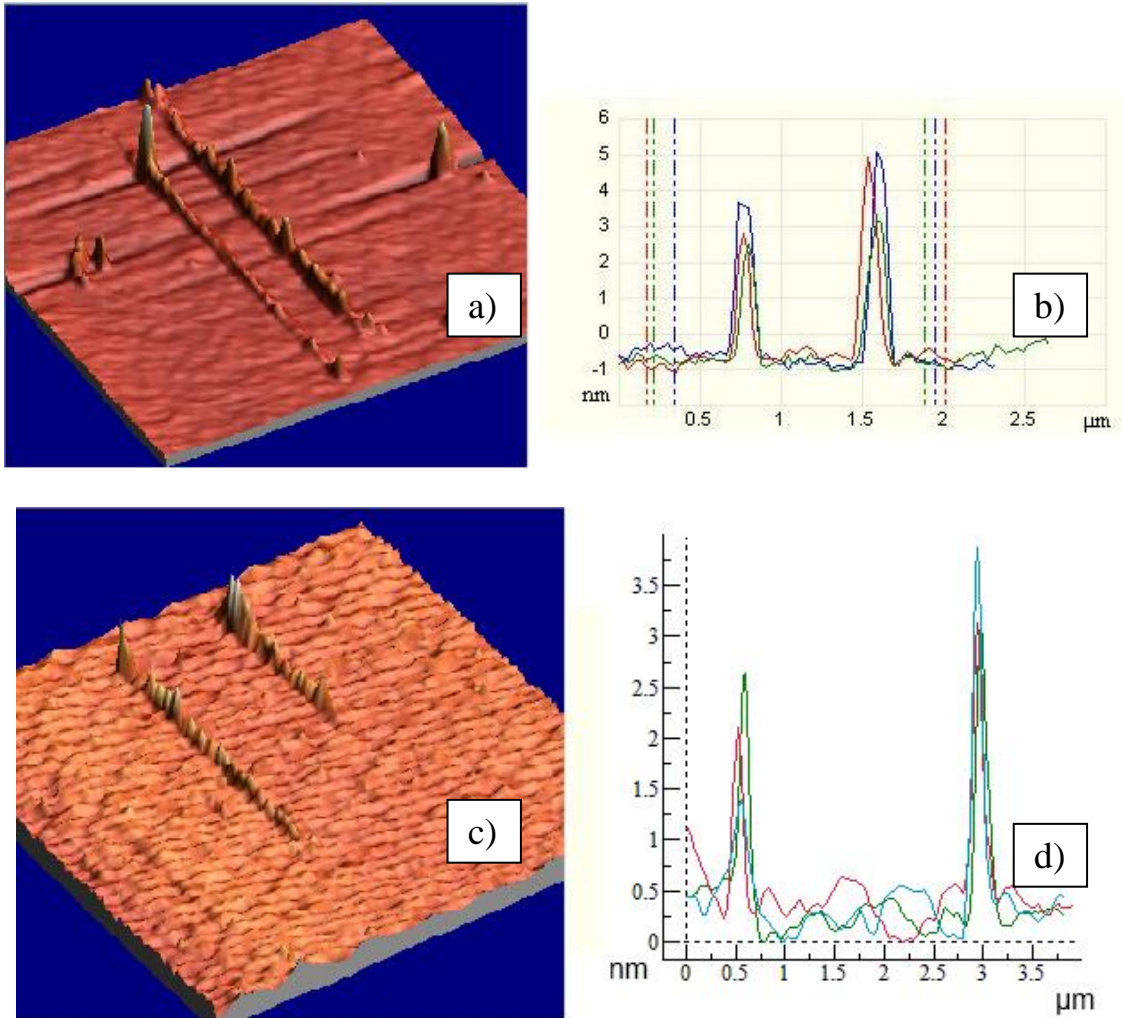


Figure 2.12. 3D AFM images (a, c) and cross-sections of oxide lines (b, d) on FeCo (a, b) and Ni (c, d) film made by 1 (left) and 2 (right) passes of the tip.

Scan size

It was noted that oxide width changes with scan size change. So we made few experiments on Ni, Fe and FeCo films to carry out dependence of oxide lines sizes on size of AFM scan and surface for oxidation respectively. Results are shown in Table 2.6. We investigated that with increase of scan size oxide structures width increases also while height stays almost the same. This fact should be taken into account in fabrication of narrow structures.

Table 2.6. Oxide lines sizes on FeCo and Fe films at different scan sizes.

	Ni		Fe		FeCo	
	h, nm	d, nm	h, nm	d, nm	h, nm	d, nm
1*1 μm^2	3.8	205	2.2	110	3.5	50
2*2 μm^2	-	-	2	170	-	-
5*5 μm^2	3.8	207	2.2	190	-	-
7*7 μm^2	-	-	-	-	3.5	197
10*10 μm^2	4	233			-	-
Δ_{max} , %	5	14	10	72	0	294

In view of results given in Tables 2.5 and 2.6 one could obtain narrow but rather high oxide nanostructures using small areas (for example 1*1 μm^2) and 2 passes on one line. But unfortunately in such case length of line is limited by the size of AFM scan. On Figure 2.13 result of fabrication of oxide structure with 20 nm width is shown on FeCo film at voltage V=-7 V.

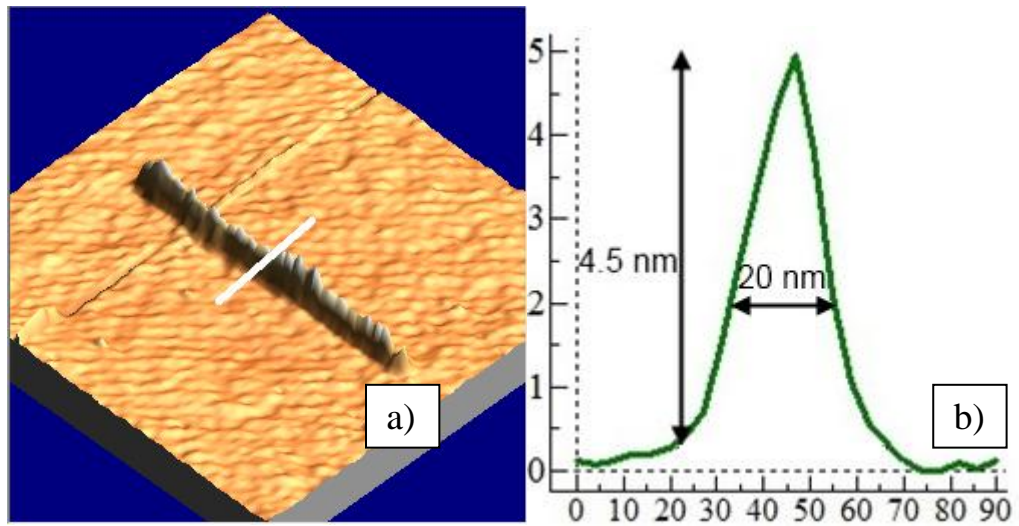


Figure 2.13. Oxide line on FeCo film made by 2 passes of the tip on $1 \times 1 \mu\text{m}^2$ scan area:
a) 3D AFM image and b) cross-section along the white line.

2.6 Local anodic oxidation and tip state

During LAO experiments it was noticed that tip working time has a big influence on oxidation results. LAO process efficiency was decreased while using one tip for oxidation process for a long time. On Figure 2.14 there are given 3D AFM image and cross-section of 3 oxide lines made at the same oxidation parameters by long used tip. One can see oxide line height reduction because of using an old tip.

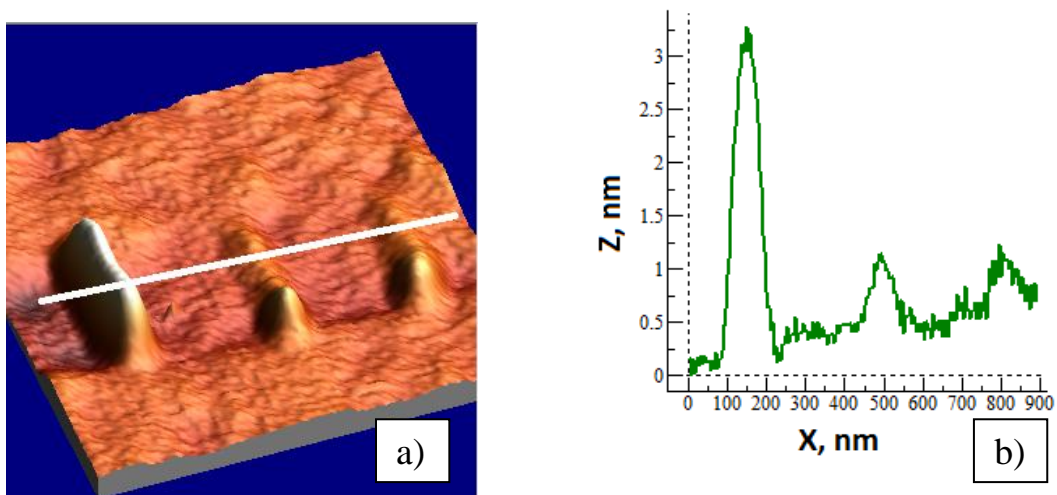


Figure 2.14. 3D AFM image (a) and cross-section (b) of 3 oxide lines along the white line made at the same oxidation parameters by an old tip.

First it was supposed that reduction of oxidation efficiency and reproducibility is related with degradation of conductive coating. So scanning electron microscope (SEM) imaging of long used diamond coated tips DCP20 was done. On Figure 2.15 SEM image of such tip is shown. It is seen that there is no damage of the tip but there is some outgrowth on it.

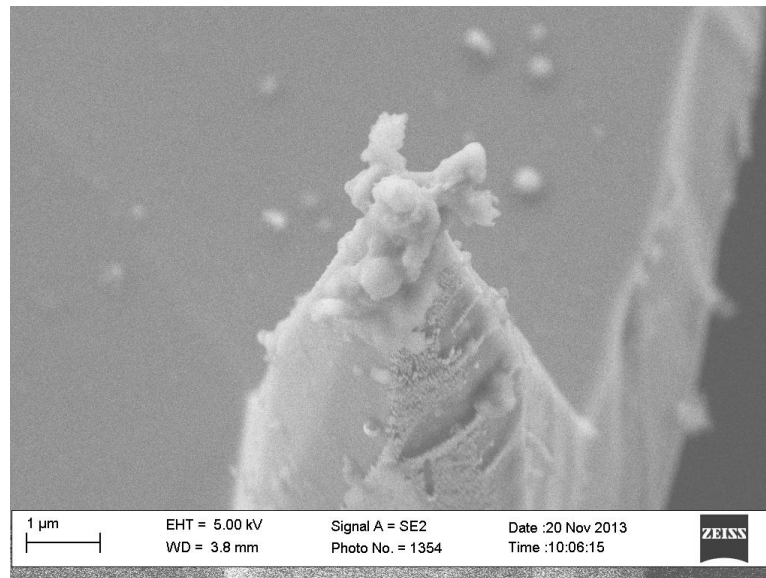
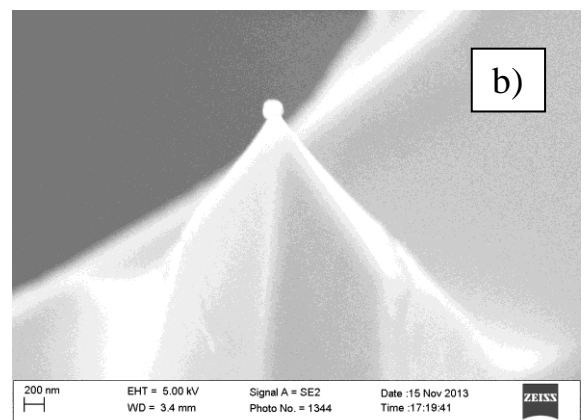
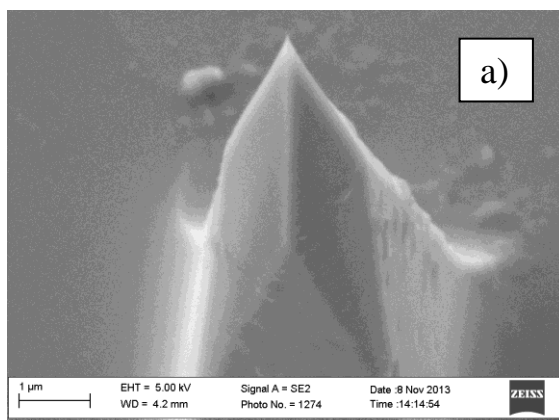


Figure 2.15. SEM image of used diamond coated tip.

It was decided to see what happens with tip after several LAO experiments. We try to use for LAO of several oxide lines new silicon tip without any coating: SEM imaging of the tip before and just after oxidation was made (Figure 2.16 a, b). One can see the sphere structure on the tip appeared after oxidation process. We tried to clean the tip from this structure by following procedure: 1) to set the tip above clean and smooth surface, 2) to reduce oscillating amplitude set point of the tip till the tip will touch the surface, 3) to start scanning of the $1 \times 1 \mu\text{m}$ surface at very low scanning speed for a short time, 4) to retrack the tip away from the sample surface. After such mechanical cleaning procedure we made SEM imaging of the tip again (Figure 2.16 c). This procedure was found to be very effective to clean the tip that was used for AFM oxidation not for a long time without destroying it. As it was found not effective to clean long used tips by this technique it is recommended to apply such procedure to the tips after every several oxidation procedures to keep the tip clean and to prolongate its life time.



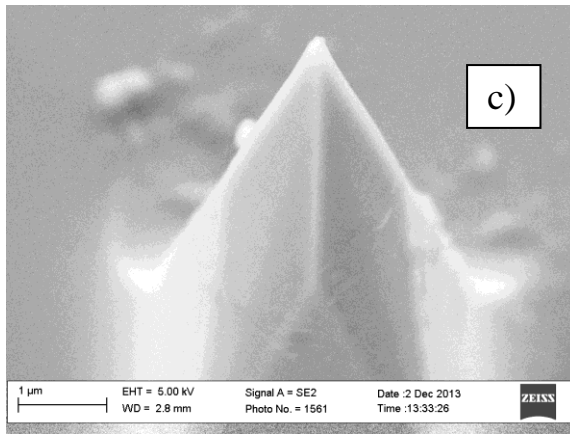


Figure 2.16. SEM images of Si tip before LAO (a), after LAO (b) and after mechanical cleaning (c).

2.7 Conclusions

In summary, in this chapter we successfully studied LAO of ferromagnetic metal films. We studied an effect of variety of LAO parameters on dimensions of fabricated oxide nanostructures and investigated dependences of oxide lines sizes on these parameters for ferromagnetic metal films Ni, Fe, Co and FeCo. Similar investigation was provided before in work [109] just for oxide dots on Ni and FeCo films and for consideration of a fewer number of parameters. We found that the most reproducible and well defined oxide lines can be obtained for Ni and FeCo films. Oxidation of Fe was very effective but it became sometimes hard to control lines sizes at big oxidation times or tip voltages. As for LAO of Co films it was found to be not effective at tip voltages below -10 V. From our experiments, the best films for fabrication by LAO of oxide lines or other oxide structures with controlled sizes are Ni and FeCo. We obtained optimal oxidation parameters for fabrication of lines with certain sizes on these films. For example in Table 2.7 there are LAO parameters for fabrication of oxide lines 500 nm in width.

Table 2.7. LAO parameters for fabrication 500 nm sized oxide lines.

	Oxidation time T_{ox} , s	Tip voltage, V	SP	Humidity, %	Tip radius R_c , nm
Ni	10	-10	0.2	70	30
FeCo	3	-10			

3. Local anodic oxidation of textured ferromagnetic metal films

3.1 Introduction

It is well known, that the surface properties of the film, in particular the crystallographic orientation affects the oxidation process [168-170]. However, influence of crystallographic orientation on sizes of oxide nanostructures produced by LAO was not studied earlier. Since the magnetic properties of the film are related to its crystallographic orientation [171], the study of oxide nanostructures formation on films with different textures can be useful for optimization of the parameters of devices fabricated using LAO technology.

In this chapter we have studied the influence of the texture of Ni and Fe films on sizes of oxide structures obtained using AFM oxidation. 100 nm thick textured polycrystalline Ni(200), Ni(111), Fe(200) and Fe(110) films were used for experiments. Recipes for textured film fabrication are obtained by magnetoelectronics research group of IRE RAS and are described in [172-173].

3.2 Film texture and oxidation of textured metal films

The orientation of a crystal plane or a crystallite may be defined by considering how the plane intersects the main crystallographic axes of the solid. The application of some rules leads to the assignment of a set of numbers which quantify the intercepts and thus may be used to uniquely identify the plane or surface. These numbers are Miller Indices (hkl) [174]. Miller Indices are determined by the following rules (see example on Figure 3.1 a):

- to find the intercepts on the axes in terms of the lattice constants a_1 , a_2 , a_3 (Example: $3a_1$, $2a_2$, $2a_3$);
- to take the reciprocals of these numbers and then reduce to three integers having the same ratio, usually the smallest three integers (Example: reciprocals - $1/3$, $1/2$, $1/2$, the smallest three integers - 2, 3, 3);
- to enclose the result in parentheses (hkl) (Example: (233)).

The indices of some important planes in a cubic crystal are illustrated by Figure 3.1 b).

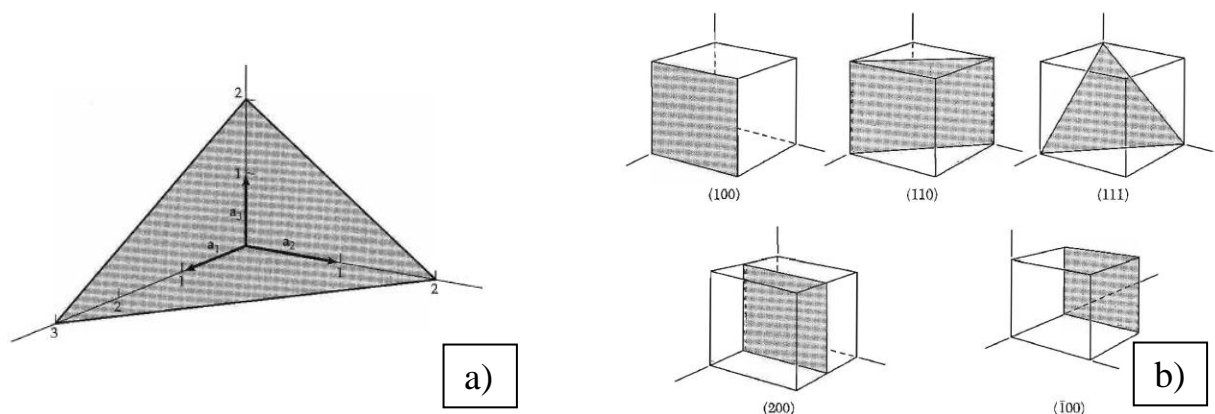


Figure 3.1. Miller indices determination example (a) and Miller indices of important planes in a cubic crystal (the plane (200) is parallel to (100)) [174].

Film texture is the preferred orientation of crystallites, it is an important characteristic of the microstructure of polycrystalline films. A sample in which crystallites orientations are fully random is said to have no texture. A common technique to measure texture is X-Ray diffraction (XRD). The interaction of the X-rays with a crystalline sample produces constructive interference (and a diffracted ray) when conditions satisfy Bragg's Law ($n\lambda=2d\sin\theta$). This law relates the wavelength of electromagnetic radiation to the diffraction angle and the lattice

spacing in a crystalline sample. These diffracted X-rays are then detected, processed and counted [175].

It is well known that film properties including the oxidation rate depend on film texture. There are a lot of works on study of Ni and Fe textured films oxidation. For example in [168-169] was obtained that thermal oxidation rate of Ni(200) is bigger than for Ni(110) and Ni(111). Investigation of Fe films oxidation both in oxygen environment and on air showed the next order of oxidation rate: (200) >> (111) > (110) [176-178].

3.3 Local anodic oxidation of textured polycrystalline Ni(111) and Ni(200) films

3.3.1 Fabrication and properties of textured Ni films

Ni(200) and Ni(111) films with thickness $d_{\text{Ni}}=100$ nm were used for experiments. A Ni target (99.95%, Williams) and argon (Ar 99.998 %) were used for films fabrication by DC sputtering with base pressure $P=0.2$ mPa. Ni films were deposited at rate of $v=17$ nm/min at room temperature (sputtering power 57 W and target voltage $U_{\text{tgt}}=-480\text{V}$) on monocrystalline Si(100) substrates with thermally oxidized $0.3 \mu\text{m}$ thick SiO_2 top layer. Before sputtering substrates were ultrasonically cleaned in acetone and then annealed in vacuum 0.2 mPa for 30 min at temperature 620-670K. Ni(111) films were deposited at work pressure $P_{\text{Ar}}=0.1$ Pa with negative substrate bias $U_{\text{b}}= -100$ V, and Ni(200) films were deposited at $P_{\text{Ar}}=0.2$ Pa with substrate bias $U_{\text{b}}=+100$ V. All aspects of deposition technological process are described in [172].

XRD ($\text{CuK}\alpha$, $\lambda_{\text{Cu}} \approx 0.15418$ nm) and SEM were used to study texture and microstructure of Ni films. Anisotropic magnetoresistance (AMR) curves were measured at different angles between current and magnetic field up to 200 Oe to study difference in magnetic properties of textured Ni films.

XRD patterns, SEM cross-sections and top views and AMR curves of Ni(200) and Ni(111) are given in Figure 3.2. Figures 3.2. c)-f) shows that Ni(200) and Ni(111) films with thickness $d_{\text{Ni}}=100\text{nm}$ have similar microstructure, but average lateral grain size for Ni(111) film $\xi \approx 40\text{nm}$ is twice bigger than for Ni(200). Root mean square roughness of Ni(111) и Ni(200) films are $\sigma^{(111)} \approx 0.38$ nm and $\sigma^{(200)} \approx 0.75$ nm respectively. Figures 3.2. g)-h) shows that Ni(200) film have a magnetoresistance up to 1.5% at angle between current and magnetic field = 0° , while the highest magnetoresistance for Ni(111) films is 0.8%.

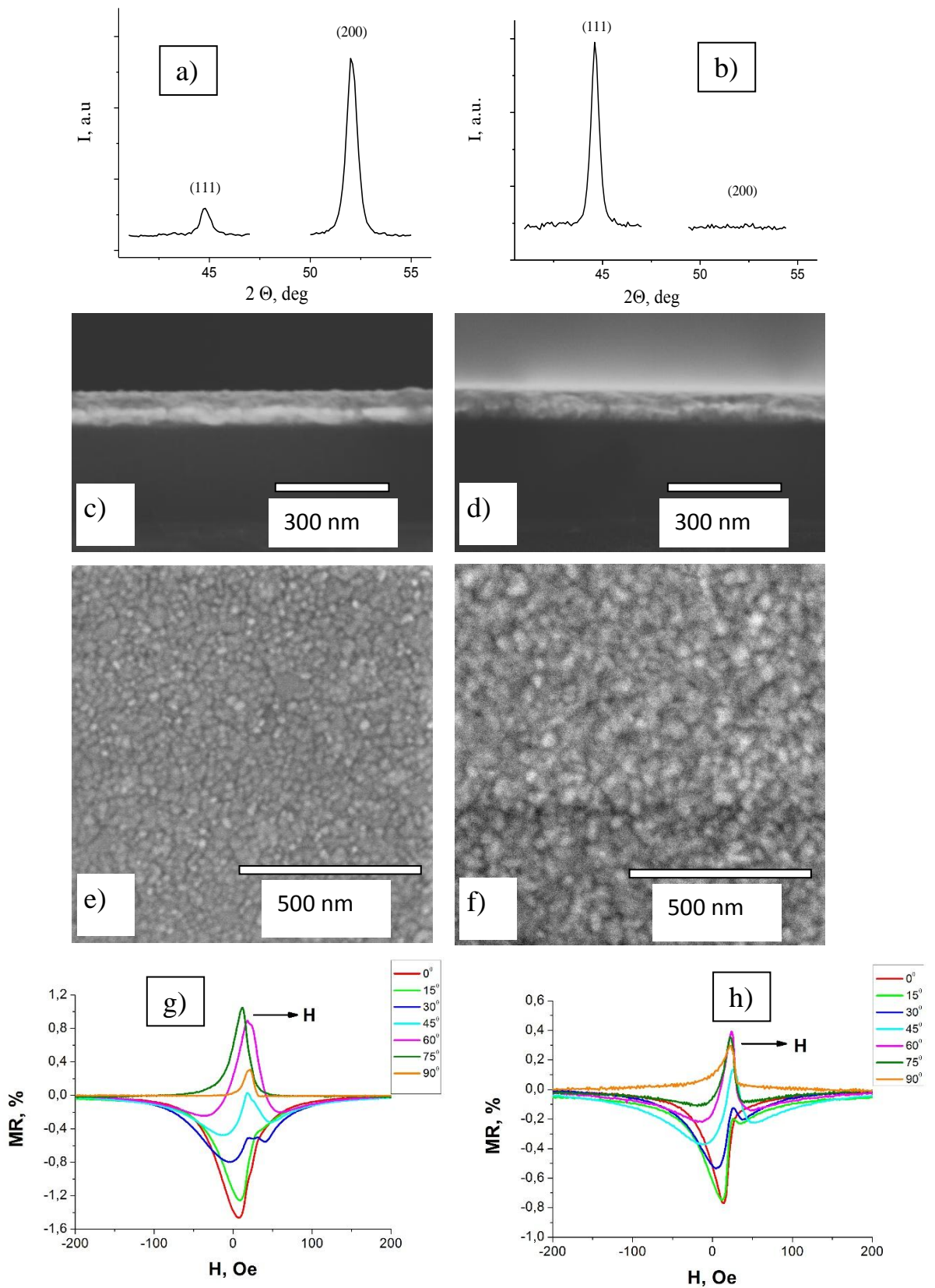


Figure 3.2. XRD patterns (a,b), SEM cross-sections (c,d), top views (e,f) and AMR curves (g,h) of Ni(200) (a,c,e, g) and Ni(111) (b,d,f, h) films.

3.3.2 Local anodic oxidation resultstextured Ni films

Scanning probe microscope (Solver P47, NTMDT) in a tapping mode was used to provide local anodic oxidation process. Cantilevers NSG30 with TiN conductive coating (NT-MDT) were used for experiments. Relative humidity was 65-70%. Oxidation was performed in the shape of lines. As result oxide lines were formed as protrusions on the modified films, see Figures 3.3 c)-f).

To investigate influence of Ni film's texture on geometrical parameters of oxide nanostructures a comparison of height (h) and width (d) of lines on Ni(111) and Ni(200) films formed at the same voltage values V and oxidation time T was performed.

Figures 3.3 a)-b) show the dependences of geometrical parameters h and d of oxide structures on the oxidation time T for a fixed voltage between the cantilever and the film $V = -10$ V. One can see that oxide pattern forms ($h > \sigma$) at oxidation time T higher than some threshold time T_{tr} .

As seen from Figures 3.3 a)-b) T_{tr} is different for Ni(200) and Ni(111) films: $T_{tr}^{(200)} = 0.01s$ and $T_{tr}^{(111)} = 0.2s$ respectively. Dependence of oxide pattern's height h on T reaches saturation at different oxidation time for Ni(200) and Ni(111) films: $T \geq 2.5s$ for Ni(200) and $T \geq 1s$ for Ni(111). Furthermore the height of oxide lines on Ni (200) films is greater than on Ni (111) films ($h^{(200)} > h^{(111)}$) but there is no noticeable difference in the width of oxide lines on Ni(200) and Ni(111) films ($d^{(200)} = d^{(111)}$). For example, Figures 3.2 c)-f) show AFM images and cross-sections of oxide lines on Ni (200) and Ni(111) films at $T = 1, 2.5$ and 5 s.

Figure 3.4 shows the dependences of geometrical parameters h and d of oxide structures on voltage V for a fixed oxidation time $T = 1$ s. One can see that threshold voltage V_{tr} for oxide formation initiation on Ni(200) film is lower than V_{tr} for Ni(111): $V_{tr}^{(200)} = -4V$ and $V_{tr}^{(111)} = 6V$. $V_{tr}^{(111)}$ is bigger than that obtained for non textured films in Chapter 2 as $V_{tr}^{(200)}$ is equal to it.

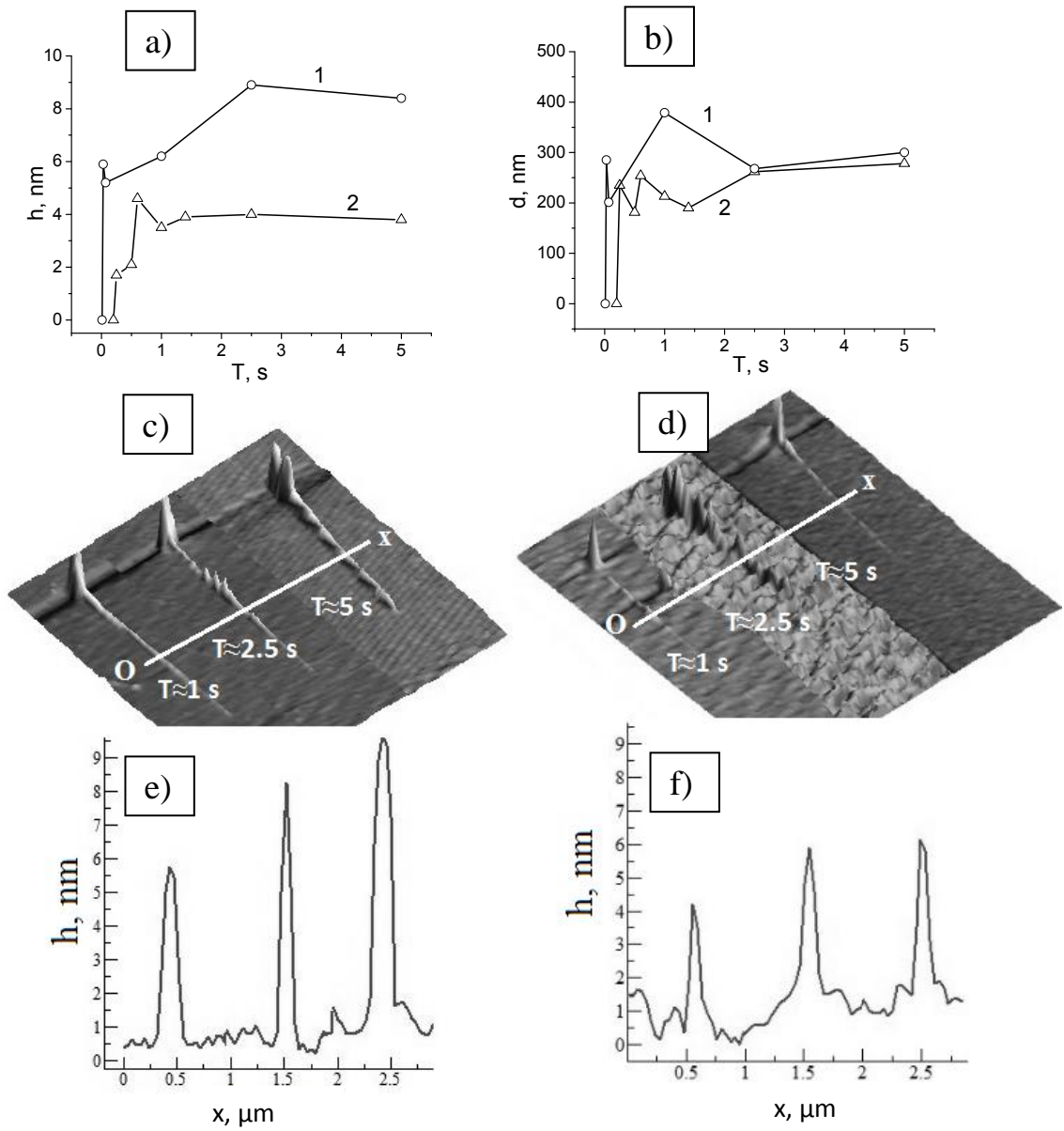


Figure 3.3. Dependences of the oxide lines height h (a) and width d (b) on oxidation time T for Ni(200) (1) and Ni(111) (2) films; AFM images (c, d) and cross-sections of oxide lines along the Ox (e, f) on Ni (200) and Ni(111) films at $T=1, 2.5$ and 5 s.

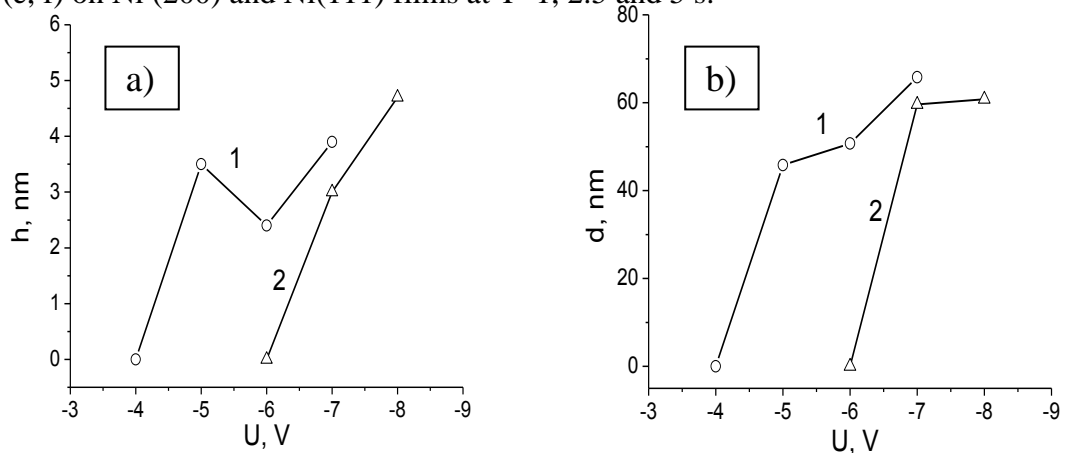


Figure 3.4. Dependences of the oxide lines height h (a) and width d (b) on tip-sample voltage V for Ni(200) (1) and Ni(111) (2) films.

In this way, oxidation of Ni(200) film occurs at lower values of threshold oxidation time T and threshold voltage V_{tr} than oxidation of Ni(111) films ($V^{(200)} < |V_{tr}^{(111)}|$, $T_{tr}^{(200)} < T_{tr}^{(111)}$). At the same time LAO causes formation of higher oxide structures on Ni(200) film: $h^{(200)} > h^{(111)}$. So we can conclude that oxidation process induced by LAO for Ni(200) is more effective than for Ni(111). These results correspond to the previously obtained and can be explained by higher oxidation rate for Ni(200) films due to the lower package density of the atoms on (100) surface in comparison with (111) surface [169-170].

We should note that the lack of difference in width of oxide structures for Ni(200) and Ni(111) films ($d^{(200)} = d^{(111)}$) can be related to locality of oxidation process. In such a way the boundary of oxidation region can act as a defect that suppresses an influence of the crystallographic orientation on the oxidation rate [74].

3.4 Local anodic oxidation of textured polycrystalline Fe(110) and Fe(200) films

First Fe(200) and Fe(110) films with thickness $d_{\text{Fe}}=100$ nm were fabricated. For films fabrication by DC sputtering a Fe target (99.95%, Williams) and argon (Ar 99.998 %) were used. Fe films like previously Ni films were deposited at room temperature, sputtering power 57 W and target voltage $U_{\text{tgt}}=-480\text{V}$ (rate of $v=18$ nm/min) on monocrystalline Si(100) substrates with thermally oxidized 0.3 μm thick SiO_2 on top cleaned as before for Ni films fabrication. Fe(110) films were deposited at work pressure $P_{\text{Ar}}= 1.3$ Pa with and Fe(200) films were deposited at $P_{\text{Ar}}= 0.13$ Pa. The details of deposition process are described in [173]. XRD patterns of Fe(200) and Fe(110) are given in Figure 3.5.

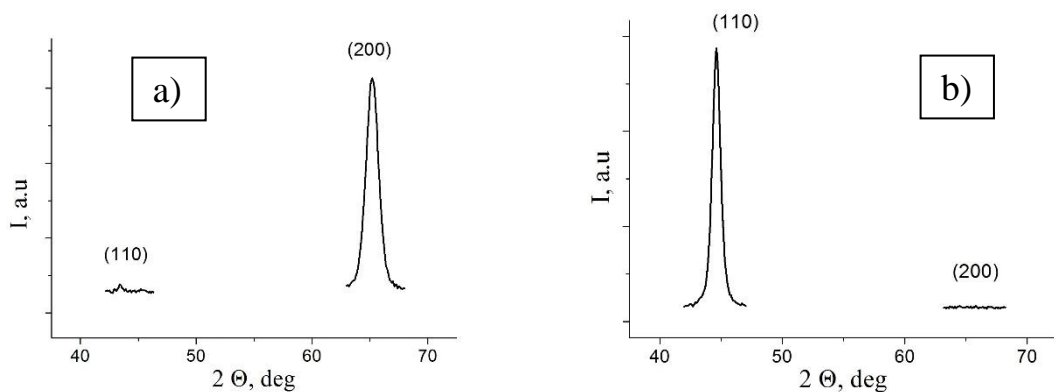


Figure 3.5. XRD patterns of Fe(200) (a) and Fe(110) (b) films [175].

Local anodic oxidation was done using the same equipment as for Ni films oxidation by NSG30 cantilevers at relative humidity of 65-75%. Comparison of height h and width d of lines on Fe(110) and Fe(200) films formed at the same voltage values V and oxidation time T was performed as before.

Figures 3.6 a)-b) show the dependences of geometrical parameters h and d of oxide structures on the oxidation time T for a fixed voltage between the cantilever and the film $V= -10$ V. One can see that $T_{\text{tr}}^{(200)}=0.2$ s and $T_{\text{tr}}^{(110)}= 0.6$ s and generally the height and width of oxide lines on Fe(200) films are greater than on Fe(110) films ($h^{(200)}> h^{(110)}$ and $d^{(200)}>d^{(110)}$). At the same time there was not found big difference in geometrical sizes of oxide structures on textured films with tip voltage V .

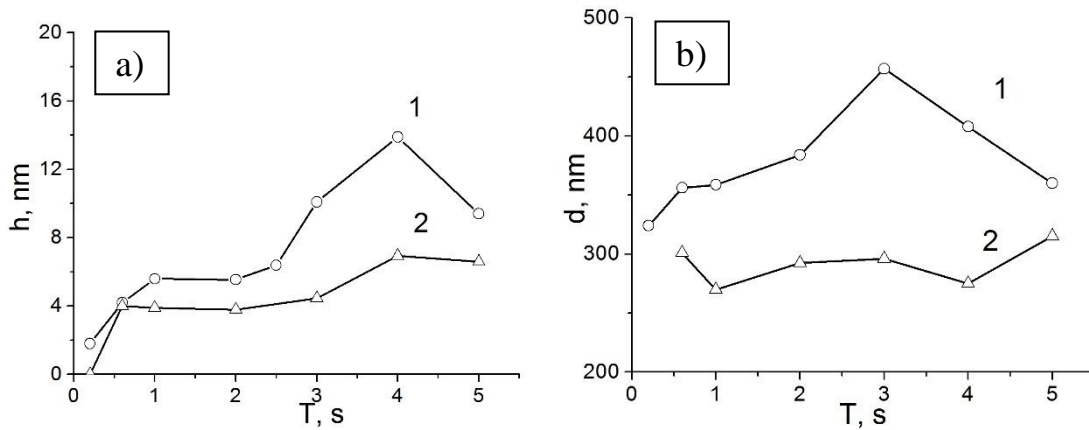


Figure 3.6. Dependences of the oxide lines height h (a) and width d (b) on oxidation time T for Fe(200) (1) and Fe(110) (2) films.

3.5 Conclusions

From these experiments it can be concluded that oxidation by SPM probe depends on the texture of the ferromagnetic film. It was found that oxidation is more efficient for films Ni(200) and Fe(200) than for films Ni(111) and Fe(110). This result is consistent with the results on the oxidation of textured Ni and Fe by other methods [168-170] and can be used for the optimization of parameters and fabrication process of the devices based on LAO nanostructures.

Results on LAO of textured Ni film showed that oxidation of Ni(200) film starts at lower values of threshold oxidation time T and threshold voltage V_{tr} than oxidation of Ni(111) films ($V^{(200)} < |V_{tr}^{(111)}|$, $T_{tr}^{(200)} < T_{tr}^{(111)}$). Thus, fabrication of oxide structures on Ni(200) film with the same dimensions as on Ni(111) film requires a lower voltage on the probe and smaller oxidation time at each point. Lower tip voltage allows to increase the tip lifetime and to decrease the probability to damage the nanostructure by the discharge, and reducing of the oxidation time at each point allows to significantly reduce the whole fabrication time of the nanostructure. Simultaneously, magnetoresistance of Ni(200) is higher than for Ni(111) that can be used in fabrication of nanostructures with good magnetic properties. And it can be concluded that using of Ni(200) film is preferred for device fabrication using LAO.

At the same time using for oxide nanostructures fabrication of Fe(200) film instead of Fe(110) cannot help to increase tip lifetime or controllability of nanostructures fabrication because there was not founded the dependence of threshold oxidation voltage V_{tr} on texture of Fe film. Nevertheless, using of Fe(200) film for LAO allows to decrease oxidation time because $T_{tr}^{(200)} < T_{tr}^{(110)}$.

4. Studying of the properties of nanostructures made by scanning probe lithography

4.1 Introduction

To have an opportunity to use oxide nanostructures made by LAO for device fabrication it is needed to know properties of these nanostructures. It was decided to know electrical properties of oxide lines on Ni and FeCo films by current-voltage characteristics measurements of metal microstripes before and after LAO. Also it was decided to make Auger electron spectroscopy with the goal to identify what kind of changes LAO produces in sample material. Simultaneously there were investigated electrical and magnetic properties of metal microstripes patterned by scanning probe mechanical scratching.

4.2. Current-voltage characteristics of nanostructures made by local anodic oxidation

Experiments on current-voltage characteristics of oxide nanolines made by LAO were performed on microstrips of Ni and FeCo (Figure 4.1 a, b). Widths of these microstrips were $D=2-8 \mu\text{m}$. Thicknesses of Ni and FeCo films were $d\sim 6 \text{ nm}$. For current-voltage measurements before and after LAO microstrips were made between gold contact pads. To fabricate microstructures the most simple lithography process - lift-off – was done. Photolithography, magnetron sputtering and ion etching were used to fabricate microstrips on glass substrates. Glass substrates were chosen because of its good insulation properties. For fabrication following equipment was used:

- Leybold Z550 and VUP-5 machines for sputtering,
- Plassys Mu 350 machine for ion beam etching

After fabrication procedure (described in Appendix 1) the samples with several microstrips were fabricated (Figure 4.1 c).

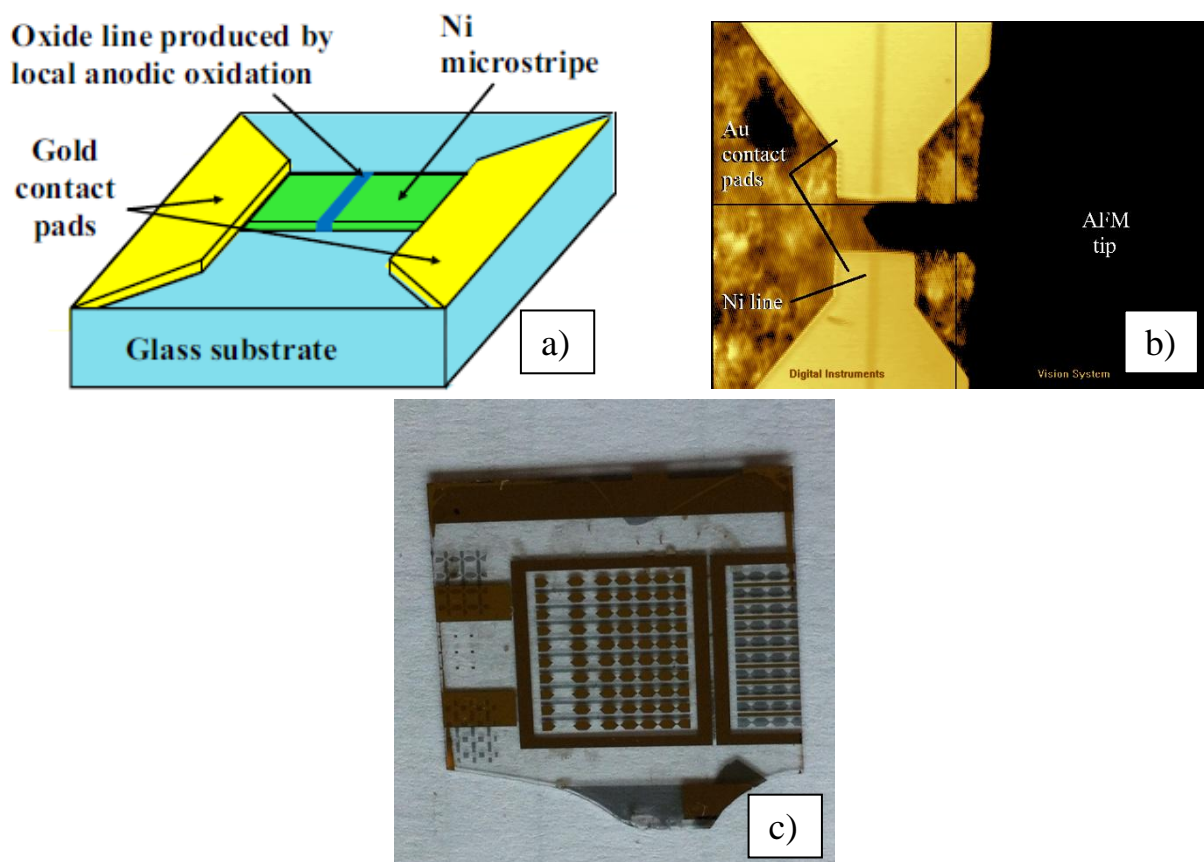


Figure 4.1. Microstrips geometry image (a) and AFM camera snapshot (b) and photo of fabricated sample (c).

The experiments on LAO were performed by AFMs MultiMode and Solver P47H (Figure 4.1 b) in tapping mode. Lithography was made in vector mode in the shape of lines crossing the microstripe. ANSCM-PA (AppNano) tips with Pt/Ir coating were used for oxidation of microstripes.

Current-voltage characteristics were measured before and after LAO. For current-voltage characteristics measuring we used Agilent B2901A unit and the four-point probe method (Figure 4.2). This method is the most common for material's resistivity measurements. Two probes are used to source current and two probes are used to measure voltage (Figure 4.2 a-b). The main advantage of four-probe method over two-probe method that the separation of current and voltage electrodes eliminates measurement errors due to the probe resistance. Characterization was also done at cryogenic temperatures to see temperature behavior of fabricated structures.

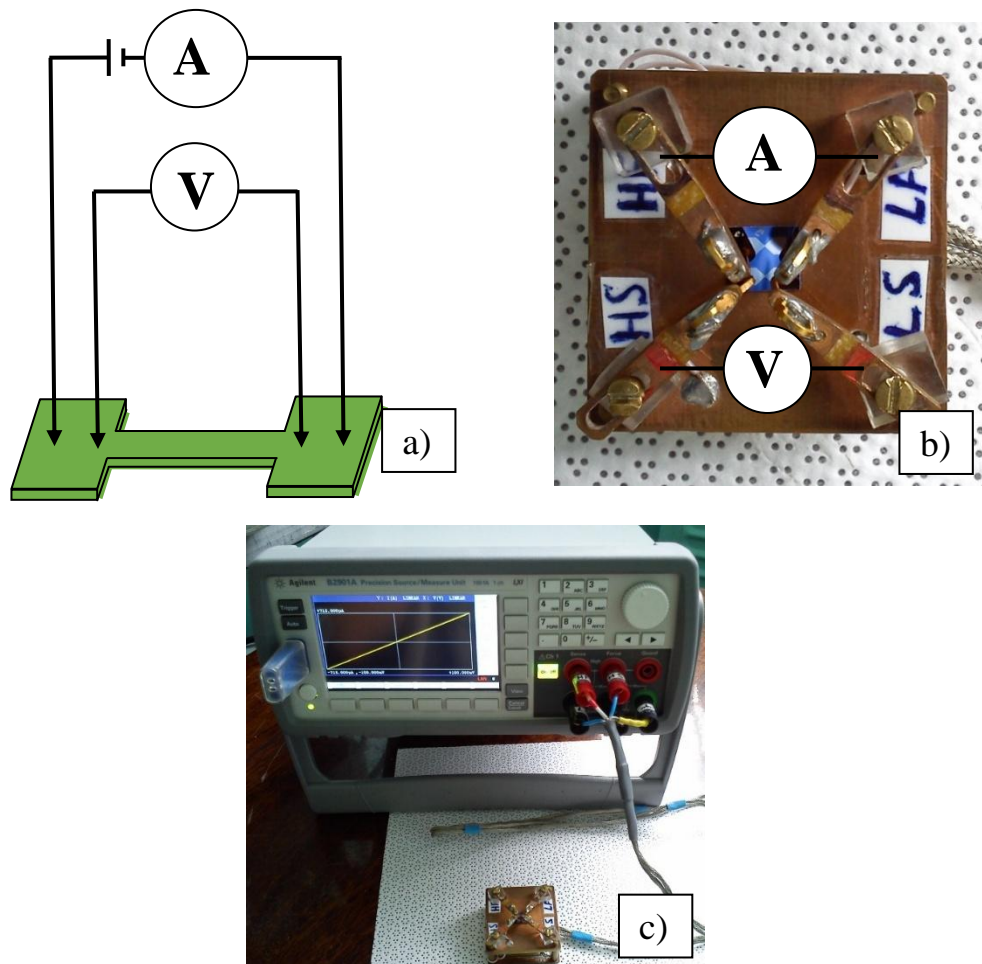


Figure 4.2. Scheme (a) and realization (b) of four-point probe current-voltage characteristics measuring method and whole measuring system (c).

We started LAO process on Ni microstripes. First we made several oxide lines to determine oxide height enough to change electrical properties of 6 nm thick metal microstripe. On Figure

4.3 AFM images of oxide lines with different heights are shown. Lines were made at $V=-7$ - -12 a)-e) respectively.

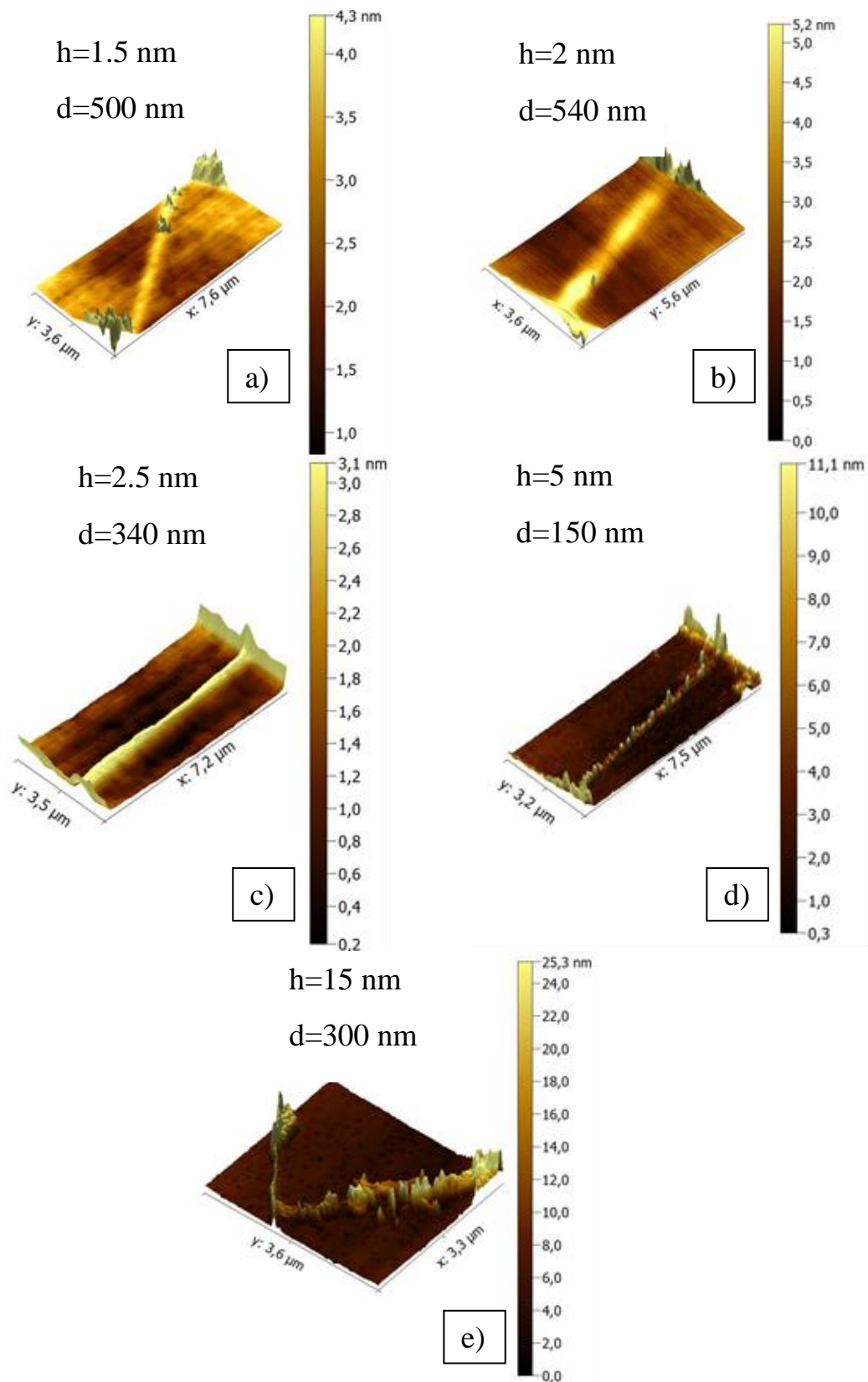


Figure 4.3. AFM images of oxide lines with different heights.

There were not found any changes in current-voltage characteristics at oxide heights below the film thickness. Resistance of one microstripe with oxide line height 15 nm (Figure 4.3 e) changed. So the oxide line with similar height and width was obtained on FeCo microstripe. AFM images of oxide lines on Ni and FeCo films are shown on Figure 4.4.

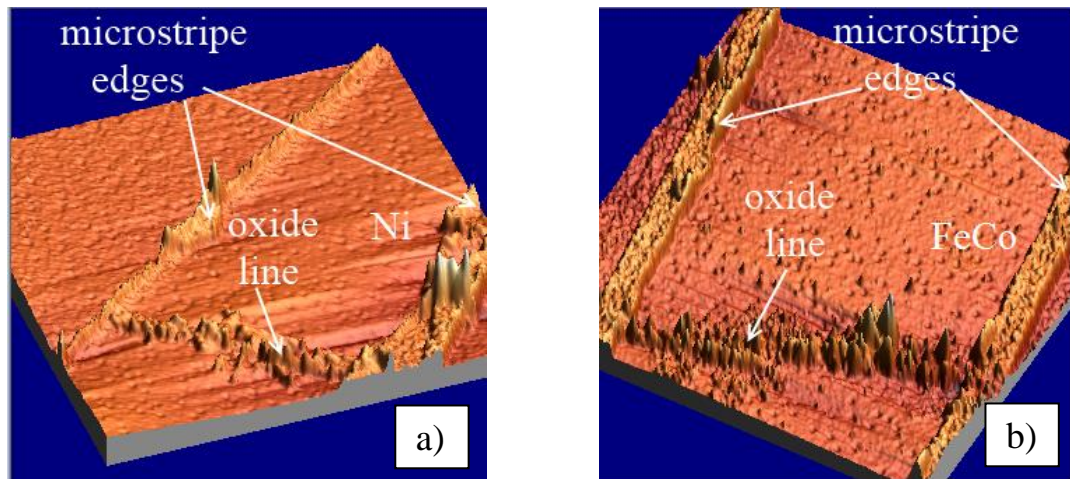


Figure 4.4. AFM images of oxide lines on Ni (a) and FeCo (b) microstrips.

On Figures 4.5-4.6 there are given current-voltage characteristics of microstrips before and after LAO at room temperature 300K and temperature of liquid nitrogen 77K. One can see that before LAO resistance of microstrips showed metallic behavior: resistance was decreased while decreasing the temperature to 77K. After LAO microstrips resistance at room temperature increased by 20 times for Ni and by 5 times for FeCo. As well resistance was increased even more at 77K and current-voltage characteristics became nonlinear.

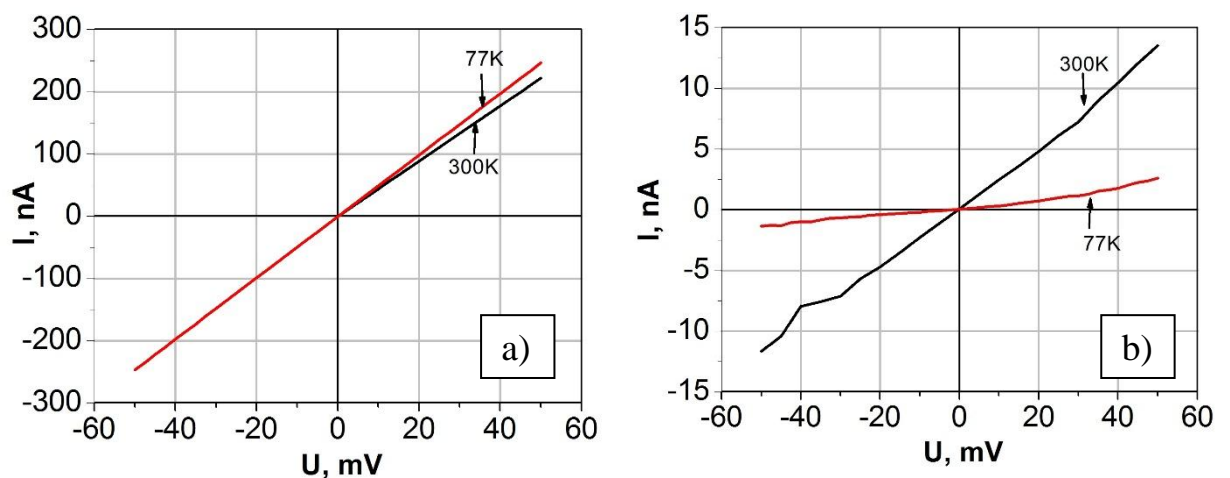


Figure 4.5. Current-voltage characteristics of Ni microstripe before (a) and after (b) LAO at 300K and 77K.

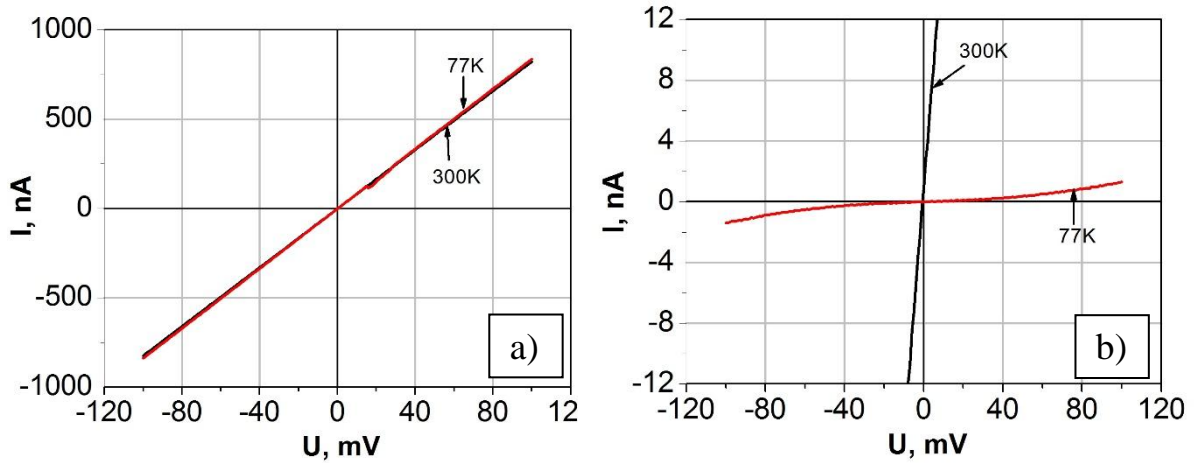


Figure 4.6. Current-voltage characteristics of FeCo microstripe before (a) and after (b) LAO at 300K and 77K.

For analysis of current-voltage characteristics nonlinearity we used coefficient α calculated on formula:

$$\alpha = \frac{d \log I}{d \log U} = \frac{U}{I} \cdot \frac{dI}{dU} \quad (4.1)$$

In Table 4.1 α values for current-voltage characteristics of microstrips before and after LAO are given. One can see that before LAO current-voltage characteristics were linear ($\alpha=1$) at both temperatures. After LAO α increased furthermore it increased with temperature decrease.

Table 4.1. Nonlinear coefficient α of microstrips current-voltage characteristics before and after LAO at temperatures 300 and 77K.

	Ni		FeCo	
	α_{300K}	α_{77K}	α_{300K}	α_{77K}
Before LAO	1	1	1	1
After LAO	1.3	1.6	1	1.6

Voltage-dependent barrier heights E_g can be obtained from measured current-voltage characteristics for a range of applied voltages using (4.2):

$$\ln\left(\frac{R(T_1)}{R(T_2)}\right) = \frac{E_g}{2k_B} \left(\frac{1}{T_1} - \frac{1}{T_2}\right) \quad (4.2)$$

We can find the zero-bias barrier height by plotting the barrier heights versus the voltage and extrapolating to $U=0$ as it's done in [179](Figure 4.7). Founded zero-bias barrier heights are ≈ 0.037 eV and 0.1 eV for barriers on Ni and FeCo respectively. As obtained barrier heights $E_g > k_B T_0$, where $k_B T_0 = 0.026$ eV we can make a conclusion that tunnel barrier was formed during probe oxidation process.

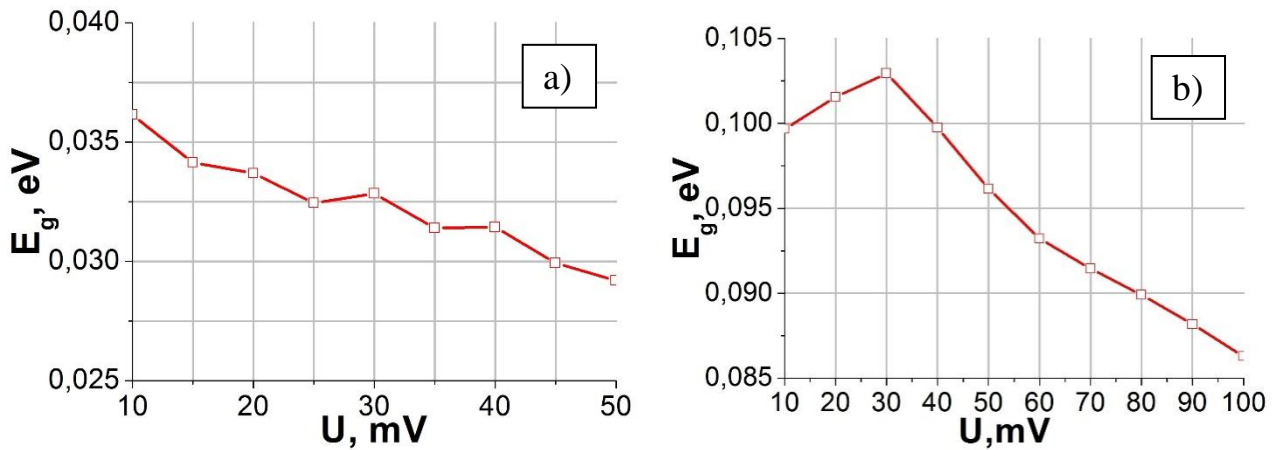


Figure 4.7 Barrier height determination of oxide lines on Ni (a) and FeCo (b) microstrips.

Thus electrical properties of oxide lines made by LAO on Ni and FeCo films were investigated. It is shown that using LAO one can change electrical properties of material and obtain oxide tunnel barrier. It is shown that oxide barriers with even bigger barrier heights than on Ni can be obtained on FeCo.

Magnetic properties of the oxide produced by AFM probe were investigated by MFM imaging of the Ni microstripe directly after the fabrication of two oxide lines (Figure 4.8). One can see that magnetic properties of oxide lines differ from those of the rest of the Ni microstripe and are close to the properties of the nonmagnetic SiO_2 sample. So such oxide structures can be used for future planar-type magnetic tunnel junctions fabrication. These magnetic tunnel junctions could be the base of new spintronic devices such as magnetoresistive memory and magnetic field detectors.

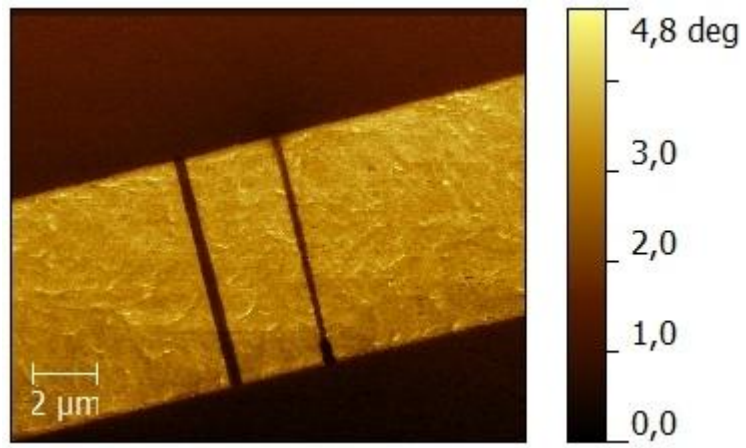


Figure 4.8 MFM image of oxide lines on Ni microstripe.

4.3 Auger electron spectroscopy of nanostructures made by local anodic oxidation

Auger electron spectroscopy (AES) is a technique that uses an electron beam to probe the surface of a solid material. Auger electrons are analyzed and their kinetic energy is determined. The identity of the elements is determined from the kinetic energy and intensity of the Auger peaks. Auger process takes place in all elements except H and He so these elements can't be determined by this technique.

Sample for AES of nanostructures produced by LAO is shown on Figure 4.9. It was a Ni microstripe with Ni contact pads. Microstripe and contact pads were fabricated on monocrystalline Si(100) substrate with thermally oxidized $0.3 \mu\text{m}$ SiO_2 layer on top by lift-off and magnetron sputtering by the same technologie as before (see Appendix A). Width of microstripe was $D=3 \mu\text{m}$ and thickness of Ni film for microstripe was $d\sim 10 \text{ nm}$, thickness of Ni film for pads was $d=100 \text{ nm}$. To confirm oxide line fabrication not only by AFM imaging but by resistance change also measurements of current-voltage characteristics at room temperature before and after oxidation were done using four-point probe method.

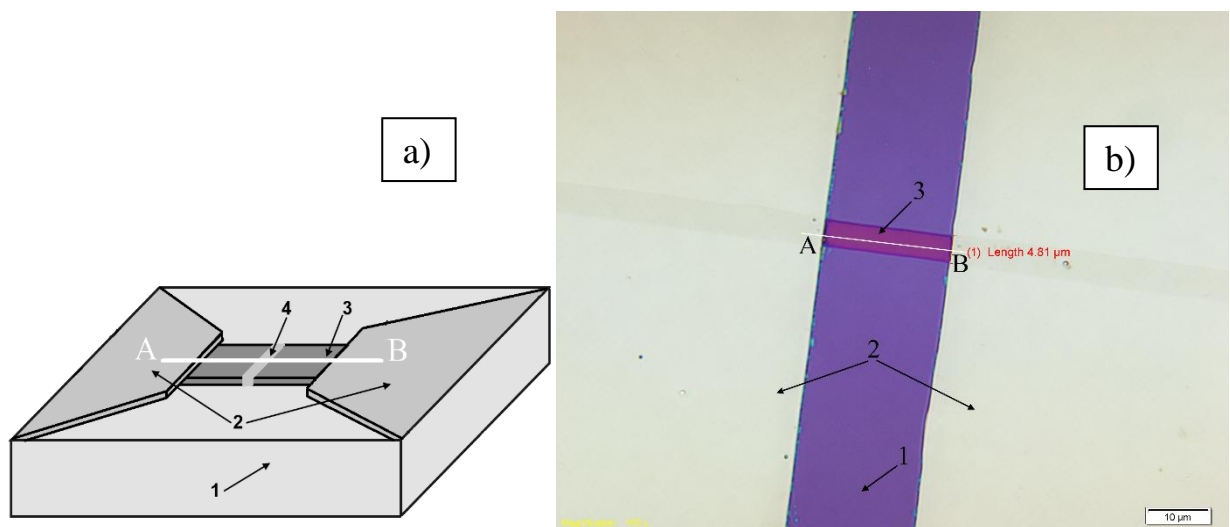


Figure 4.9. Sample for Auger-electron spectroscopy: a) schematic image, b) optical microscope image. 1 – Si(100)/ SiO_2 substrate, 2 – contact pads, 3 – Ni microstripe, 4 – oxide line, AB – line of Auger-electron passage.

LAO was done by AFM Solver P47H in tapping mode by NSG30/TiN tip using tip-sample voltage $V=-10$ V. Lithography was made in vector mode in the shape of line across the microstripe. Oxide line had 700 nm in width and 20 nm in height but it have oxid aureola of lower height and about 2 μm in width (Figure 4.10). We suggest that such structure was obtained because of electrical breakdown.

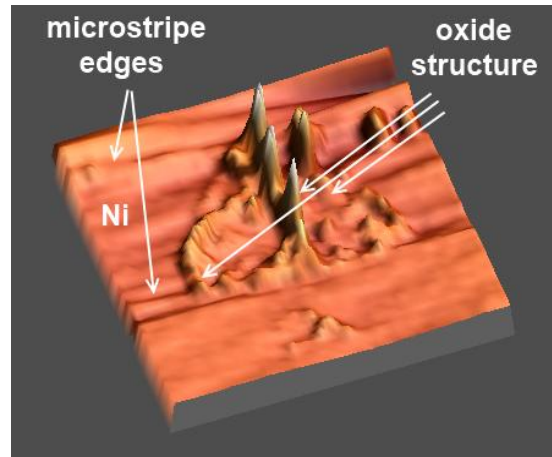


Figure 4.10. AFM image of oxide structure for AES.

Current-voltage characteristics of sample measured before and after oxidation are given on Figure 4.11. Resistance of microstripe increased in 70 times after LAO so we can say for sure that oxide line was obtained.

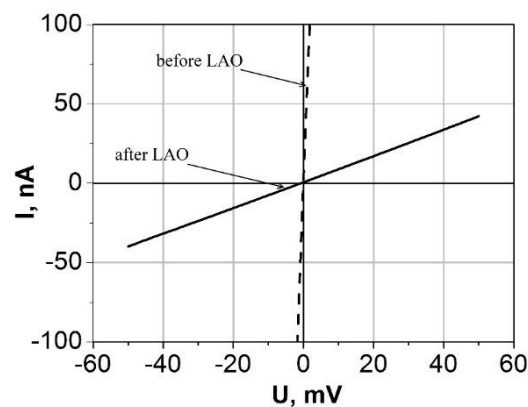


Figure 4.11. Current-voltage characteristics of sample before and after LAO.

Auger-electron spectroscopy was realized using Phi 4300 scanning Auger system (Perkin – Elmer). This system allows to get the distribution of chemical elements on the surface. Because

it was hard to target electron beam exactly to oxide pattern we made scanning along AB line (Figure 4.8) and obtained the distribution of Ni and O on the whole sample surface. Results of AES are given on Figure 4.12. It was found increased content of O in the region with the size of 2 μm which is the same to oxide structure size. So we marked this place of intersection of electron beam pass with oxide structure (on Figure 4.9 intersection of AB and 4 lines) as oxidized region on Figure 4.12. From Table 4.2 one can see that content of O in oxide line is an order of magnitude more than in the rest of microstripe while the content of Ni is almost the same in oxidized and not oxidized regions. As a result, we can conclude that LAO produces oxide of the initial material.

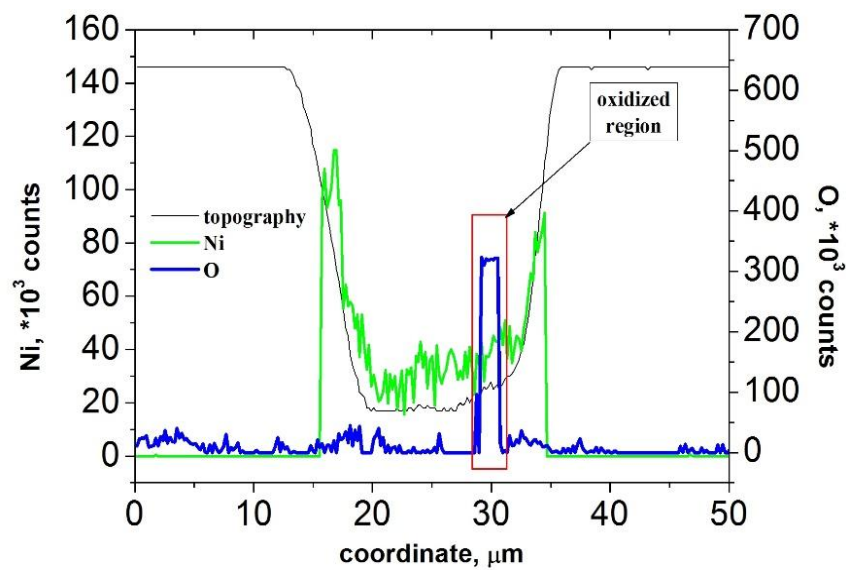


Figure 4.12. Plot of Ni and O distribution on sample surface obtained by AES.

Table 4.2. Content of Ni and O in several points of oxidized and not oxidized region.

	Content, 10^3 counts					
	Not oxidized region			Oxidized region		
Ni	48,68	30,38	43,98	42,72	37,66	39,7
O	27,74	30,79	15,5	323,78	321,36	320,38

4.4 Current-voltage characteristics and magnetoresistance of nanostructures made by mechanical scratching

After investigation of properties of oxide lines made by scanning probe we've decided to modify the Ni magnetic microstripe by scanning probe mechanical scratching and to see the difference in microstripecurrent-voltage and magnetoresistancecharacteristics before and after the scratching procedure. For experiments same geometry microstripe as before was used: Ni microstripe with Ni contact pads and width of $D=3 \mu\text{m}$ on monocrystalline Si(100) substrate with thermally oxidized $0.3 \mu\text{m}$ SiO_2 layer on top (Figure 4.9). Thickness of Ni film for microstripe was $d\sim 15 \text{ nm}$. For probe mechanical lithography AFM Solver P47 and sharp diamond tips were used. Current-voltage and magnetoresistancecharacteristics measurements at room and cryogenic temperature before and after modification were done as before by four-point probe method using Agilent B2901A unit (Figure 4.2), cryogenic system and system of magnets.

First, we made a test scratching to determine the applied tip force enough to scratch 15 nm film through the whole thickness. Well-defined tranches with depth of 10-15 nm were obtained at applied force $10 \mu\text{N}$ (Figure 4.13). It can be seen that there are some debris sediments along the tranches. Early experiments on AFM mechanical scratching showed that these debris are induced by contact stress [19]. Simultaneously, as seen from both AFM and SEM images, the width of obtained tranches was less than 50 nm.

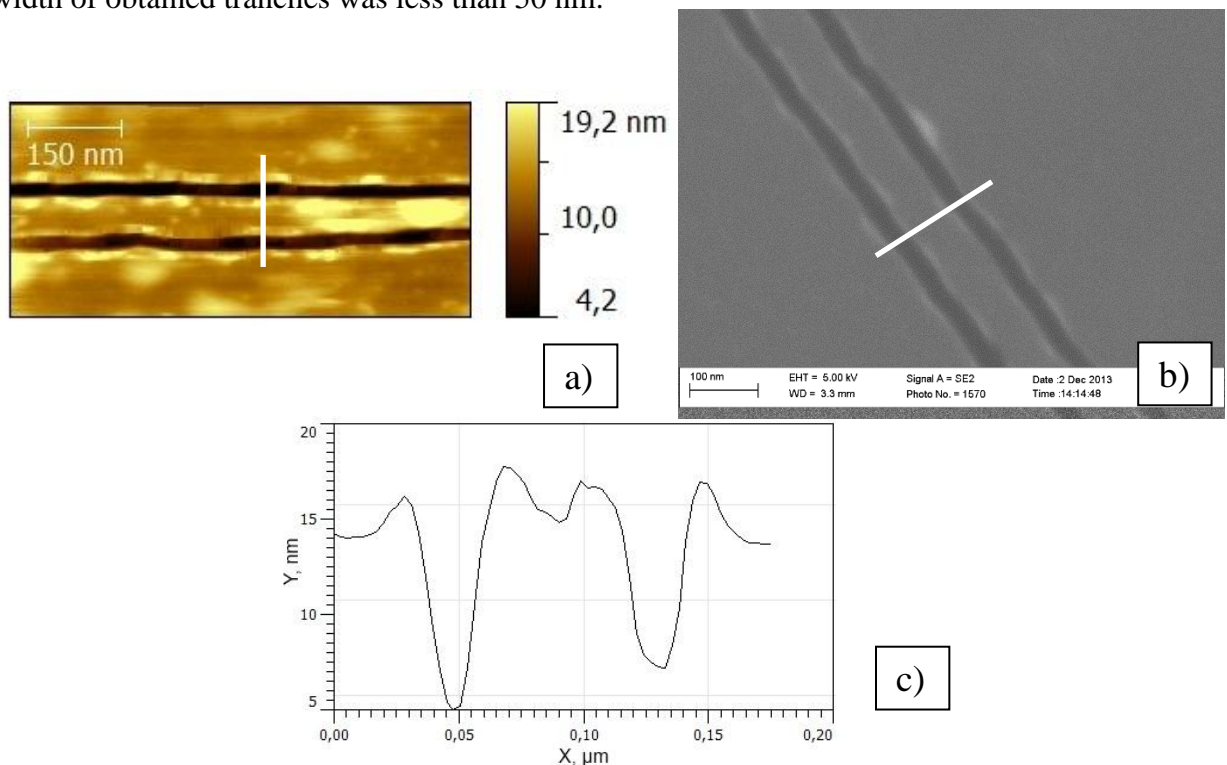


Figure 4.13. AFM (a) and SEM (b) images and made along the white line AFM cross-section image (c) of scanning probe fabricated scratches on Ni microstripe.

The next step was to fabricate scratched microstripes for electrical and magnetic measurements. We've decided to make a sample with one scratch crossing the whole microstripe (Figure 4.14 a) and a microstripe with two incomplete scratches (Figure 4.14 b).

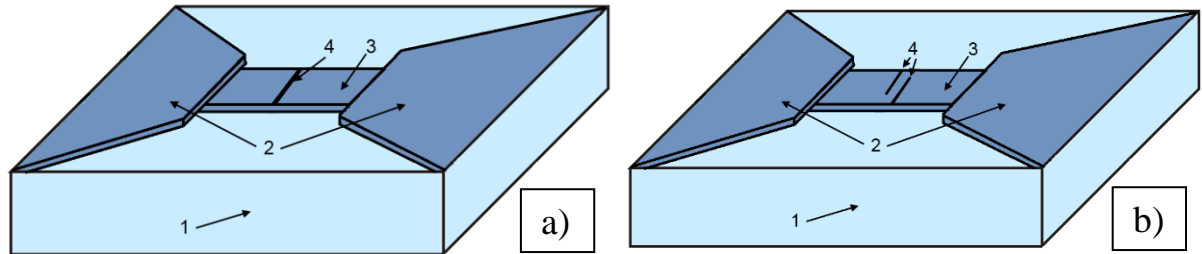


Figure 4.14. Schematic geometry of modified Ni microstripes: a) 1 complete scratch crossing the whole microstripe, b) 2 incomplete scratches. 1 – Si(100)/SiO₂ substrate, 2 – contact pads, 3 – Ni microstripe, 4 – scratched lines.

One scratch

On Figure 4.15 there are shown AFM and cross-section images of one scratch crossing the Ni microstripe on the whole width. From the cross-section it can be seen that microstripe is scratched through the whole film thickness.

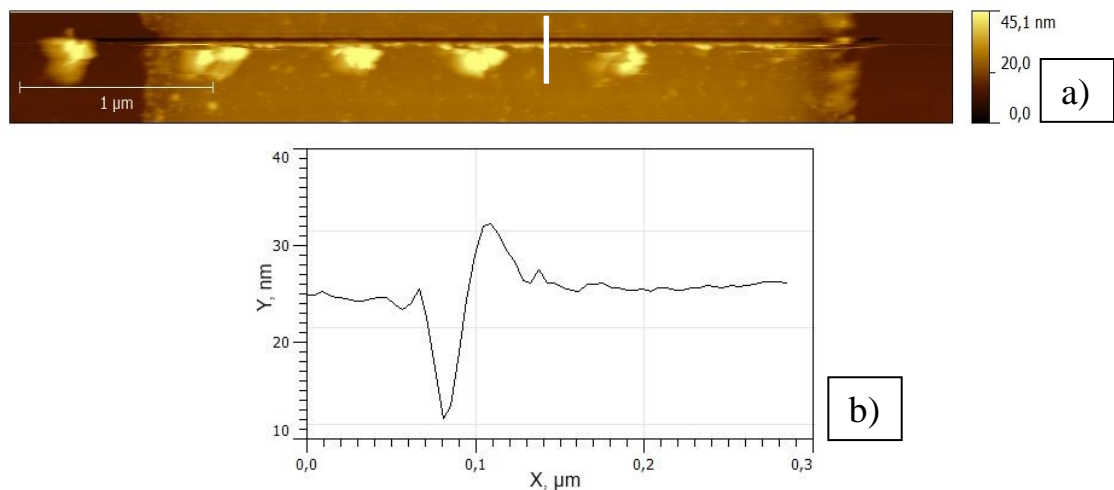


Figure 4.15. AFM (a) and cross-section images (b) of complete scratch crossing the whole Ni microstripe.

On Figures 4.16-4.17 there are given current-voltage characteristics of microstripe before and after scratching by AFM probe at room temperature 300K and after scratching at different temperatures. Before scanning probe scratching resistance of microstripe was linear and showed metallic behavior. After scratching microstripes resistance became almost infinite at low voltages. It means that microstripe material was completely removed in the place where AFM probe was applied. At voltage of about 1V small current through the structure appeared and it changed non-linearly with the increase of voltage. It can be explained by breakdown of the structure at high voltages. As well resistance was decreased with the decrease of temperature. It can be related with thermal contraction of the scratch and decreasing of the distance between scratch edges. So using AFM scratching we obtained metallic structure with high non-linear resistance.

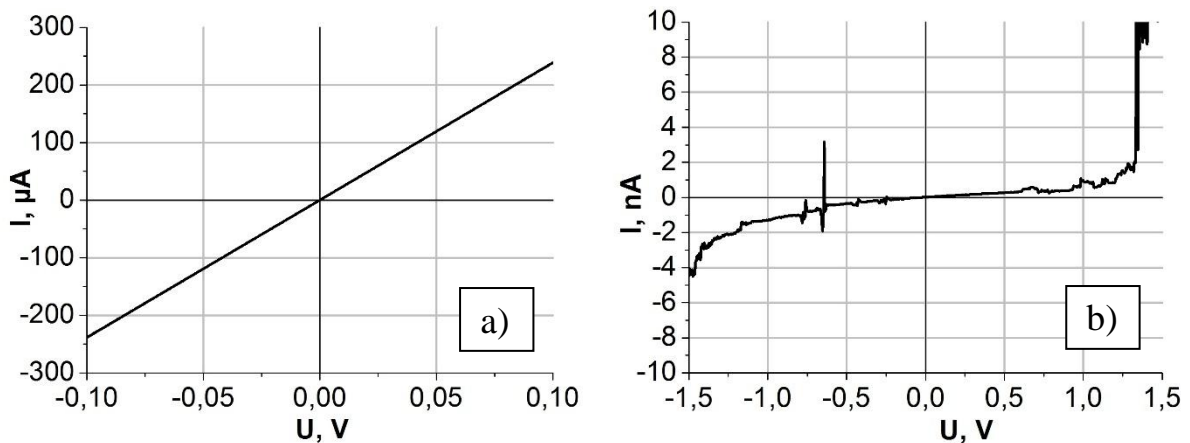


Figure 4.16. Current-voltage characteristics of Ni microstripe before (a) and after (b) scanning probe scratching at 300K.

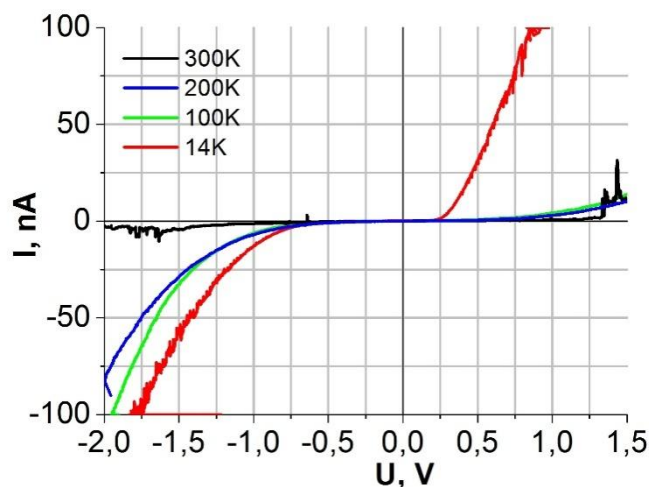


Figure 4.17. Current-voltage characteristics of Ni microstripe after scanning probe scratching at different temperatures.

Two scratches

On Figure 4.18 there are shown AFM and cross-section images of two comb scratches on Ni microstripe. From the cross-section it can be seen that microstripe is scratched through the whole film thickness.

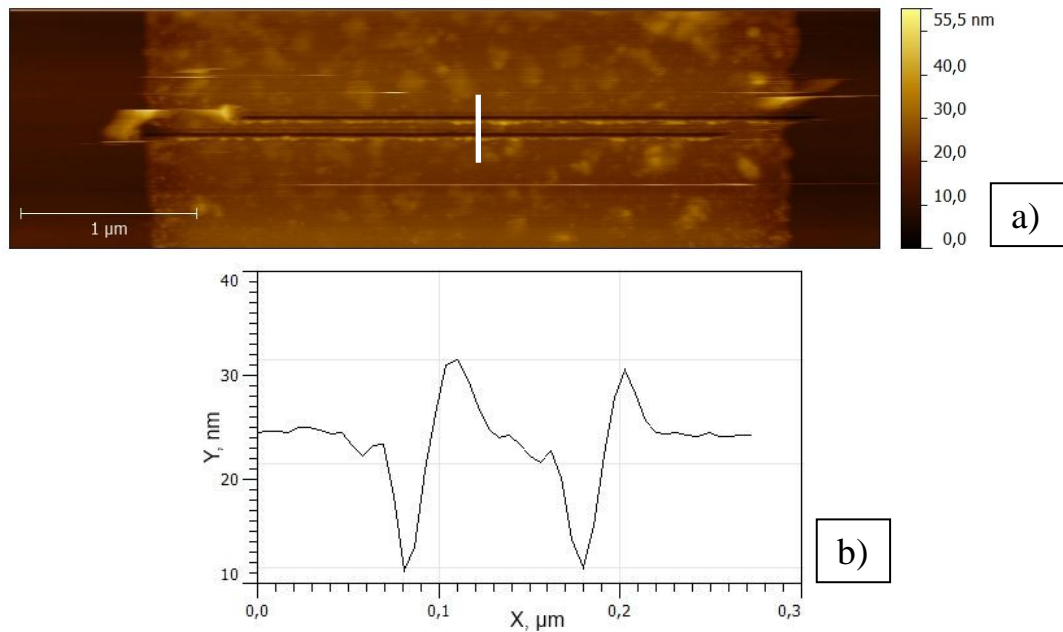


Figure 4.18. AFM (a) and cross-section images (b) of 2 comb scratches on Ni microstripe.

On Figure 4.19 there are given current-voltage characteristics of microstripe before and after scratching at room temperature 300K. It can be seen that microstripes resistance became about 3 times higher after scratching. It means that microstripe configuration was changed and narrow channel was formed by 2 comb scratches. On Figure 4.20 there are given AMR characteristics of microstripe before and after scratching. Magnetic field was applied perpendicularly to the current direction. One can see that magnetic structure of microstripe was changed also by scratching and magnetoresistance changed its behavior.

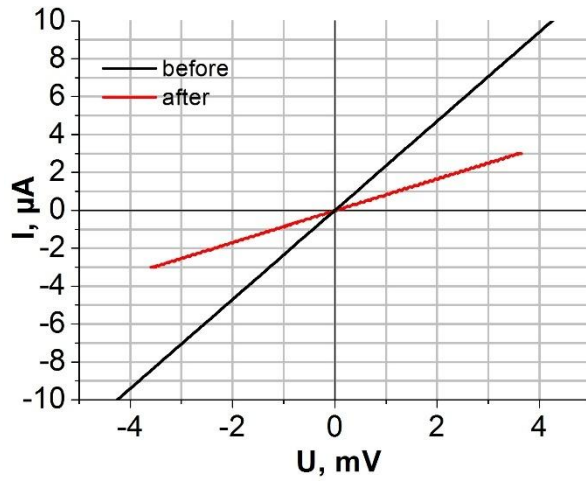


Figure 4.19. Current-voltage characteristics of Ni microstripe before and after fabrication of 2 comb scratches at 300K.

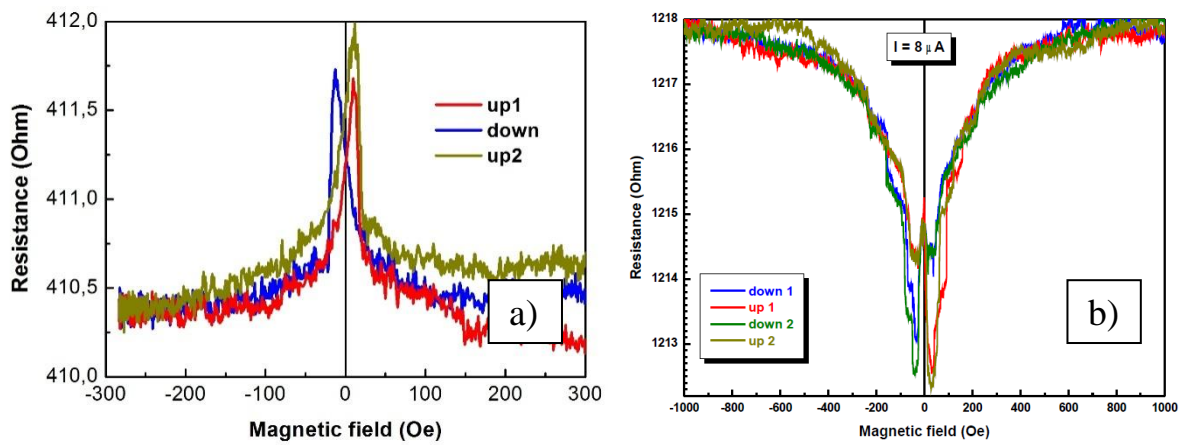


Figure 4.20. AMR characteristics of Ni microstripe before (a) and after (b) fabrication of 2 comb scratches at 300K.

4.5 Conclusions

In this chapter properties of the nanostructures fabricated by SPL especially by LAO were investigated. First, it was shown that oxide lines made by LAO change the electrical properties of Ni and FeCo microstrips. Current-voltage characteristics of such structures were non-metallic and non-linear so insulator formation during LAO process could be assumed. It was found that formation of oxide line with height not smaller than film thickness is needed to change the microstripe electrical properties. Auger electron spectroscopy of obtained oxide structures confirmed oxide formation in the place where LAO process was done. As Ni and Ni oxides have different elastic properties we propose the potential use of LAO as surface PnCs fabrication method.

As obtained oxide structures have a quite big barrier heights and are fabricated on ferromagnetic films, they can be potentially used for fabrication of planar magnetic tunnel junctions [108]. Note that the magnetic tunnel junctions ferromagnetic metal-insulator-ferromagnetic metal usually show high magnetoresistance due to spin-polarized tunneling and therefore are of practical interest for the fabrication of the magnetoresistive memory devices, magnetic field sensors and other spintronic devices. Currently, the most common method for magnetic tunnel junctions formation is fabrication of various materials multilayered structures. In this case, the main advantage of LAO as magnetic tunnel junctions formation method is opportunity to fabricate planar structures with smaller tunnel junction area what can be used for the single-electron tunneling realization [8]. At the moment, the fabrication process of planar magnetic tunnel junctions using LAO on Ni films is the most studied [108-109]. There were also done some experiments on NiFe [119]. In this work study of tunnel junctions formation not only on Ni film but on FeCo film was done. It was shown that oxide barriers with even bigger barrier heights than on Ni can be obtained on FeCo.

Also properties of scratches produced by AFM probe were studied. It was shown that one can completely remove the material in the place of probe application. So this method can also be potentially used for PnCs fabrication. Similarly, it was shown that one can change electrical and magnetoresistive characteristics of microstrips by this method what can be used in magnetoresistive and spintronic devices.

5. Hypersonic magnetically tunable surface phononic crystals

5.1 Introduction

Phononic crystals (PnCs) are created by 1D, 2D or 3D periodic arrays of structures with a big difference in their densities and elastic properties. During the last two decades the ability to control the propagation of surface acoustic wave (SAW) using such structures has been intensively studied theoretically and experimentally [180-181]. PnCs are interesting for their unique properties: the band-gaps formation [182-183] and anomalous dispersion (negative refraction) [184]. PnCs can be used for different applications depending on their operation frequency. For example, PnCs for low frequencies can be used in non destructive testing and communication [181]. Hypersonic PnCs can be used for filtering, guiding, focusing, or demultiplexing [185-187].

SAW devices are fabricated on piezoelectric substrates such as quartz, lithium niobate (LiNbO_3), lithium tantalate (LiTaO_3) to have an opportunity for excitation and detection of SAW. Since the interdigital transducers (IDTs) were first reported [188] they are widely used for excitation and detection of SAW on the surface of piezoelectric substrate. Generating IDT converts input microwave signal to SAW and receiving IDT converts SAW to output measured RF signal. IDT consist of a one-dimensional array of parallel metal electrodes. Alternate electrodes are interconnected and SAW is generated in the normal to the electrodes direction when electrical signal is applied [189]. SAW is excited on the frequency for which wavelength is equal to the IDT period. Second IDT placed at some short distance from the first is commonly used for detection of the SAW. On Figure 5.1 scheme of commonly used SAW device with PnC is shown. The same SAW device scheme was investigated in our study.

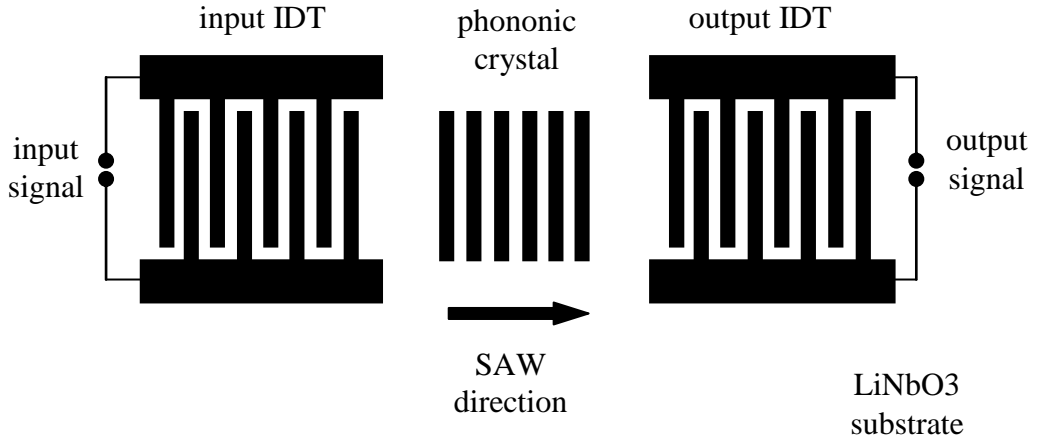


Figure 5.1. Investigated SAW delay line.

The theoretical study of SAW devices is of great importance for their design and experimental realisation. One of the main aspects in the theoretical studies of PnC is calculation of the transmission through the structure using either analytical [181] or the finite element (FEM) methods [190-191] that can give not only qualitative, but also quantitative characteristics of the wave transmission.

To simulate the SAW propagation and SAW devices two constitutive equations of piezoelectric materials are frequently used [192]:

$$T_{ij} = C_{ijkl}^E S_{kl} + e_{ijk}^T E_k \quad (5.1)$$

$$D_i = e_{ikl} S_{kl} + \varepsilon_{ij}^S E_j \quad (5.2)$$

where T_{ij} – the stress vector; C_{ijkl}^E – the elasticity matrix (N/m^2); S_{kl} – the strain vector; e_{ijk}^T and e_{ikl} – the piezoelectric stress matrixes (C/m^2), which represent the energy conversion between the electrical and mechanical fields; E_k – the electrical field vector (V/m); D_i – the electrical displacement (C/m^2); ε_{ij}^S – the permittivity matrix (F/m). The subscripts (i, j and k) represent the displacements of freedom in the x -, y - and z - directions, respectively.

By substituting the equation of motion ($F = ma$) and the equation of the electric field as the negative gradient of the potential ($E_i = \frac{\partial \varphi}{\partial r_j}$) into Eq. 5.1, the first piezoelectric constitutive equation can be obtained:

$$C_{ijkl}^E \frac{\partial^2 U_k}{\partial r_k \partial r_j} + e_{ijk}^T \frac{\partial^2 \varphi}{\partial r_k \partial r_j} = \rho \frac{\partial^2 U_i}{\partial t^2} \quad (5.3)$$

where U – the displacement and ρ – the area density (kg/m^2).

However, because the general piezoelectric thin films have almost no conducting charges, the divergence of the electrical displacement can be regarded as zero:

$$\frac{\partial D_i}{\partial r_i} = e_{ijk} \frac{\partial^2 U_k}{\partial r_k \partial r_i} + \frac{\partial}{\partial r_i} \left(-\epsilon_{ij}^S \frac{\partial \varphi}{\partial r_j} \right) = 0 \quad (5.4)$$

Therefore, the wave equation of the SAW devices can be obtained, and the displacements and the voltage of the SAW devices can be calculated by solving the wave equation:

$$e_{ijk} \frac{\partial^2 U_k}{\partial r_k \partial r_i} - \epsilon_{ij}^S \frac{\partial^2 \varphi}{\partial r_i \partial r_j} = 0 \quad (5.5)$$

In this study we used FEM-based analysis for theoretical investigation of SAW devices. For modeling COMSOL Multiphysics software was used and Eq. 5.4-5.5 were solved in frequency domain. For calculations of SAW transmission through investigated structures these equations were applied to the delay line model that consist from two IDTs and PnC placed between them on $Y + 128^\circ$ – cut of LiNbO_3 crystal (Figure 5.1).

As PnC operation frequency depends on structure sizes the most important problem in the study of hypersonic PnCs is a difficulty to develop a fabrication technology of such small structures. In this chapter feasibility of periodic planar magnetic nanosized structures fabrication using LAO and EBL methods that can serve as magnetically tunable surface PnCs for high and hypersonic frequency ranges is discussed. It was shown experimentally that one can fabricate periodic arrays of oxide lines on ferromagnetic metal films. FEM modeling of interaction between such periodical structures and SAWs showed that they can be used for a bandgap formation and tuning of a bandgap by applied magnetic field. There were given recommendations on practical realization of 1D PnCs by LAO on 2 and 4 GHz. Because of complexity and need to use of special equipment to realize such structures using LAO we investigated fabrication of 1D PnCs on 2 and 4 GHz using EBL. There was developed technology of fabrication of such structures by EBL, then transmission characteristics of obtained PnCs were studied experimentally and theoretically, and analysis of bandgap shift under magnetic field application was performed. Similarly technological process for 2D PnCs realization was developed.

5.2 Feasibility to fabrication of surface phononic crystals by local anodic oxidation

Results on study of nanostructures made by LAO on ferromagnetic metal films (see Chapter 4) showed that the properties of these nanostructures differed from the properties of original metal film. We suppose that metal oxide was fabricated during the LAO process. As Ni and Ni oxides have different elastic properties we've decided to investigate the feasibility to fabricate surface PnCs by LAO.

First we studied the possibility to fabricate by LAO periodic oxide structures. The experiments on periodic oxide lines fabrication were performed on Ni thin film with thickness $d=10$ nm fabricated by DC magnetron sputtering using system Leybold Z550 on monocrystalline Si(100) substrate. AFM MultiMode in tapping mode and ANSCM-PA tip under -10 V bias were used to provide LAO on area of $15 \times 15 \mu\text{m}^2$. Typical pattern of lines array made using AFM software is given on Figure 5.2.

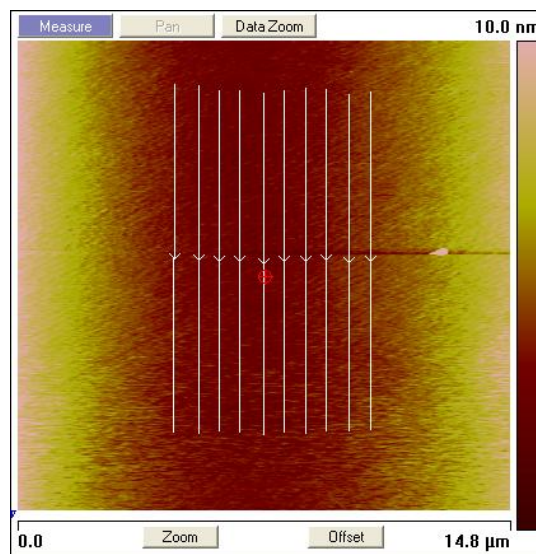


Figure 5.2. Periodic lines pattern in AFM software.

Using such pattern we obtained 1D oxide lines array with period varied from 1 to 2 μm . Oxide lines were quite smooth and had 1.4 nm in height and 500 nm in width (Figure 5.3 a). As it was mentioned before phase image contrast has strong dependence on viscoelastic properties of sample and weak dependence on topography. On Figure 5.3 b) there is given a phase image of fabricated array. It can be seen that oxide lines have viscoelastic properties different from entire ferromagnetic film. As higher phase angle corresponds to materials with higher viscoelastic

properties [67], we suppose that using tip induced oxidation we can fabricate planar arrays with periodic variation of elastic constants.

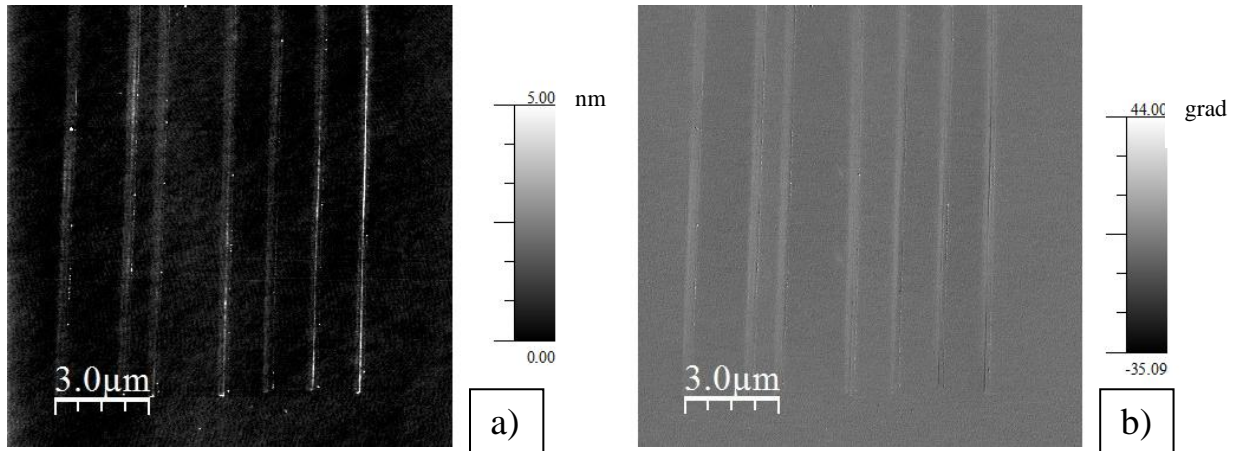


Figure 5.3. AFM images of 1D periodic oxide lines array on Ni film: a) topography, b) phase.

As well we fabricated 1D periodic oxide lines array with period $1\mu\text{m}$ (Figure 5.4a) and 2D array with period $0.7\mu\text{m}$ (Figure 5.4b). So fabrication of oxide lines arrays on ferromagnetic metal film by LAO has good reproducibility, stability and controllability of period and size of oxide lines.

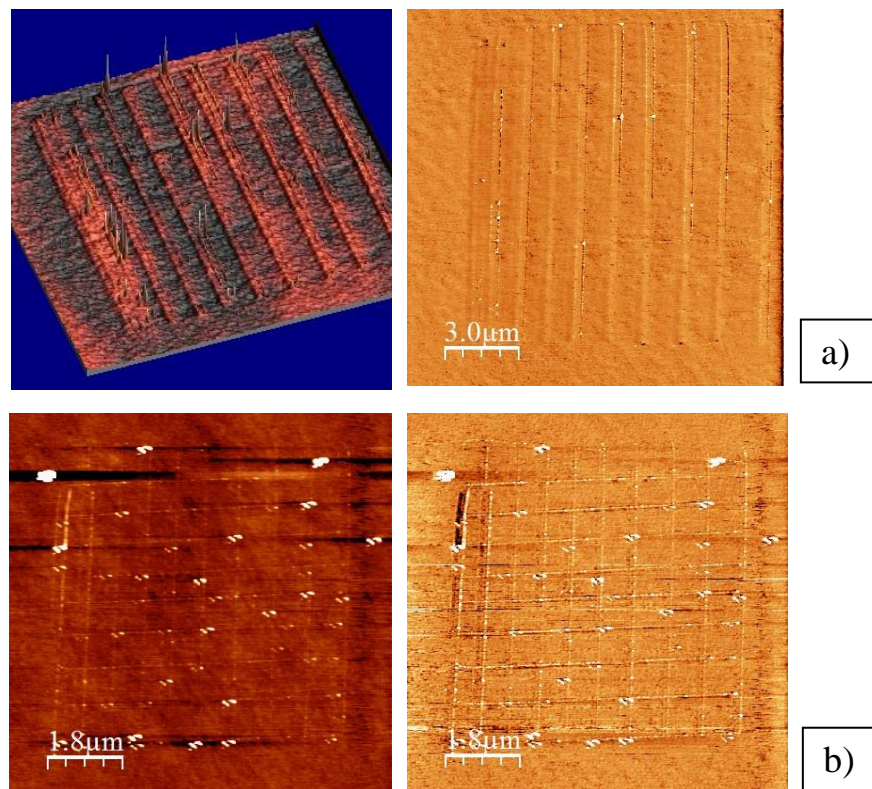


Figure 5.4. AFM images of topography and phase of 1D (a) and 2D (b) periodic oxide lines array on Ni film.

After experimental investigation of possibility of PnC fabrication by LAO FEM numerical analysis of mentioned structures in COMSOL Multiphysics software were done. It was considered that depth of oxide into the metallic film is equal to the oxide height above this film. In direction of propagation X the number N of array's element was finite, and in direction Y infinite aperture was assumed. For eliminating the influence of SAW reflection from the boundaries of LiNbO₃ wafer, absorbing boundary conditions surround the substrate. Aluminum IDTs were used for SAW generation and measurement of frequency dependence of transmission function S_{21} .

Several series of transmission characteristics were calculated for different values of oxide structure thickness and period. The frequency dependencies were studied near the Bragg bandgap for observed PnCs, which occurs when the wave vector k of the incident wave tends to the edge of a first Brillouin zone. The central frequency of Bragg gap depends only on the period of the structure or on the wave velocity in the material under PnCs. For modeling we used handbook constants for LiNbO₃ [195], Ni and its oxide [196].

On Figure 5.5 calculated frequency dependences of the transmission characteristic S_{21} for the structures with different period, oxide lines number and oxide lines height are shown. Figure 5.5 a shows S_{21} for structure with a period $a = 500$ nm at different thicknesses of oxide lines. Bandgap is formed on frequency 3.94 GHz and with an increase in the height of oxide lines maximum attenuation introduced by the PnC also increases. On Figures 5.5b)-d) series of calculations of gap formation for the oxide lines arrays with same height $h = 3.5$ nm and different periods $a = 500$ nm; 200 nm; 50 nm with variations in the number of oxide lines from 100 to 200 are given. It is clearly seen, that the maximum attenuation introduced by PnC due to Bragg scattering on the frequencies 3.94 GHz, 9.72 GHz and 35.75 GHz is increased. Because the thickness of the oxide lines is small compared with the wavelength, most of the SAW energy is reflected, and wherein the energy dissipation in the volumetric mode is negligible. These high values of frequency may in practice be achieved by using higher harmonic generation or optical excitation of SAW [197].

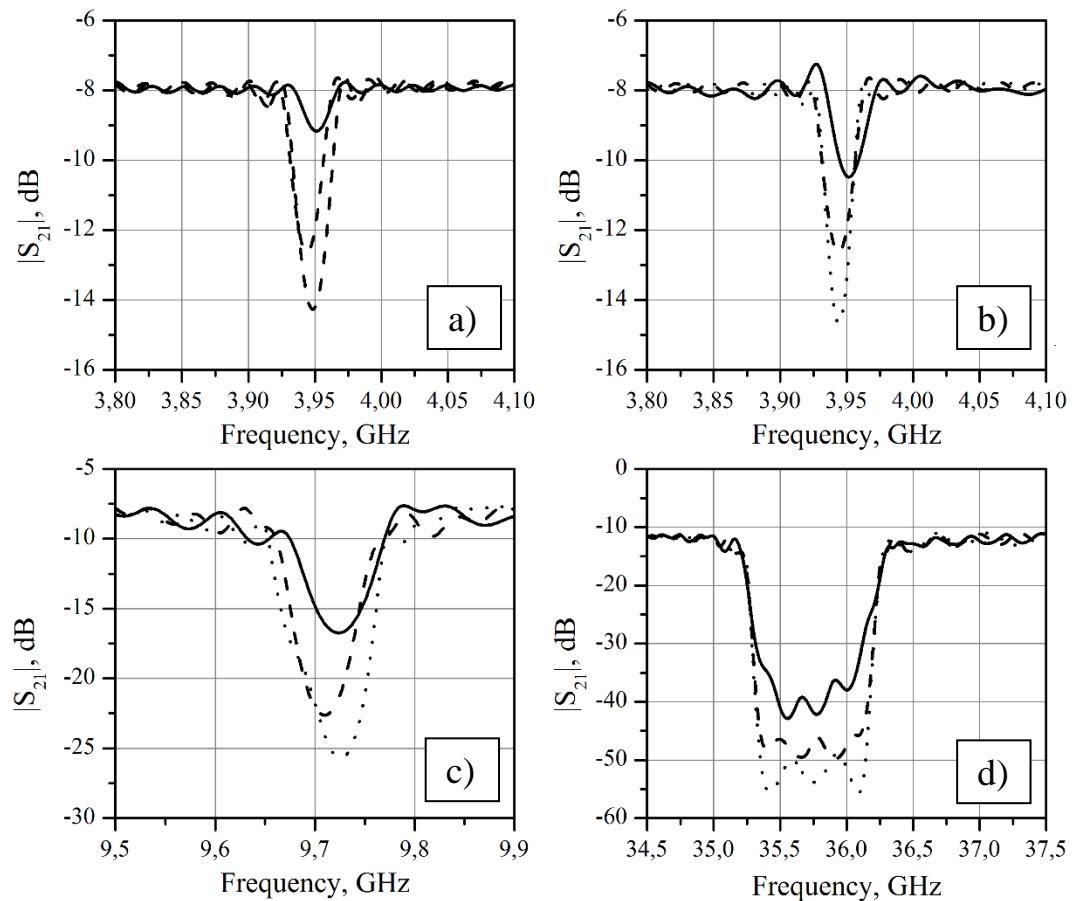


Figure 5.5. Frequency dependences of transmission function S_{21} (a) for the structure with $N = 150$ oxide lines with period $a = 500\text{nm}$ and height $h = 1.5\text{nm}$ (solid line), $h = 3.5\text{nm}$ (dashed line), $h = 5\text{nm}$ (dotted line); (b) for the structure with period $a = 500\text{nm}$, height $h = 3.5\text{nm}$ and with $N = 100$ oxide lines (solid line), $N = 150$ oxide lines (dashed line), $N = 200$ oxide lines (dotted line); (c) for the structure with period $a = 200\text{nm}$, height $h = 3.5\text{nm}$ and with $N = 100$ oxide lines (solid line), $N = 150$ oxide lines (dashed line), $N = 200$ oxide lines (dotted line); (d) for the structure with period $a = 50\text{nm}$, height $h = 3.5\text{nm}$ and with $N = 100$ oxide lines (solid line), $N = 150$ oxide lines (dashed line), $N = 200$ oxide lines (dotted line).

Calculation of the influence of the applied constant magnetic field on the investigated characteristics was also evaluated. In acoustic wave's interaction with a ferromagnetic metal film not only the mechanical stress, predicted by Hooke's law, but also an additional stress caused by the reorientation of the magnetic moments (due to the magnetostrictive effect) exists. As a result Young's modulus of demagnetized films differs from that for the film, where the magnetic moments are oriented along the external magnetic field. Such difference in Young's modulus is called an ΔE -effect [2-6]. On Figure 5.6 the results of calculations of SAW transmission through the oxide lines PnC structure, at a constant magnetic field $H = 300\text{ Oe}$ (sufficient for complete

magnetization of the film) in the SAW propagation direction are shown. From [198] at this field Young's modulus for Ni film is increased about 7% and film becomes stiffer, absorbing less energy from the wave than in the demagnetized state. As SAW velocity is proportional to the Young's modulus, the application of the magnetic field should lead to a shift of the center frequency of the Bragg bandgap to the higher range. The calculations confirmed these arguments (Figure 5.6). The bandgap shifted by 10 MHz and by 50 MHz for the structures with periods $a = 500\text{nm}$ and $a = 200\text{nm}$ respectively. Maximum insertion loss at the same time was reduced by 3-4 dB.

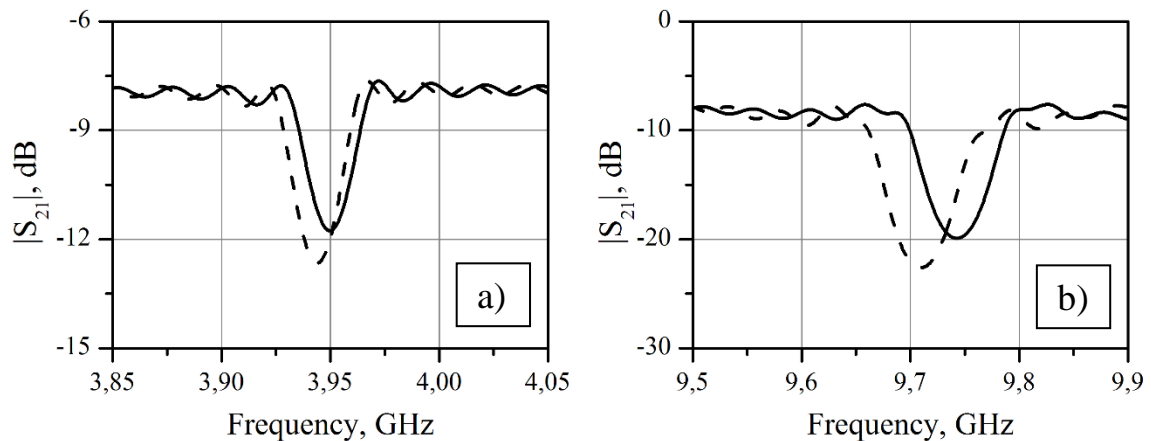


Figure 5.6. Frequency dependences of transmission function S_{21} for the structure with $N = 150$ oxide lines, height $h = 3.5\text{nm}$ in the constant magnetic field (solid line) and without it (dashed line): period $a = 500\text{nm}$ (a) and for $a = 200\text{nm}$ (b).

Finally, we showed feasibility to fabrication of magnetically tunable PnCs by LAO. Experimentally narrow lines with width of dozen nanometers can be fabricated using carbon nanotube as AFM probe [199]. For experimental realization of arrays with lot of lines and with aperture up to 100 microns multiprobe system like "Millipede" (Figure 1.6 b) is needed. As there is no such system in IEMN or IRE RAS we've developed the whole technological process for future realization of oxide lines PnCs on Ni film (Figure 5.7).

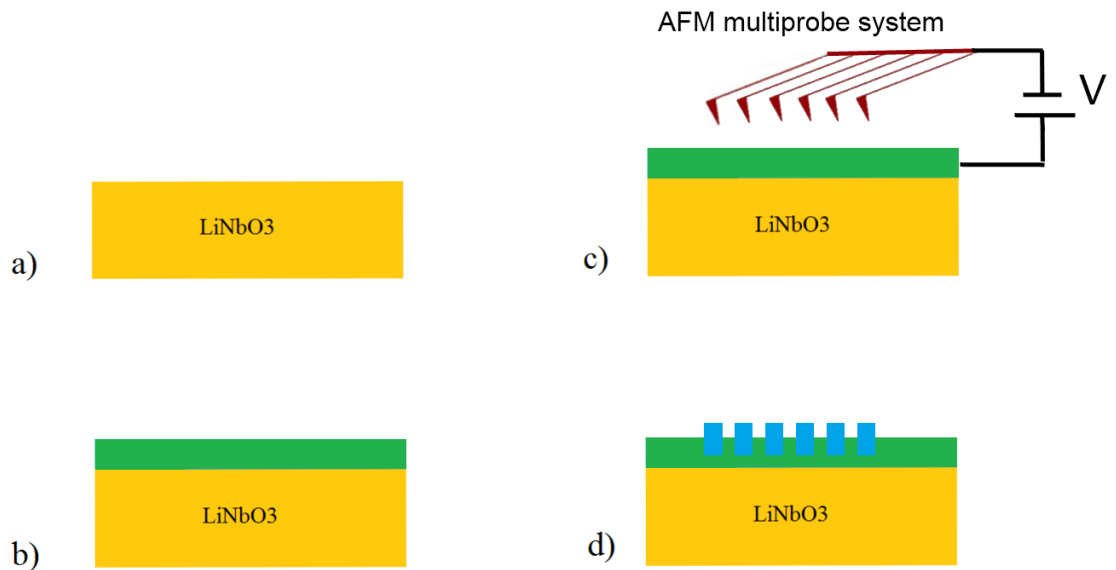
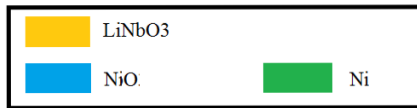


Figure 5.7. Scheme of PnC fabrication technology using local anodic oxidation by AFM multiprobe system.

1. Standard preparation of LiNbO_3 substrate (Figure 5.7 a): a) cleaning for 5 min in acetone (to remove organic impurities) and IPA (to rinse off contaminated acetone), b) drying by nitrogen.

2. Deposition of Ni film on the substrate (Figure 5.7b).

3. Local anodic oxidation of Ni film using multiprobe system (Figure 5.7c). Parameters of the system: number of probes = N number of oxide lines; probes period = a oxide lines period. Parameters of oxidation: $T_{\text{ox}}=10$ s, $\text{SP}=0.2$, $\text{RH}=70\%$, tip $R_c=30$ nm, $V=-10$ V (for $a=1000$ nm) or $V=-7$ V (for $a=500$ nm).

4. Tips mechanical cleaning procedure described in Chapter 2 (Figure 2.16) for tip life-time prolongation. These procedure should be realized on the surface far from the place of oxidation.

5. One PnC is realized (Figure 5.7d) and next PnC can be proceeded.

5.3 Fabrication of surface phononic crystals by electron-beam lithography

5.3.1 1D surface phononic crystals devices design

It was decided to fabricate 1D PnCs made from periodic Ni lines arrays for frequencies 2 GHz and 4 GHz on Y+128° cut LiNbO₃ substrate. It was assumed to use IDTs for generation and detection of SAW. Typically IDT consists of two sets of interlocking comb-shaped metallic electrodes (Figure 5.8 a). The frequency, bandwidth and time response of the PnC depend on design [193] and can be changed by the number of pairs of comb finger electrodes of IDT (N), number of lines in array (M), the width (W_E) and spacing (W_S) of adjacent fingers and Ni lines, aperture (L) (Figure 5.8). Design parameters of our SAW devices are given in Table 5.1. It was decided to make IDTs and PnCs in one technological step, so IDTs were made of Ni 50 nm as PnCs. Using LayoutEditor software we designed patterns for lithography (Figure 5.9). It was interesting to compare SAW transmission through the structures with and without PnCs so there were designed devices with and without PnCs between IDTs.

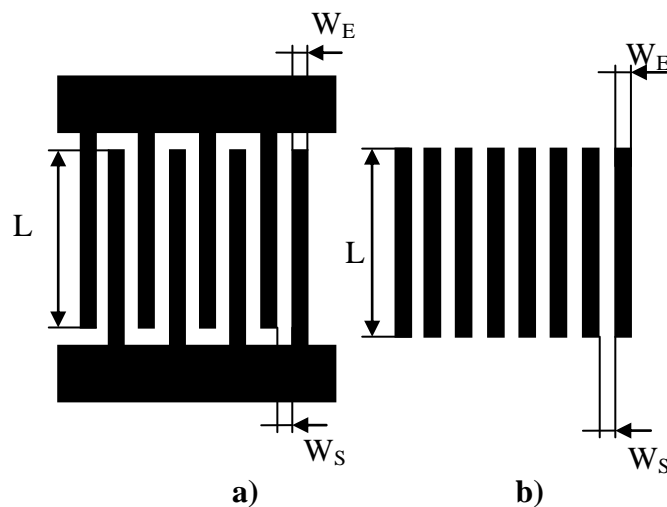


Figure 5.8. Schematic geometry of IDT (a) and lines array (b).

Table 5.1. Design parameters of SAW devices.

Substrate	Y+128° cut LiNbO3	
PnC material	Ni	
IDTs material	Ni	
Metal thickness, nm	50	
Central frequency, GHz	2	4
IDT pairs N	10	10
Lines number M	200	200
IDT aperture L, μm	70	50
IDT and lines width W_E , nm	500	250
IDT and lines spacing W_S , nm	500	250

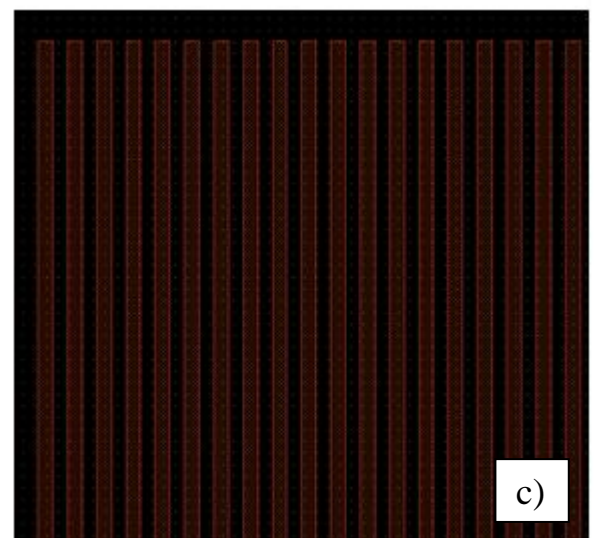
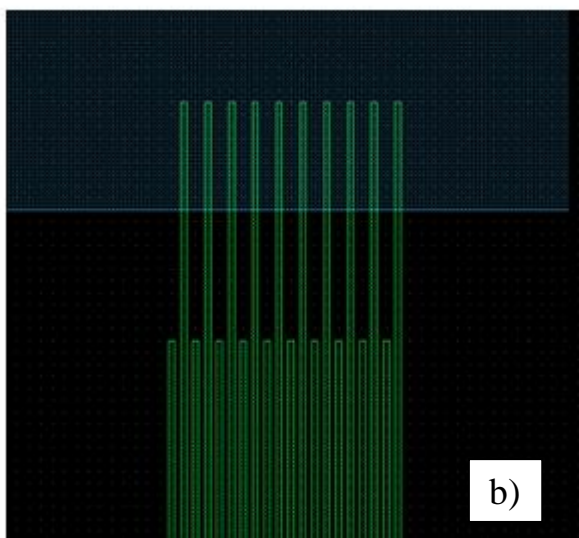
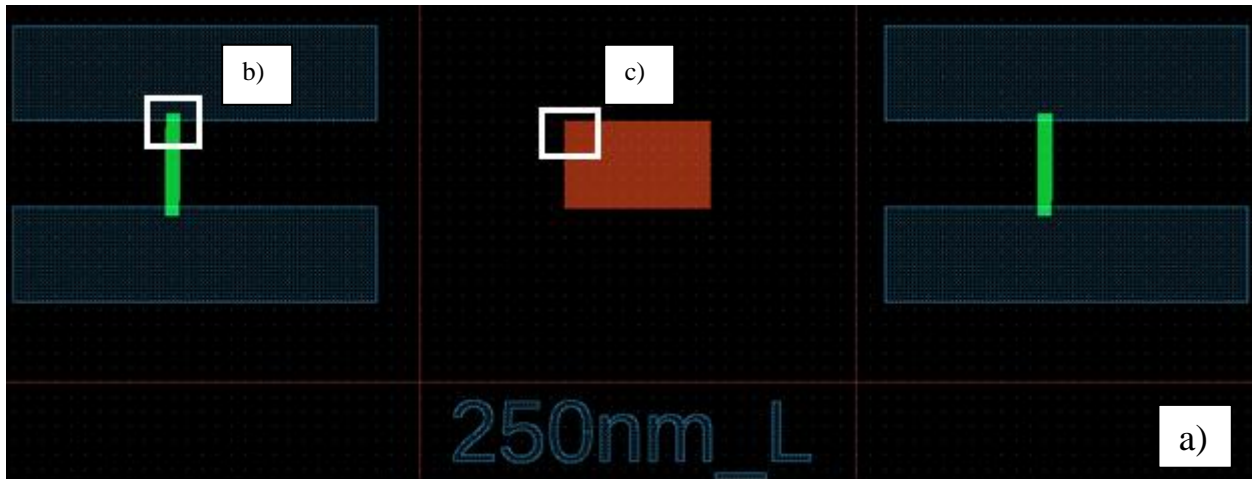


Figure 5.9. Layout of patterns for surface PnC device on 4 GHz: whole device (a) and detailed views of IDTs (b) and lines (c) patterns.

During technological step of resist baking and SEM imaging LiNbO₃ substrate can be charged. We found that charge can obstruct the tip to be engaged to the surface during AFM imaging. To flow down the charge PnC's for AFM imaging situated near the sample edge were designed to be connected to millimeter sized contact pad (Figure 5.10). It was proposed to fabricate this pad from Au using photolithography after the devices fabrication process.

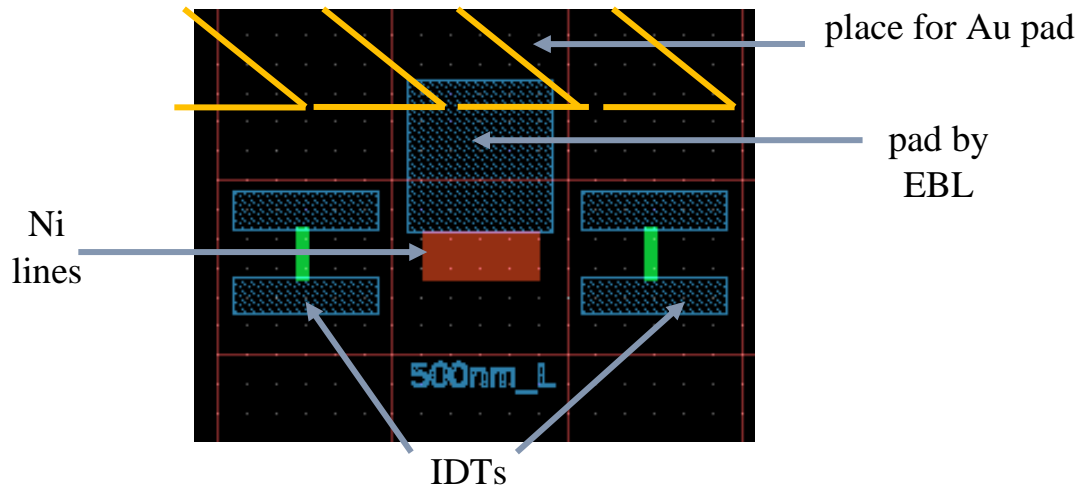


Figure 5.10. Layout of pattern for device connected to Au pad for AFM imaging.

5.3.2 Definition of 1D surface phononic crystals fabrication process

It was decided to use for fabrication process high-energy electron beam (100 keV) because it allows to obtain fine patterns with good resolution and uniformity and to escape big proximity effect. According to pattern sizes we chose suitable spot size (resolution) and beam current for every pattern. To escape proximity effect also we've decided to use different exposure dose for different patterns. So the goal was to find out suitable resist, good exposure doses and development process.

There are 2 ways to obtain patterns on thin films: etching or “etch-back” process and “lift-off” process (Figure 5.11). In “etch-back” technique thin film is deposited directly on the wafer. Then this film is coated by the resist and resist is patterned. Different acids and etchants are used to remove thin film in places not protected by resist. After removing of remaining resist patterned thin film is obtained. For lift-off process wafer without any film is coated by resist and resist is patterned. Then thin film of desired material deposits on top of the resist layer and directly on the wafer in places not protected by resist. During removing of remaining resist it is lifted-off along with film on top of it. Only film deposited in places without resist stays.

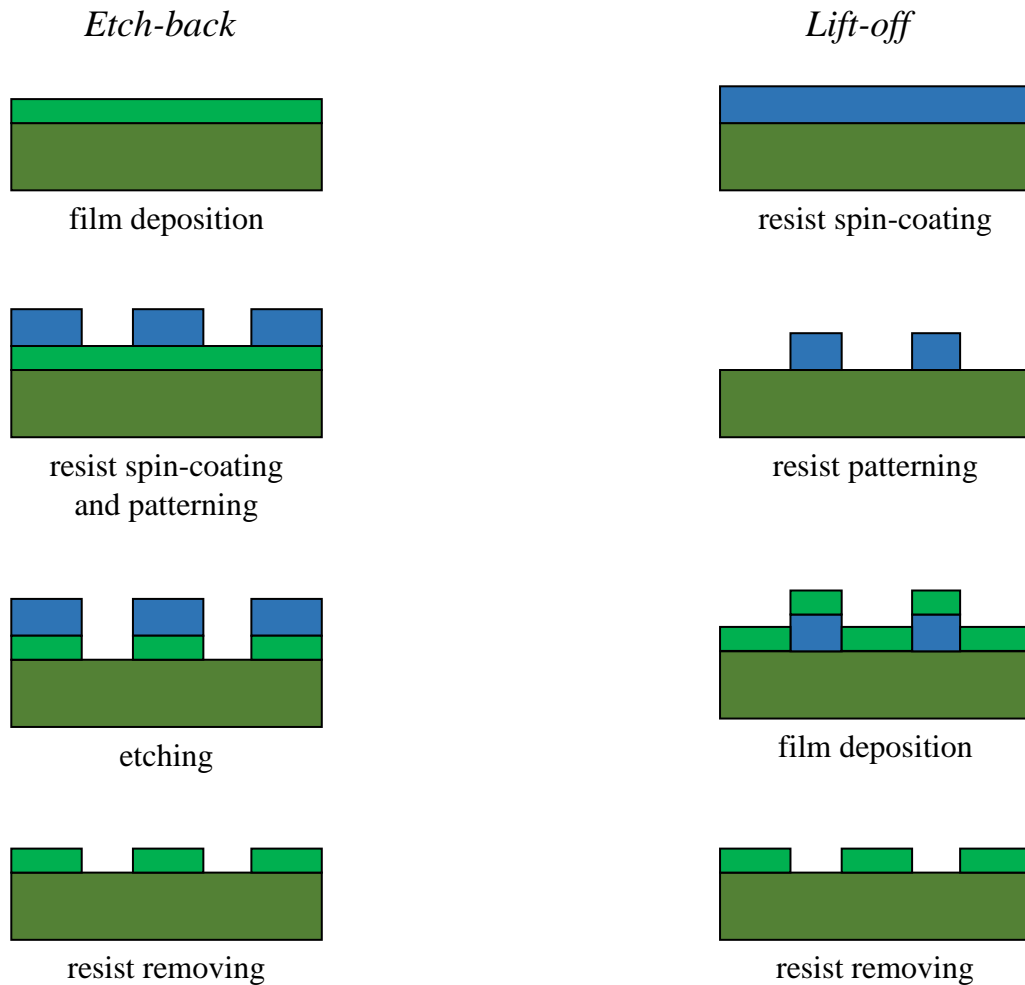


Figure 5.11. Lithography processes: etch-back and lift-off.

It was decided to try both lithographic processes. To start with, a standard etch-back and lift-off bi-layer processes developed in IEMN were used. Etch-back process was found to be too laborious. So we turned to the lift-off process. For bi-layer process there was a problem of resist adhesion. Finally, the one-layer lift-off process was found to be suitable for devices fabrication. The detailed description of the processes and its results are given below.

For structures fabrication and characterization following equipment was used:

1. LEICA EBPG 5000Plus system for realization of EBL process;
2. LEICA polyvar SC optical microscope with a magnification up to $\times 100$;
3. Ultra 55 (Carl Zeiss AG) system for SEM imaging with energy selective backscattered detector (ESB) which can provide compositional information about the sample;
4. PLASSYS MEB 550S electron beam evaporator for metal deposition;
5. AFM MultiMode (VEECO), AFM and MFM tips Nanoprobe MESP with CoCr coating;
6. Vector network analyser Agilent E5071C ENA Series and probe station.

Etch-back process EB

EB process was a standart etch-back process developed in IEMN consisted of following steps:

1. Standart cleaning procedure for LiNbO_3 substrate: acetone+IPA and drying by nitrogen flow;
2. Deposition of 50 nm Ni film by evaporation method;
3. Spinning diluted AZnLOF 20202.000 rpm/ 1000 rpm/s/ 20 s. Obtained resist thickness of approximately 1 μm ;
4. Soft-bake at 110 $^\circ\text{C}$ for 90 s;
5. Variation dose e-beam exposure;
6. Post bake at 110 $^\circ\text{C}$ for 300 s;
7. Development in AZ 326 for 85 s.

SEM imaging of obtained patterns showed that lines and fingers 500nm were quite good at dose 24 $\mu\text{C}/\text{cm}^2$ (Figure 5.12a) besides small proximity effect near the big pads for fingers (Figure 5.12b) that could be solved by using lower dose for exposure of big pads. For lines 250 nm development was not finished but problems of adhesion and bonding started (Figure 5.12 c).

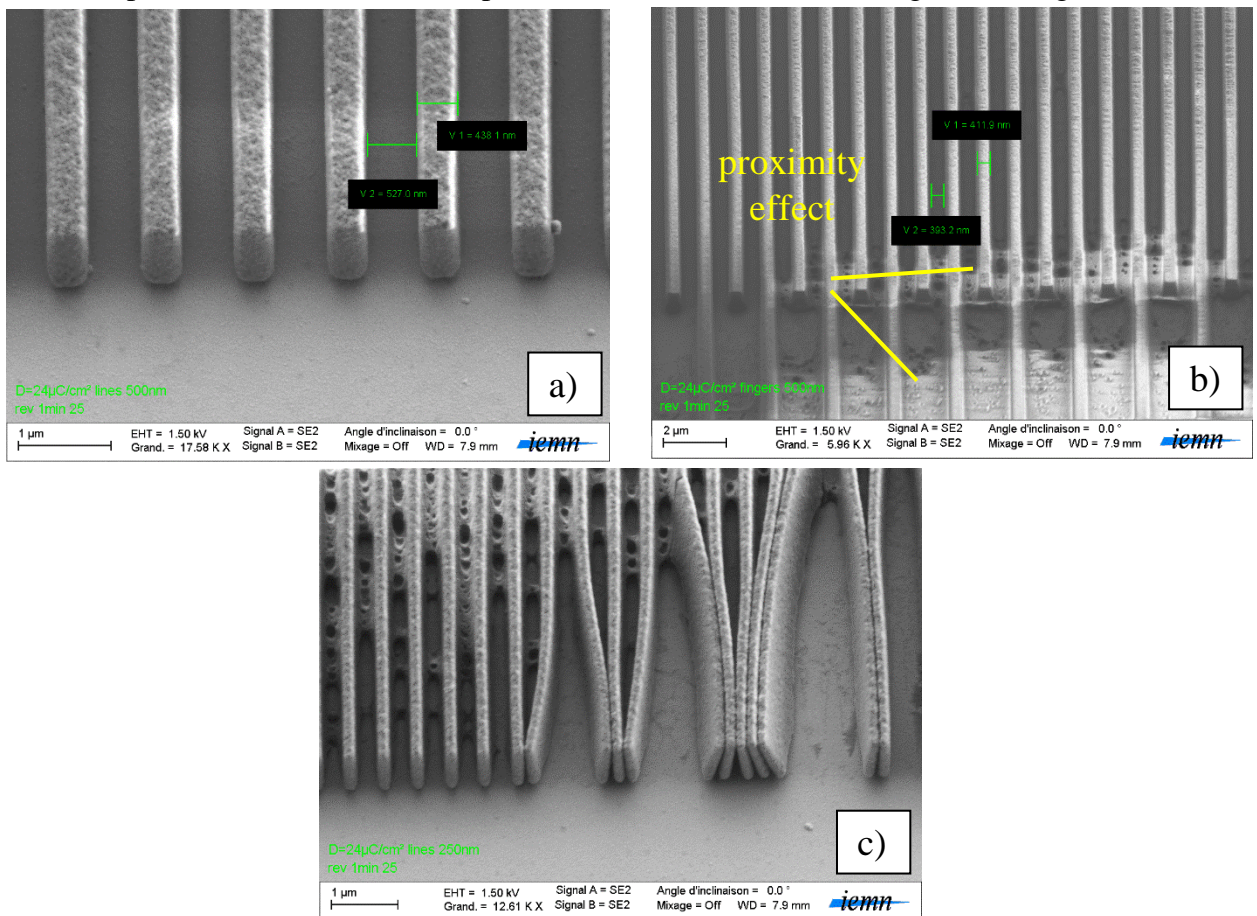


Figure 5.12. SEM images of AZnLOF resist patterns of lines (a) and comb fingers 500 nm (b) and lines 250 nm (c) at dose 24 $\mu\text{C}/\text{cm}^2$ for EB process.

Because patterns 500 nm were good we tried to do wet chemical etching. Etching was done for two different samples in different etching solutions: $\text{H}_3\text{PO}_4/\text{HNO}_3/\text{H}_2\text{O}$ ($T=50\text{ }^\circ\text{C}$) and $\text{HNO}_3/\text{H}_2\text{O}$ (1:10) for about 5 min. Patterns obtained using $\text{H}_3\text{PO}_4/\text{HNO}_3/\text{H}_2\text{O}$ ($T=50\text{ }^\circ\text{C}$) were about 50 nm in height. It means that resist on top of the Ni 50 nm film was almost removed during etching. While etching in $\text{HNO}_3/\text{H}_2\text{O}$ (1:10) led to the fabrication of patterns with not smooth edges. So to find good etchant and etching time for Ni which does not influence on resist and allows obtaining small and smooth features became a challenge. Using reactive ion etching was also difficult to apply. So it was decided to try the more simple and effective process - lift-off.

Lift-off process LO1

The first we tried was bi-layer lift-off technology (Figure 5.13). For this technology two positive resists are used to obtain undercut resist profile. Such undercut profile allows to do clean lift-off and to obtain well defined metal structures. The bottom layer should have a higher sensitivity to the exposure or a higher dissolution rate in the developer. So we've decided to use PMMA resist and its copolymer. In order to perform a good lift-off process the thickness of resist should be 2-3 times more than the thickness of deposited material. As we wanted to deposit 50-100 nm of Ni we've decided that 400-500 nm of resist would be suitable.

LO1 process consisted of following steps:

1. Cleaning LiNbO_3 substrate in acetone and IPA and drying by nitrogen flow;
2. Spinning Copo 10% (MAA17,5) 3.500 rpm/ 1000 rpm/s/ 12 s. Obtained resist thickness of approximately 400 nm;
3. Soft-bake at $180\text{ }^\circ\text{C}$ for 600 s;
4. Spinning PMMA 3% 495K 2.500 rpm/ 1000 rpm/s/ 10 s. Obtained resist thickness of approximately 75 nm (Figure 5.13 a);
5. Soft-bake at $180\text{ }^\circ\text{C}$ for 600 s;
6. Deposition of 5 nm Ge film by evaporation method to avoid discharge effect during EBL because LiNbO_3 is a dielectric;
7. Variation dose e-beam exposure;
8. Etching of Ge film in $\text{H}_2\text{O}_2/\text{DIW}$ (1:1) for 35-50 s.
9. Development in MIBK/IPA (1:2) for 80 s with agitation 110 tr/min (Figure 5.13 b).

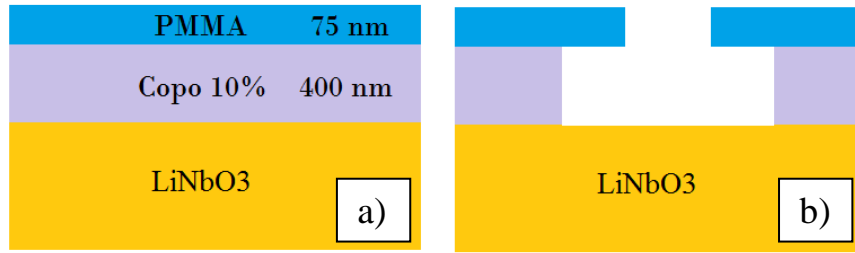
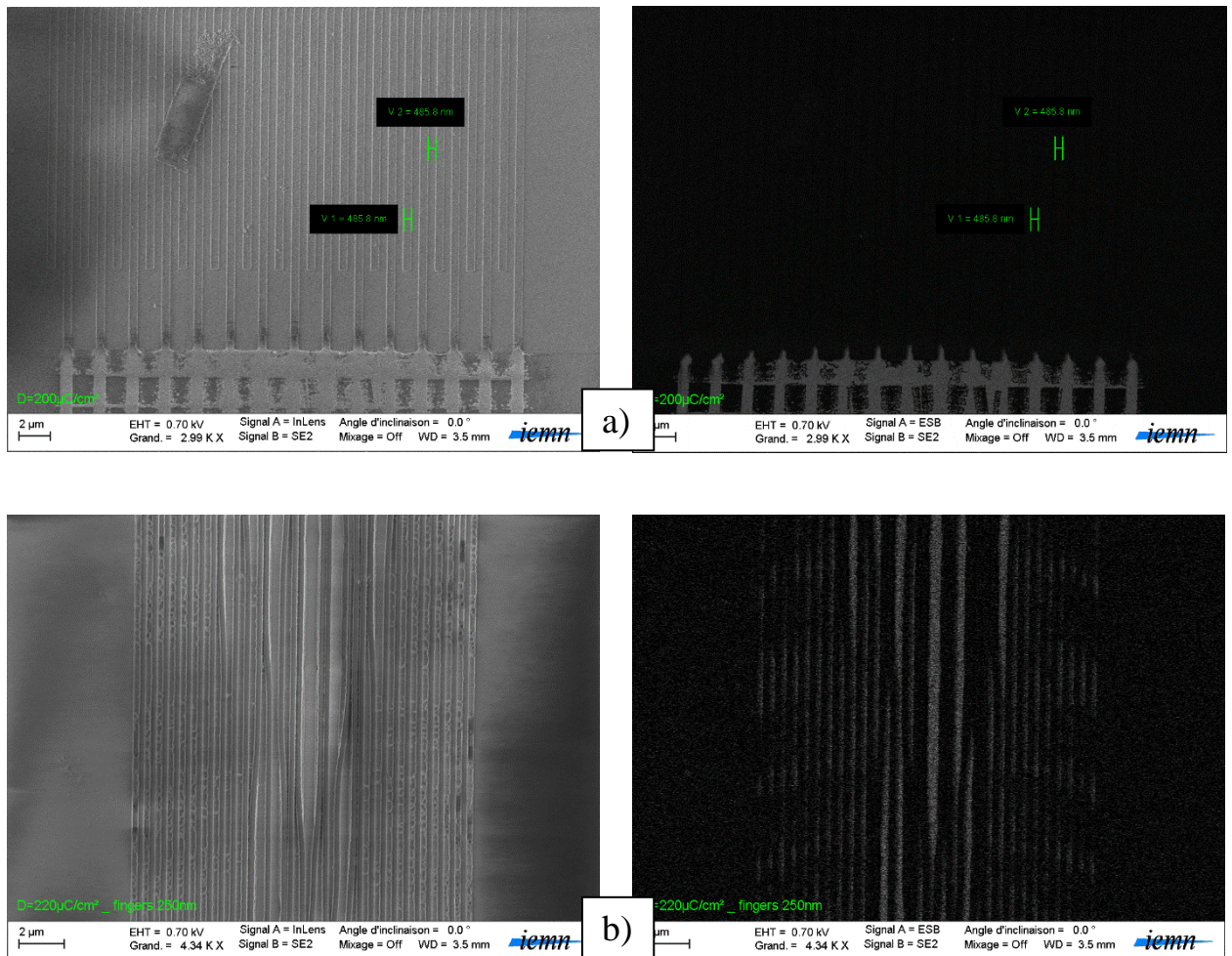


Figure 5.13. Used bi-layer lift-off technology.

Then resist patterns were visualized by SEM using ESB detector (Figure 5.14). Dark places on ESB image mean resist, white places - LiNbO₃ substrate. The good dose for LO1 technology wasn't found. At low doses development wasn't finished (Figure 5.14a) and for higher doses the problem of resist adhesion to the sample started (Figure 5.14b-c).



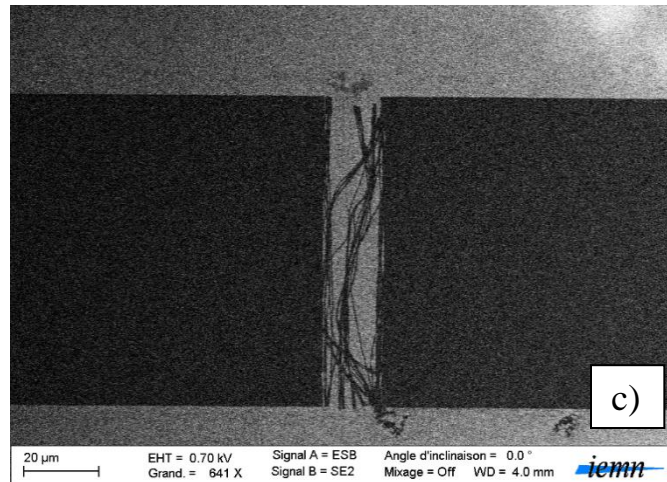


Figure 5.14. SEM and ESB SEM images of resist comb fingers patterns at doses $200 \mu\text{C}/\text{cm}^2$ (a), $220 \mu\text{C}/\text{cm}^2$ (b) and $260 \mu\text{C}/\text{cm}^2$ (c) for LO1 process.

Lift-off process LO2

Smooth surfaces with small average roughness like LiNbO_3 often pose adhesion problems. To solve this problem first we tried standard procedure to improve resist adhesion to such sample: dehydration+use of adhesion promoter. Dehydration of the substrate promotes better adhesion because resist interacts directly with substrate but not with water adsorbed on its surface. Adhesion agents are used to make surface hydrophobic and chemically attach the resist to the substrate. For this purpose, we used hexamethyldisilazane (HMDS). But unfortunately this widely used method to improve resist adhesion didn't work (Figure 5.15). LO2 steps were:

1. Cleaning LiNbO_3 substrate in acetone and IPA and drying by nitrogen flow;
2. Dehydration at 180°C for 600 s
3. Spinning HMDS 3.500 rpm/ 1000 rpm/s/ 12 s;
4. Spinning Copo 10% (MAA17,5) 3.500 rpm/ 1000 rpm/s/ 12 s;
5. Soft-bake at 180°C for 600 s;
6. Spinning PMMA 3% 495K 2.500 rpm/ 1000 rpm/s/ 10 s;
7. Soft-bake at 180°C for 600 s;
8. Deposition of 5 nm Ge film;
9. E-beam exposure;
10. Etching of Ge film in $\text{H}_2\text{O}_2/\text{DIW}$ (1:1) for 35-50 s.
11. Development in MIBK/IPA (1:2) for 80 s with agitation 110 tr/min.

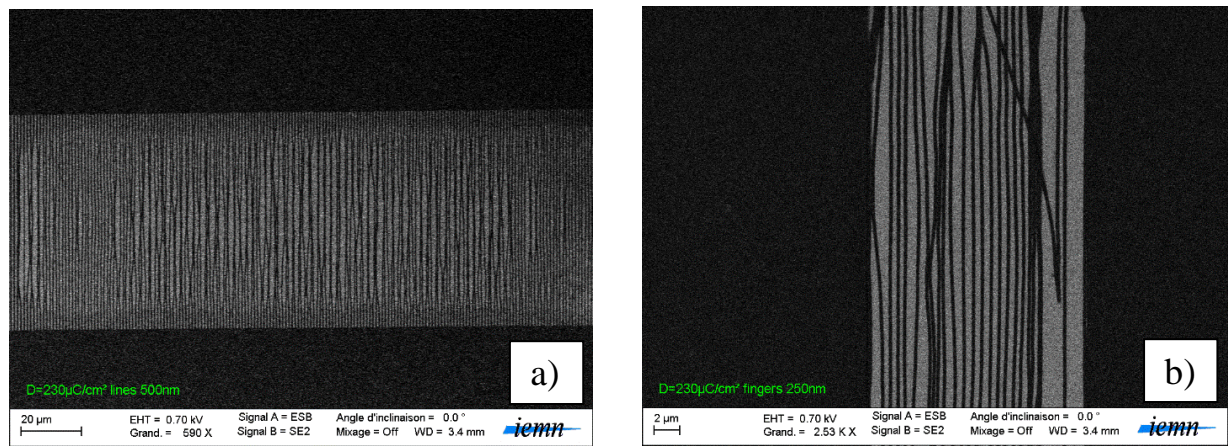


Figure 5.15. ESB SEM images of resist lines (a) and comb fingers (b) patterns for LO2 process.

Lift-off processes LO3 and LO4

Because common method to improve resist coupling to the substrate did not help to solve the problem, we supposed that problem of adhesion could be explained by undercut profile. Because of small sizes of features undercut profile obtained by used resists was too big. So we tried to solve this problem in processes LO3 and LO4 by using additional arrangements to improve resist adhesion and by reducing the size of undercut. LO3 and LO4 processes differed only by development step:

1. Cleaning LiNbO₃ substrate in acetone and IPA and drying by nitrogen flow;
2. Dehydration at 180 °C for 600 s
3. Spinning HMDS 3.500 rpm/ 1000 rpm/s/ 12 s;
4. Spinning Copo 10% (MAA17,5) 3.500 rpm/ 1000 rpm/s/ 12 s;
5. Soft-bake at 180 °C for 600 s;
6. Spinning PMMA 3% 495K 2.500 rpm/ 1000 rpm/s/ 10 s;
7. Soft-bake at 180 °C for 600 s;
8. Deposition of 5 nm Ge film;
9. E-beam exposure;
10. Etching of Ge film in H₂O₂/DIW (1:1) for 35-50 s.
11. Development for 120 s without agitation: LO3 – in MIBK/IPA (1:2), LO4 – in MIBK/IPA (1:3).

In process LO3 we terminated agitation use at development. Agitation during development is used to increase the pressure at the resist surface and accelerates development. But we supposed

that such pressure at the resist surface can provide resist separation from the substrate. Besides because of development acceleration agitation can provide bigger undercut profile. Only termination of agitation use did not help to solve adhesion problem (Figure 5.16 a). So we tried to make less strong development solution for process LO4. Before we used solution of methyl isobutyl ketone (MIBK) and isopropyl alcohol – MIBK:IPA (1:2) and then we tried MIBK:IPA (1:3) to reduce rate of bottom resist dissolution in developer and to reduce the undercut. This also didn't help to solve the problem (Figure 5.16b).

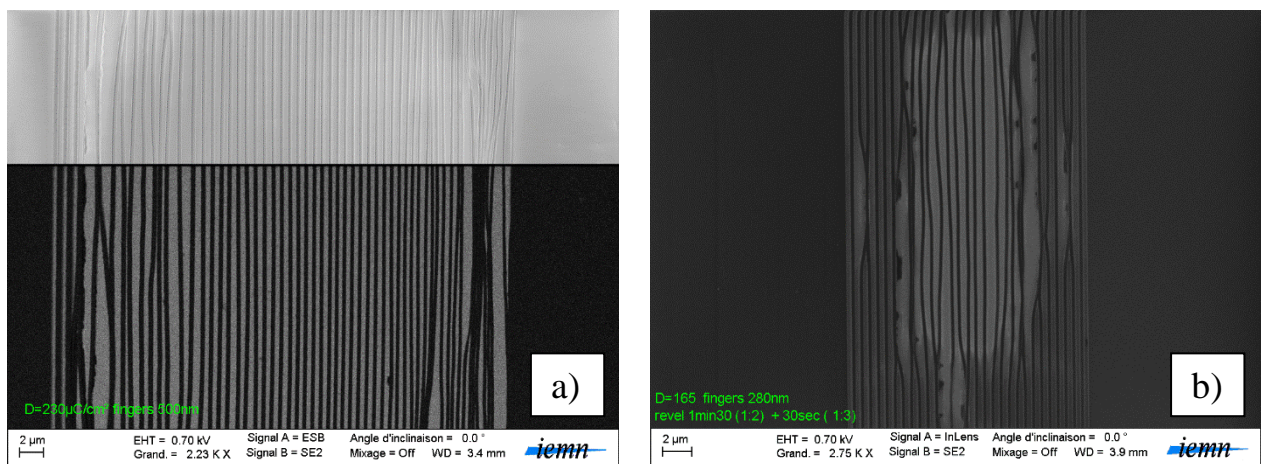


Figure 5.16. ESB SEM images of resist comb fingers patterns obtained without agitation during the development in MIBK:IPA (1:2) for LO3 process (a) and in MIBK:IPA (1:3) for LO4 process (b).

Lift-off process LO5

In process LO5 we tried to use a metal adhesion layer. Cr, Ti, Pt and etc. are usually employed as adhesion layers. We chose deposition of 30 nm layer of Ti onto the substrate prior to the application of resist layer because in work [194] it was shown that use of thin Ti film enables the reliable fabrication of high resolution resist patterns by e-beam lithography.

LO5 process steps:

1. Cleaning LiNbO₃ substrate in acetone and IPA and drying by nitrogen flow;
2. Dehydration at 180 °C for 600 s
3. Deposition of 30 nm Ti film by evaporation;
4. Spinning HMDS 3.500 rpm/ 1000 rpm/s/ 12 s;
5. Spinning Copo 10% (MAA17,5) 3.500 rpm/ 1000 rpm/s/ 12 s;
6. Soft-bake at 180 °C for 600 s;

7. Spinning PMMA 3% 495K 2.500 rpm/ 1000 rpm/s/ 10 s;
8. Soft-bake at 180 °C for 600 s;
9. Deposition of 5 nm Ge film;
10. E-beam exposure;
11. Etching of Ge film in H₂O₂/DIW (1:1) for 35-50 s.
12. Development for 90 s without agitation in MIBK/IPA (1:3).

This also didn't solve the problem, adhesion was bad even at low doses at which the development was not finished (Figure 5.17a) and .problem was increased with dose increase (Figure 5.17 b).

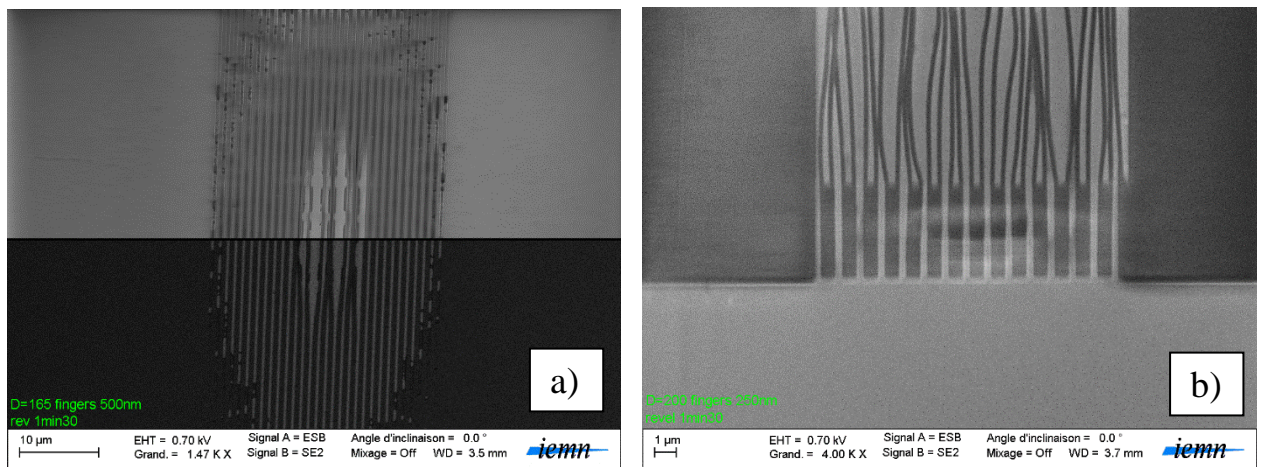


Figure 5.17. SEM images of resist comb fingers patterns obtained at 165 $\mu\text{C}/\text{cm}^2$ (a) and 200 $\mu\text{C}/\text{cm}^2$ (b) exposure doses for LO5 process.

Lift-off process LO6

It was decided to obtain less undercut of bi-layer resist system. For this purpose use of the larger molecular weight PMMA copolymer was needed. So we tried to use Copo 13% (MAA8,5) resist instead of Copo 10% (MAA17,5) (Figure 5.18 a). As before we spin-coated 400 nm of Copo 13% resist and 75 nm of PMMA 3% 495K resist on LiNbO₃ sample and tried different doses. LO6 process steps:

1. Cleaning LiNbO₃ substrate in acetone and IPA and drying by nitrogen flow;
2. Dehydration at 180 °C for 600 s
3. Spinning HMDS 4.000 rpm/ 1000 rpm/s/ 12 s;
4. Spinning Copo 13% (MAA8,5) 4.000 rpm/ 1000 rpm/s/ 12 s. Obtained resist thickness of approximately 400 nm (Figure 5.18 a);

5. Soft-bake at 180 °C for 600 s;
6. Spinning PMMA 3% 495K 2.500 rpm/ 1000 rpm/s/ 10 s. Obtained resist thickness of approximately 75 nm (Figure 5.18 a);
7. Soft-bake at 180 °C for 600 s;
8. Deposition of 5 nm Ge film;
9. E-beam exposure;
10. Etching of Ge film in H₂O₂/DIW (1:1) for 35-50 s.
11. Development for 180 s without agitation in MIBK/IPA (1:2)(Figure 5.18b).

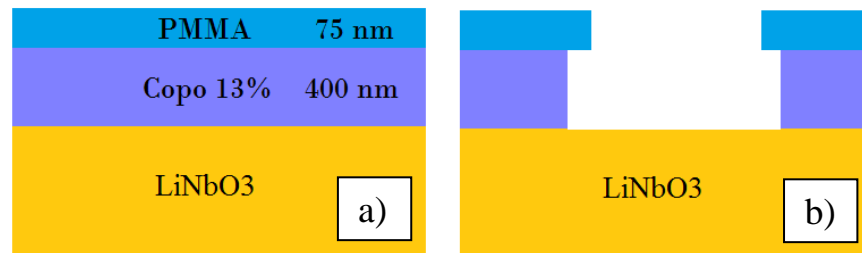


Figure 5.18. Another one used bi-layer lift-off technology.

Using another resist to reduce of undercut profile didn't solve the adhesion problem, patterns were improved but resist adhesion still was not suitable for subsequent processing (Figure 5.19).

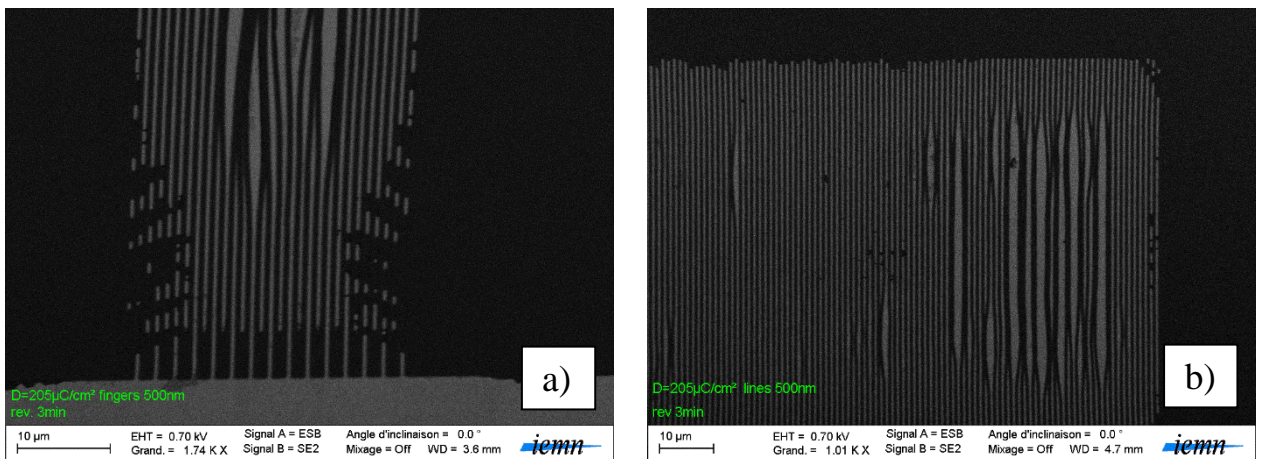


Figure 5.19. ESB SEM images of resist comb fingers (a) and lines (b) patterns for LO6 process.

Lift-off process LO7

Because bi-layer lift-off technology posed a serious adhesion challenge we decided to try fabricate structures using one resist layer (Figure 5.20) despite of risk of hard metal lift-off and

as result not smooth edges of obtained structures. PMMA 5% 950K resist was used in this process. Exposure was done using variation of dose for IDT fingers and for lines from 250 to 560 $\mu\text{C}/\text{cm}^2$ with step of 10 $\mu\text{C}/\text{cm}^2$. For contact pads the dose of 400 $\mu\text{C}/\text{cm}^2$ was used constantly. This dose was found good for big pads during previous technical processes. LO7 process steps:

1. Cleaning LiNbO₃ substrate in acetone and IPA and drying by nitrogen flow;
2. Dehydration at 180 °C for 600 s
4. Spinning HMDS 2.250 rpm/ 1000 rpm/s/ 10 s;
5. Spinning PMMA 5% 950K 2.250 rpm/ 1000 rpm/s/ 10 s. Obtained resist thickness of approximately 400 nm (Figure 5.20 a);
8. Soft-bake at 180 °C for 600 s;
9. Deposition of 5 nm Ge film;
10. E-beam exposure;
11. Etching of Ge film in H₂O₂/DIW (1:1) for 35-50 s.
12. Development for 150 s without agitation in MIBK/IPA (1:2)(Figure 5.20b).

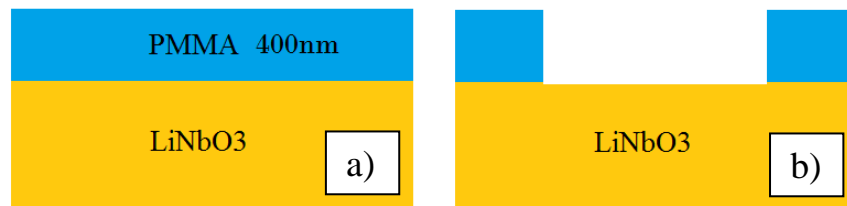


Figure 5.20. Used single resist layer lift-off process.

We vary development time from 30 s to 150 s with step of 30 s. The development time of 150 s was found good to obtain clean patterns for contact pads. Therefore, we finished development and observed obtained resist patterns. We found that using this process good resist patterns with good adhesion to the substrate were fabricated. The good dose for comb fingers and for lines was found near 530-560 $\mu\text{C}/\text{cm}^2$. So we decided to finish the process, deposited 50 nm of Ni and did the lift-off. After lift-off was finished we observed obtained metallic structures by SEM and measured its sizes.

At Figure 5.21 structures fabricated at dose 560 $\mu\text{C}/\text{cm}^2$ are shown. At this dose lift-off was finished completely, there was no residual metal, structures were well defined, with smooth edges, width of lines and fingers was close to designed.

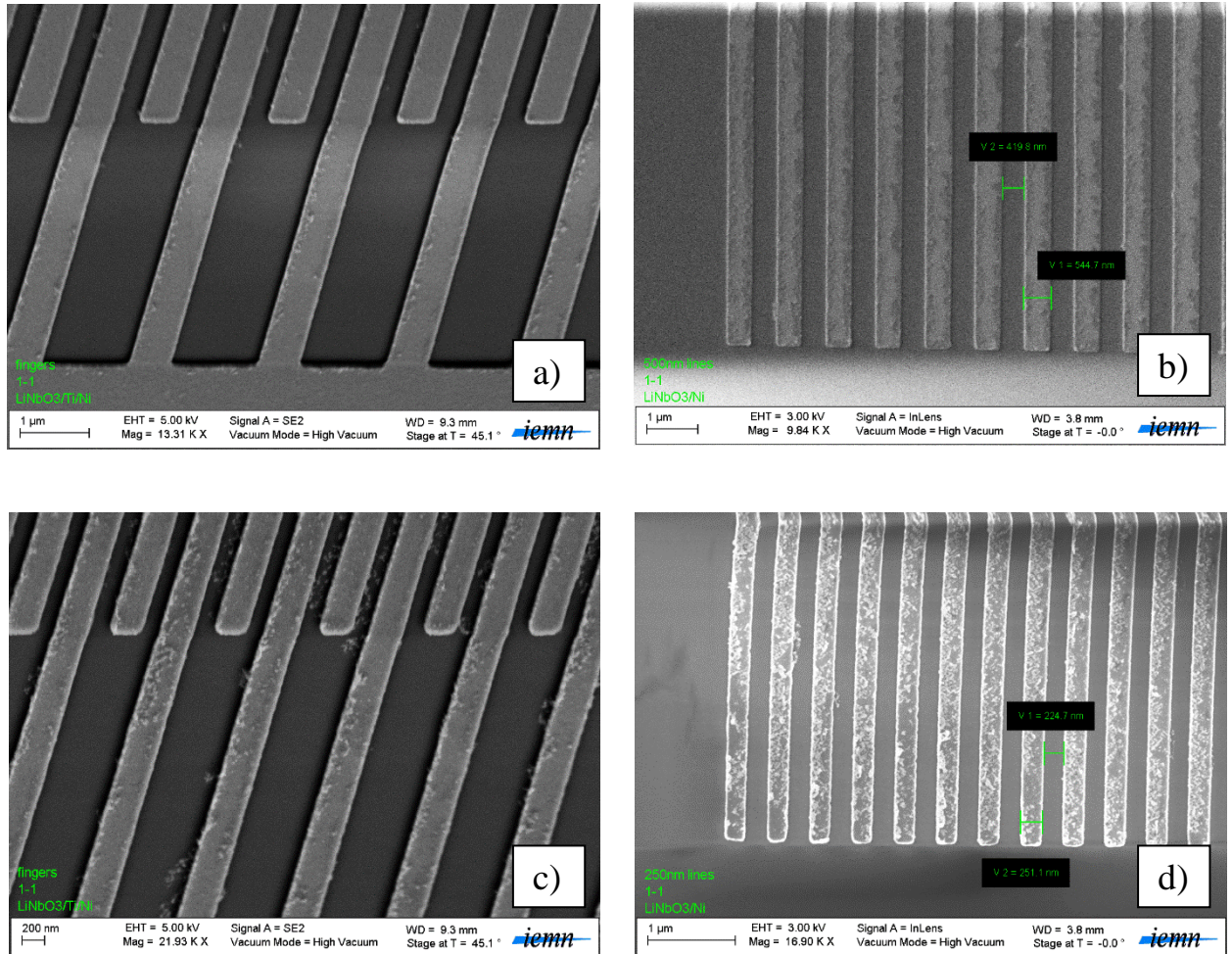


Figure 5.21. SEM images of structures obtained at dose $560 \mu\text{C}/\text{cm}^2$ using LO7 process: comb fingers 500 nm (a) and lines 500 nm (b), comb fingers 250 nm (c) and lines 250 nm (d).

At next two doses of 550 and $540 \mu\text{C}/\text{cm}^2$ sizes of structures didn't change critically. All structures except fingers 250 nm were good and clean. For fingers 250 nm some residual metal patterns were observed (Figure 5.22 a, b). At dose $530 \mu\text{C}/\text{cm}^2$ both comb fingers 250 nm and 500 nm had not lifted-off metal patterns (figure 5.22 c, d).

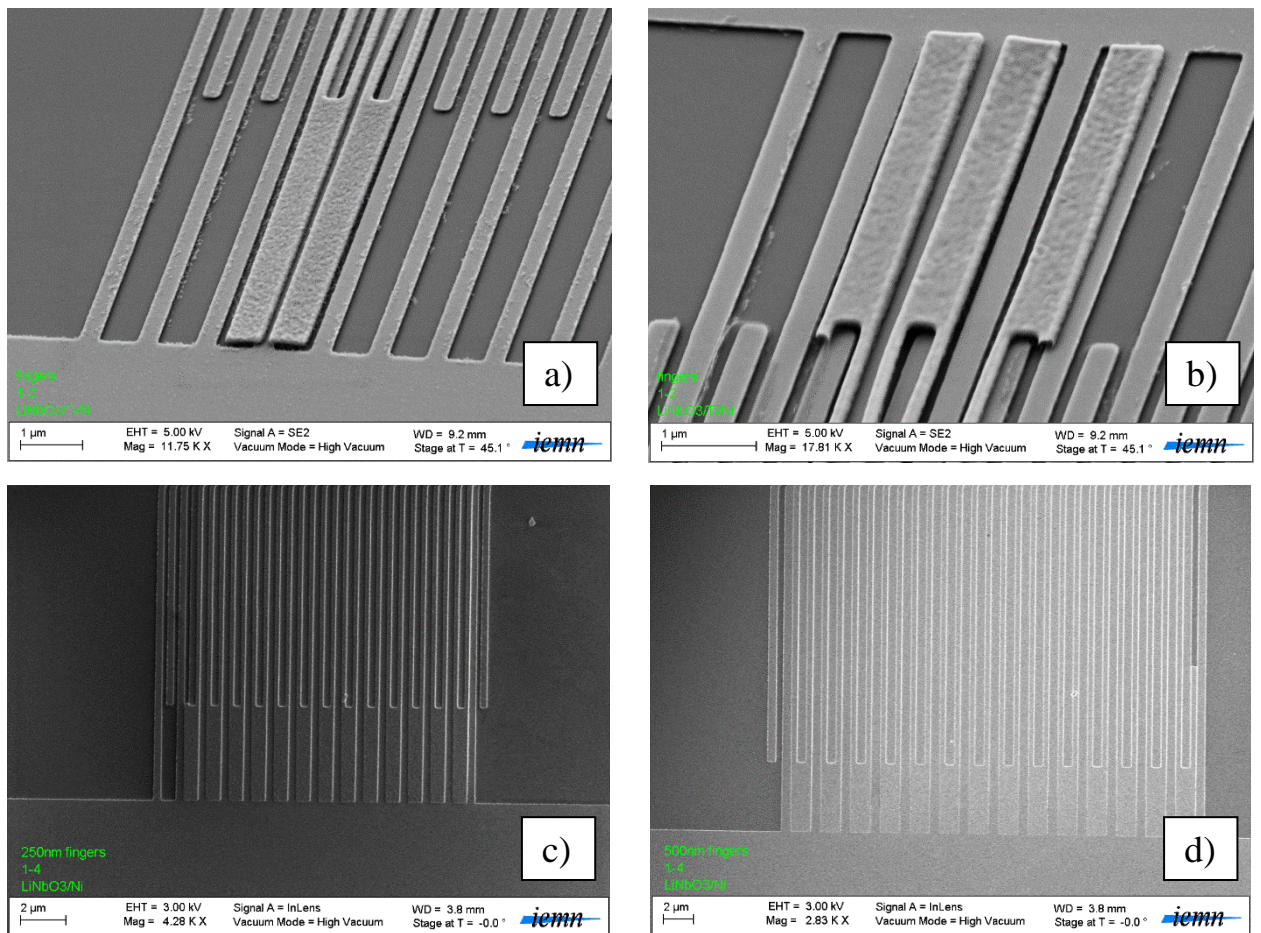


Figure 5.22. SEM images of residual metal on comb fingers 250 nm at doses 550 $\mu\text{C}/\text{cm}^2$ (a), 540 $\mu\text{C}/\text{cm}^2$ (b) and 530 $\mu\text{C}/\text{cm}^2$ (c) and on fingers 500 nm at dose 530 $\mu\text{C}/\text{cm}^2$ (d).

Then we measured reflection frequency responses of fabricated comb fingers using network analyzer. IDTs fabricated at dose 560 $\mu\text{C}/\text{cm}^2$ had a good reflection characteristics on frequencies close to desired (Figure 5.23).

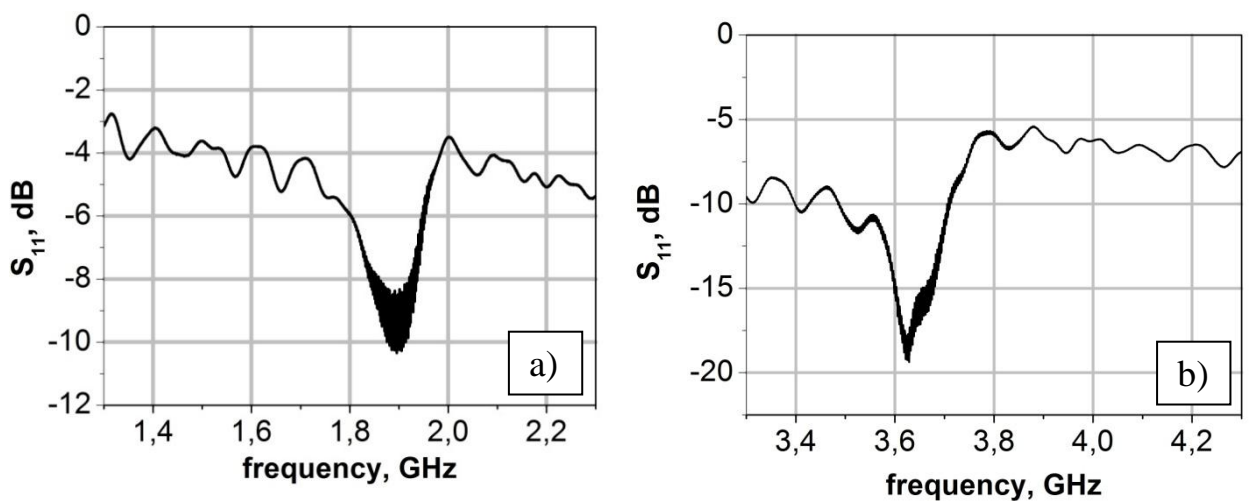


Figure 5.23. Reflection frequency responses of IDTs 500 nm (a) and 250 nm (b) obtained at dose 560 $\mu\text{C}/\text{cm}^2$.

In Table 5.2 there is given a summary of all tried fabrication processes. One can see that process LO7 provided fabrication of good patterns. At e-beam exposure dose $560 \mu\text{C}/\text{cm}^2$ pattern sizes didn't deviate much from layout patterns and the decrease of dose below $560 \mu\text{C}/\text{cm}^2$ didn't improve compliance of pattern sizes to layout sizes. But decrease of dose increased risk of lift-off process not to be finished and leaving of residual metal on fabricated structures. Thus it was decided for fabrication of IDTs comb fingers and lines by process LO7 to use e-beam dose of $560 \mu\text{C}/\text{cm}^2$. The dose of $400 \mu\text{C}/\text{cm}^2$ for big pads was found to be suitable.

Table 5.2. Summary of the fabrication processes for PnC structures.

Process name	Sample preparation	Resist	Development	Result
EB	Cleaning with acetone and IPA	AZnLOF 2020 diluted 1 μ m	AZ 326	Challenge to find etchant and etching time. Results were not suitable.
LO1	Cleaning with acetone and IPA	Copo PMMA 10% 400 nm/PMMA 3% 495K 75 nm	MIBK/IPA (1:2) + agitation	Resist adhesion problem. Results were not suitable.
LO2	Cleaning with acetone and IPA + dehydration + HMDS	Copo PMMA 10% 400 nm/PMMA 3% 495K 75 nm	MIBK/IPA (1:2) + agitation	Resist adhesion problem. Results were not suitable.
LO3	Cleaning with acetone and IPA + dehydration + HMDS	Copo PMMA 10% 400 nm/PMMA 3% 495K 75 nm	MIBK/IPA (1:2) without agitation	Resist adhesion problem. Results were not suitable.
LO4	Cleaning with acetone and IPA + dehydration + HMDS	Copo PMMA 10% 400 nm/PMMA 3% 495K 75 nm	MIBK/IPA (1:3) without agitation	Resist adhesion problem. Results were not suitable.
LO5	Cleaning with acetone and IPA + dehydration + Ti 30nm+ HMDS	Copo PMMA 10% 400 nm/PMMA 3% 495K 75 nm	MIBK/IPA (1:3) without agitation	Resist adhesion problem. Results were not suitable.
LO6	Cleaning with acetone and IPA + dehydration + HMDS	Copo PMMA 13% 400 nm/PMMA 3% 495K 75 nm	MIBK/IPA (1:2) without agitation	Resist adhesion problem. Results were not suitable.
LO7	Cleaning with acetone and IPA + dehydration + HMDS	PMMA 5% 950K 400 nm	MIBK/IPA (1:2) without agitation	Results were suitable.

When technological process was obtained we started devices fabrication (Figure 5.24).

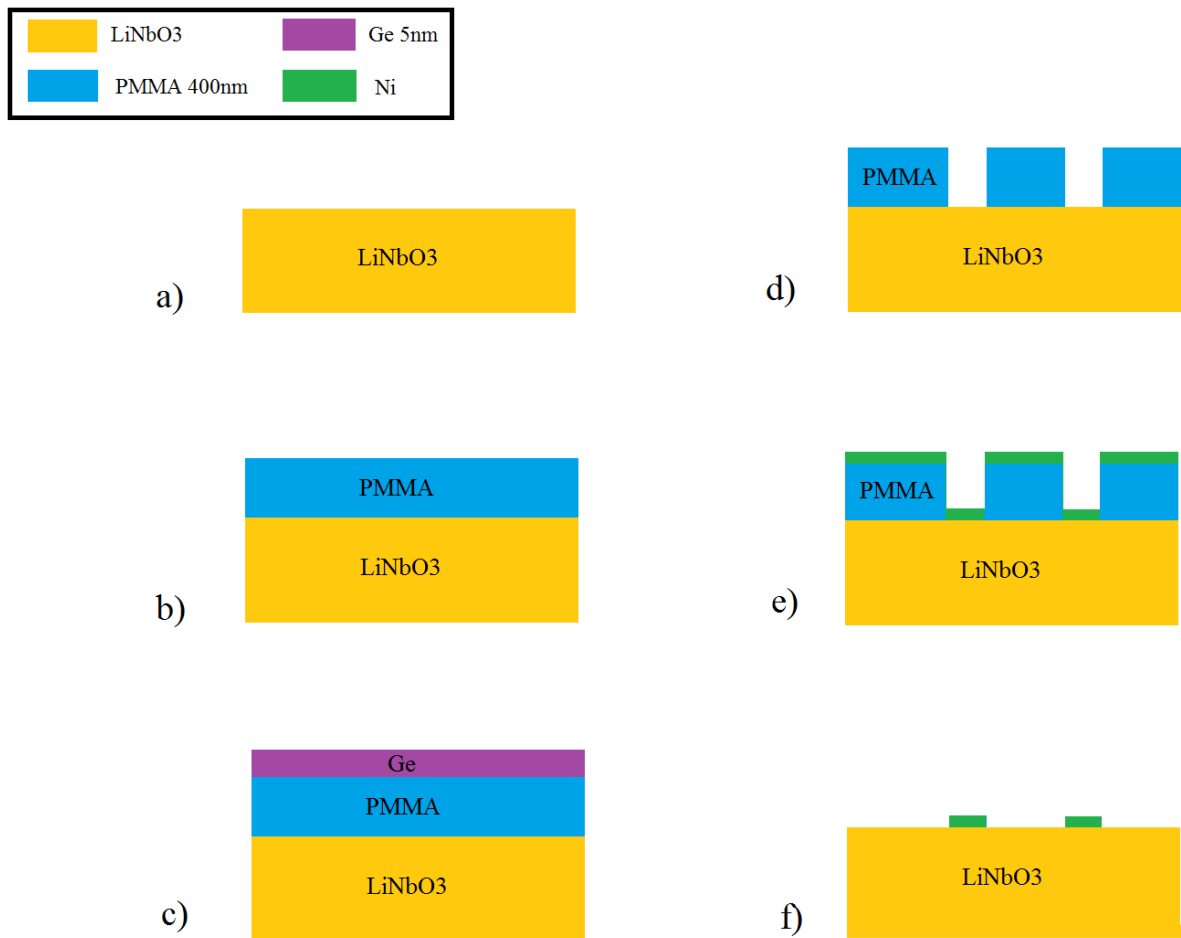


Figure 5.24. Scheme of chosen device fabrication technology using e-beam lithography.

1. Preparation of LiNbO_3 substrate (Figure 5.24 a): a) cleaning for 5 min in acetone and IPA, b) drying by nitrogen, c) dehydration bake 600s at temperature 180°C .

2. Spincoating of HMDS and positive e-beam resist PMMA 5% 950K on the substrate (Figure 5.24 b). Parameters of spincoater: speed 2.250 rpm, acceleration 1.000 rpm/s, time 10 s. 400 nm thick layer of resist was produced. Bake on a hotplate at temperature 180°C for 600 s before e-beam exposition.

3. Deposition of 5 nm of Ge (Figure 5.24 c) by evaporation. This step was needed because LiNbO_3 is an insulating substrate. It helped to avoid charge effect which could deflect the electron beam and distort the pattern. Figure 5.25 shows ESB SEM images illustrating charge effect during the fabrication of comb fingers without Ge layer on top of resist layer. Thin Ge layer is often used as a charge dissipation layer because of its good conductivity, transparency and easy processing [153]. We used it on top of the resist because resist layer was quite thick so

electrons may not reach the conductive layer underneath the resist and it would give rise to charging effect. Moreover in case of Ge layer underneath the resist difficult ion etching after resist development is needed. And Ge layer above the resist layer was easily removed by wet chemical etching before development.

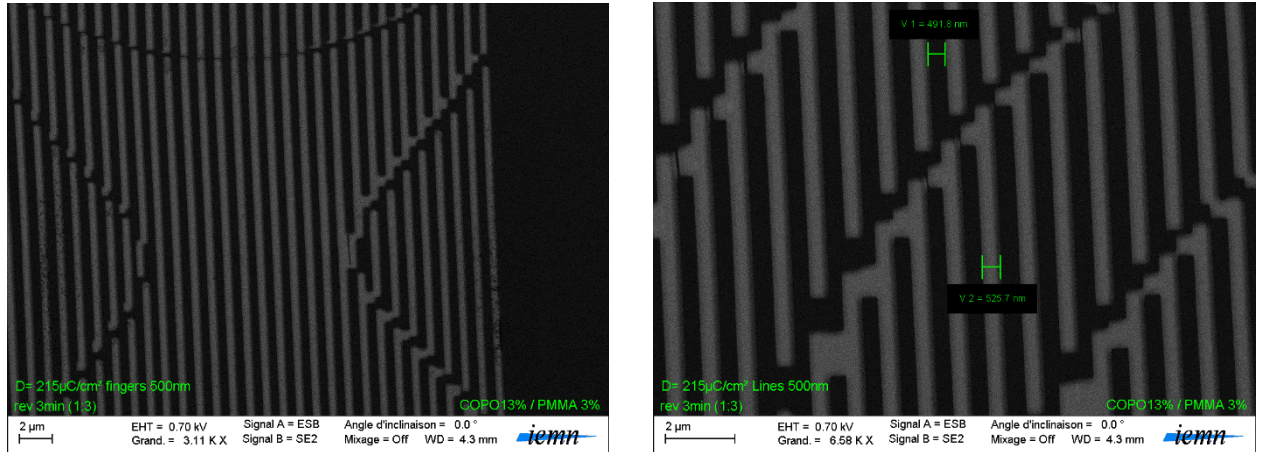


Figure 5.25. Distortion of the patterns because of charge effect.

4. Exposition of the resist by e-beam. Parameters of exposition are given in Table 5.3.

Table 5.3. Exposition parameters.

Structure	Electron energy, keV	Resolution, nm	Current, nA	Dose, $\mu\text{C}/\text{cm}^2$
<i>Lines</i>	100	10	2	560
<i>IDTs</i>	100	10	2	560
<i>Pads</i>	100	30	20	400

5. Etching of Ge layer. Good for Ge is hydrogen peroxide (H_2O_2) and its solutions including mixture with deionized water. We used H_2O_2 :DIW (1:1) solution. Etching time was about 35-50 s. When Ge was fully etched sample was rinse by deionized water and dried by nitrogen. This solution didn't influence on the resist.

6. Development of the exposed resist in solution of methyl isobutyl ketone (MIBK) and isopropyl alcohol – MIBK:IPA (1:2) for 150 s without agitation of the sample (Figure 5.24 d). Rinse by isopropyl alcohol and drying by nitrogen.

7. Deposition of Ni 50 nm (Figure 5.24 e) by evaporation. Evaporation was chosen as deposition method because evaporated films have poor step coverage due to the directional

nature (shadowing). Due to this fact it's easier to make lift-off and to obtain well defined borders of the structures using evaporated films.

8. Lift-off in Remover PG at temperature 70°C (Figure 5.24 f), rinse by IPA and dry by nitrogen.

After finish of device fabrication the process of fabrication of gold contact pad for AFM imaging was done. This process included following steps:

a) Spincoating of 1 μm layer of diluted negative resist AZnLOF 2020 on the sample and bake at temperature 110 °C for 90 s (Figure 5.26 a).

b) Overlay of mylar film on sample and alignment with contact pads made by e-beam lithography. Mylar film is a polyester film which blocks out ultraviolet (UV) radiation. So we used it as a mask for photolithography (Figure 5.26 b).

c) UV exposition of the resist (Figure 5.26c).

d) Development of the unexposed resist in AZ 326 developer for 40 s (Figure 5.26 d). Rinse by deionized water and drying by nitrogen.

e) Deposition of Ti5 nm /Au 30 nm by sputtering.

f) Lift-off in Remover PG at temperature 70°C (Figure 5.26 f), rinse by IPA and dry by nitrogen.

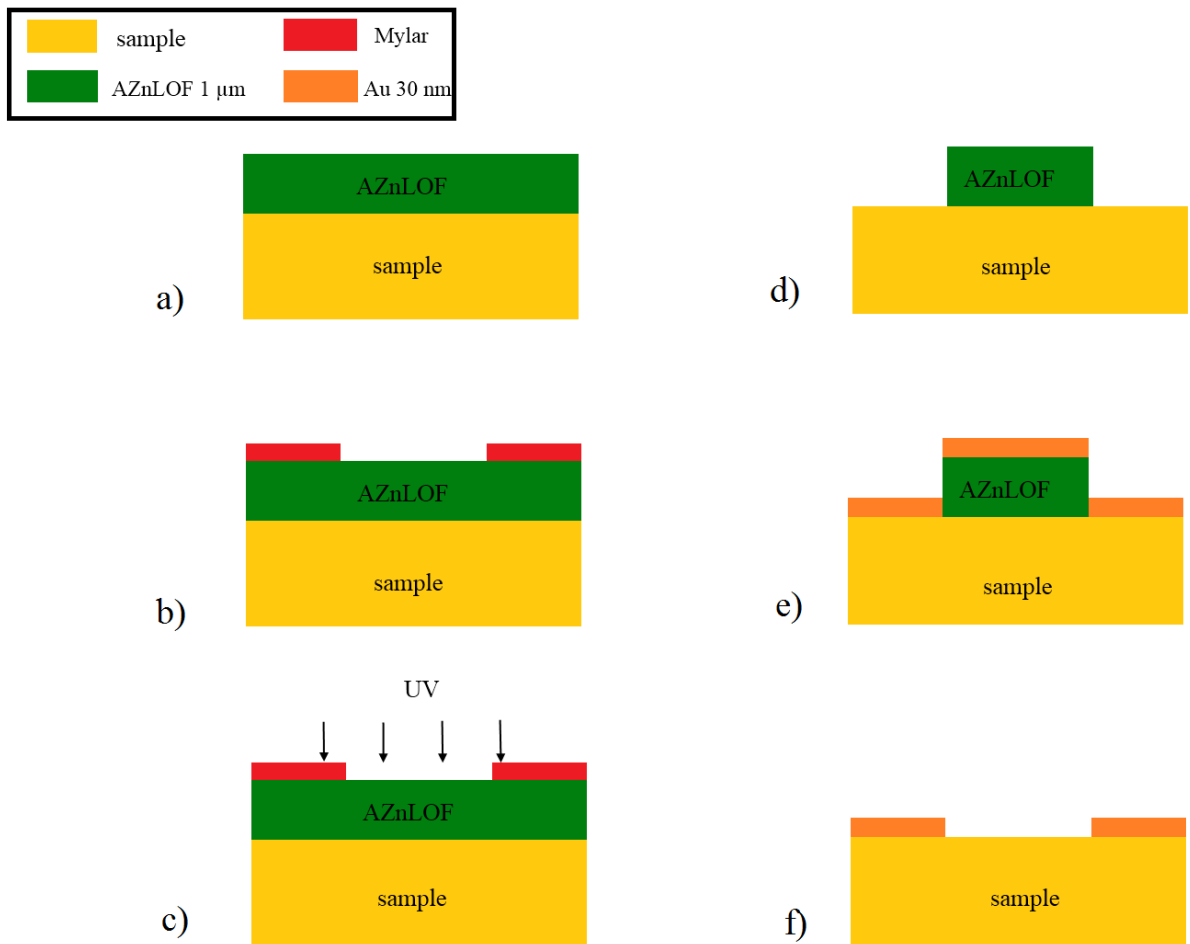


Figure 5.26. Scheme of fabrication of golden contact pad.

After all technological steps we obtained sample with devices (Figure 5.27). Then visualization of obtained structures by optical and scanning electron microscopes was done.

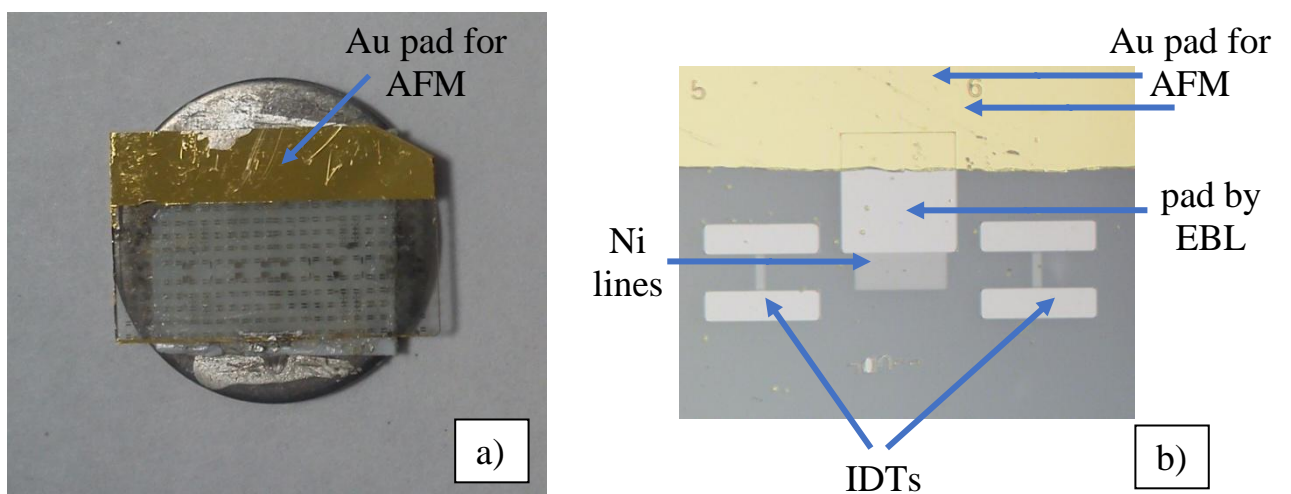


Figure 5.27. Photo of fabricated sample (a) and optical microscope image of device for AFM imaging (b).

By optical microscope visualization (Figure 5.28) we checked that technological process was done correctly: all lift-off processes were finished, there was no residual metals and resist, devices had all needed elements.

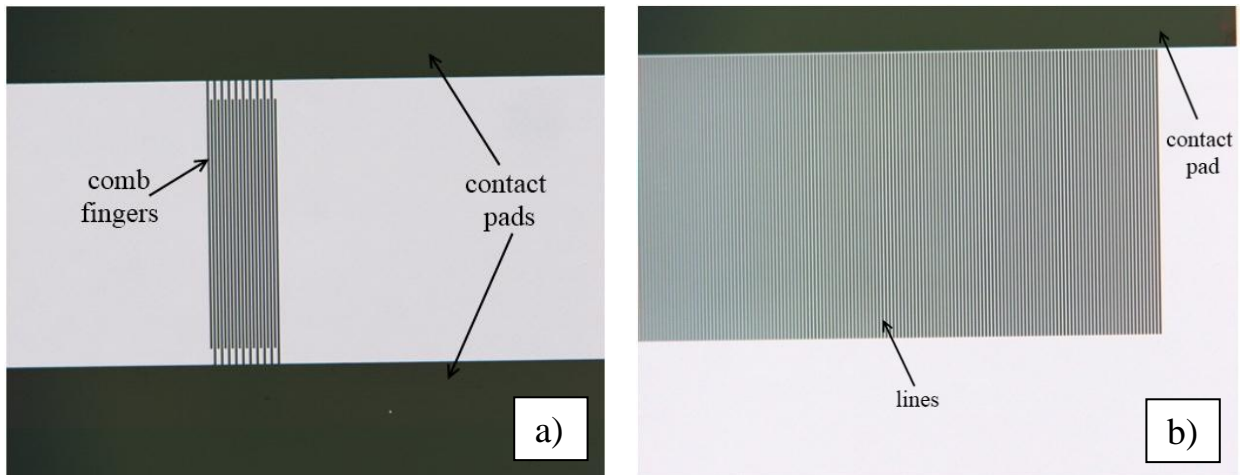


Figure 5.28. Optical microscope images of obtained devices 500 nm: IDT (a) and Ni lines (b).

More detailed images of our devices were obtained by SEM (Figure 5.29). Further measurements of actual sizes of fingers and Ni lines by SEM and AFM and investigation of devices properties were done subsequently.

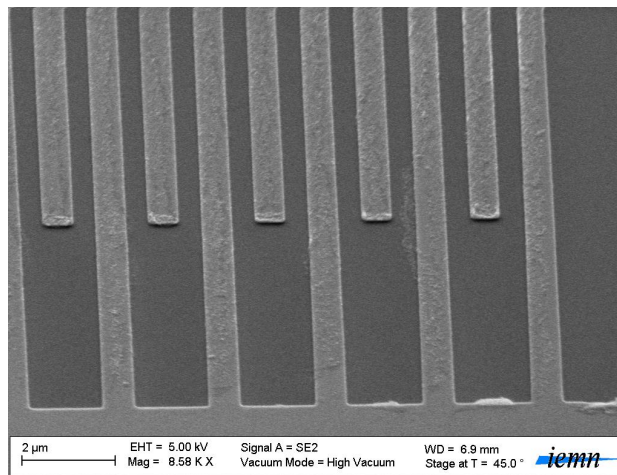


Figure 5.29. SEM image of IDT500 nm.

5.3.3 Investigation of 1D surface phononic crystals fabricated by electron-beam lithography

We measured actual sizes of fingers and Ni lines by SEM imaging (Figures 5.30, 5.31). Both comb fingers and Ni lines sizes were found to be good and suitable for chosen working frequencies.

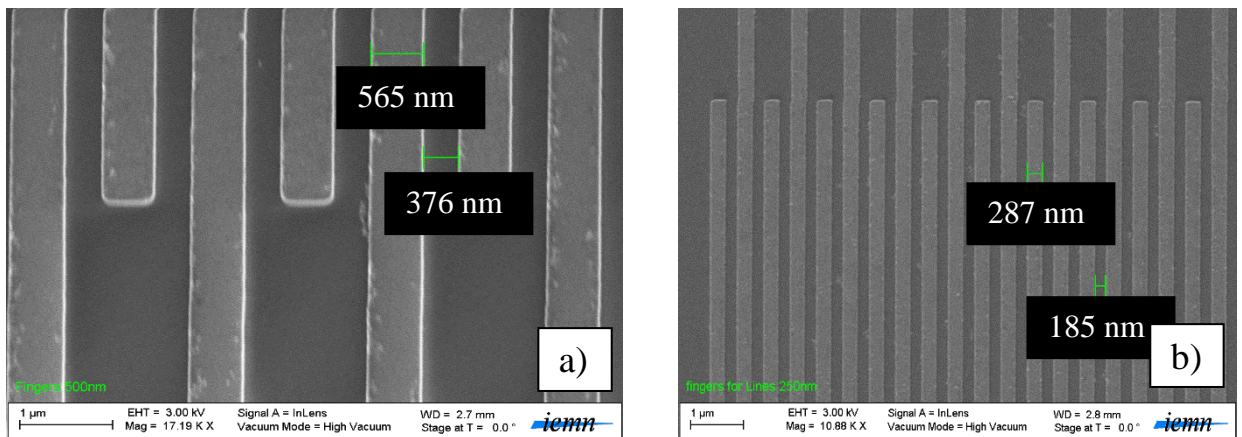


Figure 5.30. SEM images of IDTs 500 nm (a) and 250 nm (b).

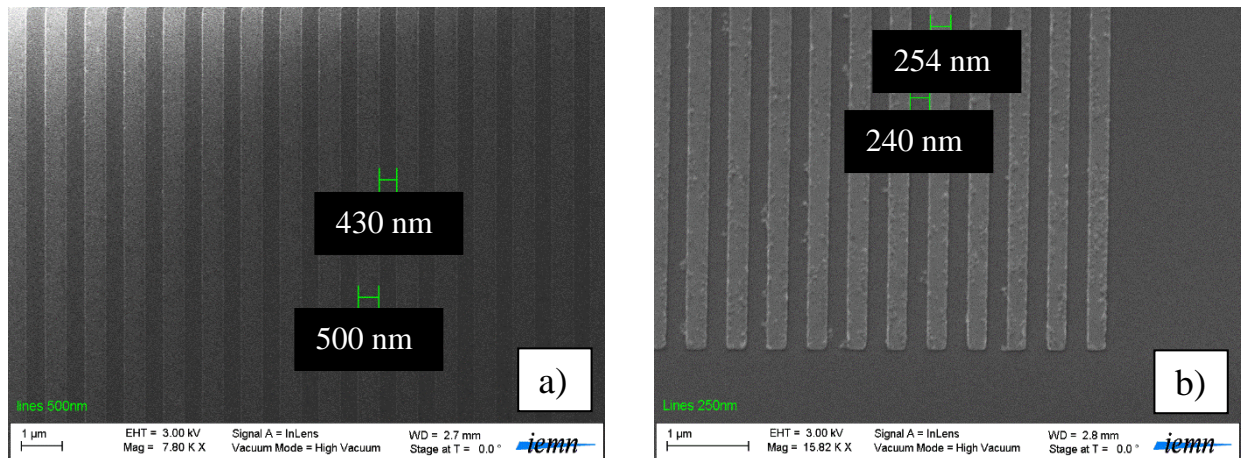


Figure 5.31. SEM images of Ni lines 500 nm (a) and 250 nm (b).

AFM imaging also showed good uniformity and smooth of obtained structures (Figure 5.32). From AFM cross-section images one can see that width and height of Ni lines are in good accordance with declared sizes.

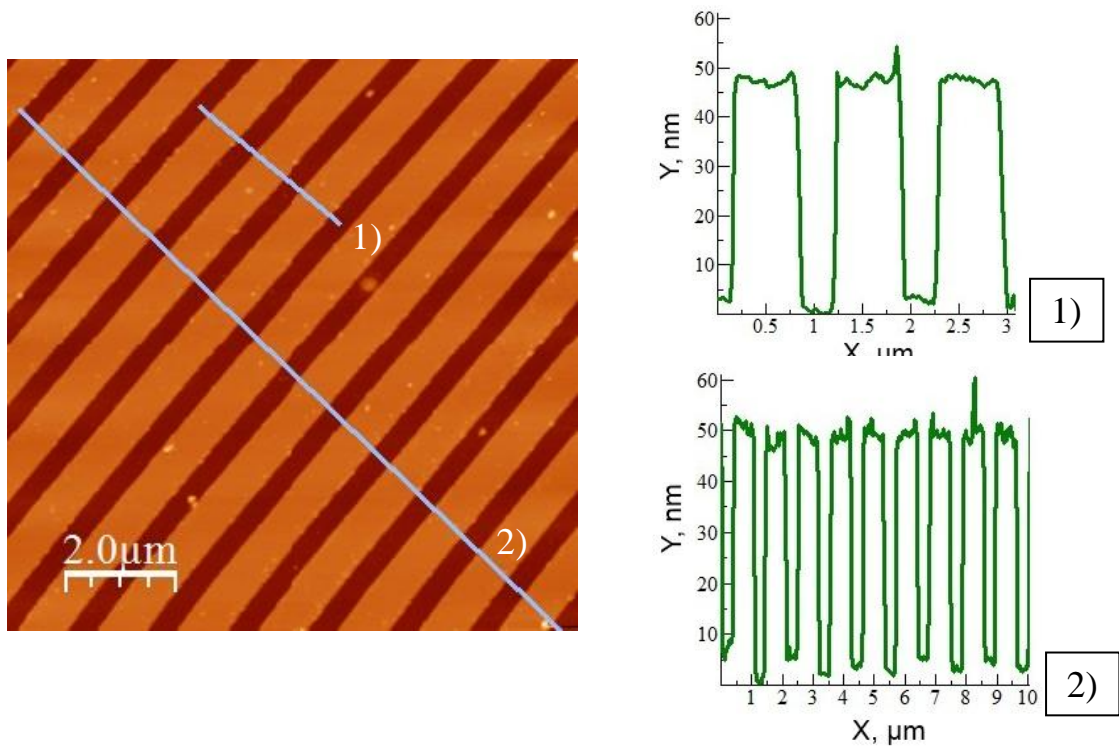


Figure 5.32. AFM image and cross-section images of Ni lines 500 nm.

Then experimental characterization of the band gap properties of the obtained PnCs was done. We used a network analyzer and probe station to excite the structure and to monitor the transmission through it (Figure 5.33). The measured transmission responses of IDTs with (solid line) and without PnCs (dashed line) are shown on Figure 5.34. For devices with arrays of 500 nm and 250 nm sized lines one can see windows of low transmission with 30 dB reduction in transmission at frequencies of 1.9 GHz and 3.5 GHz respectively. This is in excellent agreement with the theoretical predictions shown by solid line on Figure 5.35.

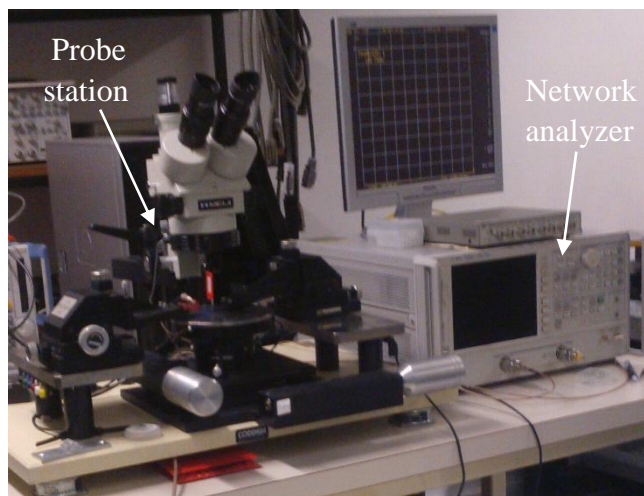


Figure 5.33. Used network analyzer and probe station.

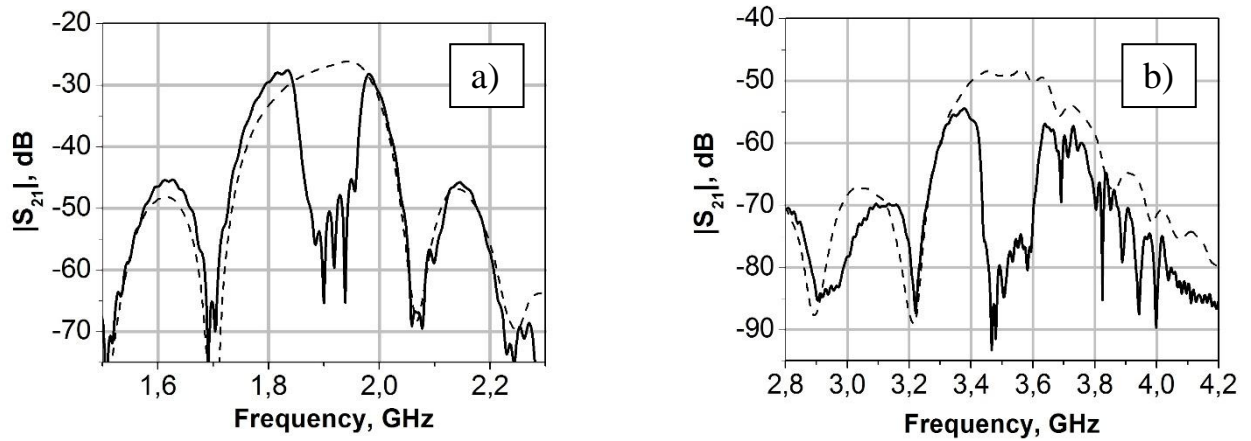


Figure 5.34. Measured transmission frequency responses of IDTs with (solid line) and without (dashed line) PnC for 2 GHz (a) and 4 GHz (b).

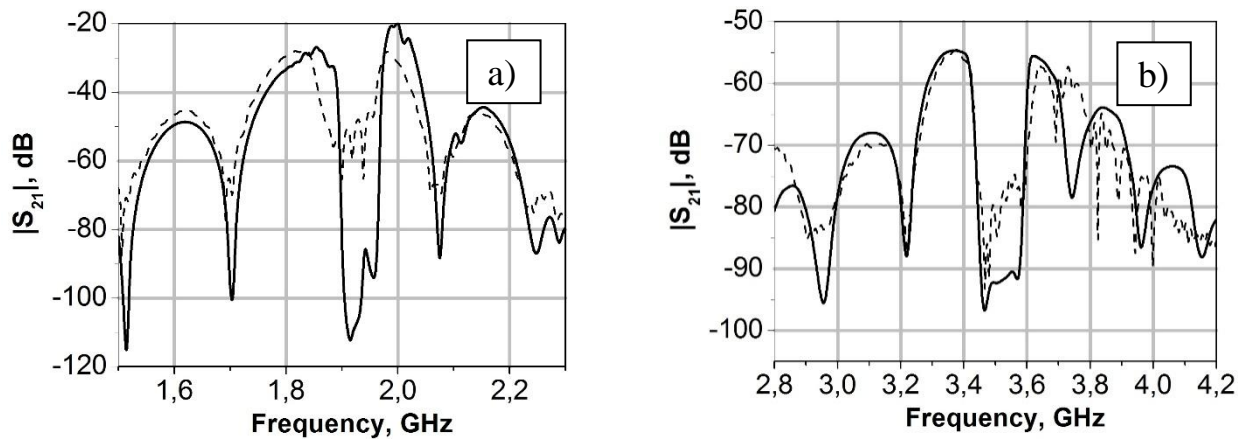


Figure 5.35. Calculated (solid line) and measured (dashed line) transmission frequency responses of IDTs with PnC for 2 GHz (a) and 4 GHz (b).

Then we experimentally confirmed magnetic properties of fabricated Ni line arrays PnCs by MFM imaging (Figure 5.36). It means that such PnCs should be sensible to applied magnetic field. The experimental investigation of magnetic field influence on transmission characteristics of developed PnCs requires designing of a new sample allowing to use magnet system in one moment with the network analyser and these study will be future prospect of this work. So the influence of applied constant magnetic field on observed characteristics was evaluated theoretically as previously for oxide line arrays PnCs made by LAO. On Figure 5.37 by dashed line calculated SAW transmission of 2 GHz PnC in magnetic field $H=300$ Oe is shown. One can see frequency shift of the band gap on 5 MHz in comparison with magnetic field $H=0$ Oe. Maximum insertion loss at the same time was reduced by 7 dB.

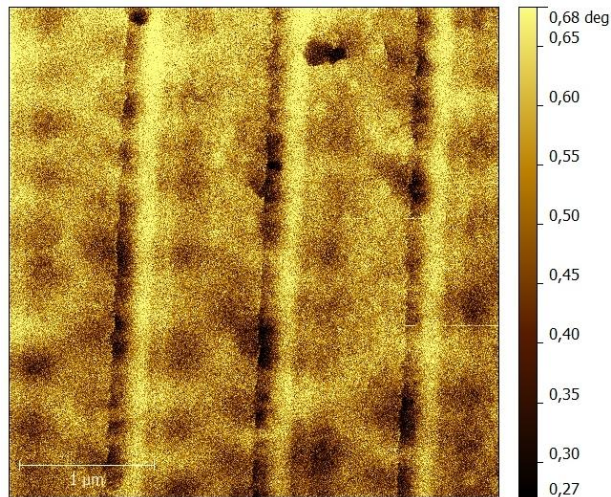


Figure 5.36.MFM image of Ni lines 500 nm.

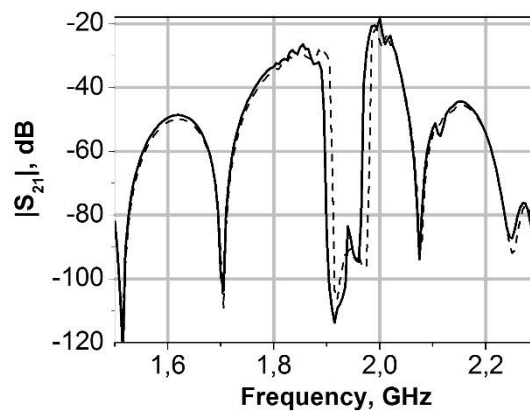


Figure 5.37.Calculated transmission frequency responses of PnC for 2 GHz (solid line) and same crystal in applied constant magnetic field $H=300$ Oe (dashed line).

5.3.4 Feasibility to fabrication of 2D surface phononic crystals

The 2D surface PnCs are gaining more and more research interest because of perspectives in designing high performance acoustoelectronic devices: resonators, pass-band and low-band filters [180-181]. That's why besides of investigation of magnetically tunable 1D PnCs made of Ni lines it was decided to study feasibility to fabrication of 2D PnC made from Ni pillars on frequencies 2GHz, 4 GHz and 6 GHz. As it was said before, frequency, bandwidth and time response of the PnC depend on design the key parameters of PnCs made of pillars are pillar

diameter(D), pillar spacing (S) and pillar height (H) (Figure 5.38).Schematic geometry of our pillars is shown on Figure and design parameters are given in Table 5.4.

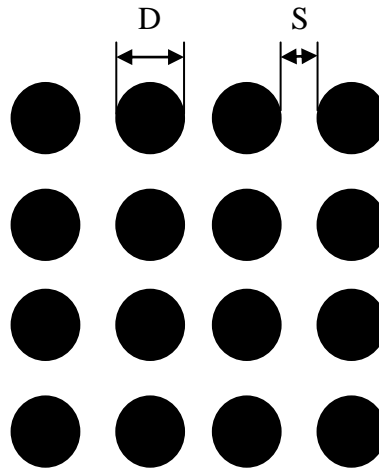


Figure5.38.Schematic geometry of pillars.

Table 5.4. Design parameters of pillars.

Substrate	Y+128° cut LiNbO ₃		
PnC material	Ni		
Metal thickness, nm	50-100		
Central frequency, GHz	2	4	6
Pillars diameter D, nm	520	320	160
Pillars spacing S, nm	130	80	40

Using program LayoutEditor we've designed patterns for lithography. On Figure 5.39 there are given layouts for pillars 160 and 320 nm as example.

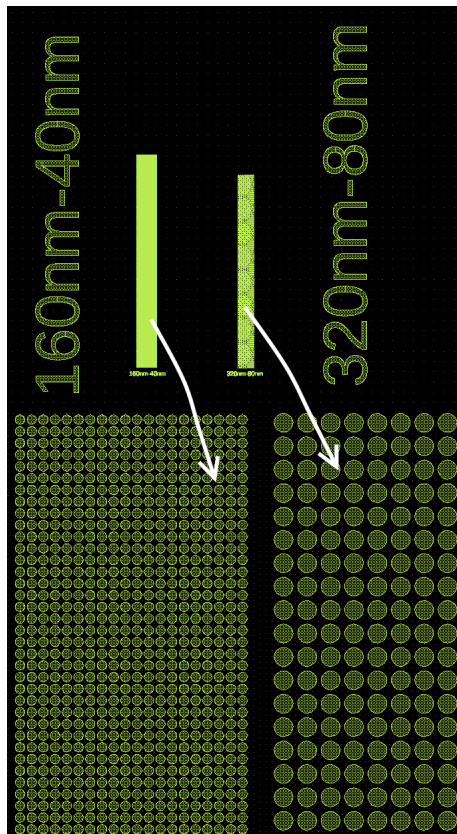


Figure 5.39. Layout of pillars 160 and 320 nm.

As previously for 1D PnCs we tried both etch-back and lift-off processes for pillars fabrication. We used EB, LO6 and LO7 processes described previously. EB and LO6 processes were found to be not suitable for 2D PnCs fabrication as previously for 1D PnCs (see Figure 5.39). In EB process because of the big thickness of the resist layer obtained resist pillars patterns were fell on the substrate (Figure 5.40 a) and in LO6 process resist adhesion problem was found (Figure 5.40 b).

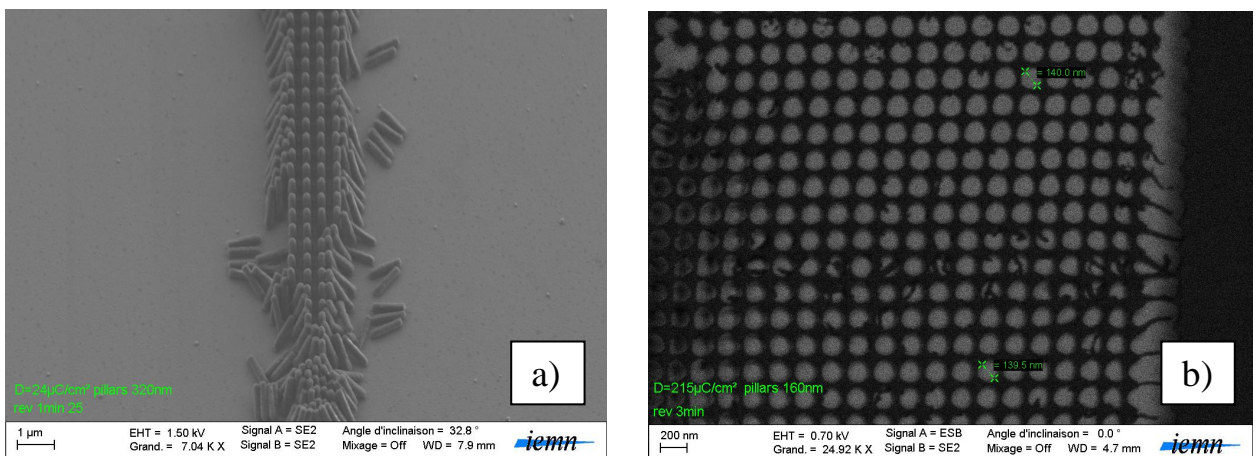
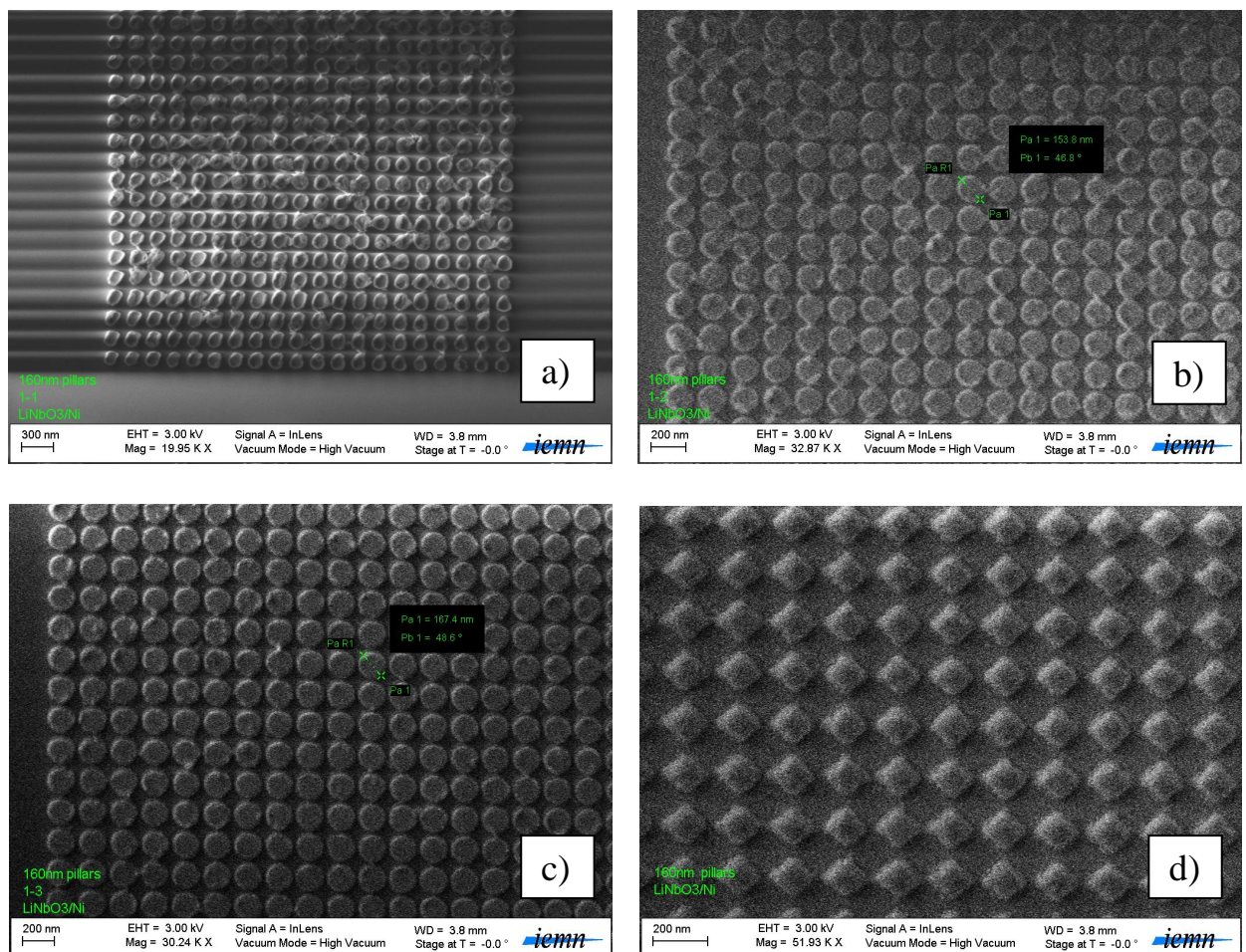


Figure 5.40. SEM images of resist patterns of pillars for EB (a) and LO6 (b) processes.

So we started LO7 process for pillars. Exposure was done with variation of dose from 250 to 560 $\mu\text{C}/\text{cm}^2$ with step of 10 $\mu\text{C}/\text{cm}^2$. For development we used time of 150 s obtained previously for 1D PnCs. Then 50 nm of Ni was deposited and the lift-off process was done. After lift-off was finished we observed obtained structures by SEM and measured its sizes. SEM images of smallest pillars 160 nm at different doses are shown on Figure 5.41. One can see that at dose 560 $\mu\text{C}/\text{cm}^2$ pillars are not well defined, have wrong shape and sizes (Figure 5.41a). At dose 550 $\mu\text{C}/\text{cm}^2$ sizes of pillars became good and shape became more round (Figure 5.41b). Pillars fabricated at dose 540 $\mu\text{C}/\text{cm}^2$ are shown on (Figure 5.41c). At this dose lift-off also was finished completely and pillars had ideal shape and sizes and smooth edges. This dose was found to be suitable for bigger pillars also. At dose 530 $\mu\text{C}/\text{cm}^2$ shape of pillars became worse (Figure 5.41d). Dose 510 $\mu\text{C}/\text{cm}^2$ was not enough to open resist after exposure and development. Some patterns were not opened at all, some of them had remains of resist in the center. During lift-off process such remaining resist was dissolved and metal on it was lifted-off. That is why great part of pillars was not obtained and all obtained pillars had holes in the center (Figure 5.41e).



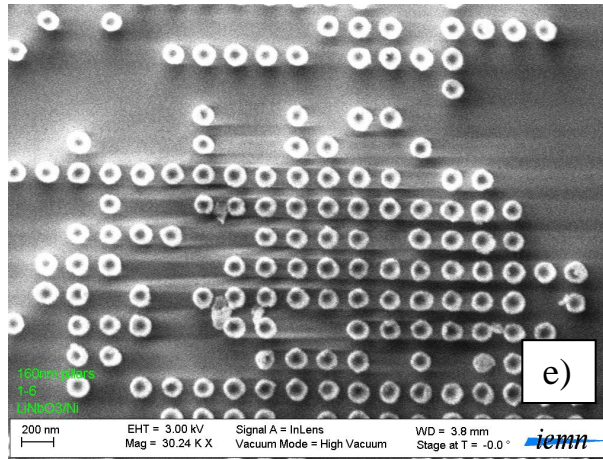


Figure 5.41. SEM images of pillars obtained by LO7 processing using different electron-beam doses: 560 (a), 550 (b), 540 (c), 530 (d) and 510 (e) $\mu\text{C}/\text{cm}^2$.

So process LO7 was found to be suitable and we started pillars fabrication process which is described previously (Figure 5.24). Exposition parameters are the same for all pillars sizes and are given in Table 5.5. We deposited 50 nm of Ni to obtain resulting structures.

Table 5.5. Exposition parameters for pillars fabrication.

Parameters of e-beam			
Electron energy, keV	Resolution, nm	Current, pA	Dose, $\mu\text{C}/\text{cm}^2$
100	5	300	540

After fabrication SEM and AFM imaging were done. On SEM images (Figure 5.42) one can see that pillars of all sizes are well defined, have good sizes and smooth edges. Just some unremoved fractions of the resist can be observed on the pillars edges. AFM imaging also showed good uniformity and smooth of obtained structures (Figures 5.43-5.44). AFM tip diameter is greater than gap between neighbor pillars so we've made scan of the edge of 520 nm pillars array to check pillars height (Figure 5.43). From AFM cross-section image it can be seen that pillars height is about 50-60 nm. On Figure 5.44 detailed AFM and AFM cross-section images of pillars 520 nm are given. One can see that pillars have a good quality and their sizes are in good accordance with declared sizes. Further theoretical and experimental investigation of such 2D PnC structures is expected.

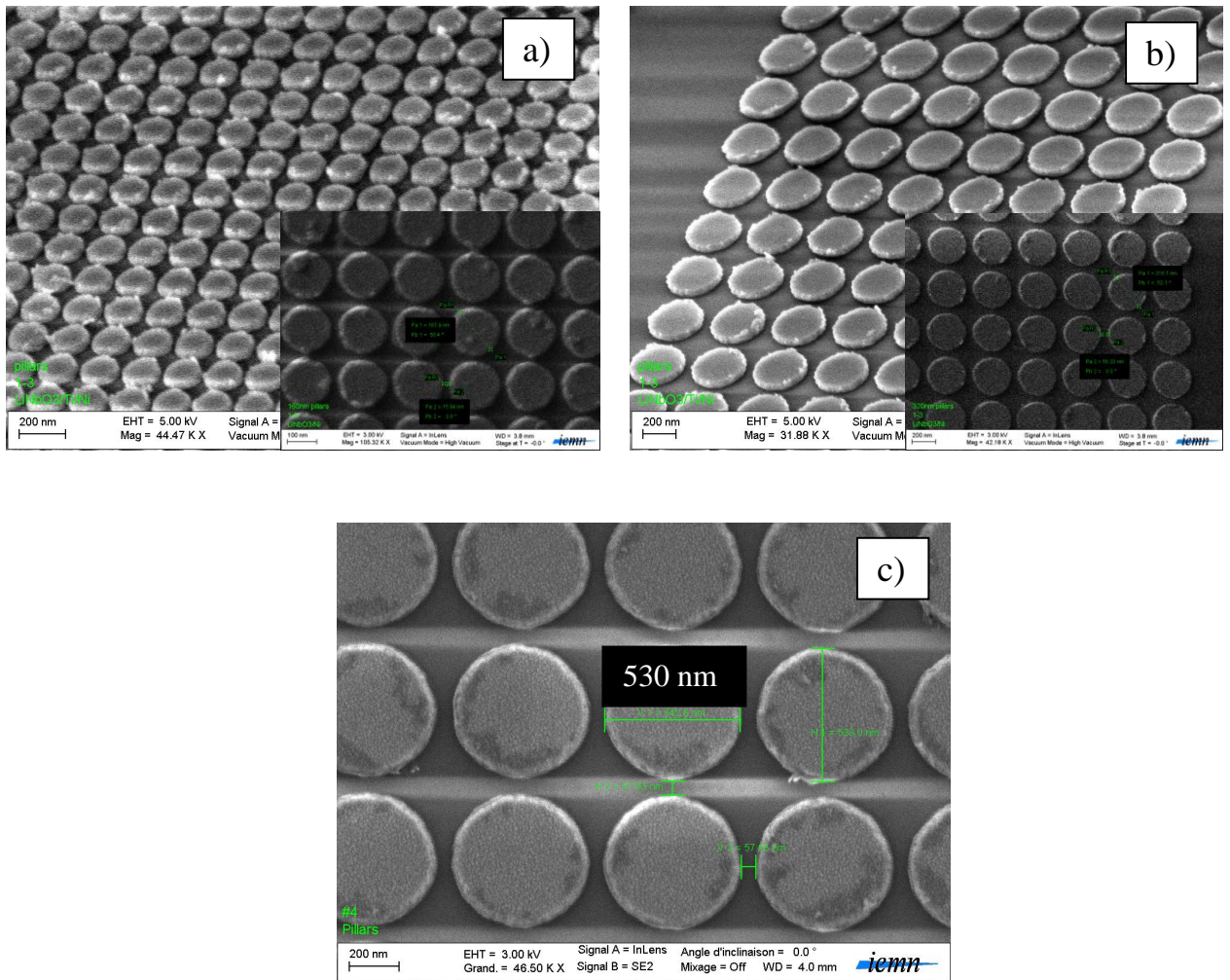


Figure 5.42. SEM images of fabricated pillars 160 nm (a), 320 nm (b), 520 nm (c).

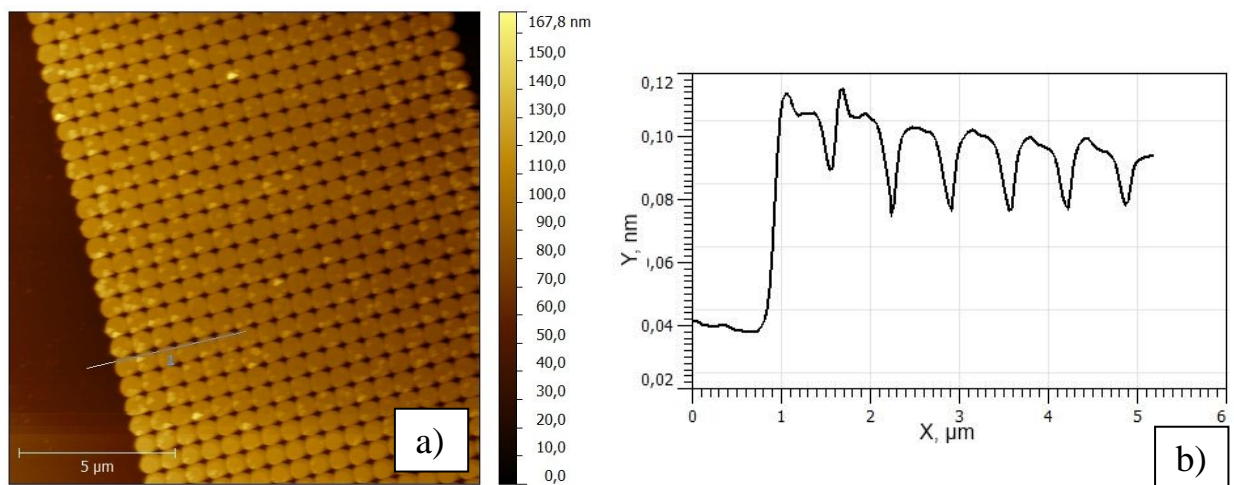


Figure 5.43. AFM (a) and cross-section (b) images of pillars 520 nm array.

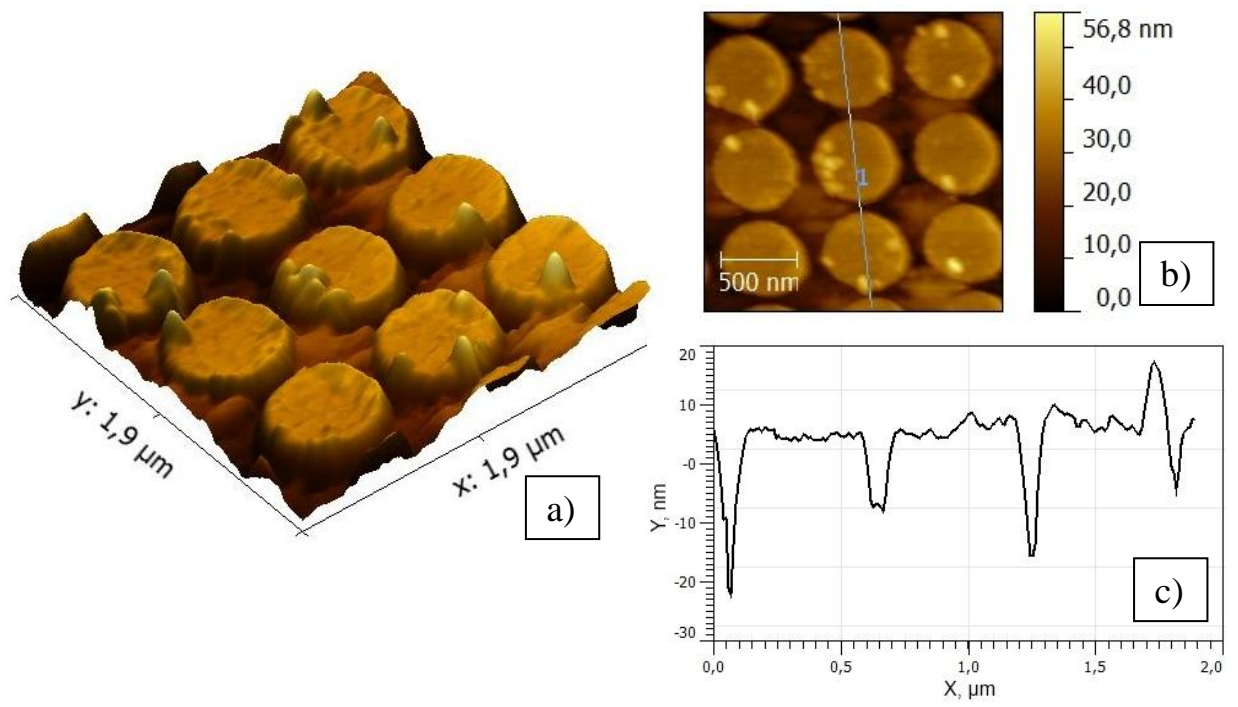


Figure 5.44. Detailed 3D AFM (a), 2D AFM (b) and cross-section (c) images of pillars 520 nm array.

5.4 Conclusions

In this chapter fabrication of high frequency magnetically tunable PnCs using two lithographic techniques – EBL and SPL – was investigated. Both techniques are used to produce nanostructures with high resolution. We proposed to use both these methods for high frequency PnCs structures fabrication. But both EBL and SPL have advantages and drawbacks.

It was not known before that periodic oxide structures obtained by SPL LAO could serve as PnCs. At the same time this technique seems to be one of the promising methods of PnCs fabrication because of simplicity and cheapness of technological process unlike EBL. LAO can produce another material from initial substrate and to make arrays of different materials with different elastic properties without additional procedures like etching. We've investigated experimentally the possibility to obtain periodic oxide structures and theoretically their possibility for a SAW bandgap formation. Also it was shown that formation of oxide structures arrays on ferromagnetic films allows tuning of a bandgap by applied magnetic field. Finally, the whole technological process for practical realization of 1D PnCs made of oxide lines by scanning probe on 2 and 4 GHz was developed. The main obstacle in practical realization of PnCs by LAO was the lack of multiprobe system needed for fabrication of big amount of structures on big area what is impossible to do by single probe. Further investigation on 2D PnCs fabrication and practical realization of studied structures is expected. Feasibility of PnCs fabrication using scanning probe mechanical scratching will be also studied.

EBL is a well known and studied technique for PnCs fabrication [200-202]. We've decided to use it for magnetically tunable PnCs realization. Fabrication process for 1D and 2D PnCs made of Ni on 2 and 4 GHz using EBL was developed. Obtained 1D PnCs were studied experimentally and bandgap formation in the spectrum of SAW was found. A bandgap shift under magnetic field application was investigated theoretically. Further fabrication of sample for experimental study of magnetic field influence on the structures will be done. Further theoretical and experimental investigation of developed 2D PnCs structures is expected. All developed periodic ferromagnetic structures made both by LAO and EBL can be subsequently used for contactless control of SAW filters.

Conclusions and future prospects

The goal of this work was to investigate experimentally fabrication of submicron structures on ferromagnetic films using two different lithographic techniques: scanning probe lithography and electron-beam lithography for potential applications in spintronics and magnetically tunable SAW devices. Similarly, the aim of this work was to make first steps in magnetically sensitive phononic crystals fabrication.

Both scanning probe lithography and electron-beam lithography technologies have their own advantages and drawbacks. We've made detailed investigation of local anodic oxidation by scanning probe for different ferromagnetic films. We also developed phononic crystals fabrication processes using both technological methods.

Main results of the work are:

1. Dependences of sizes of nanostructures fabricated on ferromagnetic metal films by LAO on variety of process parameters – tip-sample voltage, oxidation time, humidity, tip properties, film texture – were obtained. It was defined that LAO of different materials starts at different tip-sample voltages ($V_{tr}^{Ni} = V_{tr}^{FeCo} = -4V$ and $V_{tr}^{Fe} = V_{tr}^{Co} = -6V$) and oxide lines sizes increase with the voltage increase. The same way oxide lines sizes increase with the increase of oxidation time and humidity. It was also obtained that film texture have a great influence on threshold oxidation parameters and oxide lines sizes. Oxide structures with bigger sizes at decreased oxidation parameters can be fabricated by LAO on Ni(200) and Fe(200) films. As result of this investigation LAO parameters for fabrication of structures with certain sizes were obtained.
2. The possibility to produce nanostructures with different from initial material chemical, electrical and magnetic properties by SPL oxidation and mechanical scratching was shown. By Auger spectroscopy it was shown that formation of Ni oxide during LAO process on Ni film can be assumed. It was also obtained that nanostructures made by LAO

have properties of tunnel barriers: current-voltage characteristics of such structures have a non-metallic behavior and become non-linear at low temperatures. Barrier heights of 0.037 eV and 0.1 eV for structures on Ni and FeCo films respectively were defined. Similarly, it was shown that SPL mechanical scratching can be used for fabrication of magnetoresistive nanostructures. Magnetoresistance of Ni microstrips with such structures is inverted and higher than for initial microstrips.

3. The possibility to obtain by LAO periodic arrays of structures with different elastic properties was shown experimentally. Feasibility to use such arrays as hypersonic PnCs was confirmed theoretically. The technological process for practical realization of PnCs made of oxide lines by scanning probe oxidation was developed.
4. Fabrication process for 1D and 2D Ni PnCs for 2-6 GHz frequencies using EBL was developed. Properties of obtained 1D 2 GHz and 4 GHz PnCs were studied experimentally and bandgap formation in the spectrum of SAW at 1.9 GHz and 3.5 GHz respectively was found. Experimental results of transmission characteristics measurements are in good agreement with results of numerical simulations.
5. Applied constant magnetic field influence on transmission characteristics of PnCs made both by LAO and EBL was evaluated theoretically. A bandgap shift up to 50 MHz under magnetic field application was confirmed.

Results of this work will be used for further development of magnetoresistive structures and magnetically tunable phononic crystals. Practical realization of phononic crystals using probe oxidation is expected. Obtained results on theoretical analysis of magnetic field influence on phononic crystals made by local anodic oxidation and electron-beam lithography will be verified experimentally. Simultaneously, theoretical and experimental investigation of feasibility to fabricate phononic crystals using another scanning probe method – mechanical scratching – is expected.

Résumé étendu en Français

Aujourd'hui, structures fondées sur matériaux ferromagnétiques est utilisés très activement pour différentes applications: mémoire magneto-résistif à accès non séquentiel, capteurs magnétiques ou même de nouveaux composants électroniques – les dispositifs spintronique. Les dispositifs spintronique est basées sur le transfert de spins des électrons. Aussi la tendance principale de l'électronique moderne est une réduction d'éléments dimensions à l'échelle submicronique. Ainsi les nanostructures magnétiques est d'un grand intérêt et leurs méthodes de fabrication et propriétés sont étudiées activement.

Structures submicrométrique périodique peuvent être utilisées comme cristaux phononiques (PnC) de haute fréquence pour les ondes acoustiques de surface (SAW). Il ya les études de variation des paramètres acoustiques des PnC magnétoélastiques par le champ magnétique (ΔE -effet). Le bande interdite du cristal phononique peut être déplacé par le champ magnétique. Ceci peut être utilisé pour la commutation de bande passante sans fil et sans contact dans des filtres et des capteurs à SAW.

Ainsi le **but principal de ce travail** est la préparation et la recherche expérimentale et théorique des propriétés des nanostructures magnétiques pour des applications en composants magneto-résistif et phononique. Lithographie à sonde locale (SPL) et lithographie par faisceau d'électrons (EBL) ont été utilisées pour fabrication des nanostructures. De même, le but de travail était de faire les premiers pas dans le fabrication des cristaux phononiques sensible pour le champ magnétique.

Pour cela les **objectifs** suivants ont été fixes:

1. Investigation des SPL oxydation anodique locale (LAO) et development des nanostructures sur des films métalliques ferromagnétiques.
2. Recherche expérimentale des propriétés des nanostructures fabriquées par méthode SPL.

3. Investigation expérimentale de la possibilité d'obtenir par LAO des structures périodique avec différentes propriétés élastiques.
4. Investigation théorique de la faisabilité d'utiliser ces structures comme PnC hypersoniques.
5. Développement des procédés de fabrication des PnC par les deux méthodes technologiques: SPL LAO et EBL.
6. Simulations numériques d'influence de champ magnétique sur les caractéristiques de transmission de PnC fabriqué par SPL LAO et EBL.

Le manuscrit de thèse comporte cinq chapitres encadrés par une introduction et une conclusion générale. **Le premier chapitre** décrit les procédés lithographiques utilisés (SPL et EBL). Dans **le deuxième chapitre** l'étude détaillée de SPL LAO de différents films métalliques ferromagnétiques est donnée. Point clé de cette étude est une investigation de l'influence des différents paramètres sur la taille des structures fabriquées par LAO. L'influence d'oxydation de la sonde a été étudié pour la première fois. **Le troisième chapitre** se concentre sur l'oxydation à sonde locale de films métalliques ferromagnétiques des différentes textures. L'influence de texture sur LAO n'a pas été étudié précédemment et les résultats de cette étude peuvent être utilisés pour l'optimisation de la fabrication de nanostructures. **Le quatrième chapitre** comporte l'étude des propriétés électriques et chimiques des structures submicronique fabriquées par SPL méthodes: LAO et SPL mécanique méthode. Les résultats ont montré que les propriétés des structures obtenues diffèrent des propriétés du matériau de départ. Il a été conclu que ces techniques peuvent être utilisé pour la fabrication de nanostructures pour une application dans les différents dispositifs. Structures simples peuvent être utilisés comme structures tunnel et magneto-résistif pour la réalisation de dispositifs spintronique. Le rang de ceux structures peuvent être utilisés comme PnC hypersoniques. Dans **le cinquième** et dernier **chapitre** une description détaillée des procédés technologiques pour la fabrication de structures phononiques par SPL et EBL est présenté ainsi que les résultats sur la recherche théorique et expérimentale de ces structures. Il sont donnés les résultats des simulations numériques de l'influence du champ magnétique sur ces structures. Des recommandations pour le développement de structures sont également donnés.

De contenu de la thèse des **principaux points présentés à la défense** peuvent être extraits:

1. Résultats expérimentaux de l'investigation de LAO sur Ni, Fe, Co et FeCo films. Ces résultats peuvent être utilisés pour la détermination des paramètres de LAO et les instruments

nécessaires pour obtenir des nanostructures avec certaines tailles par cette méthode lithographique.

2. Résultats expérimentaux l'investigation de LAO sur Ni (200), Ni (111), Fe (200) et Fe (110) films. Ces résultats peuvent être utilisés pour contrôler le processus LAO.

3. Technologie de fabrication de 1D PnC hypersonique contrôles par champ magnétique sur Ni par LAO méthode. Cette technologie peut être utilisée pour le développement des structures phononiques pour une application dans des capteurs magnétiques et des filtres à SAW sans fil.

4. Processus de fabrication approprié pour la réalisation des 1D et 2D PnC contrôles par champ magnétique sur Ni pour 2-6 GHz par EBL méthode. Ce processus de fabrication permet d'obtenir facilement de bonnes structures phononiques avec différentes configurations.

Résultats de ce travail seront utilisés pour le développement de structures magnéto-résistif et cristaux phononiques contrôles par champ magnétique. La réalisation pratique de cristaux phononiques fabriqué par LAO est prévu. Les résultats de l'analyse théorique de l'influence du champ magnétique sur les cristaux phononiques fabriqué par LAO et EBL seront vérifiées expérimentalement. Recherche théorique et expérimentale de la faisabilité de fabrication des cristaux phononiques par SPL mécanique méthode est attendue.

References

- [1] J.L. Simonds, "Magneto-electronics today and tomorrow", *Physics Today*, vol. 48, no. 4, pp. 26-32, 1995.
- [2] M. Yamaguchi, K.Y. Hashimoto, H. Kogo and M. Naoe, "Variable saw delay line using amorphous TbFe₂ film", *Transactions on magnetics*, vol. 16, no. 5, pp. 916-918, 1980.
- [3] M. Weiler, L. Dreher, C. Heeg, H. Huebl, R. Gross, M.S. Brandt and S.T.B. Goennenwein, "Elastically driven ferromagnetic resonance in nickel thin films", *Physical review letters*, vol. 106, pp. 117601, 2011.
- [4] O. Bou Matar, J. F. Robillard, J. O. Vasseur, A.-C. Hladky-Hennion, P. A. Deymier, P. Pernod and V. Preobrazhensky, "Band gap tunability of magneto-elastic phononic crystal", *Journal of Applied Physics*, vol. 111, pp. 054901, 2012.
- [5] I. Lisenkov, A. Klimov, V. Onoprienko, V. Preobrajenski, P. Pernod and S. Nikitov, "Surface acoustic waves control with external magnetic field in TbCo₂/FeCo films" in *International Ultrasonics Symposium IUS'2013*, Prague, Czech Republic, 21-25 July 2013, paper IUS3-C-1.
- [6] H. Zhou, A. Talbi, N. Tiercelin and O. Bou Matar, "Theoretical and experimental study of multilayer piezo-magnetic structure based surface acoustic wave devices for high sensitivity magnetic sensor" in *International Ultrasonics Symposium IUS'2013*, Prague, Czech Republic, 21-25 July 2013, pp. 2130-2132.
- [7] M. Geissler and Y. Xia, "Patterning: principles and some new developments", *Advanced Materials*, vol. 15, pp. 1249-1269, 2004.
- [8] X.N. Xie, H.J. Chung, C.H. Sow and A.T.S. Wee, "Nanoscale materials patterning and engineering by atomic force microscopy nanolithography", *Materials Science and Engineering*, vol. 54, pp. 1-48, 2006.
- [9] N. Yao and Z.L. Wang, *Handbook of microscopy for nanotechnology*. Kluwer Academic Publishers, 2005.

- [10] Q. Tang, S.-Q. Shi and L. Zhou, "Nanofabrication with atomic force microscopy", *J. Nanosci. Nanotech*, vol. 4, no. 8, pp. 948-963, 2004.
- [11] B. Cappella, H. Sturm and S.M. Weidner, "Breaking polymer chains by dynamic plowing lithography", *Polymer*, vol. 43, no. 16, pp. 4461-4466, 2002.
- [12] B. Klehn and U. Kunze, "Nanolithography with an atomic force microscope by means of vector-scan controlled dynamic plowing", *Journal of Applied Physics*, vol. 85, pp. 3897 – 3903, 1999.
- [13] T.-H. Fang, W.-J. Chang and C.-I. Weng, "Nanoindentation and nanomachining characteristics of gold and platinum thin films", *Materials Science and Engineering A*, vol. 430, pp. 332–340, 2006.
- [14] H.D.F. Filho, M.H.P. Mauricio, C.R. Ponciano and R. Prioli, "Metal layer mask patterning by force microscopy lithography", *Mater. Sci. Eng. B*, vol. 112, pp. 194-199, 2004.
- [15] X. Li, P. Nardi, C.-W. Baek, J.-M. Kim and Y.-K. Kim, "Direct nanomechanical machining of gold nanowires using a nanoindenter and an atomic force microscope", *J. Micromech. Microeng*, vol. 15, pp. 551-556, 2005.
- [16] J.C. Rosa, M. Wendel, H. Lorenz, J.P. Kotthaus, M. Thomas and H. Kroemer, "Direct patterning of surface quantum wells with an atomic force microscope", *Appl. Phys. Lett.*, vol. 73, pp. 2684 – 2686, 1998.
- [17] C.K. Hyon, S.C. Choi, S.W. Hwang, D. Ahn, Y. Kim and E.K. Kim, "Direct nanometer-scale patterning by the cantilever oscillation of an atomic force microscope", *Appl. Phys. Lett.*, vol. 75, pp. 292-294, 1999.
- [18] A.A. Tseng, J. Shirakashi, S. Jou, J.-C. Huang and T.P. Chen, "Scratch properties of nickel thin films using atomic force microscopy", *Journal of Vacuum Science & Technology B*, vol. 28, pp. 202-210, 2010.
- [19] K. Miyashita, S. Nishimura, T. Toyofuku and J. Shirakashia, "Nanoscale patterning of NiFe surface by scanning probe microscopy scratch nanolithography", *Journal of Vacuum Science & Technology B*, vol. 27, pp. 953-957, 2009.
- [20] S. Pyo, Y. Oh and M. Yi, "Organic thin-film transistors with submicrometer channel length fabricated by atomic force microscopy lithography", *Chemical Physics Letters*, vol. 419, pp. 115–119, 2006.
- [21] L. Li, M. Hirtz, W. Wang, C. Du, H. Fuchs and L. Chi, "Patterning of polymer electrodes by nanoscratching", *Adv. Mater.*, vol. 22, pp. 1374–1378, 2010.

- [22] C.H. Choi, D. J. Lee, J.-H. Sung, M. W. Lee, S.-G. Lee, S.-G. Park, E.-H. Lee and B.-H. O, “A study of AFM-based scratch process on polycarbonate surface and grating application”, *Applied Surface Science*, vol. 256, pp. 7668–7671, 2010.
- [23] L.T. Hansen, A. Kuhle, A.H. Sorensen, J. Bohr and P.E. Lindelof, “A technique for positioning nanoparticles using an atomic force microscope”, *Nanotechnology*, vol. 9, pp. 337–342, 1998.
- [24] A.J. Heinrich, C.P. Lutz, J.A. Gupta and D.M. Eigler, “Molecule cascades”, *Science*, vol. 298, pp. 1381–1387, 2002.
- [25] J. Hu, Y. Zhang, H. Gao, M. Li and U. Hartmann, “Artificial DNA Patterns by mechanical nanomanipulation”, *Nano Lett.*, vol. 2, no 1, pp. 55-57, 2002.
- [26] L. Roschier, J. Penttila, M. Martin, P. Hakonen, M. Paalanen, U. Tapper, E.I. Kauppinen, C. Journet and P. Bernier, “Artificial DNA patterns by mechanical nanomanipulation”, *Appl. Phys. Lett.*, vol. 75, pp. 728-730, 1999.
- [27] T. Junno, K. Deppert, L. Montelius and L. Samuelson, “Controlled manipulation of nanoparticles with an atomic force microscope”, *Appl. Phys. Lett.*, vol. 66, pp. 3627–3629, 1995.
- [28] C. A. Mirkin, “Programming the assembly of two- and three-dimensional architectures with DNA and nanoscale inorganic building blocks”, *Inorg. Chem.*, vol. 39, pp. 2258–2272, 2000.
- [29] M. Su and V.P. Dravid, “Colored ink dip-pen nanolithography”, *Appl. Phys. Lett.*, vol. 80, pp. 4434–4436, 2002.
- [30] L.M. Demers, D.S. Ginger, S.-J. Park, Z. Li, S.-W. Chung and C.A. Mirkin, “Direct patterning of modified oligonucleotides on metals and insulators by dip-pen nanolithography”, *Science*, vol. 296, no. 5574, pp. 1836-1838, 2002.
- [31] J.C. Garno, Y. Yang, N.A. Amro, S. Cruchon-Dupeyrat, S. Chen and G.Y. Liu, “Precise positioning of nanoparticles on surfaces using scanning probe lithography”, *Nano Lett.*, vol. 3, no. 3, pp. 389–395, 2003.
- [32] L. Fu, X. Liu and Y. Zhang, “Nanopatterning of “hard” magnetic nanostructures via dip-pen nanolithography and a sol-based ink”, *Nano Lett.*, vol. 3, pp. 757-760, 2003.
- [33] X. Liu, L. Fu, S. Hong, V.P. Dravid and C.A. Mirkin, “Arrays of magnetic nanoparticles patterned via “dip-pen” nanolithography”, *Adv. Mater.*, vol. 14, no. 3, pp. 231-234, 2002.
- [34] G. Gundiah, N.S. John, P.J. Thomas, G.U. Kulkarni, C.N.R. Rao and S. Heun, “Dip-pen nanolithography with magnetic Fe₂O₃ nanocrystals”, *Appl. Phys. Lett.*, vol. 84, pp. 5341-5343, 2004.

- [35] H. J. Mamin and D. Rugar, “Thermomechanical writing with an atomic force microscope tip“, *Appl. Phys. Lett.*, vol. 61, pp. 1003–1005, 1992.
- [36] B.D. Terris, S.A. Rishton, H.J. Mamin, R.P. Ried and D. Rugar, “Atomic force microscope-based data storage: track servo and wear study”, *Appl. Phys.*, vol. 66, pp. S809 – S813, 1998.
- [37] H.J. Mamin, B.D. Terris, L.-S. Fan, S. Hoen, R.C. Barrett and D. Rugar, “High-density data storage using proximal probe techniques”, *IBM J. Res. Dev.*, vol. 39, no. 6, pp. 681–700, 1995.
- [38] W.P. King, T.W. Kenny, K.E. Goodson, G. Cross, M. Despont, U. Durig, H. Rothuizen, G.K. Binnig and P. Vettiger, “Atomic force microscope cantilevers for combined thermomechanical data writing and reading”, *Appl. Phys. Lett.*, vol. 78, pp. 1300-1302, 2001.
- [39] P. Vettiger, M. Despont, U. Drechsler, U. Durig, W. Haberle, M.I. Lutwyche, H. Rothuizen, R. Stutz, R. Widmer and G.K. Binnig, “The “Millipede” – more than thousand tips for future AFM storage”, *IBM J. Res. Dev.*, vol. 44, no. 3, pp. 323–340, 2000.
- [40] H.J. Mamin, P.H. Guethner and D. Rugar, “Atomic emission from a gold scanning-tunneling-microscope tip”, *Phys. Rev. Lett.*, vol. 65, no. 19, pp. 2418–2421, 1990.
- [41] H. Andoh and M. Takai, “Nanofabrication with a metal-covered scanning tunneling microscope tip“, *Physica B*, vol. 227, pp. 276-278, 1996.
- [42] M. Shirai, K. Hiruma and T. Katsuyama, “Gold cluster formation using an atomic force microscope and its applications to GaAs whisker growth”, *Superlattices and Microstructures*, vol. 24, no. 2, pp. 157-162, 1998.
- [43] J.Y. Park, R.J. Phaneuf and E.D. Williams, “Variation of threshold field in field induced fabrication of Au nanodots on ultrathin in situ grown silicon oxide”, *Surface Science*, vol. 470, pp. L69-L74, 2000.
- [44] W.-K. Lee, S. Chen, A. Chilkoti and S. Zauscher, “Fabrication of gold nanowires by electric-field-induced scanning probe lithography and in situ chemical development”, *Small*, vol. 3, no. 2, pp. 249–254, 2007.
- [45] D.M. Kolb, R. Ullmann and T. Will, “Nanofabrication of small copper clusters on gold(111) electrodes by a scanning tunneling microscope”, *Science*, vol. 275, pp. 1097–1099, 1997.
- [46] D.H. Huang, T. Nakayama and M. Aono, “Platinum nanodot formation by atomic point contact with a scanning tunneling microscope platinum tip“, *Appl. Phys. Lett.*, vol. 73, pp. 3360–3362, 1998.

- [47] E.E. Ehrichs, R.M. Silver and A. L. de Lozanne, "Direct writing with the scanning tunneling microscope", *J. Vac. Sci. Tech. A*, vol. 6, pp. 540-543, 1988.
- [48] M.A. McCord, D.P. Kern and T.H.P. Chang, "Direct deposition of 10-nm metallic features with the scanning tunneling microscope", *J. Vac. Sci. B*, vol. 6, pp. 1877-1880, 1988.
- [49] A.D. Kent, T.M. Shaw, S. von Molnar and D.D. Awschalom, "Growth of high aspect ratio nanometer-scale magnets with chemical vapor deposition and scanning tunneling microscopy", *Science*, vol. 262, pp. 1249-1252, 1993.
- [50] F. Marchi, D. Tonneau, H. Dallaporta, R. Pierrisnard, V. Bouchiat, V.I. Safarov, P. Doppelt and R. Even, "Nanometer scale patterning by scanning tunnelling microscopeassisted chemical vapour deposition", *Microelectronic Engineering*, vol. 50, pp. 59 –65, 2000.
- [51] M.A. McCord and R.F.W. Pease, "Exposure of calcium fluoride resist with the scanning tunneling microscope", *J. Vac. Sci. Technol. B*, vol. 5, pp. 430-433, 1987.
- [52] M.A. McCord and R.F.W. Pease, "Lift-off metallization using poly(methyl methacrylate) exposed with a scanning tunneling microscope", *Journal of Vacuum Science & Technology B: Microelectronics and Nanometer Structures*, vol. 6, no. 1, pp. 293-296, 1988.
- [53] T.R. Albrecht, M.M. Dovek, C.A. Lang, P. Grutter, C.F. Quate, S.W.J. Kuan, C.W. Frank and R.F.W Pease, "Imaging and modification of polymers by scanning tunneling and atomic force microscopy", *Journal of Applied Physics*, vol. 64, no. 3, pp. 1178-1184, 1988.
- [54] E.A. Dobisz and C.R.K. Marrian, "Sub30 nm lithography in a negative electron beam resist with a vacuum scanning tunneling microscope", *Applied Physics Letters*, vol. 58, pp. 2526-2528, 1991.
- [55] J. A. Dagata, J. Schneir, H.H Harary, C.J. Evans, M.T.Postek and J. Bennett, "Modification of hydrogen-passivated silicon by a scanningtunneling microscope operating in air", *Appl. Phys. Lett.*, vol. 56, pp. 2001-2003, 1990.
- [56] H.C. Day and D.R. Allee, "Selective area oxidation of silicon with a scanning force microscope", *Appl. Phys. Lett.*, vol. 62, pp. 2691-2693, 1993.
- [57] Ph. Avouris, R. Martel, T. Hertel, R. Sandstrom, "AFM-tip-induced and current-induced local oxidation of silicon and metals", *Applied Physics A-Materials Science & Processing*, vol. 66, pp. 659–667, 1998.
- [58] J. Cervenka, R. Kalousek, M. Bartosik, D. Skoda, O. Tomanec and T. Sikola, "Fabrication of nanostructures on Si(100) and GaAs(100) by local anodic oxidation", *Applied Surface Science*, vol. 253, pp. 2373–2378, 2006.

- [59] E. Dubois and J.-L. Bubbendorff, “Nanometer scale lithography on silicon, titanium and PMMA resist using scanning probe microscopy”, *Solid-State Electronics*, vol. 43, pp. 1085–1089, 1999.
- [60] R. Held, T. Heinzl, P. Studerus and K. Ensslin, “Nanolithography by local anodic oxidation of metal films using an atomic force microscope”, *Physica*, vol. E, no 2, pp. 748–752, 1998.
- [61] D. Wang, L. Tsau, K.L. Wang and P. Chow, “Nanofabrication of thin chromium film deposited on Si(100) surfaces by tip induced anodization in atomic force microscopy”, *Appl. Phys. Lett*, vol. 67, no. 9, pp. 1295–1297, 1995.
- [62] G. Binnig, C.F. Quate and Ch. Gerber, “Atomic force microscope”, *Physical review letters*, vol. 56, no. 9, pp. 930-934, 1986.
- [63] Instruction manual SolverP47.
- [64] R. Raiteri, M. Grattarola and R. Berger, “Micromechanics senses biomolecules”, *Materials today*, vol. 5, no. 1, pp. 22–29, 2002.
- [65] F.J. Giessibl, “Advances in atomic force microscopy”, *Rev. Mod. Phys.*, vol. 75, no. 3, pp. 949-983, 2003.
- [66] Y. Martin, C.C. Williams and H.K. Wickramasinghe, “Atomic force microscope–force mapping and profiling on a sub 100-Å scale”, *J. Appl. Phys.*, vol. 61, pp. 4723-4729, 1987.
- [67] W.W. Scott and B. Bhushan, “Use of phase imaging in atomic force microscopy for measurement of viscoelastic contrast in polymer nanocomposites and molecularly thick lubricant films”, *Ultramicroscopy*, vol. 97, pp. 151–169, 2003.
- [68] H.-J. Butt, B. Cappella and M. Kappl, “Force measurements with the atomic force microscope: Technique, interpretation and applications”, *Surface Science Reports*, vol. 59, pp. 1–152, 2005.
- [69] MultiMode SPM instruction manual.
- [70] E.S. Snow, G.G. Jernigan and P.M. Campbell, “The kinetics and mechanism of scanned probe oxidation of Si”, *Applied Physics Letters*, vol. 76, no. 13, pp. 1782–1784, 2000.
- [71] R. Garcia, R.V. Martinez and J. Martinez, “Nano-chemistry and scanning probe nanolithographies”, *Chem. Soc. Rev.*, vol. 35, pp. 29-38, 2006.
- [72] H. Sugimura, T. Uchida, N. Kitamma and H. Masuhara, “Scanning tunneling microscope tip-induced anodization for nanofabrication of titanium”, *J. Phys. Chem.*, vol. 98, pp. 4352-4357, 1994.

- [73] H. Sugimura and N. Nakagiri, "Chemical approach to nanofabrication: modifications of silicon surfaces patterned by scanning probe anodization", *Jpn. J. Appl. Phys.*, vol. 34, pp. 3406–3411, 1995.
- [74] N. Cabrera and N.F. Mott, "Theory of the oxidation of metals", *Rep. Prog. Phys.*, vol. 12, pp. 163-184, 1949.
- [75] A.E. Gordon, R.T. Fayfield, D.D. Litfin and T.K. Higman, "Mechanisms of surface anodization produced by scanning probe microscopes", *J. Vac. Sci. Technol. B*, vol. 13, pp. 2805-2808, 1995.
- [76] D.V. Sheglov, A.V. Latyshev and A.L. Aseev, "The deepness enhancing of an AFM-tip induced surface nanomodification", *Applied Surface Science*, vol. 243, pp. 138–142, 2005.
- [77] T. Teuschler, K. Mahr, S. Miyazaki, M. Hundhausen and L. Ley, "Nanometer-scale field-induced oxidation of Si(111):H by a conducting-probe scanning force microscope: Doping dependence and kinetics", *Appl. Phys. Lett.*, vol. 67, pp. 3144-3146, 1995.
- [78] D. Stievenard, P.A. Fontaine and E. Dubois, "Nanooxidation using a scanning probe microscope: An analytical model based on field induced oxidation", *Appl. Phys. Lett.*, vol. 70, pp. 3272-3274, 1997.
- [79] H. Sugimura, N. Kitamura and M. Mushuhara, "Modification of n-Si(100) surface by scanning tunneling microscope tip-induced anodization under nitrogen atmosphere", *Jpn. J. Appl. Phys.*, vol. 33, L143-L145, 1994.
- [80] M. Yasutake, Y.Y. Ejiri and T. Hattori, "Modification of silicon surface using atomic force microscope with conducting probe", *Jpn. J. Appl. Phys.*, vol. 32, pp. L1021-L1023, 1993.
- [81] J.A. Dagata, T. Inoue, J. Itoh and H. Yokoyama, "Understanding scanned probe oxidation of silicon", *Appl. Phys. Lett.*, vol. 73, pp. 271-273, 1997.
- [82] J.A. Dagata, F. Perez-Murano, G. Abadal, K. Morimoto, T. Inoue, J. Itoh and H. Yokoyama, "Predictive model for scanned probe oxidation kinetics", *Appl. Phys. Lett.*, vol. 76, pp. 2710-2712, 2000.
- [83] J.A. Dagata, F. Perez-Murano, C. Martin, H. Kuramochi and H. Yokoyama, "Current, charge, and capacitance during scanning probe oxidation of silicon. I. Maximum charge density and lateral diffusion", *J. Appl. Phys.*, vol. 96, pp. 2386-2392, 2004.
- [84] Ph. Avouris, T. Hertel and R. Martel, "Atomic force microscope tip-induced local oxidation of silicon: kinetics, mechanism, and nanofabrication", *Appl. Phys. Lett.*, vol. 71, pp. 285-287, 1997.

- [85] H. Jungblut, D. Wille and H.J. Lewerenz, "Nano-oxidation of H-terminated p-Si(100): influence of the humidity on growth and surface properties of oxide islands", *Applied Physics Letters*, vol. 78, no. 2, pp. 168-170, 2001.
- [86] M. Calleja and R. Garcia, "Nano-oxidation of silicon surfaces by noncontact atomic-force microscopy: Size dependence on voltage and pulse duration", *Appl. Phys. Lett.*, vol. 76, no. 23, pp. 3427-3429, 2000.
- [87] K. Hu, S. Wu, M. Huang, X. Hu and Q. Wang, "Effect of the tip-sample contact force on the nanostructure size fabricated by local oxidation nanolithography", *Ultramicroscopy*, vol. 115, pp. 7-13, 2012.
- [88] S. Nishimura, T. Ogino, Y. Takemura and J. Shirakashi, "Tapping mode SPM local oxidation nanolithography with sub-10 nm resolution", *Journal of Physics: Conference Series*, vol. 100, pp. 052021, 2008.
- [89] S. Nishimura, T. Toyofuku, K. Miyashita, Yasushi Takemura and J. Shirakashi, "Improvement of scanning probe microscopy local oxidation nanolithography", *J. Vac. Sci. Technol. B*, vol. 27, no. 2, pp. 948-952, 2009.
- [90] P.A. Fontaine, E. Dubois and D. Stievenard, "Characterization of scanning tunneling microscopy and atomic force microscopy-based techniques for nanolithography on hydrogen-passivated silicon", *J. Appl. Phys.*, vol. 84, pp. 1776-1781, 1998.
- [91] M. Tello and R. Garcia, "Nano-oxidation of silicon surfaces: Comparison of noncontact and contact atomic-force microscopy methods", *Appl. Phys. Lett.*, vol. 79, pp. 424-426, 2001.
- [92] M. Bartošik, D. Škoda, O. Tomanec, R. Kalousek, P. Jánký, J. Zlámal, J. Spousta, P. Du and T. Šikola, "Role of humidity in local anodic oxidation: A study of water condensation and electric field distribution", *Physical Review B*, vol. 79, pp. 195406, 2009.
- [93] U.F. Keyser, H.W. Schumacher, U. Zeitler, R.J. Haug and K. Eberl, "Fabrication of a single-electron transistor by current-controlled local oxidation of a two-dimensional electron system", *Applied Physics Letters*, vol. 76, no. 4, pp. 457-459, 2000.
- [94] T. Heinzl, R. Held, S. Luscher, K. Ensslin, W. Wegscheider and M. Bichler, "Electronic properties of nanostructures defined in Ga[Al]As heterostructures by local oxidation", *Physica E*, vol. 9, pp. 84-93, 2001.
- [95] J. Voves, M. Cukr and V. Novák, "The AFM LAO lithography on GaMnAs layers", *Microelectronic Engineering*, vol. 86, pp. 561-564, 2009.
- [96] J. Voves, Z. Soban, M. Janousek, V. Komarnickij, M. Cukr and V. Novak, "Nanostructures defined by the local oxidation of the ferromagnetic GaMnAs layer", *Microelectronics Journal*, vol. 40, pp. 697-705, 2009.

- [97] M. Janoušek, J. Halada and J. Voves, “Lithography on GaMnAs layer by AFM local anodic oxidation in the AC mode”, *Microelectronic Engineering*, vol. 87, pp. 1066–1069, 2010.
- [98] F.S.-S. Chien, Y.C. Chou, T.T. Chen, W.-F. Hsieh, T.-S. Chao and S. Gwo, “Nano-oxidation of silicon nitride films with an atomic force microscope: Chemical mapping, kinetics, and applications”, *Journal of Applied Physics*, vol. 89, no. 4, pp. 2465-2472, 2001.
- [99] E Tranvouez, P Budau and G Bremond, “Topographical and electrical study of contact and intermittent contact mode InP AFM lithography”, *Nanotechnology*, vol. 17, pp. 455–460, 2006.
- [100] L. Pellegrino, I. Pallecchi, D. Marre, E. Bellingeri and A.S. Siri, “Fabrication of submicron-scale SrTiO_{3-δ} devices by an atomic force microscope”, *Applied Physics Letters*, vol. 81, no. 20, pp. 3849-3851, 2002.
- [101] L. Pellegrino, Y. Yanagisawa, M. Ishikawa, T. Matsumoto, H. Tanaka and T. Kawai, “(Fe,Mn)₃O₄ nanochannels fabricated by AFM local-oxidation nanolithography using Mo/Poly(methyl methacrylate) nanomasks”, *Adv. Mater.*, vol. 18, pp. 3099–3104, 2006.
- [102] M. Rolandi, C.F. Quate and H. Dai, “A new scanning probe lithography scheme with a novel metal resist”, *Adv. Mater.*, vol. 14, no. 3, pp. 191-194, 2002.
- [103] J. Shirakashi, K. Matsumoto, N. Miura and M. Konagai, “Single-electron charging effects in Nb/Nb oxide-based single-electron transistors at room temperature”, *Applied Physics Letters*, vol. 72, no. 15, pp. 1893-1895, 1998.
- [104] A.B Oliveira, G. Medeiros-Ribeiro and A. Azevedo, “Submicron fabrication by local anodic oxidation of germanium thin films”, *Nanotechnology*, vol. 20, pp. 345301, 2009.
- [105] J.T.H. Tsai, B.H.B. Lee and M.S. Yang, “Fabrication of ZnO thin film transistors by atomic force microscopy nanolithography through zinc thin films”, *Physical Review B*, vol. 80, pp. 245215, 2009.
- [106] J.-H. Hsu, H.-W. Lai, H.-N. Lin, C.-C. Chuang and J.-H. Huang, “Fabrication of nickel oxide nanostructures by atomic force microscope nano-oxidation and wet etching”, *J. Vac. Sci. Technol B*, vol. 21, no 6. pp. 2599–2601, 2003.
- [107] H.-N. Lin, Y.-H. Chang, J.-H. Yen, J.-H. Hsu, I.-C. Leu and M.-H. Hon, “Selective growth of vertically aligned carbon nanotubes on nickel oxide nanostructures created by atomic force microscope nano-oxidation”, *Chemical Physics Letters*, vol. 399, pp. 422–425, 2004.
- [108] J. Shirakashi and Y. Takemura, “Ferromagnetic ultra-small tunnel junction devices fabricated by scanning probe microscope (SPM) local oxidation”, *Transactions on Magnetics*, vol. 40, no 4, pp. 2640-2642, 2004.

- [109] Y. Takemura, S. Kidaka, K. Watanabe, Y. Nasu, T. Yamada and J. Shirakashi, “Applied voltage dependence of nano-oxidation of ferromagnetic thin films using atomic force microscope”, *J. Appl Phys.*, vol. 93, no. 10, pp. 7346-7347, 2003.
- [110] M. Calleja, M. Tello and R. Garcia, “Size determination of field-induced water menisci in noncontact atomic force microscopy”, *J. Appl. Phys.*, vol. 92, 5539-5542, 2002.
- [111] M. Calleja, J. Anguita, R. Garcia, K. Birkelund, F. Perez-Murano and J. A. Dagata, “Nanometre-scale oxidation of silicon surfaces by dynamic force microscopy: reproducibility, kinetics and nanofabrication”, *Nanotechnology*, vol. 10, pp. 34–38, 1999.
- [112] E.B. Cooper, S.R. Manalis, H. Fang, H. Dai, K. Matsumoto, S.C. Minne, T. Hunt and C.F. Quate, “Terabit-per-square-inch data storage with the atomic force microscope”, *Applied Physics Letters*, vol. 75, no. 22, pp. 3566-3568, 1999.
- [113] R. Garcia, M. Calleja and H. Rohrer, “Patterning of silicon surfaces with noncontact atomic force microscopy: Field-induced formation of nanometer-size water bridges”, *Journal of Applied Physics*, vol. 86, no. 4, pp. 1898-1903, 1999.
- [114] A. Dorn, M. Sigrist, A. Fuhrer, T. Ihn, T. Heinzel, K. Ensslin, W. Wegscheider and M. Bichler, “Magnetotransport through AFM-defined antidot arrays”, *Physica E*, vol. 13, pp. 719–722, 2002.
- [115] B. Legrand, D. Deresmes and D. Stievenard, “Silicon nanowires with sub 10 nm lateral dimensions: from atomic force microscope lithography based fabrication to electrical measurements”, *J. Vac. Sci. Technol. B*, vol. 20, pp. 862–870, 2002.
- [116] S.C. Minne, H.T. Soh, P. Flueckiger and C.F. Quate, “Fabrication of 0.1 μm metal oxide semiconductor field-effect transistors with the atomic force microscope”, *Appl Phys Lett*, vol. 66, pp. 703-705, 1995.
- [117] E.S. Snow, P.M. Campbell, R.W. Rendell, F.A. Buot, D. Park, C.R.K. Marrian and R. Magno, “A metal/oxide tunneling transistor”, *Applied Physics Letters*, vol. 72, no. 23, pp. A75-A78, 1998.
- [118] J. Martinez, R.V. Martinez and R. Garcia, “Silicon nanowire transistors with a channel width of 4 nm fabricated by atomic force microscope nanolithography”, *Nano Lett.*, vol. 8, no. 11, pp. 3636-3639, 2008.
- [119] S. Hasegawa, S. Yamada, T. Yamada, J. Shirakashi and Y. Takemura, “AFM nano-oxidation of NiFe thin films capped with Al-oxide layers for planar-type tunnel junction”, *Transactions on Electrical and Electronic Engineering*, vol. 3, pp. 382–385, 2008.

- [120] Y. Takemura, S. Hayashi, F. Okazaki, T. Yamada and J. Shirakashi, “Direct modification of magnetic domains in Co nanostructures by atomic force microscope lithography”, *Japanese Journal of Applied Physics*, vol. 44, no. 9, pp. L285–L287, 2005.
- [121] A.N. Broers, “Resolution limits for electron-beam lithography”, *IBM J. Res. Dev.*, vol. 32, no. 4, pp. 502-513, 1988.
- [122] W. Chen and H. Ahmed, ““Fabrication of 5–7 nm wide etched lines in silicon using 100 keV electron beam lithography and polymethylmethacrylate resist””, *Appl. Phys. Lett.*, vol. 62, pp. 1499-1501, 1993.
- [123] D.R.S. Cumming, S. Thoms, S.P. Beaumont and J.M.R. Weaver, “Fabrication of 3 nm wires using 100 keV electron beam lithography and poly(methyl methacrylate) resist”, *Appl. Phys. Lett.*, vol. 68, pp. 322-324, 1996.
- [124] J.A. Liddle and S.D. Berger, “High-throughput projection electron-beam lithography employing SCALPEL”, *Proc SPIE*, vol. 2014, pp. 66–76, 1993.
- [125] Mapper Lithography, www.mapperlithography.com
- [126] P. Rai-Choudhury, *Handbook of Microlithography, Micromachining, and Microfabrication*, vol. 1 “Microlithography”, ch. 2 “Electron Beam Lithography”. SPIE Optical Engineering, 1997.
- [127] M. Altissimo, “E-beam lithography for micro-/nanofabrication”, *Biomicrofluidics*, vol. 4, pp. 026503, 2010.
- [128] M. Hatzakis, “Electron resists for microcircuit and mask production”, *J. Electrochem. Soc.*, vol. 116, no. 7, pp. 1033-1037, 1969.
- [129] G.H. Bernstein, D.A. Hill and W.P. Liu, “New high-contrast developers for PMMA resist,” *J. Appl. Phys.*, vol. 71, no. 8, pp. 4066-4075, 1992.
- [130] B. Berčič, *Introduction to Electron Beam Lithography*.
- [131] G.H. Bernstein and D.A. Hill, “On the attainment of optimum developer parameters for PMMA resist”, *Superlattices and Microstructures*, vol. 11, no. 2, pp. 237–240, 1992.
- [132] M. Wang, *Lithography*, ch. 13 “High-energy electron beam lithography for nanoscale fabrication”, 2010.
- [133] J. Golden, H. Miller, D. Nawrocki and J. Ross, “Optimization of Bi-layer Lift-Off Resist Process”, in *CS MANTECH Conference*, Tampa, Florida, USA, May 18th-21st, 2009.

- [134] Y. Chen, D.S. Macintyre, X. Cao and E. Boyd, "Fabrication of ultrashort T gates using a PMMA/LOR/UVIII resist stack", *Journal of Vacuum Science & Technology*, vol.21, no. 6, pp. 3012-3016, 2003.
- [135] I. Adesida and T.E. Everhart, "Substrate thickness considerations in electron beam lithography", *Journal of Applied Physics*, vol. 51, no. 11, pp. 5994, 1980.
- [136] W. Chen and H. Ahmed, "Fabrication of 5–7 nm wide etched lines in silicon using 100 keV electron beam lithography and polymethylmethacrylate resist", *Appl. Phys. Lett.*, vol. 62, pp. 1499-1501, 1993.
- [137] G.H. Bernstein and D.A. Hill, "On the attainment of optimum developer parameters for PMMA resist", *Superlattices and Microstructures*, vol. 11, no. 2, pp. 237-240, 1992.
- [138] M.J. Rooks, E. Kratschmer, R. Viswanathan, J. Katine, R.E. Fontana, Jr. and S.A. MacDonald, "Low stress development of poly(methylmethacrylate) for high aspect ratio structures", *J. Vac. Sci. Technol. B*, vol. 20, no. 6, pp. 2937-2941, 2002.
- [139] R. Brolsardt, F. Gotz and B. Rapp, "100 keV electron beam lithography process for high aspect ratio submicron structures", *Microelectronic Engineering*, vol. 27, pp. 139-142, 1995.
- [140] T.H.P. Chang, "Proximity effect in electron-beam lithography", *J. Vac. Sci. Technol.*, vol. 12, pp. 1271-1275, 1975.
- [141] K. Murata and D.F. Kyser, "Monte Carlo methods and microlithography simulation for electron and X-ray beams", *Advances in electronics and electron physics*, vol. 69, pp. 175-328, 1987.
- [142] M. Wang, *Lithography*, ch. 17 "Computer simulation of processes at electron and ion beam lithography, Part 1: exposure modeling at electron and ion beam lithography", 2010.
- [143] K. Harafuji, A. Misaka, K. Kawakita, N. Nomura, H. Hamaguchi and M. Kawamoto, "Proximity effect correction data processing system for electron beam lithography", *Journal of Vacuum Science and Technology B*, vol. 10, no. 1, pp. 2741-2745, 1992.

- [144] S. Lee and B. Cook, "PYRAMID – a hierarchical, rule-based approach toward proximity effect correction – part II: correction", *Transactions on Semiconductor Manufacturing*, vol. 11, no. 1, pp. 117-128, 1998.
- [145] S. J. Wind, P. D. Greber and H. Rothuizen, "Accuracy and efficiency in electron beam proximity effect correction", *Journal of Vacuum Science B*, vol. 16, no. 6, pp. 3262-3268, 1998.
- [146] E.H. Anderson, D.L. Olynick, W. Chao, B. Harteneck and E. Veklerov, "Influence of sub-100 nm scattering on high-electron beam lithography", *Journal of Vacuum Science*, vol. 19, no. 6, pp. 2504-2507, 2001.
- [147] D.J. Grant, *Electron-Beam Lithography: From Past to Present*. 2003.
- [148] E.A. Dobisz, R.B. Susan, L. Brandow, M.-S. Chen and W.J. Dressick, "Electroless metal discharge layers for electron beam lithography", *Applied Physics Letters*, vol. 82, no. 3, pp. 478-480, 2003.
- [149] W.-S. Huang, "Synthesizing and processing conducting polythiophene derivatives for charge dissipation in electron-beam lithography", *Polymer*, vol. 35, no. 19, pp. 4057-4064, 1994.
- [150] Z.C.H. Tan, C. Sauer, "Application of charge dissipation material in MEBES® phase shift mask fabrication", *Photomask Technology and Management*, Proc. SPIE, vol. 2322, pp. 141-148, 1994.
- [151] R. Steingruber, M. Ferstl and W. Pilz, "Micro-optical elements fabricated by electron-beam lithography and dry etching technique using top conductive coatings", *Microelectronic Engineering*, vol. 57–58, pp. 285–289, 2001.
- [152] P. Kirsch, M.B. Assouar, O. Elmazria, M.E. Hakiki, V. Mortet and P. Alnot, "Combination of e-beam lithography and of high velocity AlN/diamond-layered structure for SAW filters in X band", *Transactions on Ultrasonics, Ferroelectrics, and Frequency Control*, vol. 54, no. 7, pp. 1486-1491, 2007.

- [153] L.D. Jackel, R.E. Howard, E.L. Hu, D.M. Tennant and P. Grabbe, “50-nm silicon structures fabricated with tri level electron beam resist and reactive ion etching”, *Appl. Phys. Lett.*, vol. 39, no. 3, pp. 268-270, 1981.
- [154] L. Guo, E. Leobandung and S.Y. Chou, “A silicon single-electron transistor memory operating at room temperature”, *Science*, vol. 275, no. 5300, pp. 649-651, 1997.
- [155] S.W. Lee, S.J. Park, E.E.B. Campbell and Y.W. Park, “A fast and low-power microelectromechanical system-based non-volatile memory device”, *Nat Commun.*, vol. 20, art. no. 220, pp. 1-6, 2011.
- [156] W.Y. Chiu, T.W. Huang, Y.H. Wu, F.H. Huang, Y.J. Chan, C.H. Hou, H.T. Chien, C.C. Chen, S.H. Chen and J.I. Chyi, “Directional coupler formed by photonic crystal InAlGaAs nanorods”, *Journal of Lightwave Technology*, vol. 26, no. 5, pp. 488-491, 2008.
- [157] M.B. Assouar, O. Elmazria, P. Kirsch, P. Alnot, V. Mortet and C. Tiusan, “High-frequency surface acoustic wave devices based on AlN/diamond layered structure realized using e-beam lithography”, *J. Appl. Phys.*, vol. 101, pp. 114507, 2007.
- [158] Y.-W. Su, C.-S. Wu, C.-C. Chen and C.-D. Chen. “Fabrication of two-dimensional arrays of CdSe pillars using e-beam lithography and electrochemical deposition”, *Advanced materials*, vol.15, no. 1, pp. 49-51, 2003.
- [159] S.Y. Chou, P.R. Krauss and L. Kong, “Nanolithographically defined magnetic structures and quantum magnetic disk”, *Journal of Applied Physics*, vol. 79, no. 8, pp. 6101-6106, 1996.
- [160] C. Shearwood, S.J. Blundell, M.J. Baird, J.A.C. Bland, M. Gester, H. Ahmed and H.P. Hughes, “Magnetoresistance and magnetization in submicron ferromagnetic gratings”, *Journal of Applied Physics*, vol. 75, no. 10, pp. 5249-5256, 1994.
- [161] J.I. Martn, Y. Jaccard, A. Hoffmann, J. Nogués, J.M. George, J.L. Vicent and I.K. Schuller, “Fabrication of submicrometric magnetic structures by electron-beam lithography”, *Journal of Applied Physics*, vol. 84, no.1, pp. 411-415, 1998.
- [162] M. Ohring, *Materials science of thin films*. Academic press, 2001.
- [163] P.J. Kelly and R.D. Arnell, “Magnetron sputtering: a review of recent developments and applications”, *Vacuum*, vol. 56, pp. 159-172, 2000.
- [164] <http://www.directvacuum.com>
- [165] <http://www.sputter-coater.com>
- [166] I. Horcas, R. Fernández, J.M. Gómez-Rodríguez, J. Colchero and J. Gómez-Herrero, “WSXM: A software for scanning probe microscopy and a tool for Nanotechnology”, *Review of Scientific Instruments*, vol. 78, pp. 013705, 2007.

- [167] <http://www.gwyddion.net>
- [168] F. Czerwinski and J.A. Szpunar, “The influence of crystallographic orientation of nickel surface on oxidation inhibition by ceria coatings”, *Acta mater.*, vol. 46, no. 4, pp. 1403-1417, 1998.
- [169] L.P. Bonfisco and M. Frary, “Effects of crystallographic orientation on the early stages of oxidation in nickel and chromium”, *J. Mater. Sci.*, vol. 45, pp. 1663-1671, 2010.
- [170] I. Flis-Kabulska, B. Handke, N. Spiridis, J. Haber and J. Korecki, “Corrosion of epitaxial Fe(0 0 1) films studied with CEMS and AFM”, *Surface Science*, vol. 507–510, pp. 865–871, 2002.
- [171] C.A.F. Vaz, J.A.C. Bland, G. Lauhoff, “Magnetism in ultrathin film structures”, *Rep. Prog. Phys.*, vol. 71, pp. 056501, 2008.
- [172] A.S. Dzhumaliev, Y.V. Nikulin and Y.A. Filimonov, “Influence of the sample bias on the structure, the morphology and magnetic properties of the nickel films fabricated by magnetron DC sputtering”, *Nanoengineering*, no. 2, pp. 24-29, 2013 (on Russian).
- [173] A.S. Dzhumaliev, Y.V. Nikulin and Y.A. Filimonov, “The formation of the (200) and (110) textures in iron films prepared by magnetron sputtering”, *Technical Physics Letters*, vol. 39, no. 11, pp. 938-941, 2013.
- [174] C. Kittel, *Introduction to solid state physics*. John Wiley & Sons, 2005.
- [175] H.P. Klug and L.E. Alexander, *X-ray diffraction procedures: for polycrystalline and amorphous materials*. Wiley, 1974.
- [176] J.B. Wagner, K.R. Lawless and A.T. Gwathmey, “The rates of formation and structure of oxide films formed on single crystal of iron”, *Trans. Am. Inst. Mining Met. Eng.*, vol. 221, p. 257, 1961.
- [177] W.E. Boggs, R.H. Kachik and G.E. Pellissier, “The effects of crystallographic orientation and oxygen pressure on the oxidation of iron”, *J. Electrochem. Soc.*, vol. 114, no.1, pp. 32-39, 1967.
- [178] R.F. Mehl and E.L. McCandless, “Oxide Films on Iron”, *Trans. Am. Inst. Mining Met. Eng.*, vol. 125, pp. 531, 1937.
- [179] B.N. Shimbo, “Fabrication of lateral oxide barriers for metal singleelectron transistors”, Stanford University, Dissertation 2009.
- [180] P. A. Deymier, “Acoustic Metamaterials and Phononic Crystals”, *Springer Series in Solid-State Sciences*, vol. 173, 2013.

- [181] Y. Pennec, J.O. Vasseur, B. Djafari-Rouhani, L. Dobrzyński and P.A. Deymier, “Two-dimensional phononic crystals: Examples and applications”, *Surf. Sci. Rep.*, vol. 65, no 8, pp. 229-291, 2010.
- [182] M. Sigalas and E.N. Economou, “Band structure of elastic waves in two dimensional systems”, *Solid State Commun.*, vol. 86, no 3, pp. 141-143, 1993.
- [183] Y. Tanaka and S. Tamura, “Surface acoustic waves in two-dimensional periodic elastic structures”, *Phys. Rev. B*, vol. 58, no 12, pp. 7958-7965, 1998.
- [184] M. Torres and F.R. Montero de Espinosa, “Ultrasonic band gaps and negative refraction”, *Ultrasonics*, vol. 42, pp. 787-790, 2004.
- [185] A. Khelif, A. Choujaa, S. Benchabane, B. Djafari-Rouhani and V. Laude, “Experimental study of guiding and filtering of acoustic waves in a two dimensional ultrasonic crystal”, *Z. Kristallogr.*, vol. 220, pp. 836, 2005.
- [186] J.H. Page, S. Yang, Z.Y. Liu, M.L. Cowan, C.T. Chan and P. Sheng, “Tunneling and dispersion in 3D phononic crystals”, *Z. Kristallogr.*, vol. 220, pp. 859-870, 2005.
- [187] V. Laude, L. Robert, W. Daniau, A. Khelif and S. Ballandras, “Surface acoustic wave trapping in a periodic array of mechanical resonators”, *Appl. Phys. Lett.*, vol. 89, pp. 083515, 2006.
- [188] R.M. White and F.W. Voltmer, “Direct piezoelectric coupling to surface elastic waves”, *Appl. Phys. Lett.*, vol. 7, pp. 314-316, 1965.
- [189] R.F. Milsom, N.H.C. Reilly and M. Redwood, “Analysis of generation and detection of surface and bulk acoustic waves by interdigital transducers”, *IEE Transactions on Sonics and Ultrasonics*, vol. SU-24, no 3, pp. 147-166, 1977.
- [190] A. Darinskii, M. Weihnacht and H. Schmidt, “Surface acoustic wave scattering from steps, grooves, and strips on piezoelectric substrates,” *IEEE Transactions on Ultrasonics, Ferroelectrics, and Frequency Control*, vol. 57, pp. 2042–2050, 2010.
- [191] M. Hofer, N. Finger, G. Kovacs, J. Schoberl, S. Zaglmayr, U. Langer and R. Lerch, “Finite element simulation of wave propagation in periodic piezoelectric surface acoustic wave structures,” *IEEE Transactions on Ultrasonics, Ferroelectrics, and Frequency Control*, vol. 53, pp. 1192–1200, 2006.
- [192] D. Morgan, *Surface Acoustic Wave Filters*. Academic, London, 2007.
- [193] F. S. Hickernell, “Surface acoustic wave devices: a rewarding past, a significant present, and a promising future”, in *12th Int. Conf. Microwaves and Radar*, vol. 4, 1998, pp. 159–168.

- [194] D.S. Macintyre, I. Young, A. Glidle, X. Cao, J.M.R. Weaver and S. Thoms, “High resolution e-beam lithography using a thin titanium layer to promote resist adhesion”, in *31st International Conference on Micro- and Nano-Engineering*, vol. 83, 2006, pp. 1128–1131.
- [195] G. Kovacs, M. Anhorn, H. Engan, G. Visintini and C. Ruppel, “Improved material constants for LiNbO_3 and LiTaO_3 ,” in *Proceedings of 1990 IEEE International Ultrasonics Symposium*, pp. 435–438, IEEE, 1990.
- [196] G. Kaye and T. Laby, *Tables of physical and chemical constants and some mathematical functions*. Longman, London, 1986.
- [197] D. Nardi, E. Zagato, G. Ferrini, C. Giannetti, and F. Banfi, “Design of a surface acoustic wave mass sensor in the 100 GHz range,” *Applied Physics Letters*, vol. 100, pp. 253106, 2012.
- [198] J. Chicharro, A. Bayon and F. Salazar, “Dependence of δE -effect on internal stresses in nickel: Experimental results by laser interferometry,” *Journal of Magnetism and Magnetic Materials*, vol. 297, pp. 44–53, 2006.
- [199] R. Stevens, N. Frederick, B. Smith, D. Morse, G. Stucky, P. Hansma, “Carbon nanotubes as probes for atomic force microscopy”, *Nanotechnology*, vol. 11, pp. 1-5, 2000.
- [200] B. Bonello, A. Ajinou, V. Richard, Ph. Djemia and S.M. Cherif, “Surface acoustic waves in the GHz range generated by periodically patterned metallic stripes illuminated by an ultrashort laser pulse,” *Journal of Acoust. Soc. Of America*, vol. 110, pp. 1943–1949, 2001.
- [201] T. Palacios, F. Calle, J. Grajal, E. Monroy, M. Eickhoff, O. Ambacher and F. Omnès, “High frequency saw devices on algan: fabrication, characterization and integration with optoelectronics”, in *IEEE Ultrasonics Symposium-59*, 2002.
- [202] H. Hatakeyama, T. Omori, K. Hashimoto and M. Yamaguchi, “Fabrication of SAW devices using SEM-based electron beam lithography and lift-off technique for lab use”, in *IEEE International Ultrasonics, Ferroelectrics, and Frequency Control Joint 50th Anniversary Conference*, pp. 1896-1900, 2004.

Appendix A

Microstripes fabrication technology

Preparation of Au contact pads

1. Preparation of glass substrate: a) cleaning for 5 min in ultrasound bath by dichlormethan (CH_2Cl_2), acetone, IPA and DIW b) drying by nitrogen.
2. Deposition of Ti 20 nm /Au 100 nm for contact pads by sputtering (Figure A1 a). Deposition of Ti is needed to improve adhesion of Au.
3. Spincoating the adhesion promoter HMDS and negative resist AZnLOF 2020 on the substrate (Figure A1 b). Parameters of spincoater: speed 2.000 rpm, acceleration 1.000 rpm/s, time 20 s. 1 μm thick layer of resist is produced. A hotplate bake at temperature 110 °C for 60 s.
4. Exposure of the resist by UV light for 3 s using photomask of contact pads and post-bake on a hotplate at temperature 110 °C for 60 s (Figure A1 b).
5. Development of the unexposed resist in AZ 326 developer for 20 s (Figure A1 c). Rinsage by deionized water and dry by nitrogen.
6. Ion beam etching of Au (Figure A1 c-d). Orientation of the substrate on beam: 90°. The whole time of etching is 5-6 min.
7. Checking the conductivity of the substrate to confirm that Au was etched completely.
8. Removing remaining resist in Remover PG (Figure A1 e). Then rinsage by DIW and drying by nitrogen. Au contact pads are prepared.

Preparation of microstripes

9. Spincoating the adhesion promoter HMDS and positive resist AZ 1518 on the substrate (Figure A1 f). Parameters of spincoater: speed 4.500 rpm, acceleration 1.000 rpm/s, time 10 s. 1.6 μm thick layer of resist is produced. Bake on a hotplate at temperature 110 °C for 60 s.
10. Exposure of the resist by UV light for 2.3 s using photomask of microstripes and post-bake at temperature 110 °C for 60 s (Figure A1 f).
11. Development of the exposed resist in solution of AZ 400K developer and deionized water – AZ:DIW (1:3) for 30 s (Figure A1 g). Then to rinse by deionized water and dry by nitrogen.
12. Deposition of metal (Ni, FeCo) by sputtering (Figure A1 h).
13. Lift-off in Remover PG at temperature 70°C (Figure A1 i), rinsage by IPA and drying by nitrogen. Microstripes are prepared.

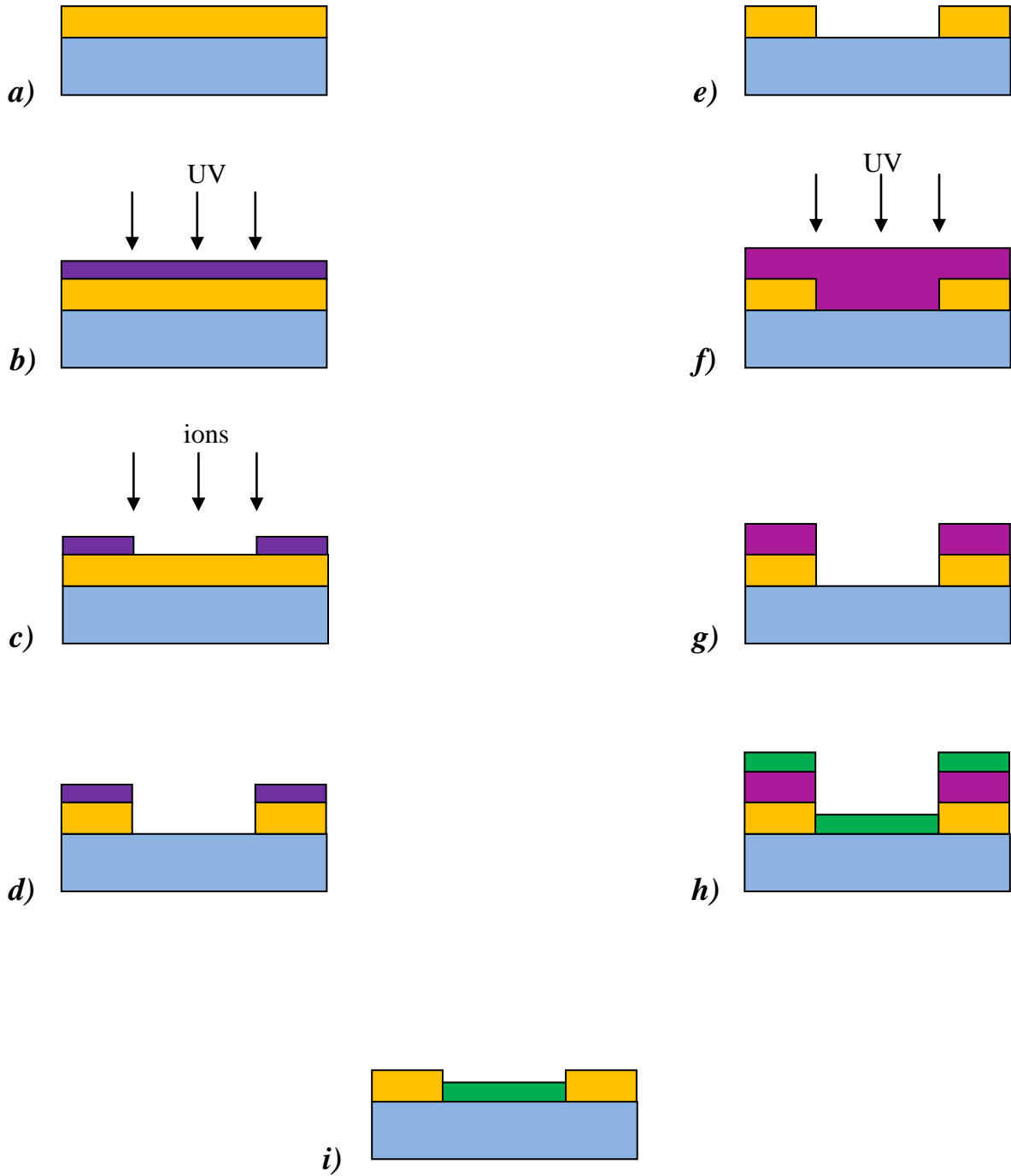
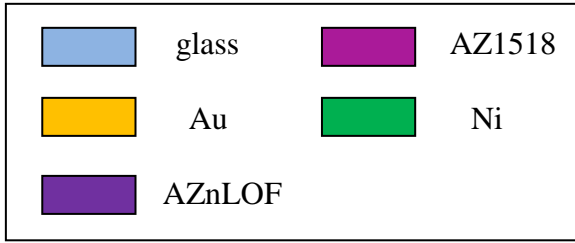


Figure A1. Scheme of microstripe fabrication technology.

For fabrication of microstripes with more clean edges bi-layer lift-off technology can be applied. For this technology 2 positive resists are used to obtain undercut resist profile. Such undercut profile will allow to do clean lift-off and to obtain well defined metal structures. The bottom layer should have a higher sensitivity to the exposure or a higher dissolution rate in the developer.

9. Preparation of glass or silicon substrate as before: a) cleaning for 5 min in ultrasound bath by dichloromethan (CH_2Cl_2), acetone, IPA and DIW b) drying by nitrogen.

10. Spincoating HMDS. Parameters of spincoater: speed 2.500 rpm, acceleration 3.000 rpm/s, time 12 s.

11. Spincoating positive resist LOR 10 (Figure A2 a). Parameters of spincoater: speed 2.500 rpm, acceleration 3.000 rpm/s, time 12 s with open cover and speed 1.500 rpm, acceleration 1.000 rpm/s, time 8 s with closed cover. 1 μm thick layer of resist is produced. Bake on a hotplate at temperature 180 °C for 240 s.

12. Spincoating positive resist S1805 (Figure A2 a). Parameters of spincoater: speed 3.700 rpm, acceleration 2.000 rpm/s, time 10 s. 0.5 μm thick layer of resist is produced. Bake at temperature 110 °C for 60 s.

13. UV exposure of the resist for 1.8 s with light intensity of 7.4 mW/cm^2 using photomask of microstripes and post-bake at temperature 120 °C for 60 s (Figure A2 a).

14. Development of the exposed resist in MF 319 developer for 15s with agitation + 120 s without agitation (Figure A2 b). Rinsage by DIW and drying by nitrogen.

15. Deposition of metal (Ni, FeCo) by sputtering (Figure A2 c).

16. Lift-off in Remover PG at temperature 70°C + applying of ultrasound for 2 minutes (Figure A2 d), rinsage by IPA and drying by nitrogen. Microstripes are prepared.

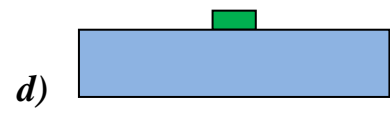
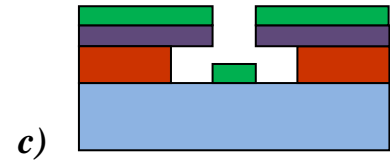
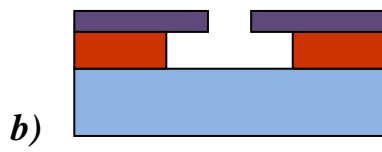
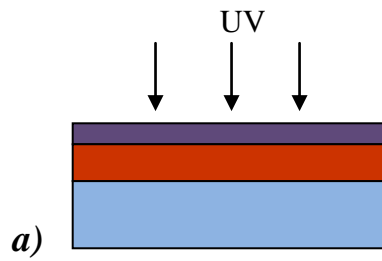
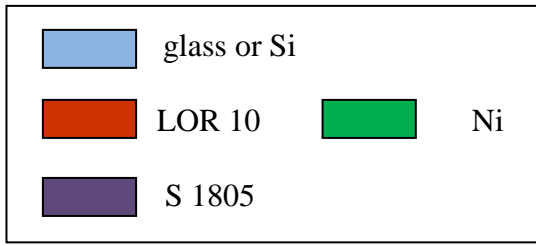


Figure A2. Scheme of bi-layer microstripe fabrication technology.

Préparation et études des propriétés des films magnétiques nanostructures pour des applications en dispositifs magneto-acoustiques et spintroniques

Aujourd'hui, les structures basées sur les matériaux ferromagnétiques sont largement utilisées pour différentes applications: mémoires magnéto-résistives à accès non séquentiel, capteurs magnétiques et également nouveaux composants électroniques et dispositifs spintroniques. La tendance générale de l'électronique moderne est une réduction de la dimension des éléments à l'échelle submicronique. Ainsi, les nanostructures magnétiques sont d'un grand intérêt et leurs méthodes de fabrication et propriétés sont étudiées activement.

Le but principal de ce travail est la préparation et la recherche expérimentale et théorique des propriétés de nanostructures magnétiques pour applications aux composants magneto-résistifs et phononiques. La lithographie à sonde locale (SPL) et la lithographie par faisceau d'électrons (EBL) ont été utilisées pour la fabrication des nanostructures. De premiers pas ont également été réalisés en fabrication des cristaux phononiques sensibles au champ magnétique.

Mots-clefs:

- Films magnétiques	- Lithographie à sonde locale
- Nanostructures	- Microscope à force atomique
- Ondes acoustique de surface	- Oxydation anodique locale
- Cristal phononique surface	-Lithographie par faisceau d'électrons

Preparation and studies of properties of nanostructured magnetic films for applications in magnetoacoustic and spintronic devices

Nowadays, structures based on ferromagnetic materials are largely used for different applications: random access magneto-resistive memories, magnetic sensors, and also new electronic components and spintronic devices. The general trend of modern electronic is the reduction of dimensions down to submicronic scales. Therefore, the magnetic nanostructures are of great interest and their methods of fabrication and properties largely studied.

The main goal of this work is the preparation and experimental and theoretical research on properties of magnetic nanostructures for applications in magnetoresistive and photonic devices. The Scanning Probe Lithography (SPL) and Electron Beam Lithography (EBL) were used for the nanostructures fabrications. First steps were also achieved in fabrication of phononic crystals sensitive the magnetic field.

Mots-clefs:

- Magnetic films	- Scanning probe lithography
- Nanostructures	- Atomic force microscope
- Surface acoustic waves	- Local anodic oxidation
- Surface phononic crystal	- Electron beam lithography